Film Cooling Heat Transfer Mechanism and Applications

Hao-Ming Li

A Thesis
In the Department
of
Mechanical, Industrial and Aerospace Engineering

Presented in Partial Fulfillment of the Requirements
For the Degree of
Doctor of Philosophy (Mechanical Engineering) at
Concordia University
Montreal, Quebec, Canada

February 2021

© Hao-Ming Li, 2021

CONCORDIA UNIVERSITY

School of Graduate Studies

This is to certify that the thesis prepared

By: Hao-Ming Li

Entitled: Film Cooling Heat Transfer Mechanism and Applications

and submitted in partial fulfillment of the requirements for the degree of

Doctor of Philosophy (Mechanical Engineering)

complies with the regulations of the University and meets the accepted standards with respect to originality and quality.

Signed by the final examining committee:

Pouya Valizadeh	Chair
Eric Laurendeau	External Examiner
Abdel Razik Sebak	External to Program
Hoi Dick Ng	Examiner
Ion Stiharu	Examiner
Wahid Ghaly	Thesis Supervisor(s)
Ibrahim Hassan	

Approved by: Ivan Contreras
Chair of Department or Graduate Program Director

July 28, 2021 Mourad Debbabi
Dean of Faculty

Abstract

Film Cooling Heat Transfer Mechanism and Applications

Hao-Ming Li, Ph.D.
Concordia University, 2021

Film cooling is a mainstay in cooling technology that is imperative in modern gas turbines. However, the improvement in film cooling performance research has leveled at a plateau for decades. Hence, it is urgent to clarify the film cooling heat transfer mechanism.

Recently, the effect of the counter-rotating vortex pair (CRVP) intensity on film cooling effectiveness was found to be more critical than the velocity related factor like momentum flux ratio. The present dissertation began with that factor of CRVP and concluded that the essential source of CRVP is the velocity gradients in the mainstream-coolant shear layer; the CRVP is mostly mainstream flow direction; and its main components are the relevant velocity gradients.

Along these findings, a mechanism of the film cooling heat transfer has been proposed: Film cooling heat transfer is mostly advection; strong velocity gradients at the mainstream-coolant interface produce secondary flow that penetrates the interface, hence drastically increases advection. These secondary flows are classified into mainstream entrainment, in which the flow is from the mainstream to the coolant, and coolant expansion, in which the flow is from the coolant to the mainstream. Mainstream entrainment drastically decays film cooling effectiveness, while coolant expansion is likely to increase film cooling effectiveness.

Therefore, two advanced film cooling schemes, named comb scheme and High Aspect Ratio (HAR) scheme, have been developed. The comb scheme was aimed to eliminate the mainstream entrainment by trapping the CRVP in its blind slot, while the HAR scheme was aimed to exploit the coolant expansion by drastically prolonging the coolant supply.

The new schemes were investigated numerically and experimentally, with transient thermochromic liquid crystal technique and steady RANS simulations coupled with realizable κ-ε turbulence model. Addition to demonstrating the so-called 'ideal performance', it has been shown that CRVP was trapped in the blind slot of the comb scheme, and coolant dominated the vicinity of the HAR exit trailing edge. They matched the designs. It convincingly proved the proposed film cooling heat transfer mechanism, established a solid fundamental for the film cooling research.

Dedication

To my wife, Xiao-Li WANG.

To my mother, Run-tian LI.

Contribution of Authors

All four manuscripts in this thesis are co-authored by Hao-Ming Li (H-M. L.), Wahid Ghaly (W. G.) and Ibrahim Hassan (I. H.).

H-M. L. thought up the idea and developed the theory. I. H. and H-M. L. devised the investigating outlines.

H-M. L. performed the computations and the experiments, acquired the data. H-M. L., W. G. and I. H. interpreted the data.

I. H. and H-M. L. framed the manuscripts. H-M. L. drafted the manuscripts. W. G. and I. H. gave critical feedbacks, and revised the manuscripts.

W. G. and I. H. supervised the results and the findings.

Table of Contents

Table of Contents vi
List of Figures ix
List of Tables xii
Nomenclature xiii
Greek Symbols xiii
Subscripts xiii
Superscripts xiv
Chapter 1 Introduction 1
1.1 Introduction 1
1.2 Motivation, Objectives and Organization 3
Chapter 2 The Formation of Counter-Rotating Vortex Pair and the Nature of Liftoff-Reattachment in Film-Cooling Flow 6
Abstract 6
2.1 Introduction 7
2.2 Methodology and Models 9
2.2.1 Geometry, Boundary Conditions and Numerical Models 9
2.2.2 Grid Independence and Validation 11
2.2.3 Variables Normalization 11
2.3 Results and Discussion 12
2.3.1 Formation of the Counter-Rotating Vortex Pair (CRVP) 14
2.3.2 The Mechanism of CRVP Formation 14
2.3.3 The Effect of the In-Tube Boundary Layer 18
2.3.4 Concluding Argument on the CRVP 22
2.3.5 The Nature of Liftoff and Reattachment 22
2.4 Conclusions 26
Chapter 3 New High Performance Schemes for Film Cooling Mechanisms 28
Abstract 28
3.1 Introduction 29
3.2 Methodology and Models 30
3.2.1 The Mechanism Underlying the CRVP Crucial Effect 31
3.2.2 The New Schemes Configuration 34
3.2.3 The TLC technique 35

3.2.4 Experimental Setup 39
3.2.5 Test Matrix and Parameter Normalization 39
3.3 Results and Discussions 40
3.3.1 Validation of the Experimental Facilities 42
3.3.2 Performance of the New Schemes 42
3.3.3 BR Effect of the New Schemes 45
3.3.4 Detail η Distributions 48
3.3.5 The $\overline{\eta_A}$ Performance of the New Schemes 50
3.4 Conclusions 50
Chapter 4 Experimental and Computational Investigations of a Comb-Like Film-Cooling Scheme 51
Abstract 51
4.1 Introduction 52
4.2 Methodologies and Models 54
4.2.1 Mechanism Underlying the CRVP Crucial Effect 55
4.2.2 Comb Scheme Configuration 57
4.2.3 Experimental Facility 59
4.2.4 Computational Setup 62
4.2.5 Test Matrix and Parameters Normalization 64
4.3 Results and Discussion 66
4.3.1 Validation of the Experimental Facility 67
4.3.2 Experimental Performance of the Comb Scheme 67
4.3.3 Experimental η Profiles 68
4.3.4 Validation of the Numerical Simulation 71
4.3.5 Geometric Effect of the Comb (New) Scheme 75
4.3.6 Detailed η and CRVP Distributions 85
4.4 Conclusions 89
Chapter 5 On The Use of High-Aspect-Ratio Film Cooling Scheme 91
Abstract 91
5.1 Introduction 92
5.2 Methodologies and Models 93
5.2.1 The Mechanism Underlying the CRVP Crucial Effect 95
5.2.2 The HAR Configuration 96
5.2.3 Experimental Facilities 98

5.2.4 Numerical Settings 100
5.2.5 Test Matrix and Parameters Normalization 102
5.3 Results and Discussion 102
5.3.1 Validation on the Experimental Facility 104
5.3.2 The Performance of the HAR Configuration 105
5.3.3 Assessment of the Computational Results 114
5.3.4 HAR Performance 121
5.3.5 Details of ω_x and η near the Hole Exit 121
5.3.6 CRVP and the Coolant Expansion 123
5.4 Conclusions 123
Chapter 6 Conclusions 125
6.1 A Summary 125
6.2 Contributions 127
6.3 Limitations 127
References 128

List of Figures

Figure 1.1 Figure 41 in [1]: Core engine performance evolution. 1
Figure 1.2 Film cooling..... 2
Figure 1.3 A sketch of the film cooling heat transfer mechanism 4
Figure 2.1 Geometry and boundary conditions of the baseline geometry 8
Figure 2.2 Grid independence and validation (BR = 1, DR = 2). 10
Figure 2.3 The near-field surface grid of the baseline case 11
Figure 2.4 Baseline 2D streamlines at the Y-Z planes around the exit (Br = 1)..... 13
Figure 2.5 2D streamlines of the unsteady case at the Y-Z planes close to the exit. (a) X/D = -1; (b) X/D = -0.75; (c) X/D = -0.5; (d) X/D = 0..... 15
Figure 2.6 Contours of vorticity and velocity gradients for the baseline (Case 1), at Y/D = 0.1 for Br = 1..... 17
Figure 2.7 Vorticity at the CRVP core..... 18
Figure 2.8 2D streamlines of the FSIT and baseline cases at the Y-Z plane of X/D = -0.25 18
Figure 2.10 Impact of the in-pipe boundary layer on the CRVP development 19
Figure 2.9 Contours of ω_x above the exit plane in FSIT (Y/D = 0.1)..... 19
Figure 2.11 Effectiveness contours on the test plate..... 20
Figure 2.12 The temperature contours downstream of the cooling duct hole. (a) Temperature contours θ at different span-wise planes right above the cooling duct hole; (b) θ at Z/D = 0, the hole centerline; (c) θ at Z/D = 0.125; (d) θ at Z/D = 0.25; (e) θ at Z/D = 0.375; (f) θ at Z/D = 0.5, near the hole edge.....21
Figure 2.13 Span-wise film-cooling effectiveness..... 22
Figure 2.14 θ contours on Y-Z planes before liftoff. (a) X/D = 0; (b) X/D = 0.5; (c) X/D = 1; (d) at liftoff position..... 23
Figure 2.15 θ contours on Y-Z planes before reattachment. (a) X/D = 2; (b) X/D = 3; (c) X/D = 4; (d) At reattachment position 24
Figure 3.1 Analysis on the mechanism of the film cooling heat transfer 31
Figure 3.2 The comb scheme configuration 32
Figure 3.3 The high-respect-ratio configuration..... 33
Figure 3.4 The calibration curves of the sample positions 34
Figure 3.5. The schematic diagram of the experimental system..... 36
Figure 3.6 Present and published data for the cylindrical hole [48] 40
Figure 3.7 The published data for the simple slot [49] 41
Figure 3.8 The simple slot comparison on blowing ratios with the published data [49]..... 43
Figure 3.9 The new scheme performance at BR = 1..... 44
Figure 3.10 The comb scheme performance of the configuration H = 1D, ts = 0.1D and P = 2ts..... 45
Figure 3.11 The slot η contours at BR = 1 46
Figure 3.12 The η distribution of the configuration $H = 1D$, $t_s = 0.1D$ and $P = 2t_s$ (cases of 12), BR = 1..... 46
Figure 3.13 The η distribution of the configuration $H = 0.5D$, $t_s = 0.1D$ and $P = 3t_s$ BR = 1 47
Figure 3.14 The η distribution of the configuration $HAR\ P = 3t$ BR = 1..... 47
Figure 3.15 $\overline{\eta_A}$ performance of the new schemes..... 49
Figure 4.1 The mechanism of film cooling heat transfer..... 53
Figure 4.2 Elimination of the mainstream entrainment 54

Figure 4.3 Comb scheme configuration 55
Figure 4.4. Schematic diagram of the experimental setup 56
Figure 4.5 Computational flow simulation domain 57
Figure 4.6 Simulation grids 58
Figure 4.7 Comparisons of measurements for a cylindrical hole (Cases 1-3 of Table 4.1 with [48]) 61
Figure 4.8 Comparisons of measurements for a simple slot (Cases 5 and 7 of Table 4.1 with [49]) 63
Figure 4.9 The Comb Scheme performance (Cases 10, 11 and 15 of Table 4.1) 65
Figure 4.10 BR effect while $H = D$, $t_s = 0.1D$ and $P_s = 2t_s$ (Cases 9-12 of Table 4.1) 66
Figure 4.11 The η distribution at BR = 1 (Case 6, 11 and 15 of Table 4.1) 69
Figure 4.12 Comparison of cylindrical hole at BR = 1 (cases 3 and 4 of Table 4.1 with [5, 10, 48]) 70
Figure 4.13 Comparison of slot at BR = 0.5 (Cases 5 and 8 of Table 4.1 with [49, 56]) 71
Figure 4.14 Comparison for the case $H = D$, $t_s = 0.1D$ and $P_s = 2t_s$ (Cases 10 and 13 of Table 4.1) 72
Figure 4.15 Effect of H on $\overline{\eta_L}$ 74
Figure 4.16 Effect of t_s on $\overline{\eta_L}$ 76
Figure 4.17 P_s/t_s effect on $\overline{\eta_L}$ 77
Figure 4.18 H effect on interface ω_x (Cases 16, 21 and 26 Table 4.1) 78
Figure 4.19 t_s effect on interface ω_x while $H = D$, $P_s = 2t_s$ (cases 14, 17 and 19 of Table 4.1) 79
Figure 4.20 P_s/t_s effect on interface ω_x while $H = D$, $t_s = 0.1D$ (Cases 14 and 16 of Table 4.1) 82
Figure 4.21 θ contours for Cases A and B at Y=0 (Cases 14 and 26 of Table 4.1) 83
Figure 4.22 Interface ω_x distributions for Cases A and B, at Y=0 (Cases 14 and 26 of Table 4.1) 84
Figure 4.23 CRVP for Case A (Case 14 of Table 4.1) 85
Figure 4.24 CRVP for Case B (Case 26 of Table 4.1) 86
Figure 4.25 The CRVP core positions for Case A and Case B of Table 4.1 89
Figure 5.1 Film cooling heat transfer mechanism 94
Figure 5.2 High-Aspect-Ratio scheme configuration 95
Figure 5.3 Schematic diagram of the experimental system 97
Figure 5.4 The computational domain 98
Figure 5.5 Grid independency 100
Figure 5.6 A close look of the mesh near the cooling hole exit 101
Figure 5.7 Experimental cylindrical hole data compared with published data (Cases 1-3 with [48]) 104
Figure 5.8 Experimental simple slot data compared with published data [68] (Cases 5 and 7) 106
Figure 5.9 Measured HAR performance for the case $t = 0.1D$ and $P = 2t$ at BR = 1 (Cases 3, 6 and 10) 107
Figure 5.10 Measured HAR performance for the case $t = 0.1D$ and $P = 2t$ at BR = 0.5 (Cases 1, 5 and 9) 108
Figure 5.11 Measured HAR performance for the case $t = 0.1D$ and $P = 2t$, (Cases 9-11) 109
Figure 5.12 Measured HAR performance for the case $t = 0.1D$ and $P = 3t$ at BR = 1, (Cases 3, 6 and 16) 110
Figure 5.13 Measured HAR performance for the case $t = 0.1D$ and $P = 3t$, (cases 16-18) 111

Figure 5.14 η distribution for the case t = 0.1D and P = 2t, at BR = 1 (Case 10) 112
Figure 5.15 η distribution for the case t = 0.1D and P = 2t, at BR = 0.5 (Case 9) 113
Figure 5.16 The η distribution of the case t = 0.1D and P = 3t, at BR = 1 (Case 16) 113
Figure 5.17 Comparison of cylindrical hole results at BR = 1 (Cases 3 and 4 with [10, 48])..... 114
Figure 5.18 Comparison of slot results at BR = 0.5 (Cases 5 and 8 with [37, 39])..... 115
Figure 5.19 Comparison of measured with numerical results for the case of t = 0.1D & P = 2t (Cases 9 & 12) 116
Figure 5.20 Comparison of numerical & measured results for the case of t = 0.1D & P = 3t (Cases 16 & 19) 117
Figure 5.21 The HAR performance at BR = 2 (cases 14, 20, 23, 26) 118
Figure 5.22 ω_x contours at the exit plane..... 119
Figure 5.23 η contours at the exit plane 120
Figure 5.24 CRVP and expansion..... 122

List of Tables

Table 2.1 Coolant flow trajectories 26
Table 3.1 Test matrix 38
Table 4.1 Test matrix 60
Table 4.2 CRVP intensity and the core positions 88
Table 5.1 Test matrix 103

Nomenclature

a	thermal diffusivity (m^2/s)
AR	aspect ratio (l/t); or cooling hole area ratio (hole exit-inlet area)
BR	blowing ratio ($\rho_j U_j/\rho_m U_m$)
CRVP	counter-rotating vortex pair
D	characteristic dimension (m)
DES	detached eddy simulation
DR	density ratio (ρ_j/ρ_m)
h	heat transfer coefficient ($w/(m^2 \cdot K)$)
HAR	high aspect ratio
I	momentum flux ratio ($\rho_j U_j^2/\rho_m U_m^2$)
JICF	jet in cross-flow
k	thermal conductivity ($W/(m \cdot K)$)
l	longitudinal length of cooling hole exit (m)
L	length of cooling hole passage (m)
P	lateral space of the film cooling geometry (m)
P_s	lateral space between two comb slits (m)
RANS	Reynolds-averaged Navier-Stokes
RKE	realizable κ-ε model
RLV	ring-like vortex
RSM	Reynolds stress model
t	lateral width of cooling hole exit (m)
t/P	lateral coverage ratio
T	temperature (K)
TLC	thermochromic liquid crystal
t_s	lateral width of comb slit (m)
U	velocity (m/s)
u, v, w	Cartesian coordinate velocities (m/s)
x, y, z	Cartesian coordinates
X, Y, Z	coordinate values (m)

Greek Symbols

η	adiabatic film cooling effectiveness ($(T_f - T_m)/(T_j - T_m)$)
ρ	density (kg/m^3)
θ	normalized temperature ($(T - T_m)/(T_j - T_m)$)
τ	transient time (s)
ω	vorticity

Subscripts

A	area
c	centerline
f	cooling film
i	initial state
j	jet

L	lateral
m	main stream
sp	span-wise
x	*x* component
w	wall conditions

Superscripts

*	value before normalization
-	averaged value

Chapter 1 Introduction

1.1 Introduction

Cooling technologies are imperative in modern gas turbine. Film cooling is the mainstay among them. Nowadays, the turbine inlet temperature (TIT) has been extremely high, over the melting temperature of the turbine components, due to its links to many key performance indicators such as the thermal efficiency of the gas turbine, the core power, the thrust to weight ratio, and so on. For example, core power is a parameter well suited in representing gas turbine performance; Figure 1.1, taken from [1] shows such relation, the green curve in the figure represents the ideal performance. It is a function of TIT, which goes up to 2000K, even higher TIT is targeted to obtain higher performance in the future. Film cooling is indispensable to the advanced gas turbine development to achieve the targeted temperatures.

Film cooling is intended to form a coolant film layer over the blade surface to protect it from the high temperature main flow. In a gas turbine, compressed air bled from the high stage compressor, bypasses the combustor, and impinges through the film cooling hole, onto the surface of the protected components like a vane or a blade surface. Ideally, the coolant jet is hoped to form a film covering the protected surface and separate it from the hot gases. A sketch of film cooling is shown in Figure 1.2. As film cooling uses the compressed air, film cooling effectiveness (η) is the most important parameter. It's defined as:

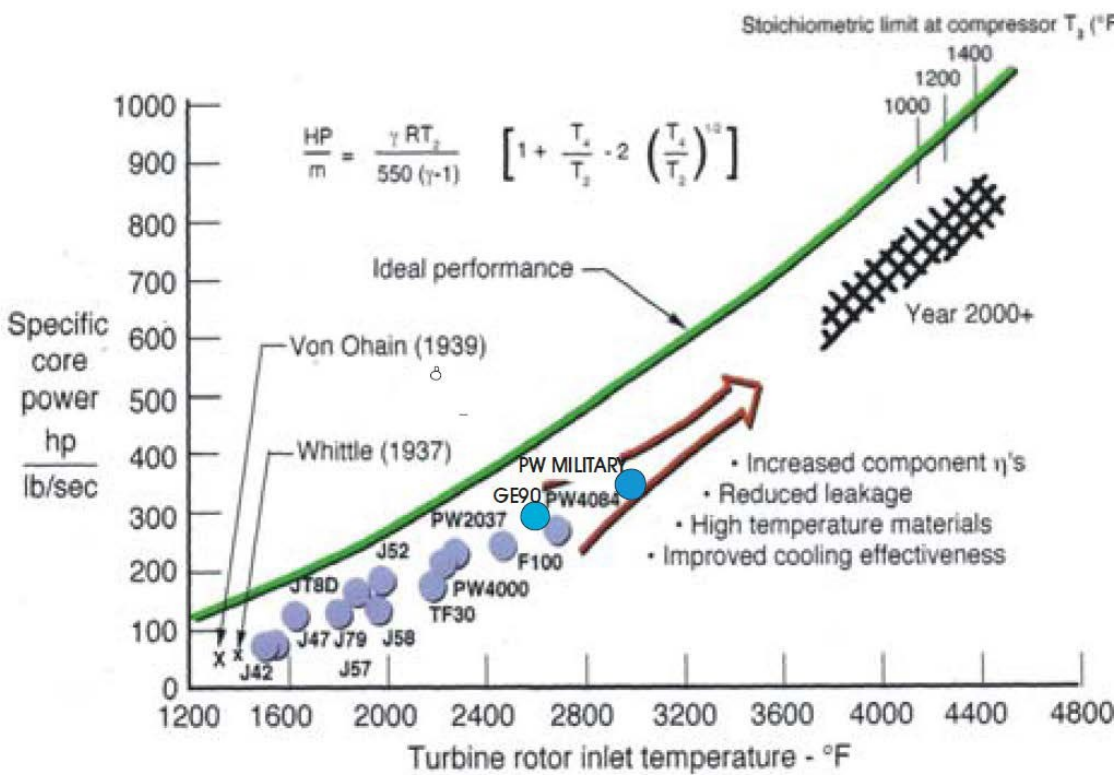

Figure 1.1 Figure 41 in [1]: Core engine performance evolution.

$$\eta = \frac{T_f - T_m}{T_j - T_m} \tag{1.1}$$

Film cooling geometry plays a main role on η. A slot is a simple rectangular film cooling geometry. Its thermal performance is so perfect that it is considered as 'ideal'. But it is rarely used on an airfoil, mostly because of its unpractical mechanical integrity. The discrete film cooling geometries, such as the cylindrical hole and the shaped holes, are applied on a real engine. The performance improvement of the shaped hole was so drastic that it is considered as a revolutionary discovery. In the past decades after the revolution, even large research efforts have been dedicated, no equivalent improvement has been achieved. The research in the gas turbine heat transfer and thermal management has reached a plateau [2]. It is urgent to clarify the complex mechanisms of the film cooling heat transfer, to guide the researcher in the new film cooling scheme.

As film cooling flow is so complicated, film cooling heat transfer mechanism is not clear yet. Many factors impact η [3]. Conventionally, it is most prevailing that the velocity relevant factors like the momentum flux ratio (I) and the blowing ratio (BR) of the film cooling flow are thought of as the crucial factors on η [3–5]. According to it, the researchers are encouraged to decrease the coolant jet velocity when they design new film cooling geometries, for example, to expand the exit as large as possible. However, some new research results are found to contradict this crucial effect [6].

A vortical structure in film cooling flow is named counter-rotating vortex pair (CRVP). Li and Hassan [7] discovered its crucial effect on η. They designed a special geometry, separated the factors of the CRVP intensity and the flux momentum ratio I, hence the CRVP intensity was found to be the most crucial factor on η, and proposed a correlation in the form:

$$\overline{\eta_A} = t/P + a\overline{\omega_x} \tag{1.2}$$

Here, $\overline{\eta_A}$ is the space averaged η; a is a constant; $\overline{\omega_x}$ is the stream wise CRVP intensity.

The present dissertation is aimed to clarify the film cooling heat transfer mechanism, and use it to obtain high performance film cooling scheme. As the CRVP intensity has been found as the most crucial factor on η, the present research starts with analyzing this flow structure in detail, aimed to find out the reasons underlying the crucial effect. Looking into the analyzing outputs

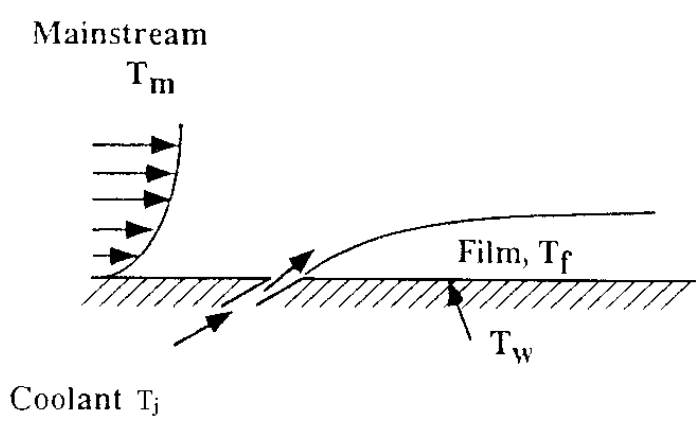

Figure 1.2 Film cooling

leads to a film cooling heat transfer mechanism. Applying the mechanism, two high performance film cooling schemes are developed. The investigations on these two new schemes show that their behaviors match the initial design.

1.2 Motivation, Objectives and Organization

As one of the most important directions in gas turbine researches, the improvement on film cooling has stalled for decades. The film cooling heat transfer mechanism has to be clarified immediately. The main objectives on this research are:

1. To compare the steady and unsteady simulation, and different turbulence models in film cooling flow simulations, particularly on capturing CRVP, thereby to prepare the computational investigations. Validate computation with measurements on present new film cooling schemes, addition to the open published data of a row of cylindrical holes and a simple slot.
2. To investigate the flow structure CRVP, including its essential source, its main components, its relations with the reattachment and the kidney shape of the coolant flow. Try to discover what is underlying its crucial effect on η, and find out ways to manipulate this flow structure.
3. To discover the film cooling heat transfer mechanism, it is underlying the crucial factor on η.
4. To apply the film cooling heat transfer mechanism, develop new film cooling schemes. The mechanism reveals two kinds of secondary flows, mainstream entrainment and coolant expansion. Two film cooling schemes, named comb scheme and high-aspect-ratio (HAR) scheme, are developed based on the new mechanism. The comb scheme is aimed to eliminate the mainstream entrainment, and the HAR scheme is aimed to exploit the coolant expansion.
5. To update the test rig, the test plate material and the test modules in particular. Validate the measurements with the open published data of a row of cylindrical holes and the simple slot.
6. To investigate the new schemes experimentally and numerically, demonstrate their high performance.
7. To investigate the geometric parameter effect on η, to observe the new scheme configurations changing the secondary flow, hence affecting η.

The current thesis is manuscript-based. It mostly consists of four journal manuscripts, from Chapter 2 to Chapter 5. As the CRVP intensity has been found to be the crucial factor on η, this flow structure is further investigated. The results are presented in Chapter 2, “The Formation of Counter-Rotating Vortex Pair and the Nature of Liftoff-Reattachment in Film-Cooling Flow”, in which the essential source of this flow structure, its main components, and its relations with the reattachment and the kidney shape of the coolant flow are analyzed.

Analysis of the outputs of the first paper shows that the crucial effect on η is caused by the velocity gradients (or the vorticity dynamics) in the mainstream-coolant shear layer. It demonstrated that strong velocity gradients occurring in this shear layer, which is mostly the vertical velocity at lateral direction in film cooling flow, produce secondary flows. Continuous secondary flow comes out as CRVP. Some of the secondary flows that penetrate the interface increase heat transfer drastically. They play a crucial role in film cooling heat transfer where advection is the dominant factor and diffusion is negligible.

This film cooling heat transfer mechanism is sketched in Figure 1.3. The following simplification is shown in the figure:

1. The mainstream-coolant interface thickness is deemed to be 0;
2. The CRVP size is ignored;
3. The offset between the CRVP position and the mainstream-coolant interface is also ignored.

The midline in this figure is the mainstream-coolant interface and is simplified into a line where the coolant flows to its left and the mainstream to its right. In the vicinity of the interface, large vorticity and associated velocity gradients occur, and lead to flow rotation. The vorticity ω on the interface produces mainstream flow penetration into the coolant side, which drastically increases the heat transfer between these two streams. The flow from the mainstream into the coolant is referred to as the mainstream entrainment. Meanwhile, the coolant penetration into the mainstream is the coolant expansion, which expands the coolant into the mainstream, likely to improve η.

According to the new mechanism, two film cooling schemes, named comb scheme and HAR scheme, are developed. The comb scheme is aimed to eliminate the mainstream entrainment, and the HAR scheme is aimed to exploit the coolant expansion. They are investigated experimentally and numerically. Their results compose three chapters (manuscripts) listed below:

1. The experimental results compose the 2nd manuscript, which is Chapter 3, titled as "New High Performance Schemes for Film Cooling Mechanisms"

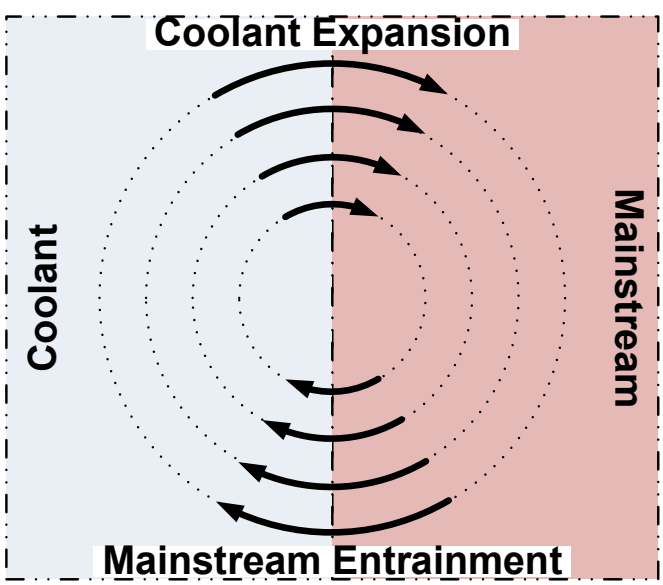

Figure 1.3 A sketch of the film cooling heat transfer mechanism

2. The results about the comb scheme compose the 3rd manuscript, which is Chapter 4, titled as "Experimental and Computational Investigations of a Comb-Like Film-Cooling Scheme"
3. The results about the HAR scheme compose the 4th manuscript, which is Chapter 5, titled as "On The Use of High-Aspect-Ratio Film Cooling Scheme".

Finally, the last chapter, Chapter 6, summarizes the conclusions of the present research.

Chapter 2 The Formation of Counter-Rotating Vortex Pair and the Nature of Liftoff-Reattachment in Film-Cooling Flow

Published in Fluids[1]

Abstract

Traditionally, the formation of the Counter-Rotating Vortex Pair (CRVP) has been attributed to three main sources: the jet-mainstream shear layer where the jet meets with the mainstream flow right outside the pipe, the in-tube boundary layer developing along the pipe wall, and the in-tube vortices associated with the tube inlet vorticity; whereas the liftoff-reattachment phenomenon occurring in the main flow along the plate right downstream of the jet has been associated with the jet flow trajectory. The jet-mainstream shear layer has also been demonstrated to be the dominant source of CRVP formation, whereby the shear layer disintegrates into vortex rings that deform as the jet convects downstream, becoming a pair of CRVPs flowing within the jet and eventually turning into the main flow direction. These traditional findings are assessed qualitatively and quantitatively for film-cooling flow in gas turbines by simulating numerically the flow and evaluating the extent to which the traditional flow phenomena are taking place particularly for CRVP and for flow liftoff-reattachment. To this end, three flow simulation cases are used; they are referred to as 1—the baseline case; 2—the free-slip in-tube wall case (FSIT); and 3—the unsteady flow case. The baseline case is a typical film-cooling case. The FSIT case is used to assess the in-tube boundary layer. Cases 1 and 2 are simulated using the Reynolds-averaged Navier-Stokes equations (RANS), whereas Case 3 solves a Detached Eddy Simulation (DES) model. It is concluded that decreasing the strength of the CRVP, which is the case for e.g., shaped holes, provides high cooling performance, and the liftoff-reattachment phenomenon was thus found to be strongly influenced by the entrainment caused by the CRVP, rather than the jet flow trajectory. These interpretations of the flow physics that are more relevant to gas turbine cooling flow are new and provide a physics-based guideline for designing new film-cooling schemes.

Keywords: counter-rotating vortex pair; source; CRVP formation; liftoff; reattachment

[1]Co-authors: Wahid Ghaly, Ibrahim Hassan

2.1 Introduction

Advanced gas turbines operate at extremely high temperatures to achieve high engine performance. Cooling techniques are indispensable to ensure the durability of the turbine components by protecting them from the hot mainstream gases. Film cooling is a widely used cooling technique. However, while protecting the turbine blades, film cooling impacts the engine performance negatively, particularly when the coolant penetrates the mainstream. Over the past decades, research efforts have been dedicated to improving film-cooling efficiency. Film cooling is accomplished by injecting jets of colder air bled from the compressor over the turbine blade vanes which gives rise to a series of fluid mechanical phenomena, the counter-rotating vortex pair (CRVP or CVP) being the one affecting the film-cooling effectiveness (η) most significantly.

Sinha *et al.* [5] proposed the momentum flux ratio (I) as the key factor influencing η. The coolant jet liftoff was also observed, and the film-cooling flow was classified into three flow types: attached, detached and reattached flow. The detachment-reattachment development was thought to be a function of the momentum flux ratio (I). Goldstein and Eckert [4] and Yu *et al.* [8] attributed the high performance of the diffusing cooling holes to the decrease in the jet mean velocity. Consequently, research efforts of improving film-cooling efficiency focused on decreasing the jet velocity by expanding the exit of the cooling hole. Ghorab *et al.* [9] and Zhang and Hassan [10] proposed the louver scheme. It has a large exit, and provides a performance superior to other film-cooling schemes. Zhang and Hassan [10] also compared the performance of four different RANS turbulence models: the κ-ε, κ-ω, Reynolds stress model (RSM) and Spalart-Allmaras model, coupled with different near-wall treatments. The realizable κ-ε (RKE) model coupled with the standard wall functions correctly predicted this flow and demonstrated good agreement with experimental data and was therefore used in this work in simulating cases 1 and 2.

The CRVP was thought to decrease the film-cooling performance significantly. Fric and Roshko [11] presented, in Figure 1 of their paper, an illustration to clarify the near-field vortical structures observed in their experimental investigation of a jet in crossflow (JICF). Their work was based on the assumption of circulation forming in the boundary layer. Accordingly, the CRVP was also thought to be formed from the in-hole boundary layer. Haven and Kurosaka [12] described the mechanisms of two vortical structures observed in a JICF. They were named kidney and anti-kidney vortices (another name for CRVP). The former were supposed to form from the span-wise boundary layers of the cooling hole, while the latter from the leading edge and trailing edge boundary layers. The anti-kidney vortices were supposed to decrease the strength of the kidney vortices. Correspondingly, Haven *et al.* [13] attributed the superior performance of the shaped hole to the anti-kidney vortices that could cancel out the negative effect of the kidney vortices.

Leylek and Zerkle [14] visualized a pair of counter-rotating in-tube vortices and the CRVP. The authors deduced that the jet trajectory was an important indicator of η. Walters and Leylek [15] identified the CRVP and deduced that the main source of the CRVP was the vorticity generated in the in-hole boundary layer. Based on this assumption, Hyams and Leylek [16] compared the performance of several hole shapes with the cylindrical hole, and proposed that the CRVP came from the X-component of the in-hole vorticity (X being the mainstream flow direction). Accordingly, the forward-diffused holes should have better performance than the laterally-diffused holes. However, their numerical study produced the opposite result which suggests that their argument is probably incomplete.

Kim and Hassan [17] employed a RKE-based DES model to simulate the film-cooling flow. CRVP was captured in this simulation. Its origin was thought to be due to the vorticity generated in the jet boundary layer. It was the only pattern that could be observed in steady flow.

CRVP is also an important topic in JICF. Kelso *et al.* [17] experimentally demonstrated that the in-hole boundary layer led to CRVP formation, and the in-hole flow separation at the cooling pipe entrance was an important factor affecting the CRVP formation. Yuan *et al.* [18] introduced a mechanism named hanging vortex. It was suggested to lead to the formation of the CRVP. This mechanism was also proposed by Recker *et al.*[19] . Guo *et al.* [20] suggested that the jet-crossflow shear layer and the in-hole vorticity were the two main contributors to CRVP. Marzouk and Ghoniem [21] performed an unsteady numerical simulation of the JICF. The shear layer was thought to be the source of CRVP and the ring-like vortex (RLV). The authors concluded that the shear layer rolled up and formed the RLV, which elongated axially on its lee side to form the CRVP. The authors also identified a crucial feature, namely that the CRVP was in the mean (steady) flow field, even though the roll-up of RLVs was periodic (unsteady). Their work was subsequently extended by Schlegel *et al.* [22] who focused on the boundary layer effects on

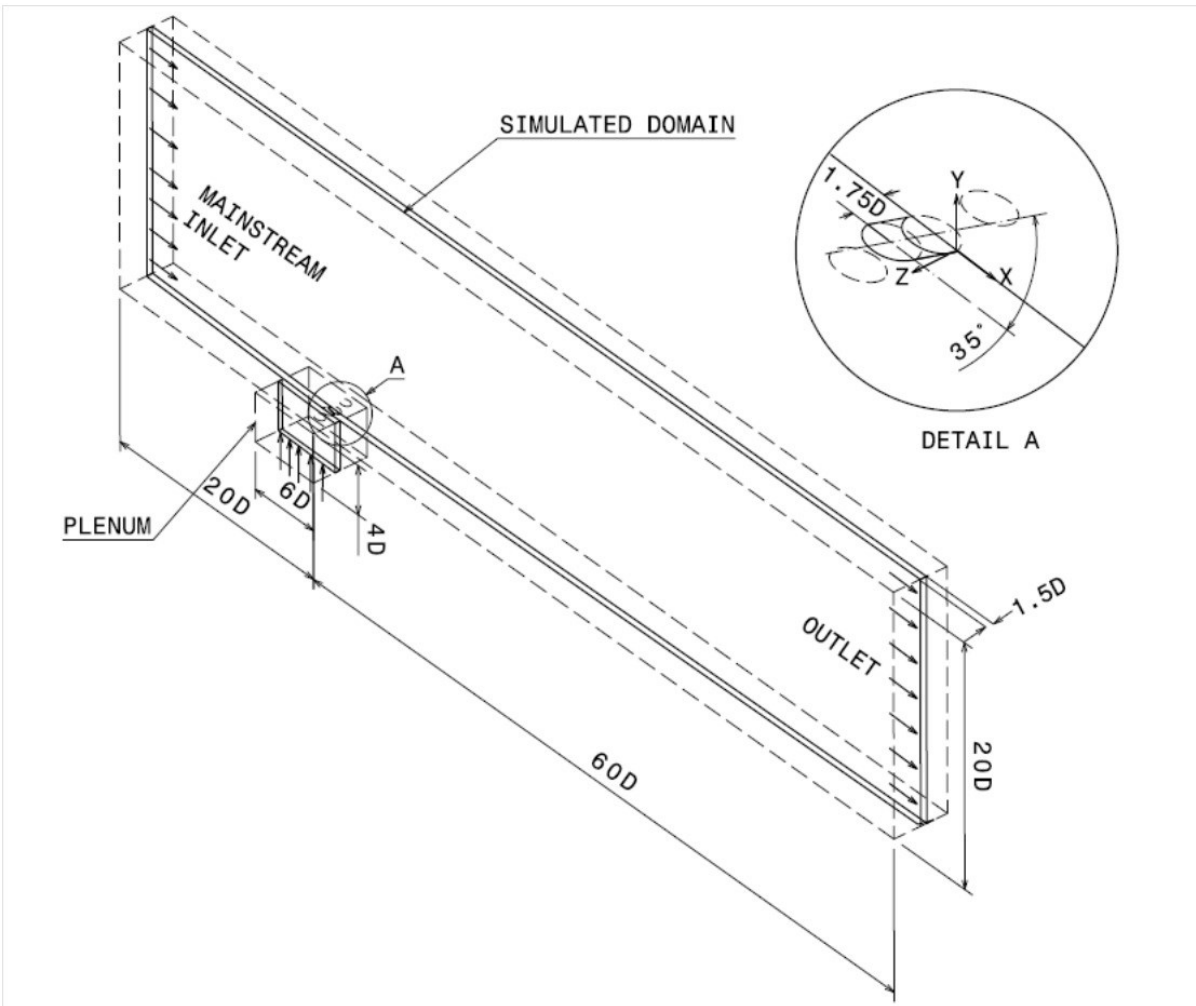

Figure 2.1 Geometry and boundary conditions of the baseline geometry

vortical structures. They proved that the wall boundary layer was not necessary for the initiation of CVP, but it enhanced the CRVP strength; however, its influence is at best a second-order effect on the large-scale structure of the jet flow field.

Several new film-cooling schemes related to CRVP have been proposed such as the double-jet proposed by Kusterer *et al.* [23], the branch holes proposed by Heidmann and Ekkad [24] and Dhungel *et al.* [25], and the sister hole scheme proposed by Ely and Jubran [26, 27]. The increased cooling performances were attributed to the decrease of the CRVP strength.

Li and Hassan [7] clarified the effects of the momentum flux ratio I and the CRVP on the film effectiveness η. The authors proposed that the CRVP strength is the most critical factor governing the film-cooling performance. Additionally, the momentum flux ratio has no direct impact on the film-cooling effectiveness, though it takes effect through CRVP.

As CRVP was identified as the key factor affecting η, the research direction of a new film-cooling scheme should aim to decrease CRVP strength. Therefore, the investigation of CRVP physics has become urgently needed. The CRVP was suggested to originate from in-tube vortices entering from the pipe inlet, in-tube boundary layer and/or jet-mainstream shear layer. The present paper is intended to clarify the main source of CRVP. Furthermore, the detached-reattached flow phenomenon was thought to be evidence of the momentum effect. The present paper will endeavor to determine the fundamentals of this phenomenon in the context of film-cooling flow in gas turbines.

2.2 Methodology and Models

2.2.1 Geometry, Boundary Conditions and Numerical Models

In the present investigation, three cases were numerically simulated. The first case corresponds to the experimental work of Sinha *et al.* [5] and was used as a baseline case for comparison with other cases. The computational domain (solid lines) and the test section of the experimental facility (dashed lines) are shown in Figure 2.1. The wind tunnel bottom surface is considered as the test plate. The wind tunnel is connected to the plenum through a row of inclined cylindrical holes. The hole inclination angle is 35°, its length (L) is 1.75D, and its pitch p is 3D. For further details related to the experimental setup, please refer to Sinha *et al.* [5].

The computational domain was extracted from the experimental facility. It is shown as solid lines in Figure 2.1. Only a half film-cooling hole is included in the domain; its span-wise width is 1.5D, i.e. half a pitch. The computational domain is bound by two symmetry planes in the span-wise direction. One is the center-plane passing through the cooling hole centerline, and the other is the plane passing midway between two cooling holes. The inlet velocity was set at 20 m/s at the wind tunnel inlet, along with an inlet temperature of 300 K. A velocity of 0.436 m/s was chosen to set the blowing ratio Br to 1, and a temperature of 150 K were specified at the plenum inlet. A pressure outlet with a zero-gage pressure was applied at the wind tunnel exit. The remaining walls were defined as adiabatic and no slip boundary condition, except the wind tunnel top wall that was set as a free slip wall.

As there was an opinion that the in-tube boundary layer effect was the main source of CRVP, Case 2, namely the free slip in-tube (FSIT) case, was simulated. It isolated the in-tube boundary layer effect. In the FSIT case, the geometry was the same as the baseline case, and all the boundary conditions were also identical to the baseline case except the in-tube wall, which was set as a free-slip wall. Therefore, the comparison of the baseline case and the FSIT case will indicate the effect of the in-tube boundary layer on the CRVP.

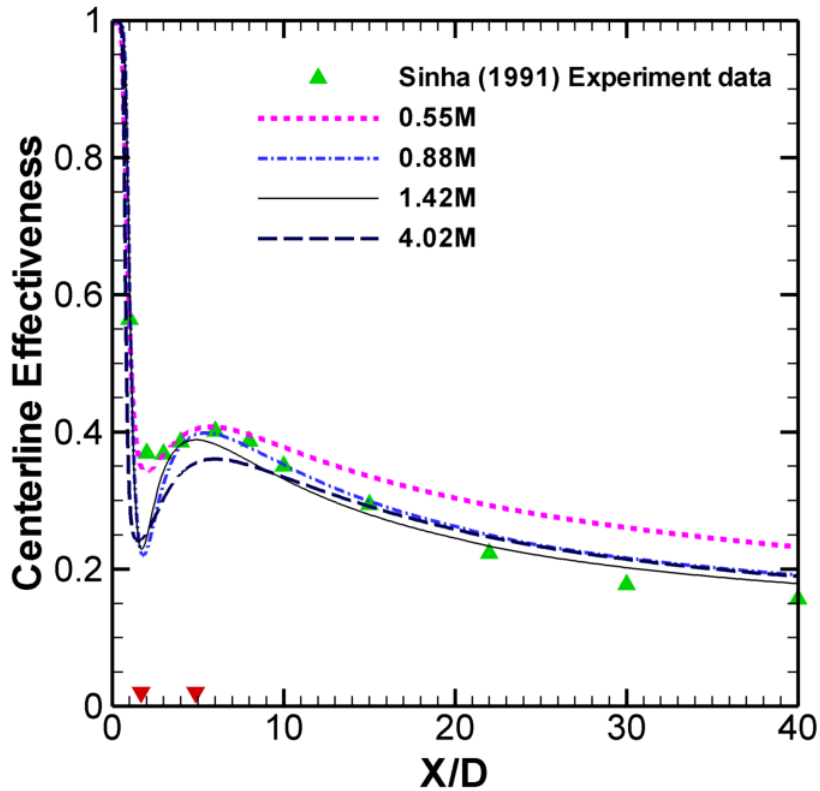

Figure 2.2 Grid independence and validation (BR = 1, DR = 2).

ANSYS-FLUENT, which is a CFD solver included in the ANSYS package, was used to simulate the flow in all three previously mentioned cases. A RANS turbulence model, the realizable κ-ε model (RKE) model, coupled with standard wall functions was used in the baseline and the FSIT cases. For further details about the computational domain, the boundary conditions and comparison of different turbulence models and near-wall treatments, please refer to Zhang and Hassan [10].

As the unsteady turbulence model is generally thought to capture more flow structures than the RANS models, Case 3, namely the unsteady flow simulation using DES developed by Kim and Hassan [17], was chosen. The computational domain was a full domain containing the whole cooling hole, its span-wise width was 3D (a full pitch). Case 3 used the RKE-based DES model. An extra 25,000 time steps (0.25 s) were added to the run to compute the time-averaged values

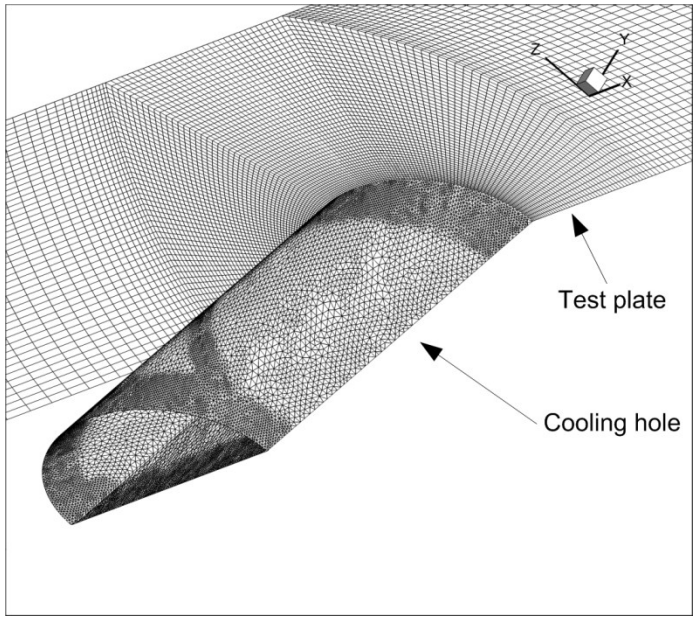

Figure 2.3 The near-field surface grid of the baseline case

of all variables such as velocity, temperature, and so on. Its near-field vortical structure was compared with that of the baseline. For further details about the unsteady case please refer to Kim and Hassan [17].

For all simulation cases, the origin of the Cartesian coordinates was located on the symmetry plane at the downstream edge of the hole exit, as shown in Figure 2.1. The X, Y, and Z axes were aligned with the mainstream, vertical, and span-wise directions, respectively.

2.2.2 Grid Independence and Validation

ANSYS-ICEM-CFD was used to generate the hybrid structured-unstructured mesh used in the baseline and FSIT cases. The computational domain was divided into two sub-domains, separated by the film-cooling hole exit. To test the grid independence, four grids were created for the baseline geometry. Their sizes ranged from approximately 0.55 million to 4.02 million cells. The baseline case was simulated using these four grids. The resulting film-cooling centerline effectiveness, presented in Figure 2.2, shows that a good agreement is obtained between experimental data and numerical results, and the typical phenomenon of liftoff and reattachment is well captured. Figure 2.2 shows also that, except for the coarsest mesh, the film-cooling effectiveness coincides rather well except in the range of $2 < X/D < 10$. To achieve a good compromise between saving computing resources and accurately capturing the vortical structures, the grid containing 1.42M cells was chosen for the baseline and FSIT. The positions of liftoff and reattachment, at X/D = 1.69 and 4.85, are labeled on the figure with red inverted triangles. The near-field surface mesh containing 1.42M grid points is shown in Figure 2.3.

2.2.3 Variables Normalization

Vorticity (ω), its X-component ω_x, and temperature θ were normalized with the following reference quantities: U_m = 20 m/s, D = 0.0127 m, T_m = 300 K and T_j = 150 K. ω and ω_x were defined as:

$$\omega = \frac{\omega^*}{U_m/\mathrm{D}} \tag{2.1}$$

$$\omega_x = \frac{\omega_x^*}{U_m/\mathrm{D}} \tag{2.2}$$

The asterisk refers to dimensional variables, e.g., ω_x^* was:

$$\omega_x^* = (-\frac{\partial v}{\partial z})^* + (\frac{\partial w}{\partial y})^* \tag{2.3}$$

And:

$$-\frac{\partial v}{\partial z} = \frac{(-\partial v/\partial z)^*}{U_m/\mathrm{D}} \tag{2.4}$$

$$\frac{\partial w}{\partial y} = \frac{(\partial w/\partial y)^*}{U_m/\mathrm{D}} \tag{2.5}$$

θ is defined in a way similar to η but it is valid in the whole simulated domain:

$$\theta = \frac{T_m - T}{T_m - T_j} \tag{2.6}$$

2.3 Results and Discussion

To assess the relative importance of each of the three sources that affect the formation and development of the CRVP, the flow fields for Cases 1–3 described in the previous section, are simulated numerically and used to visualize and analyze the CRVP formation and development in the main flow direction. These flow fields are also used to analyze the in-tube boundary layer effect. Finally, the mechanism of jet liftoff and reattachment is closely examined.

Before getting into presenting the results and discussing the flow physics, let us note that papers [4, 21, 22] are the papers that elaborated most on the flow physics of a jet in a cross flow and that these papers focused on a jet entering at 90° to the main flow and at a blowing ratio between 6 and 10. Because in the present case the jet enters at 35° and at a blowing ratio of 1, these differences have a drastic impact on interpreting the flow physics as will be evident in what follows.

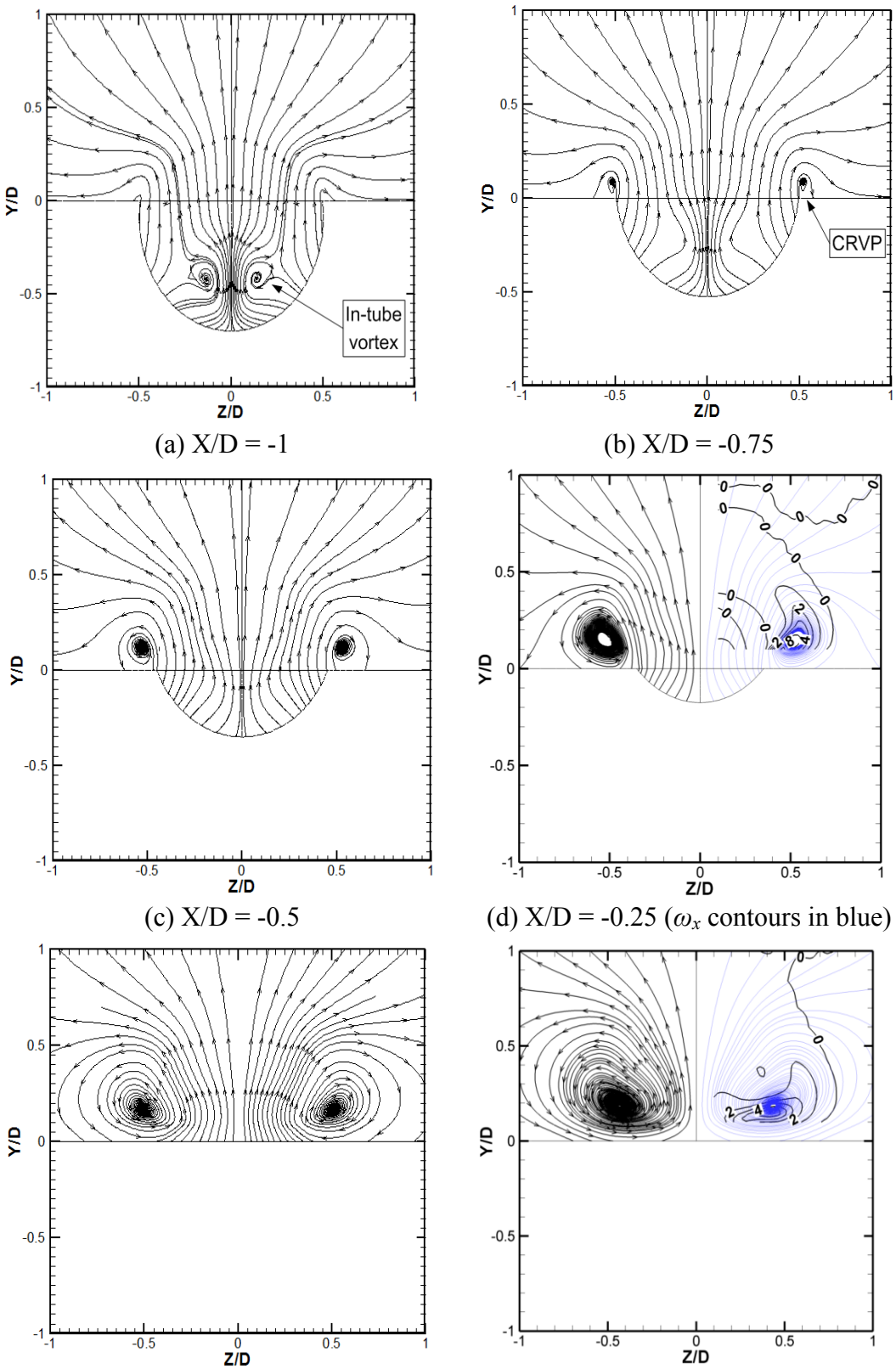

(a) X/D = -1

(b) X/D = -0.75

(c) X/D = -0.5

(d) X/D = -0.25 (ω_x contours in blue)

(e) X/D = 0

(f) X/D = 0.5 (ω_x contours in blue)

Figure 2.4 Baseline 2D streamlines at the Y-Z planes around the exit (Br = 1)

2.3.1 Formation of the Counter-Rotating Vortex Pair (CRVP)

From the results of Case 1—the baseline case—the CRVP formation process was visualized with 2D streamlines projected on the Y-Z plane near the jet exit, as shown in Figure 2.4. The computational domain is composed of half a cooling hole, while the figures are showing as a full hole domain by mirroring the data from the right side onto the left. At X/D = -1, shown in Figure 2.4a, the nascent CRVP is emerging at the edge of the hole exit. At positions (±0.14, -0.42), the in-tube vortices can still be identified. No direct relation between the in-tube vortices and the CRVP can be detected in this figure.

In Figure 2.4b, a small CRVP is formed at (±0.52, 0.09) and the in-tube vortices do not show as they do not pass by this axial location; however, its vestiges can still be recognized at (±0.2, -0.3). As the CRVP develops (Figure 2.4c), it becomes more distinct, and the core positions are located at (±0.53, 0.12). The CRVP continues to develop in Figure 2.4d, e, and the positions of the CRVP cores are located at (±0.53, 0.15) and (±0.51, 0.17), respectively. In Figure 2.4f, the CRVP is fully developed, dominating the jet flow and extending downstream. The cores are located at (±0.43, 0.19). Figure 2.4d, f show the ω_x contours (in blue) overlaid onto the streamlines so as to show the relation between the vortex core and the peak ω_x field. This relation will be described in the following subsection.

The previous investigations suggested three main sources contributing to the formation of CRVP. They are the jet-mainstream shear layer, the in-tube boundary layer and/or the in-tube vorticity. In Figure 2.4, neither the direct relation of the in-tube vortex nor the turning up of the boundary layer vortex from the tube can be detected. Therefore, the jet-mainstream shear layer effect is identified as the major source of the CRVP. The following paragraph will present Case 3, the unsteady flow simulation case, to demonstrate further the development of the in-tube vortices. In the following subsection, a comparison of Cases 1 and 2, the baseline and the FSIT cases, will demonstrate further the in-tube boundary layer effect.

A similar CRVP formation process was observed in Case 3, the unsteady flow simulation case. In Figure 2.5a, at X/D = −1, the budding CRVP is growing at the outer periphery of the hole exit. Additionally, a pair of in-tube vortices, referred to as "inner vortices" in Kim and Hassan [17], are observed at (−0.1, −0.4) and (0.15, −0.35). Compared with Figure 2.4a, the difference is negligible. In Figure 2.5b–d, the CRVP variation from the corresponding plots in Figure 2.4 is also negligible. However, the difference of the in-tube vortices cannot be neglected. They are still distinct in these three figures and stretch into the downstream direction, in contrast with the vanishing in-tube vortices in Figure 2.4. Interestingly, the unsteady simulation demonstrates more clearly that the CRVP formation has no direct relation with the in-tube vortices. Moreover, no turning up of the in-tube boundary layer vortex from the tube can be observed either.

2.3.2 The Mechanism of CRVP Formation

A key factor controlling the CRVP formation and development is the vorticity dynamics developing in the shear layer that forms near the pipe exit and its convection further downstream.

Figure 2.4 demonstrated that the CRVP cores and the vorticity peak were located at around Y/D = 0.1. Therefore, vorticity contours as well as other relevant variables for Case 1, the baseline case, are plotted at a horizontal plane Y/D = 0.1 (right above the hole exit) and are presented in Figure 2.6; the edge of the hole exit is shown as an ellipse. Figure 2.6a gives the distribution of ω, the peak value is approximately 15, and is located at (-0.9, 0.5) mainly along

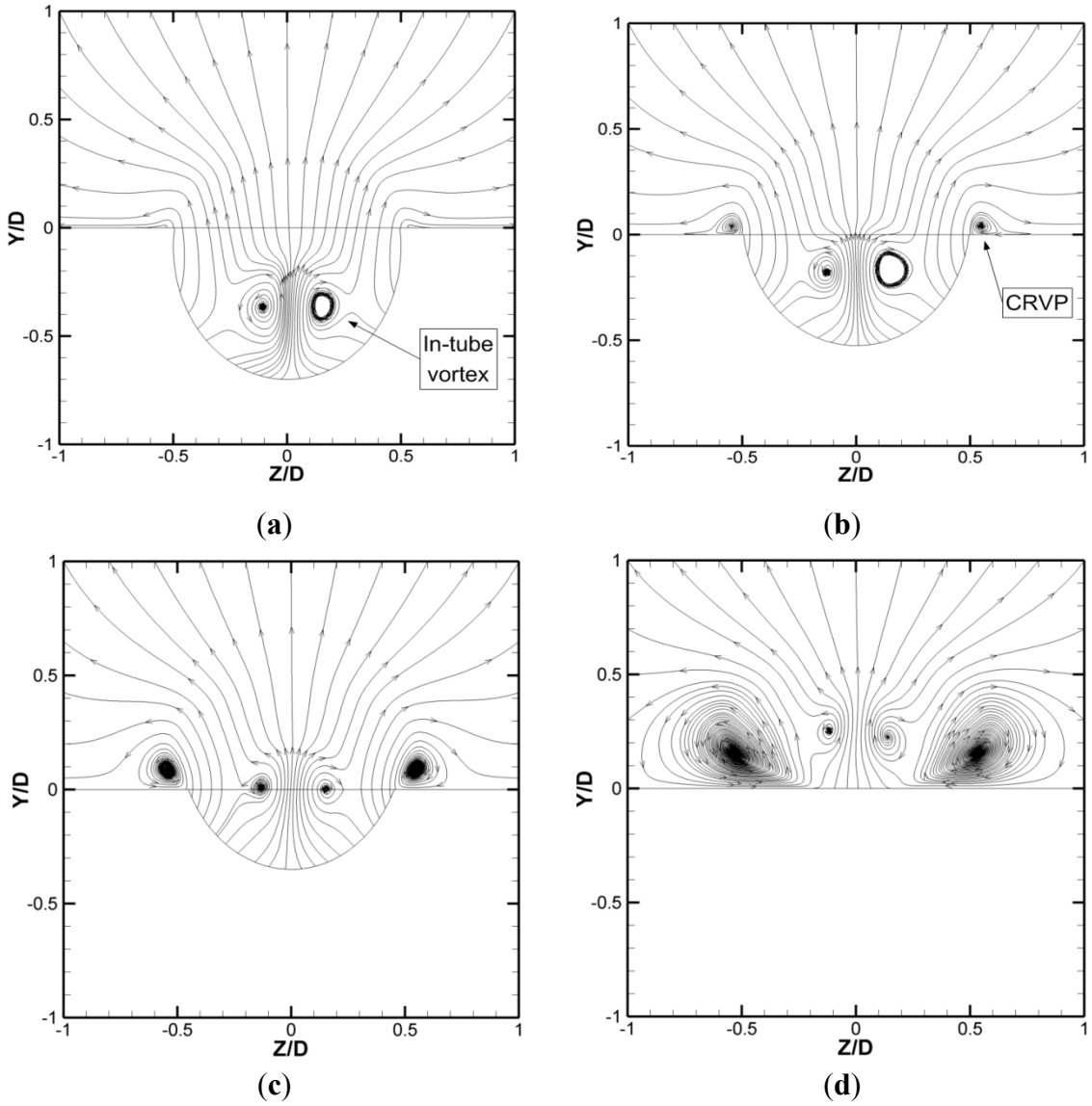

Figure 2.5 2D streamlines of the unsteady case at the Y-Z planes close to the exit. (a) X/D = -1; (b) X/D = -0.75; (c) X/D = -0.5; (d) X/D = 0

the edge of the hole exit, where the jet-mainstream interface is located. Note that this interface which is indicative of the shear layer (and the vortex sheet) convects with the jet flow into the mainstream direction, and gradually diffuses due to shear action.

The contours of ω_x, given in Figure 2.6b, are almost identical to those shown in Figure 2.6a. In fact, the maximum value of ω_x is about 14.7, and is located at the same position as that of ω. In summary, ω_x is the main component of the vorticity while the other two components can be safely neglected.

$$\|\vec{\omega}\|^2 = {\omega_x}^2 + {\omega_y}^2 + {\omega_z}^2, \tag{2.7}$$

$$\|\vec{\omega}\| \approx \omega_x \text{ and } \omega_y \approx 0, \omega_z \approx 0\,. \tag{2.8}$$

Based on Equation (2.3), $-\partial v/\partial z$ and $\partial w/\partial y$ contribute to ω_x hence to ω. They are presented in Figure 2.6c, d, for completeness. $-\partial v/\partial z$ has distribution similar to that of Figure 2.6a, b. Its maximum is approximately 11.6 and is located at (−0.9, 0.5), the same position in Figure 2.6a, b. In this position, $\partial w/\partial y$ is much less than $-\partial v/\partial z$, which is approximately 3. However, at X/D > −0.3, $\partial w/\partial y$ exceeds $-\partial v/\partial z$, and becomes the main contributor in this region. Its maximum is approximately 5.5 and is located at (0, 0.4). Figure 2.6c, d demonstrate that $-\partial v/\partial z$ is the main contributor of the CRVP in a cylindrical hole, and the main contributor switches to $\partial w/\partial y$ when the flow approaches the cooling hole exit.

As the CRVP strength influences, rather strongly, the film-cooling effectiveness, Figure 2.6 can guide the design of new film-cooling schemes as well as explain the high performance of the shaped holes, e.g., diffusing conical pipes. For example, decreasing the Y component velocity v decreases $-\partial v/\partial z$, which explains why expanding the exit or reducing the inclination angle can improve the film-cooling effectiveness. This observation is consistent with the conclusions found in the literature about the effect of the momentum flux ratio, I, on film-cooling effectiveness. Furthermore, increasing the Z value of the exit hole also decreases $-\partial v/\partial z$, which explains why the laterally expanded hole is better than the forward-expanded hole [16]. This observation also explains the experimental results of Haven and Kurosaka [12], where the CRVP of the stream-wise rectangular hole is much stronger than that in the span-wise rectangular hole, which results from the difference in $-\partial v/\partial z$.

In Figure 2.4d, f, the ω_x contours were overlaid onto the streamlines. In the region above the exit, e.g., Figure 2.4d, the CRVP cores coincide with the ω_x peak field. When moving downstream, these two positions branch out progressively, but remain very close in the near field, e.g., Figure 2.4f. The vorticity ω and the relevant variables along the trajectory of the CRVP cores are plotted in Figure 2.7. Compared with Figure 2.6, which reflected the CRVP character just above the exit, Figure 2.7 presents the character in the near field. Its ω_x distribution is coincident with that of ω. After X/D = 0.7, their values begin to deviate from each other very slowly. Their maxima, approximately 12, are located at X/D = −0.9. Their values start decreasing continuously. At X/D = 0, they are still greater than 6.5. Then, they drop down quickly to 2.2 at X/D = 0.7. Subsequently, they begin to decline slowly until reaching an asymptotic value of approximate 0.5 in the far field.

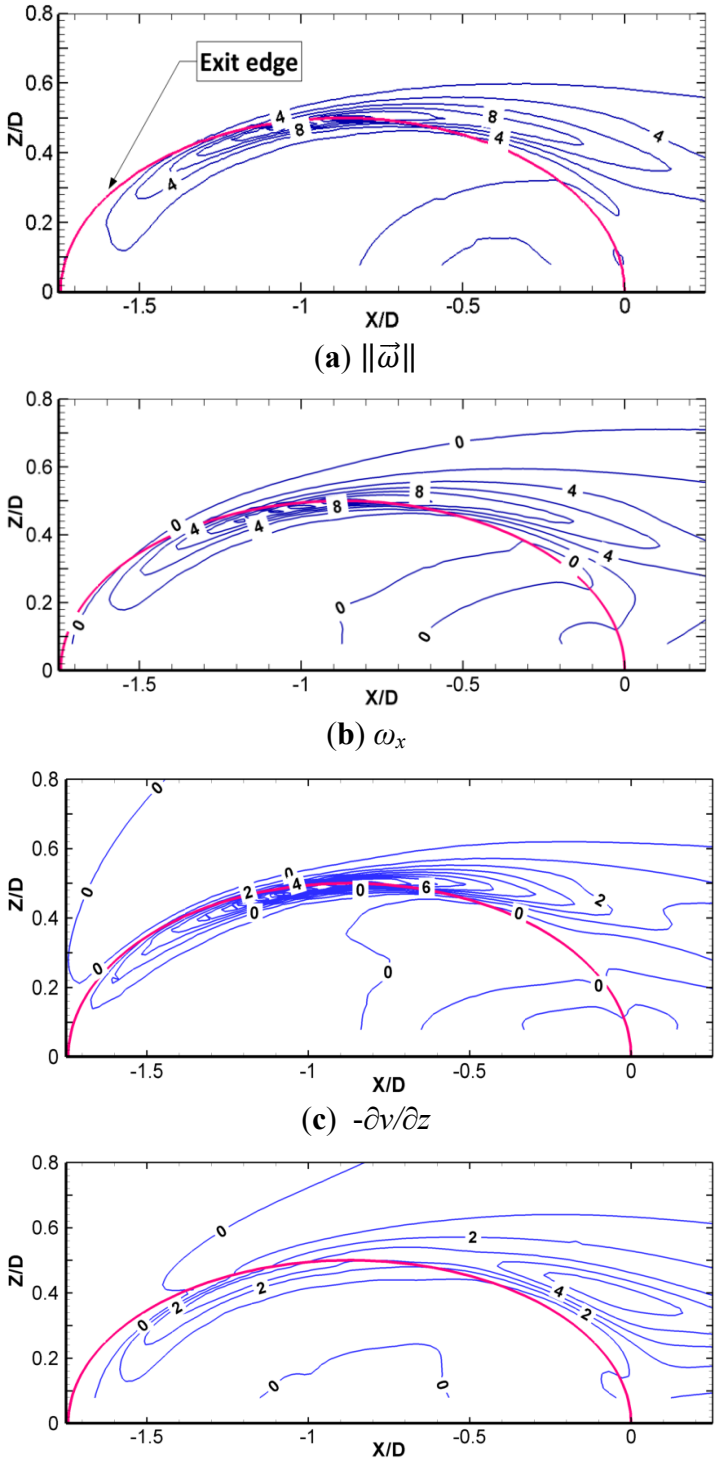

(**a**) $\|\vec{\omega}\|$

(**b**) ω_x

(**c**) $-\partial v/\partial z$

(**d**) $\partial w/\partial y$

Figure 2.6 Contours of vorticity and velocity gradients for the baseline (Case 1), at Y/D = 0.1 for Br = 1

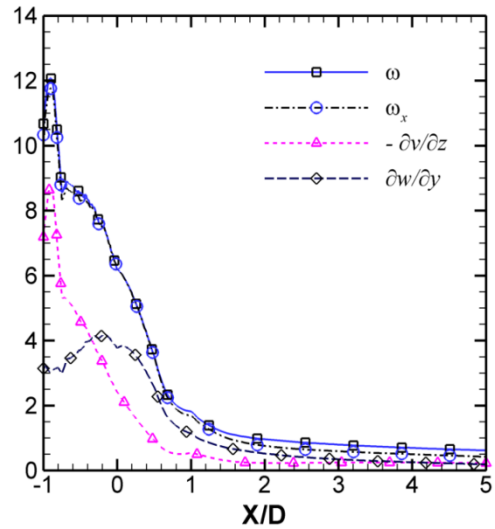

Figure 2.7 Vorticity at the CRVP core

2.3.3 The Effect of the In-Tube Boundary Layer

Figure 2.8 compares the CRVP of the FSIT case to that of the baseline at the Y-Z plane of X/D = 0.25. The left part (Z/D < 0) is the FSIT case and the right part (Z/D > 0) is the baseline. No distinction can be identified between the two cases. As the in-tube boundary layer effect was isolated in the FSIT case, the in-tube boundary layer also has no significant influence on the CRVP.

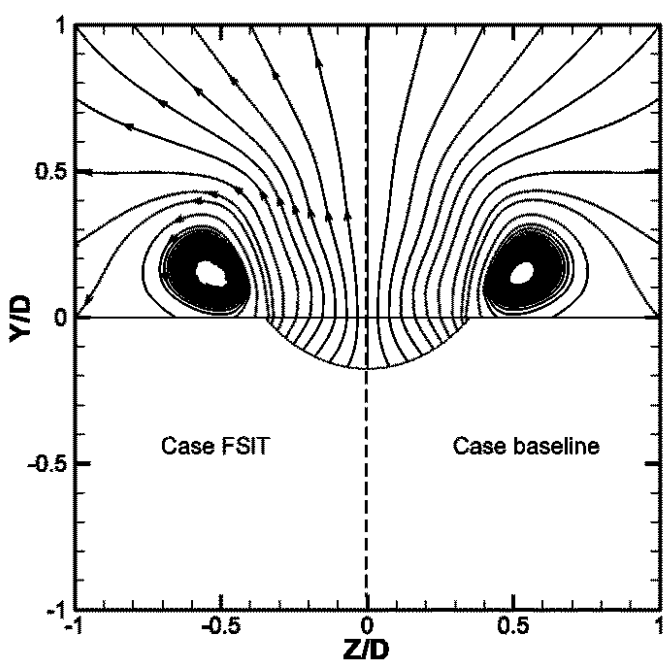

Figure 2.8 2D streamlines of the FSIT and baseline cases at the Y-Z plane of X/D = -0.25

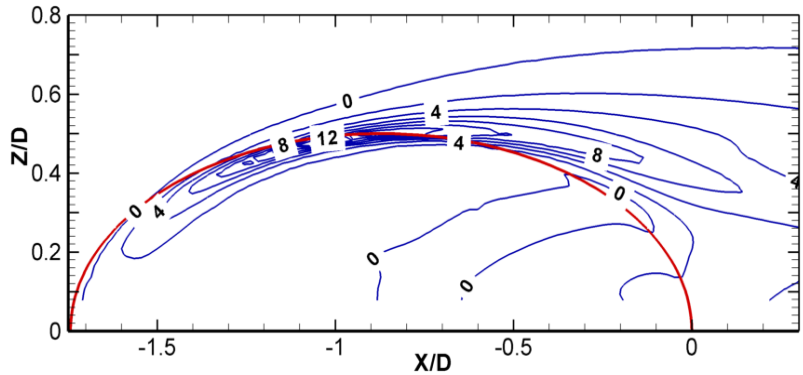

Figure 2.10 Contours of ω_x above the exit plane in FSIT (Y/D = 0.1)

Figure 2.9 presents the ω_x contour of the FSIT case. In contrast with Figure 6b, the difference can be neglected. In fact, the local maximum value in this case is approximately 15, and is slightly higher than that of the baseline. The comparison of the vorticity along the CRVP cores between Case 2, the FSIT case, and Case 1, the baseline case, is shown in Figure 2.10. Minute differences can be observed for ωx; in the near field ω_x for Case 2 is slightly higher than that of the baseline and is slightly smaller in the region from X/D = 0 to 1. These small differences in ω_x are a direct consequence of the elimination of the no-slip boundary condition on the in-pipe walls resulting in higher vorticity strength in the near-wall region. These comparisons demonstrate that, compared with the shear layer effect on the CRVP, the in-tube boundary layer has a second-order effect. This conclusion is true at least for L/D = 1.75 which is used in this work.

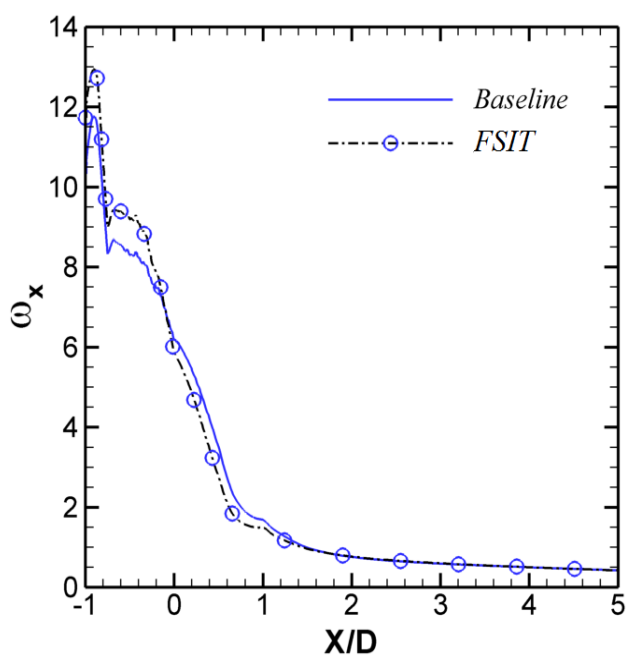

Figure 2.9 Impact of the in-pipe boundary layer on the CRVP development

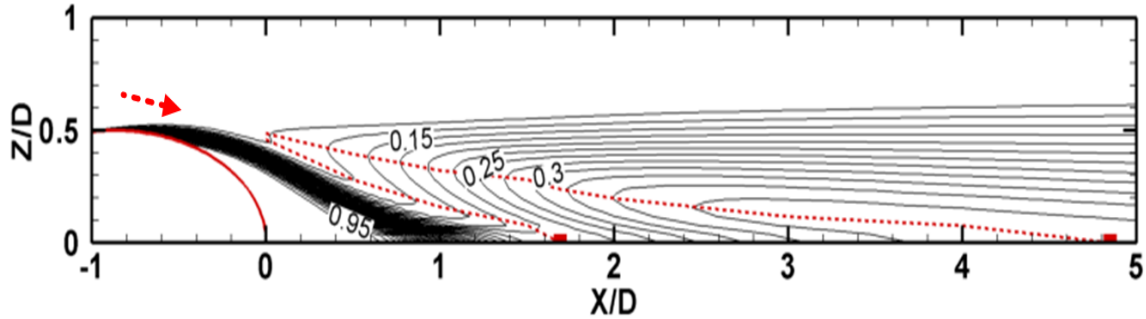

Figure 2.11 Effectiveness contours on the test plate

It is worth noting that this reduction seems opposite to the conclusion of Schlegel *et al.* [22], where the boundary layer effect was found to strengthen the CRVP significantly. These opposite effects are supposed to result from the difference of the CRVP mechanisms in these two types of flow. We speculate that the main component of the CRVP in JICF is ω_y, which is mainly driven by $\partial u/\partial z$. In film-cooling flow, v in the jet flow is higher than that in the mainstream. A sharp velocity profile in the in-tube boundary layer can raise the velocity gradient in the shear layer. On the other hand, in JICF, the jet axial velocity component is lower than that of the mainstream. A sharp velocity profile will reduce the velocity gradient. As this opposite effect is not the focus of the present investigation, it will not be considered here.

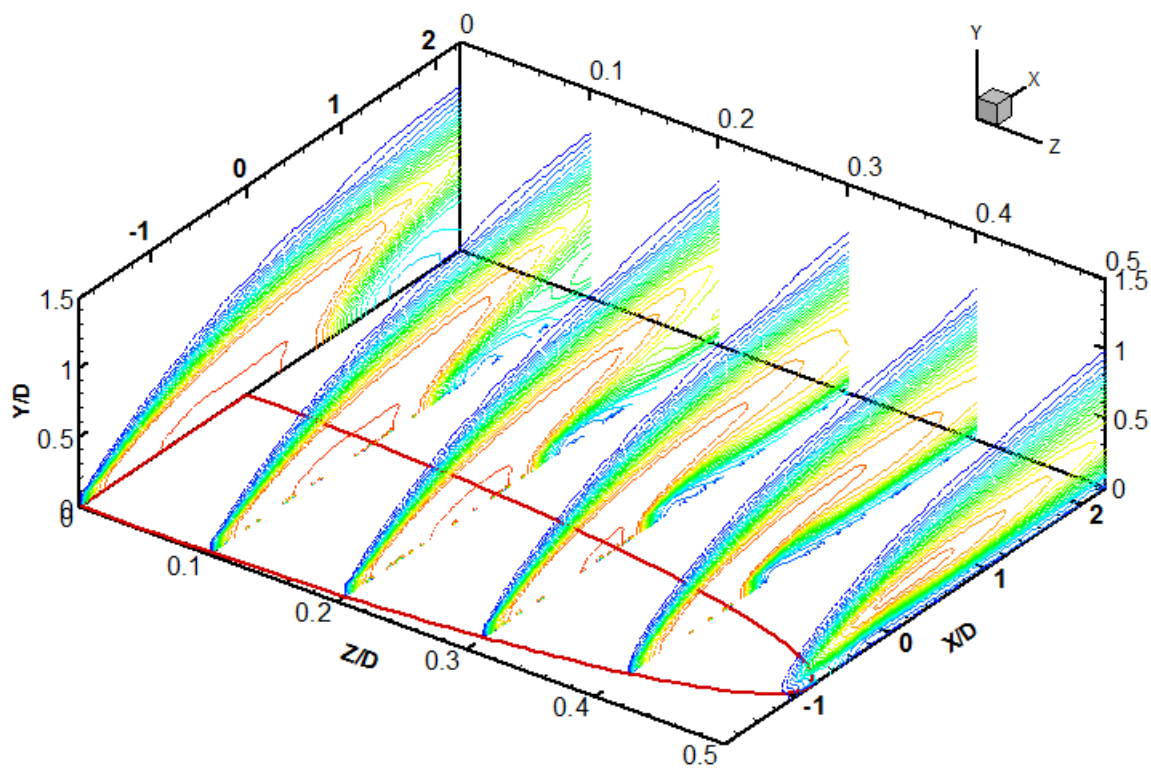

(**a**)

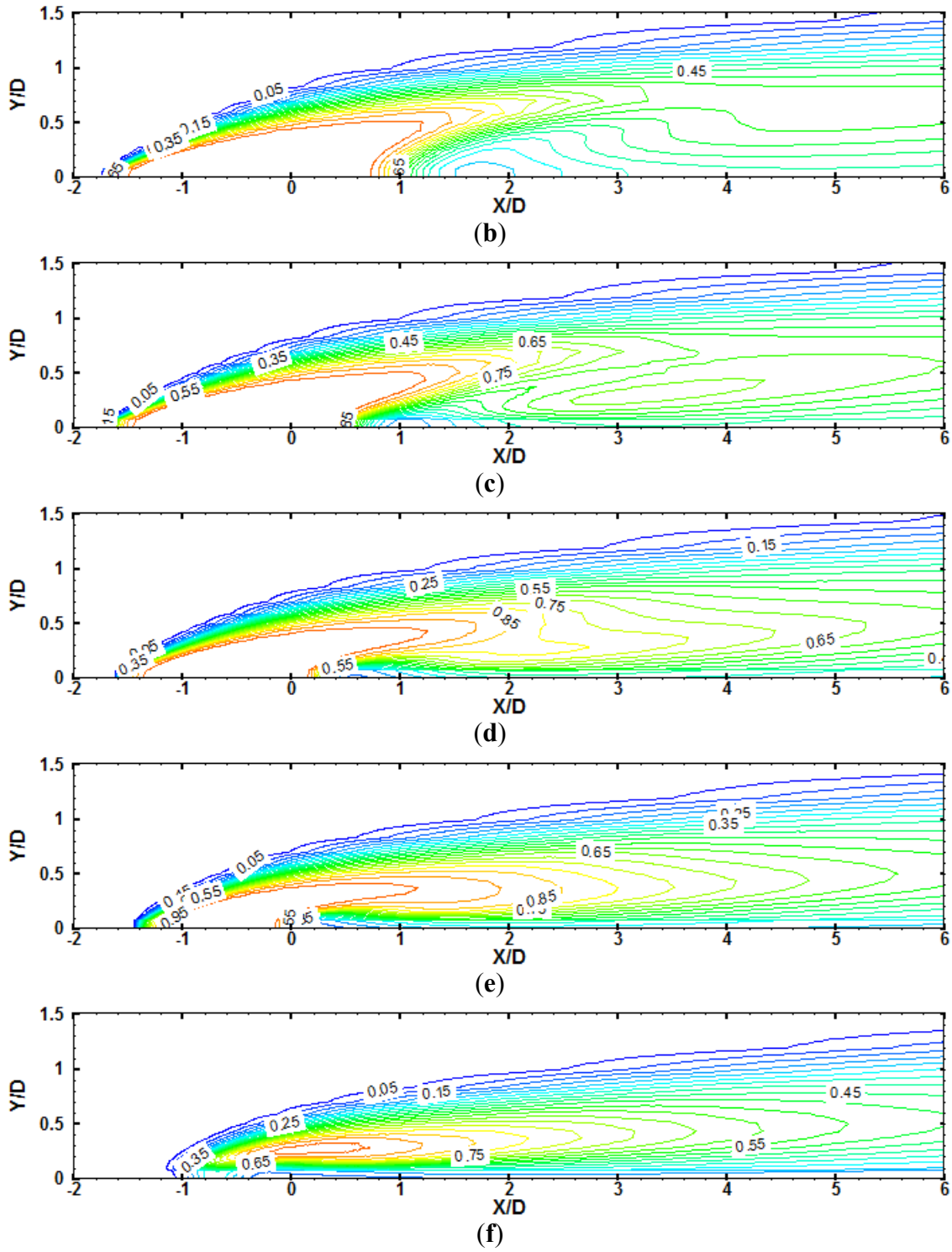

Figure 2.12 The temperature contours downstream of the cooling duct hole. (a) Temperature contours θ at different span-wise planes right above the cooling duct hole; (b) θ at Z/D = 0, the hole centerline; (c) θ at Z/D = 0.125; (d) θ at Z/D = 0.25; (e) θ at Z/D = 0.375; (f) θ at Z/D = 0.5, near the hole edge

2.3.4 Concluding Argument on the CRVP

Experimental as well as numerical research on the topic of jet in a crossflow agrees that the CRVP is generated from the shear layer, after this layer breaks down into vortex rings due to Kelvin-Helmholtz instability. Lots of valuable flow details are given in the literature, some of which are stated in the "Introduction" section. In the context of film cooling, other than the shear layer, there are at least two factors that are examined in this paper: the in-tube boundary layer and the in-tube vorticity which is convected with the flow entering the pipe. The following argument is an attempt to sort out these factors by importance.

In the limit of infinite Reynolds number (inviscid flow), the shear layer can be ideally represented by a vortex sheet whose strength is proportional to the velocity jump across that sheet, i.e., the difference between the jet velocity and the mainstream velocity projected onto the jet direction. Therefore, in essence, the velocity jump across the shear layer, which is related to the blowing ratio Br, is the controlling factor in generating the CRVP. This is confirmed in Figure 2.4, Figure 2.5 and Figure 2.8 where the location and strength of the vortex pair is almost the same for Cases 1–3. As for the impact of the boundary layer thickness, ω_x for Case 1 is very similar to that of Case 2 where the boundary layer thickness is set to zero. The effect of the boundary layer development on the CRVP is expressed as the aerodynamic blockage which is of the order of a few percent (e.g., less than 10%). Note also that the in-tube vorticity which is clearly depicted in Figure 2.5 has no impact on the CRVP formation or development.

2.3.5 The Nature of Liftoff and Reattachment

The behavior of the film-cooling flow was classified into three types: attached flow, liftoff then reattached flow, and complete liftoff with no reattached flow. The phenomenon of liftoff-reattachment was captured in the present simulation and can be seen in Figure 2.2, where the positions of liftoff and reattachment are marked with inverted red triangles. In the present paper, we still use terminology such as liftoff, detached and reattached flow. It will be shown in this

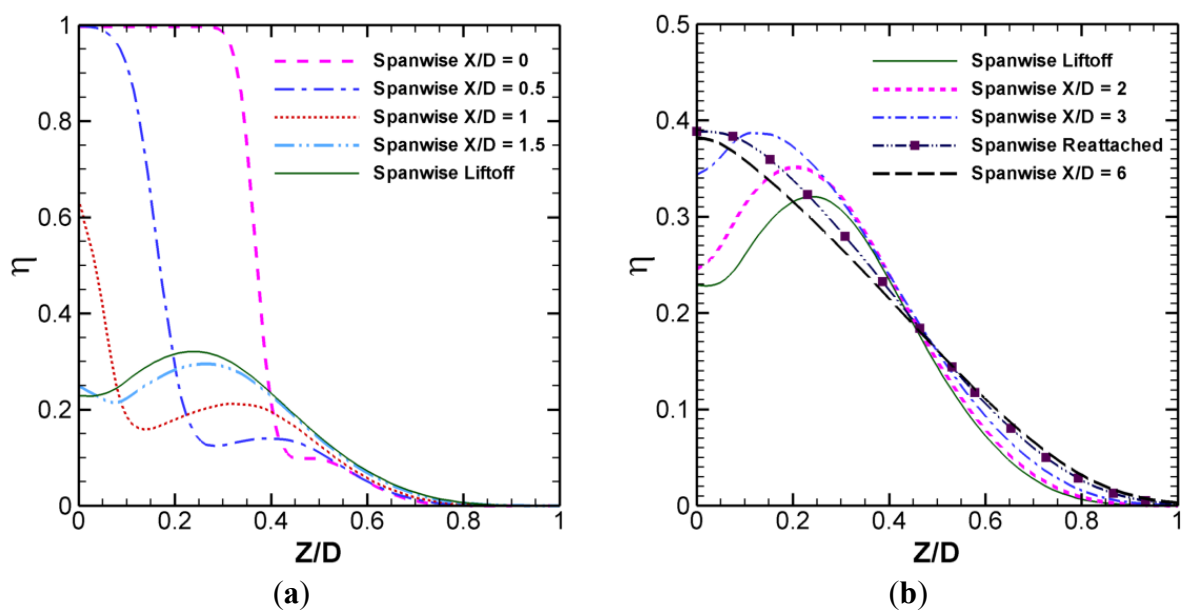

Figure 2.13 Span-wise film-cooling effectiveness

subsection that the phenomenon of liftoff-reattachment is not as simple as the jet flow leaving the test plate and then flowing back along it.

Figure 2.11 presents the near-field η contours, where the value of the outer contour line is 0.1. The region outside the outer line is considered as dominated by the hot mainstream. The positions of liftoff and reattachment at the jet centerline are marked with square symbols. A local minimum field, which is traceable from (0, 0.46) and ends at the liftoff position, is marked with a dashed line. Another dashed line, originating from (0, 0.49) and ending at the reattachment position, marks a local maximum field. To understand the implication of this figure, the relevant characteristics of CRVP are worth summarizing:

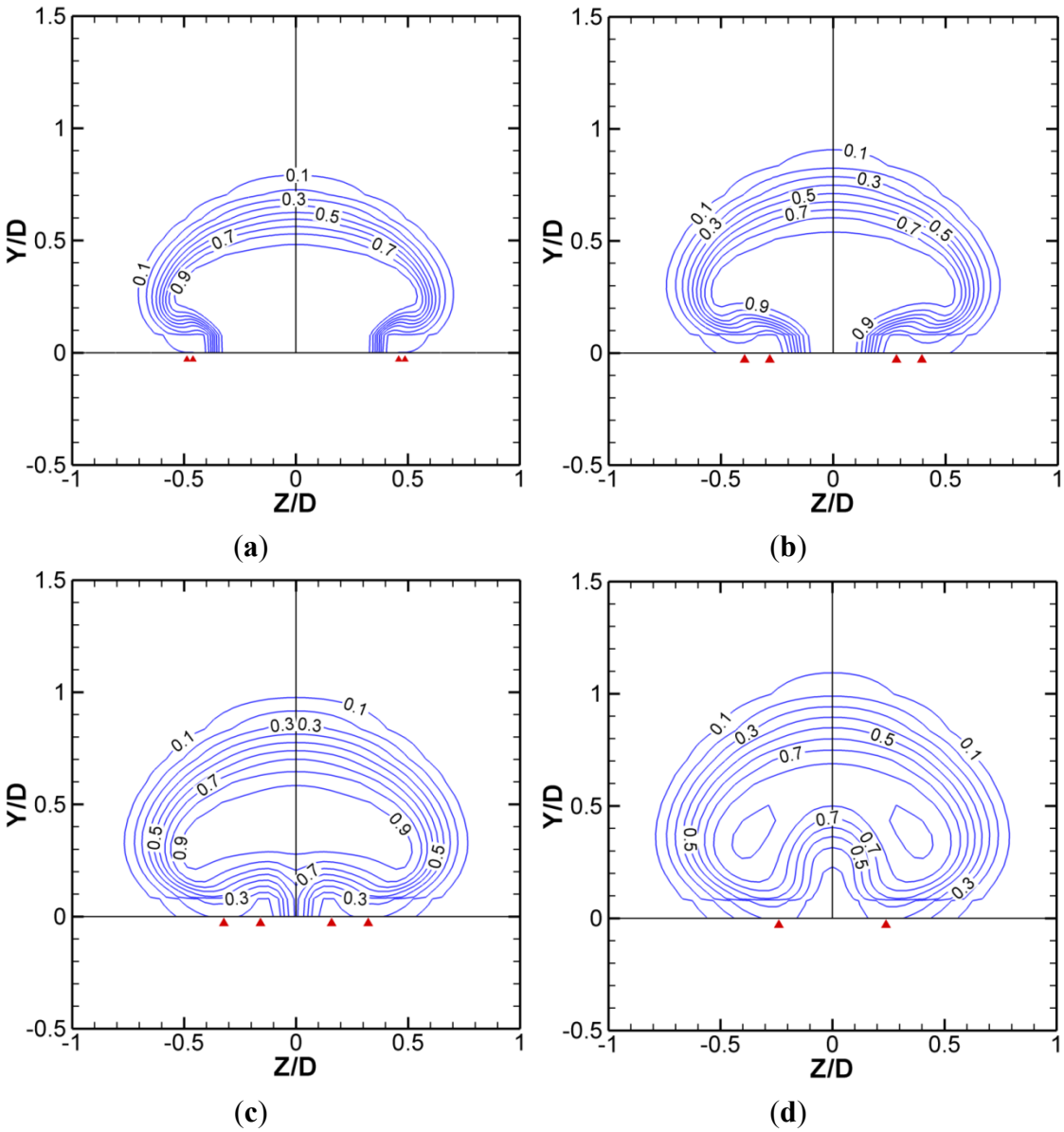

Figure 2.14 ***θ*** **contours on Y-Z planes before liftoff. (a) X/D = 0; (b) X/D = 0.5; (c) X/D = 1; (d) at liftoff position**

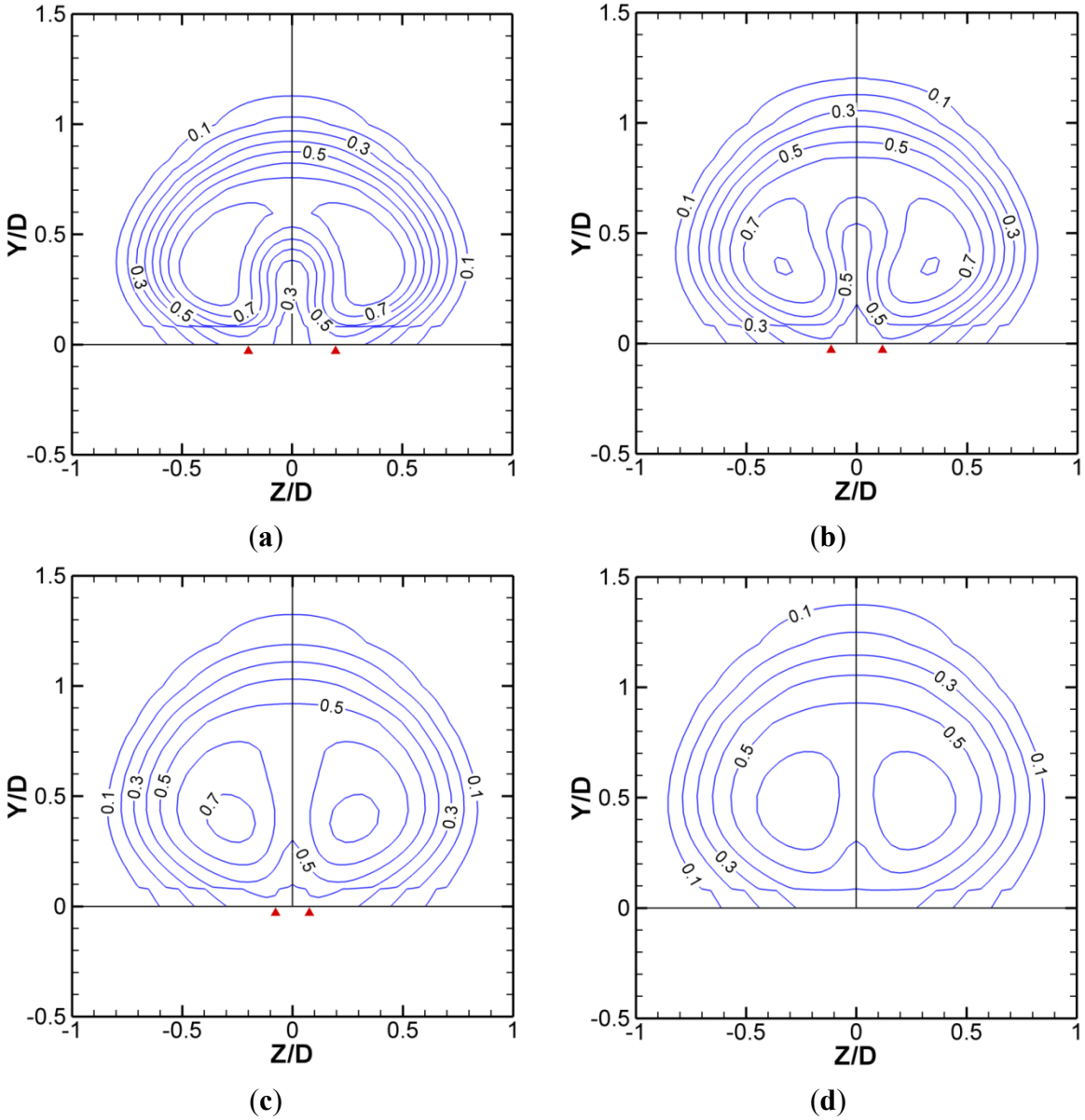

Figure 2.15 ***θ*** **contours on Y-Z planes before reattachment. (a) X/D = 2; (b) X/D = 3; (c) X/D = 4; (d) At reattachment position**

1. The CRVP is formed mainly above the exit. CRVP vorticity is very high in the region above the exit and decreases steeply when moving away from this region, as shown in Figure 2.6 and Figure 2.7.
2. The core of the CRVP is located at the interface in the region above the exit, and then it moves gradually into the jet flow. At X/D = 1.69, where liftoff occurs, the core is completely inside the coolant.
3. In contrast to some strong vortices rotating in situ, CRVP has a high advecting velocity, *u*, when rotating. The maximum ratio of the rotating velocity to the advecting velocity is approximately 0.3 in Case 1, the baseline case.

4. For the convection at the jet-mainstream interface, in the case of diffusion, the coolant temperature increases smoothly and slowly; in the case of advection, the temperature can change drastically.

Considering these flow characteristics and Figure 2.11, we can conclude that a stream of hot gas is strongly entrained into and around the coolant stream. The strong CRVP leads to the entrainment indicated by a red arrow in Figure 2.11. The footprint of the main body of this entrainment is the first dashed line, which extends to the liftoff position. The inner edge of the entrainment is very close to the first dashed line, and the outer edge is the second dashed line, which extends to the reattachment position. When the main body of the entrainment reaches the liftoff position, its moving distance in the Z direction is approximately 0.5D and approximately 1.7D in the X direction. Their ratio is approximately 0.29, and corresponds to the aforementioned ratio of 0.3 of the rotating velocity to the advection velocity of the CRVP.

To make the argument more evident, the flow in the jet-mainstream region is viewed from a different angle in Figure 2.12. Contours of the dimensionless temperature θ are plotted in Figure 2.12a at different Y-Z planes covering the full extent of the cooling hole. The θ-contours at each Z/D plane between 0 and 0.5 are then reproduced individually for more clarity in Figure 2.12b–f. At the hole centerline, Z/D = 0, there is a hot spot between X/D = 1.5 and 2—this is mainstream hot gases. As one moves away from the centerline, this hotspot becomes thinner and spreads over a longer extent downstream of the hole. This is a direct consequence of the CRVP which rotates the flow from above the wall, where the hot gases are flowing, into the-near wall region. This results in raising the wall temperature downstream of the hole hence lowering the cooling effectiveness. As one moves further away from the hole centerline (i.e., for larger values of Z/D) this region becomes thinner and assumes a longer extent which is also reflected in the decrease in the cooling effectiveness.

The near-field span-wise effectiveness (η_{sp}) is presented in Figure 2.13. Figure 2.13a is the η_{sp} before liftoff. Each curve has a "step," which results from the entrained hot gas. The width of the step corresponds to the Z direction distance between the main body and the outer edge of the entrainment. At X/D = 0, this width is 0.03D; the widths are 0.11D, 0.16D and 0.2D at X/D = 0.5, 1 and 1.5, respectively. At liftoff position, the width increases to 0.24D. When the entrained gases expand, their thermal effectiveness η also increases from approximately 0.1 to 0.23. The expanding and increasing trend implies that the entrainment is mixing with the coolant. At the liftoff position, the main body of the entrained gases leave the test plate. Figure 2.13b presents η_{sp} after liftoff. The η value continues to increase until it reaches the reattachment position, where the entrained gas leaves the test plate completely.

As the CRVP is a complicated 3D phenomenon, θ contours in the near field on Y-Z planes are shown in Figure 2.14 and Figure 2.15, to clarify the process of liftoff and reattachment. The contours before liftoff are presented in Figure 2.14. Triangles showing on the X axis are used to mark the footprints of the main body and outer edge of the entrainment region. At X/D = 0, hot gases are entrained at the bottom around Z/D = ±0.5; then at X/D = 0.5 and 1, they advect inwards and expand while their temperature θ increases. At liftoff position, the entrained gases turn up and thrust into the coolant jet, resulting in the hot gases/coolant jet mixing. The turning up cuts the coolant into two parts. The CRVP is also named kidney vortices because of its shape. Figure 2.14d shows that the formation of the kidney shape, particularly the formation of the kidney hilum, is the result of the entrained gases turning up.

Table 2.1 Coolant flow trajectories

X/D	Y/D Coolant Center	Y/D Coolant Top
0.00	0.3	0.8
0.50	0.3	0.9
1.00	0.3	1.0
Liftoff	0.3	1.1
2.00	0.3	1.1
3.00	0.3	1.2
4.00	0.4	1.3
Reattachment	0.5	1.4

The θ contours before the reattachment are presented in Figure 2.15. The entrained gases keep advecting upwards and mixing with the coolant. Its outer edge keeps advecting inwards until reaching the reattachment position, where the entrained gases leave the test plate completely and mix with the coolant.

The Y/D values of each θ peak and top edges of $\theta = 0.1$ are extracted from Figure 2.13 and Figure 2.15, and listed in Table 2.1 to present the jet trajectory. The values at both the center and the top edge increase with increasing X/D. The phenomenon of the jet flow leaving the surface at the liftoff position then returning to the surface at the reattachment position, as proposed in literature, cannot be detected.

Combining Figure 2.11 to Figure 2.15, the phenomenon of liftoff and reattachment can be considered as the vestige of a strong entrainment, which is caused by the CRVP. At the region above the exit, where CRVP vorticity is strong and its cores are located at the mainstream-coolant interface, a significant amount of hot gas is entrained into the coolant and becomes a small part of the CRVP. Then, it advects leeward and inward, mixing with the coolant. At the centerline, it turns up, leaves the test plate, and finally mixes with the coolant. At the same time, it forms the kidney shapes.

2.4 Conclusions

The present study simulated numerically the flow field for three film-cooling cases, namely Case 1—a baseline case; Case 2—the FSIT case; and Case 3—the unsteady flow case. The comparison of Cases 1 and 2 and Cases 1 and 3 demonstrated that the Counter-Rotating Vortex Pair (CRVP) formation process is the main source of CRVP formation, while the effect of the in-tube boundary layer and the in-tube vorticity on the CRVP formation are at best of a secondary nature.

This investigation has proved that the CRVP in film-cooling flow is due to a vortical structure in the mainstream flow direction. Therefore, its main promoter is the velocity jump

across the shear layer which determines the strength of the vortex rings forming at the pipe exit. This mechanism explained the effects of Br on η. It is also the fundamental mechanism responsible for the high cooling performance of diverging holes. Therefore, the guideline for creating new high performance film-cooling schemes ought to be decreasing the strength of these vortex rings.

The liftoff-reattachment phenomenon in film-cooling flow was also investigated. It was shown that this phenomenon did not result from the jet flow leaving the test plate and then returning to it. In fact, it resulted from the entrainment effect of the CRVP. When a strong CRVP above the cooling holes exit entrains hot gases into its path, the footprints of the entrained gases, advecting and mixing with the coolant, led to liftoff and reattachment. The main body of the entrainment corresponded to the liftoff, and its outer edge corresponded to the reattachment. In other words, an attached jet flow is due to a CRVP that is not strong enough to entrain much hot gas, or to the fact that the entrained gases mix with the coolant before it reaches the pipe centerline. The phenomenon of attachment, liftoff and then reattachment strongly depends on the CRVP strength, rather than the jet flow trajectory.

Chapter 3 New High Performance Schemes for Film Cooling Mechanisms

A part has been published on the ASME - JSME - KSME Joint Fluids Engineering Conference 2019 as AJKFLUIDS2019-4659: Experimental Investigations of a Comb-Like Film Cooling Scheme

A part was submitted to Heat Transfer Engineering Journal as: On the Use of High-Aspect-Ratio Film Cooling Scheme

Abstract

Along discovery of the counter-rotating vortex pair crucial effect on film cooling effectiveness, a mechanism of the film cooling heat transfer has been proposed. Analysis of that mechanism showed that the mainstream entrainment and the coolant expansion, guided the design of two new film cooling schemes, the comb scheme and the high-aspect-ratio (HAR) scheme. They were intended to eliminate the mainstream entrainment, and exploit the coolant expansion, respectively. The new schemes were experimentally investigated using a properly validated test facility with the transient thermochromic liquid crystal technique. The density ratio was set to unity, and the blowing ratio ranged from 0.18 to 1.5. The comb scheme showed performance comparable with that of the slot, and the HAR scheme showed performance much higher than their lateral coverage ratios. Both match the design. Successfully obtaining the prospective performance convincingly proved the proposed mechanism, and established a solid base for the film cooling research.

3.1 Introduction

Modern gas turbines operate at extremely high inlet total temperature, the next-generation gas turbine is hoped to operate at even higher temperature to achieve a high thermal performance. Nowadays, the cooling technology has become one of the most important development directions [3]. The film cooling is the mainstay among them [28].

The film cooling of a real vane generally uses the cylindrical hole and shaped holes [28]. The high performance of the shaped hole was found by Goldstein and Eckert [4]. It is a revolutionary progress. However, over the past decades after this revolution, no equivalent breakthrough has been achieved. The research in the relative spheres has reached a plateau [2]. To break the plateau, the complex mechanisms of the film cooling heat transfer are urgent to be clarified.

The momentum flux ratio (I) is conventionally thought of as the most crucial factor on the film cooling effectiveness (η) [3–5]. The film-cooling flow behavior was classified by Sinha *et al.* [5] into three types. They are the attached flow, the detached flow and the reattached flow. Usually, the attached flow results in high η, and the detached flow has poor performance. The mechanism of the liftoff-reattachment, which represents the transition between the attached and the detached, was thought to be a function of the momentum flux ratio (I). Goldstein and Eckert [4] attributed the performance improvement of the shaped hole to the decrease of the jet mean velocity. This opinion on the momentum flux ratio effect encouraged the film cooling researchers to decrease the I value by expanding the hole exit, such as the film cooling geometry in [10].

Investigating the correlation between η and the pertaining variables needs to include the prospective crucial factors. Based on analyzing large amount of experimental data of the cylindrical hole, a correlation was proposed by Baldauf *et al.* [29]. It took important parameters into account, such as the hole pitch (P), density ratio (DR), to list a few. Based on the analysis of the shaped hole, a correlation was proposed by Colban *et al.* [30]. The lateral coverage ratio (t/P), as well as the blowing ratio (BR) is the main parameters taken into account. Their generalization about the characteristics of the lateral averaged film cooling effectiveness ($\overline{\eta_L}$) distributions is worth noting: At X = 0, the $\overline{\eta_L}$ value is maximum, which is t/P; and it goes down monotonously in the increasing X-direction.

The counter-rotating vortex pair (CRVP) has also been considered as an important factor affecting η. It was one of the main vortical structures described by Fric and Roshko [11]. Because of the distinct shape, it was named kidney vortices by Haven and Kurosaka [12]. Haven *et al.* [13], then Hyams and Leylek [16] concluded that the weak CRVP of the shaped holes results in a superior performance. Therefore, some new film cooling schemes have been introduced [23, 25, 31, 32], and the increased film cooling effectiveness has been attributed to the weakened CRVP.

The previous work of Li and Hassan [7] clarified that the most crucial factor is the CRVP strength, instead of the momentum flux ratio. A correlation was proposed, which can be translated into the following format: $\overline{\eta_A} = t/P + a\,\overline{\omega_x}$. Here $\overline{\eta_A}$ is the space averaged film cooling effectiveness, 'a' is a constant, $\overline{\omega_x}$ is the CRVP intensity. Therefore, to achieve highest performance, t/P should be maximum (= 1), and the CRVP intensity should be minimum (= 0). Li *et al.* [33] analyzed the CRVP, including the source, the relation of the CRVP intensity and the phenomenon of the liftoff-reattachment.

Attracted by the high performance of the slot, the novel schemes with high *t/P* values have been proposed. Sargison *et al.* [34] designed the Console scheme. Their $\overline{\eta_L}$ values were similar to the shaped hole. A parameter named minimum cross-section area (MCSA) was used to quantify the structural integrity. The MCSA values are 0.25, 0.52 and 0.67 for the Console, the shaped hole and the cylindrical hole in the investigation, respectively. Bunker [35] proposed the 'Trench scheme', which is a blind transverse slot fed by cylindrical holes. Its geometrical parameters were investigated [36]. The performance was close to (and a bit smaller than) the shaped holes. Bunker [37] proposed a novel scheme named 'Mesh-Fed Slot'. Its performance was higher than the shaped holes, but less than the two-dimensional slot. It used the internal wall mesh to provide the structural integrity. The MCSA was not mentioned in the paper. However, based on the two investigated configurations of the scheme, the MCSA values were estimated as 0.27 and 0.16, respectively. Davidson *et al.* and Bruce-Black *et al.* [38, 39] designed a practical slot configuration, which is a blind angled slot fed by impinging cylindrical holes. The $\overline{\eta_L}$ values were around 0.5-0.7.

The performance of a simple slot is compliant with the correlation in [7]. The main component of the CRVP intensity is the *X*-direction component, which is composed of $-\partial v/\partial z$ and $\partial w/\partial y$ [7]. Theoretically, they are all negligible in the slot flow. So the CRVP intensity of the slot is negligible. At the same time, the *t/P* of the slot is 1. Therefore, the simple slot has extremely high η, which is considered as ideal or perfect performance [3] however, its MCSA is 0 which restricts the application.

The η investigation needs to measure temperatures. The thermochromic liquid crystal (TLC) is a thermographic technique measures temperature in high resolution. The TLC features the varying of its color relies on the temperature. Since Wang *et al.* [40, 41] applied the TLC technique in measuring the η distribution, it has been widely used in film cooling investigations, in many kinds of film cooling geometries [8, 9, 42–47]. The present investigations also used this technique to measure η distribution.

It has been demonstrated that, for the ambiguity on the film cooling heat transfer, the research on the film cooling geometry remains sluggish, at the η far less than perfect. Along the discovery of the CRVP crucial effect [7], and the analysis underlying this effect on film cooling flow [33], the present paper proposes a mechanism of film cooling heat transfer. The mainstream entrainment and the coolant expansion among with the CRVP effect are revealed by dissecting this mechanism. Furthermore, new advanced film-cooling schemes aimed to obtain the 'ideal' performance are developed based on this mechanism.

3.2 Methodology and Models

A mechanism of the film cooling heat transfer was proposed based on analyzing the crucial effect of CRVP on η. Applying this mechanism, two advanced film cooling schemes, named comb scheme and high-aspect-ratio (HAR) scheme, were developed. The new schemes were investigated experimentally. The experiments were performed on a two-loop wind tunnel, with the transient TLC technique.

3.2.1 The Mechanism Underlying the CRVP Crucial Effect

The crucial effect of the CRVP intensity was observed first by Li and Hassan [7], and the vortical structure was further analyzed by Li *et al.* [33] who concluded that the essential source of the CRVP is the velocity gradients in the mainstream-coolant interface. Figure 6 in [33] presented the detailed distributions of CRVP and velocity gradients. Figure 6c shows the velocity gradient $\partial v/\partial z$, which is copied and shown here as Figure 3.1a. The edge of the cooling hole exit

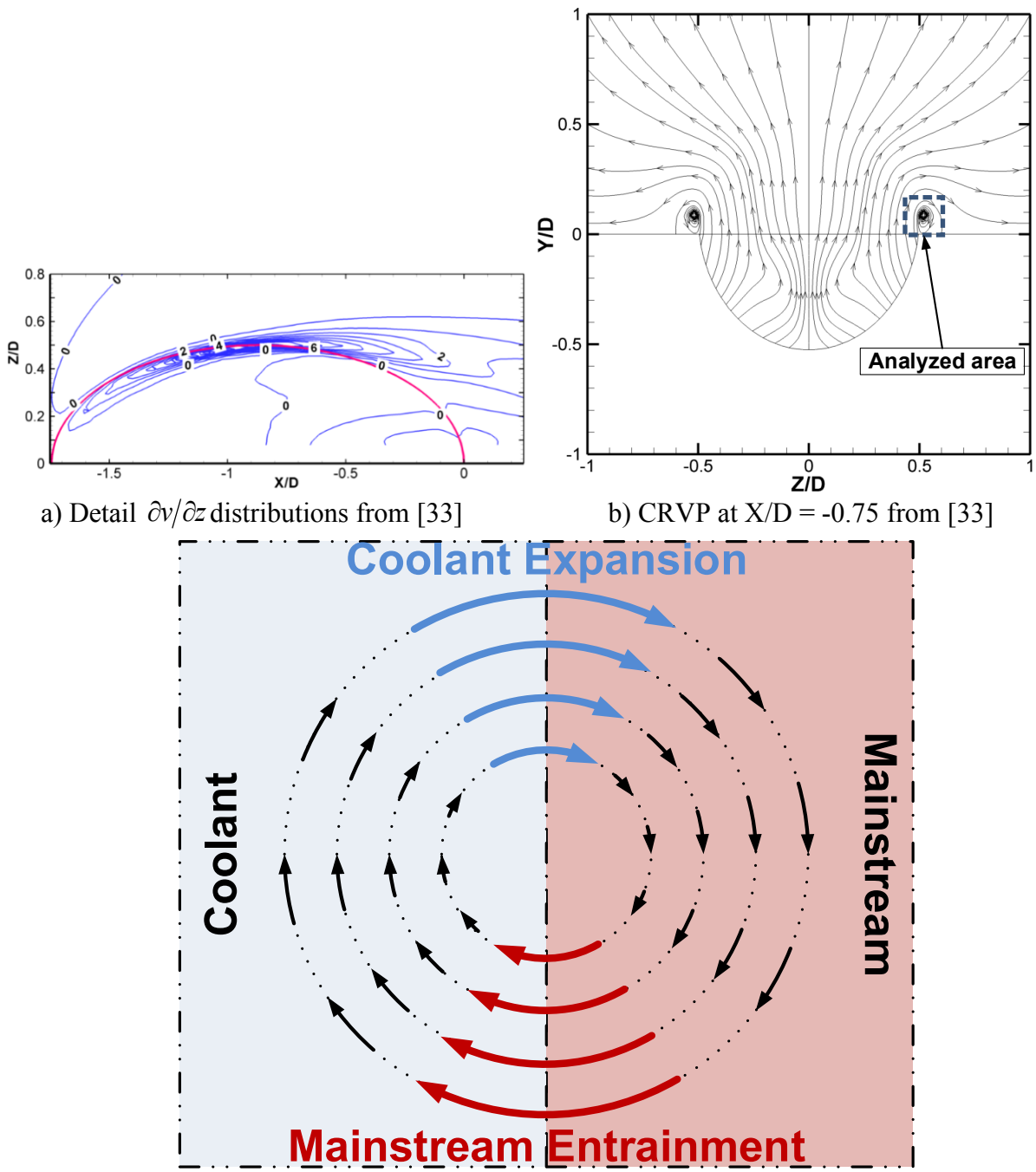

a) Detail $\partial v/\partial z$ distributions from [33]

b) CRVP at X/D = -0.75 from [33]

c) Mechanism of the film cooling heat transfer

Figure 3.1 Analysis on the mechanism of the film cooling heat transfer

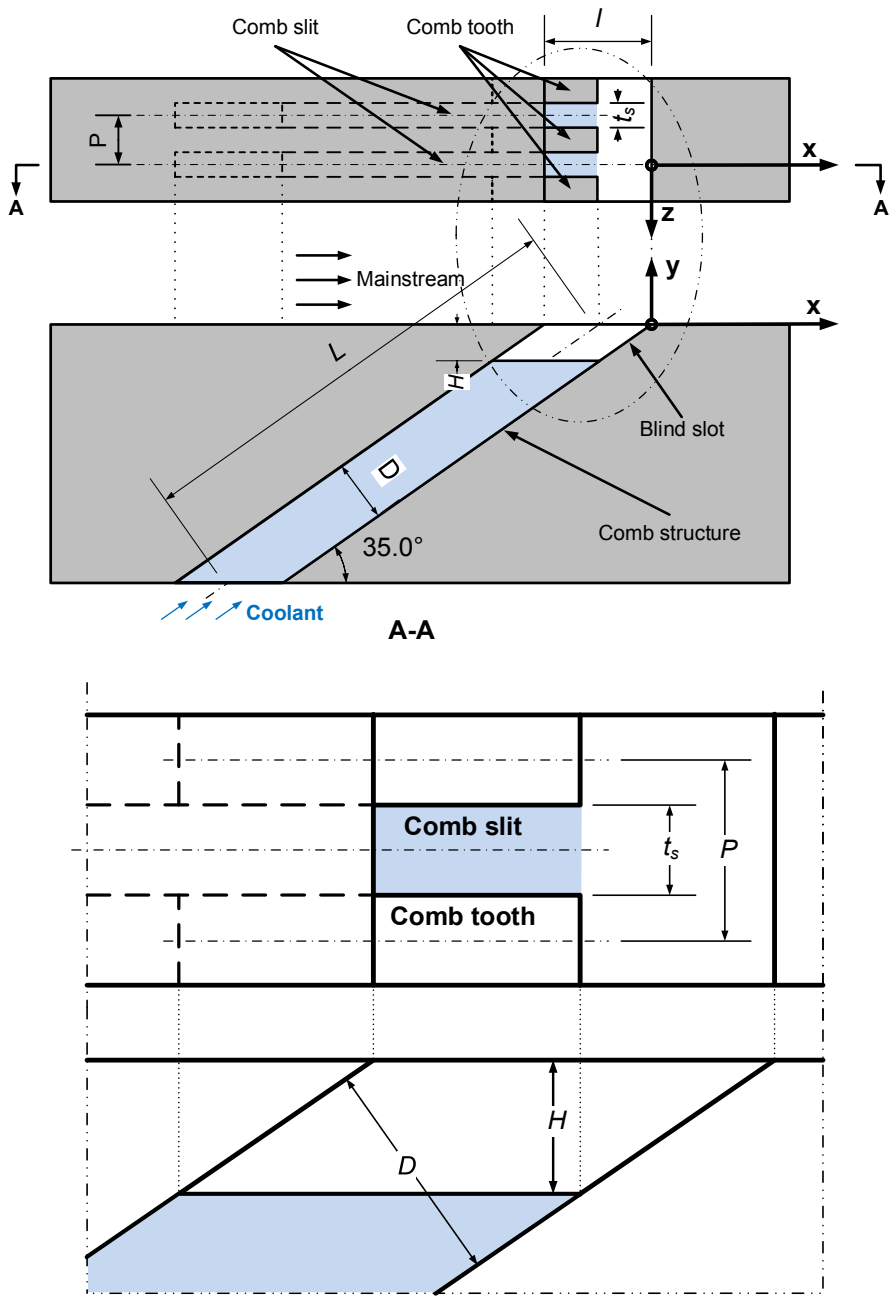

Figure 3.2 The comb scheme configuration

is shown in the background. It demonstrates that the local peak of $\partial v/\partial z$ is right above the edge of the exit. Inside the edge is mostly coolant, which jets out with velocity v. Outside the edge is mostly the mainstream, of which v is deemed to be 0. Hence severe velocity gradients occur in the mainstream-coolant interface. The $\partial v/\partial z$ and $\partial w/\partial y$ mostly drive the CRVP.

Figure 4 in [33] described the forming process of the CRVP with 2D streamlines; figure 4b is copied and is shown here as Figure 3.1b. The area around the CRVP is framed with dash lines and is sketch in Figure 3.1c. The situation in the sketch has been simplified: 1. The mainstream-coolant interface thickness is deemed to be 0; 2. the CRVP size is ignored; 3. the offset between

the CRVP position and the mainstream-coolant interface is also ignored. Figure 3.1c illustrates the mechanism of the film cooling heat transfer with the mainstream-coolant interface at the center; it is simplified into a line. Its left side is deemed to be the coolant, and the right side is deemed to be the mainstream. In the vicinity of the interface, severe velocity gradients occur, and lead to a large rotation value ω on the interface which produces penetrations, that drastically increase the heat transfer. The penetration from the mainstream to the coolant is the mainstream entrainment, which wedges the mainstream into the coolant and decays η drastically. Meanwhile, the penetration from the coolant into the mainstream is the coolant expansion, which expands the coolant into the mainstream, likely to improve the effectiveness η. The mainstream entrainment is notable, in the conventional film cooling research, it has been the only appreciable CRVP effect on η. The coolant expansion is fully ignored.

The film cooling convection is mostly by advection and the diffusion is neglected [33]. So without advection (CRVP intensity is 0), the mainstream-coolant interface is steady, and the outermost position of the interface is *t/P*. In the case of highlighting the mainstream entrainment, which immediately impacts η, the highest available performance is *t/P*, on the condition that ω_x is 0. It is the reason under the correlations proposed in [7, 30], in which $\overline{\eta_L}$ maximum is *t/P*. In this case, the mainstream has to be eliminated to obtain high performance. A new scheme named comb scheme was developed in the present investigations to eliminate the mainstream

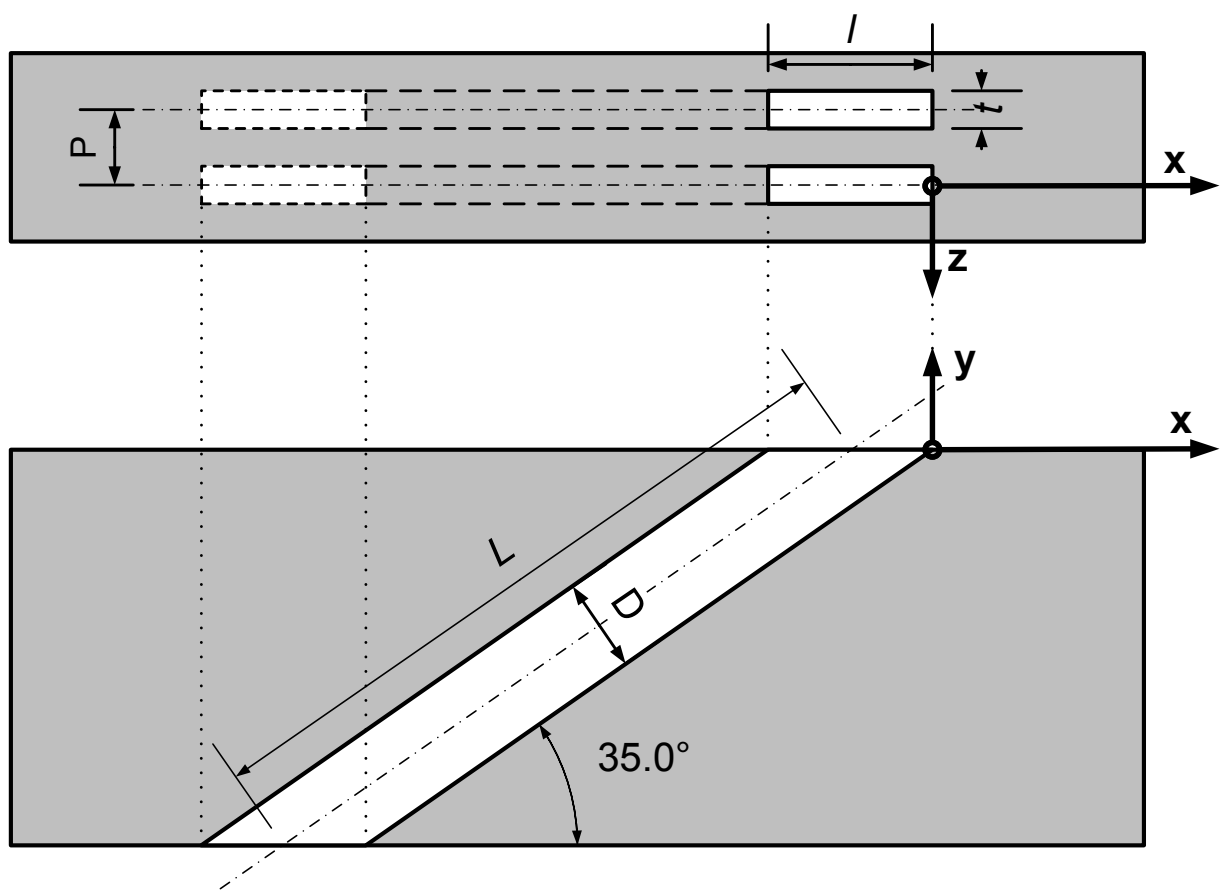

Figure 3.3 The high-respect-ratio configuration

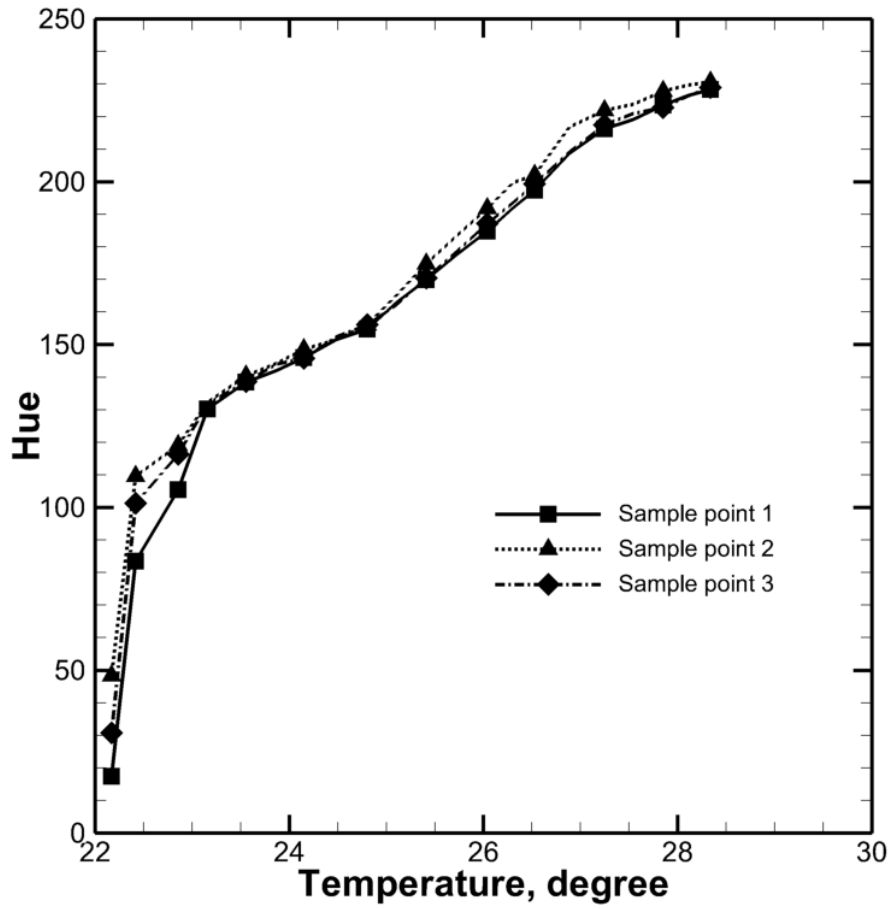

Figure 3.4 The calibration curves of the sample positions

entrainment.

In contrast to the mainstream entrainment, even the coolant expansion is in favor of improving η, its impact on η is hard to be perceived in the conventional film cooling geometries. A new scheme named high-aspect-ratio (HAR) scheme has been developed to exploit the coolant expansion. In the case of the coolant expansion dominating, the mainstream-coolant interface tends to move outside, hence η breaks the value restriction of the *t/P*, obtains high values.

3.2.2 The New Schemes Configuration

Two new film cooling schemes were developed in this work: the comb scheme and the HAR scheme. The structure of the comb scheme is shown in Figure 3.2. It is composed of an inclined blind slot fed by a comb-like structure. The inclination angle is 35°. Due to the blind slot exit, *t/P* is 1. In the comb-like structure, the coolant gets out through the comb-slits, and the comb-teeth provide the structural integrity. The new scheme was named comb scheme because of the characteristic of the comb-like structure. For the blind slot, the slot width is *D*, it is 5 mm in the present investigations. The exit longitudinal dimension is *l*, and the vertical depth is *H*. The axial

length of the geometry, L, is 7D. For the comb structure, the comb slit lateral dimension is t_s, and the lateral spacing between two comb-slits is P.

The Cartesian coordinates for this investigation are also shown in the figure. The origin is located on the central plan of the comb slit crossing the exit trailing edge. The x-, y- and z-axes are aligned with the mainstream, vertical, and span-wise directions, respectively.

As the coolant jets out of the comb slits, severe velocity gradients occur and lead to a CRVP. Hence, the CRVP in this geometry is expected to be located close to the bottom of the blind slot. Meanwhile, the mainstream-coolant interface is usually higher than the wall Y = 0. The distance between the CRVP and the interface is approximately H. The CRVP effect on the interface is expected to be manipulated by mostly changing H values. As this geometry has a slot-like exit, its t/P is 1. According to the correlation in [7], the perfect performance would be obtained as the CRVP effect on the interface is eliminated.

The MCSA is a parameter of the mechanical integrity, which is very important for the practical application of a film cooling scheme. The MCSA of the comb scheme is calculated from the parameters L, H, t_s and P.

$$MCSA = \left(1 - \frac{t_s}{P}\right) * \left(1 - \frac{H}{L * \sin 35°}\right) \tag{3.1}$$

To exploit the coolant expansion, the HAR scheme was developed as shown in Figure 3.3. It is a row of rectangular holes inclined at 35° to the x-direction (flow direction). To compare the results with traditional film cooling geometries, its longitudinal dimension of the perpendicular plane was named D, to follow the traditional nomenclature like the diameter of the cylindrical hole. D is also 5 mm. The axial length of the coolant passage, L, is 7D. The lateral dimension is t, and the exit longitudinal dimension is l. The lateral space is pitch (P). The Cartesian coordinates for these investigations are also shown in the figure. The origin locates on the center of the exit trailing edge. The x-, y- and z- axes were aligned with the mainstream, vertical, and span-wise directions, respectively.

The coolant expansion occurs at a place further away from the protected surface. The new scheme has to provide enough period for it to take effect. The main geometrical characteristic of the new scheme is on its exit aspect ratio (AR), of which the definition is AR = l/t. To exploit the coolant expansion, the longitudinal length, l, was prolonged drastically. The AR value of the new scheme was 17.5 in the present investigations, much higher than the conventional film cooling geometries, which is usually less than 2. Therefore, the new scheme was named high-aspect-ratio (HAR) scheme.

3.2.3 The TLC technique

The present investigations have used the transient TLC technique to measure the effectiveness η. The TLC is a thermographic technique where the plate color varies on the temperature. Hence the temperature was measured by capturing images of the TLC sheet with 3CCD camera.

Before measured temperatures, an in situ calibration for the TLC sheet had been performed. In the calibration, the temperatures were set, and the corresponding images, thus the colors were captured. The color is quantified by hue value. Curves of the hue-temperature were produced in

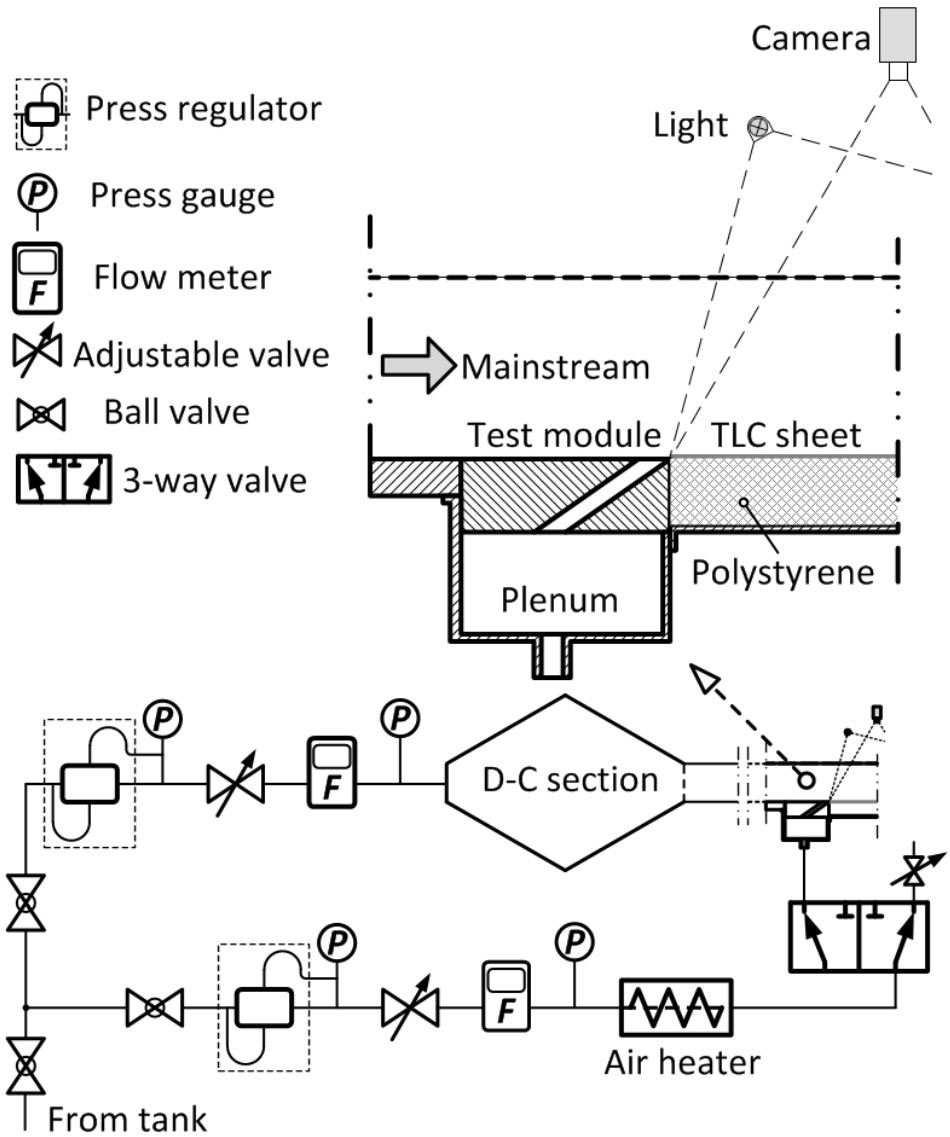

Figure 3.5. The schematic diagram of the experimental system

the calibration. Figure 3.4 shows some sample curves. In the η test, the color is converted into temperature with these curves.

The transient film cooling heat transfer in the present tests is considered as a semi-infinite solid transient conduction case. The heat transfer equation is

$$\alpha \frac{\partial^2 T}{\partial x^2} = \frac{\partial T}{\partial t} \tag{3.2}$$

with boundary and initial conditions:

$$\left.\begin{aligned} T &= T_i @ t = 0 \\ -k \left.\frac{\partial T}{\partial x}\right|_{x=0} &= h(T_f - T_w) \end{aligned}\right\} \tag{3.3}$$

The solution at x = 0 is

$$\left.\begin{aligned} &\frac{T_w - T_i}{T_f - T_i} = 1 - \exp(\beta^2) erfc(\beta) \\ &\text{where } \beta = \frac{h\sqrt{\alpha t}}{k}. \end{aligned}\right\} \tag{3.4}$$

Combining with the η definition:

$$\eta = \frac{T_f - T_m}{T_j - T_m} \tag{3.5}$$

The solution becomes

$$T_w - T_i = \left[1 - \exp(\beta^2) erfc(\beta)\right]\left[\eta\left(T_j - T_m\right) - T_m - T_i\right] \tag{3.6}$$

in the present tests, T_w is converted from the TLC color, T_j, T_m and T_i are measured by thermocouples. In this equation, only η and h needed to be solved in the post processing.

Table 3.1 Test matrix

Case No.	Geometry	MCSA	BR	$\overline{\eta_A}$ (X/D=0-20)
1	Cylinder, D=5mm	0.67	0.5	0.1404
2			0.75	0.1252
3			1	0.0882
4	Slot, D=5mm	0	0.5	0.6187
5			0.65	0.6810
6			0.8	0.6995
7			1	0.7342
8			1.5	0.6798
9	comb Scheme, $H = 1D$, $t_s = 0.1D$, $P = 2t_s$	0.38	0.25	0.5170
10			0.5	0.6969
11			0.75	0.7487
12			1	0.7933
13			1.5	0.8091
14	comb scheme, $H = 1D$, $t_s = 0.1D$, $P = 3t_s$	0.5	0.17	0.3951
15			0.33	0.6131
16			0.5	0.6454
17			0.7	0.6988
18			1	0.7262
19	comb Scheme, $H = 0.5D$, $t_s = 0.1D$, $P = 2t_s$	0.44	0.25	0.5620
20			0.5	0.6923
21			0.75	0.7678
22			1	0.7717
23	comb scheme, $H = 0.5D$, $t_s = 0.1D$, $P = 3t_s$	0.58	0.17	0.4224
24			0.33	0.6277
25			0.5	0.6655
26			0.7	0.6727
27			1	0.6662
28	HAR Scheme, $t = 0.1D$, $P = 2t$	0.5	0.25	0.6065
29			0.5	0.7325
30			0.8	0.7792
31			1	0.7793
32	HAR Scheme, $t = 0.1D$, $P = 3t$	0.67	0.17	0.2167
33			0.33	0.5347
34			0.5	0.5098
35			0.7	0.6168
36			1	0.6358

3.2.4 Experimental Setup

The experiments have been performed in a two-loop wind tunnel, which is shown in Figure 3.5. Its first loop is for the mainstream flow, and the second loop is for the coolant flow. Both loops have adjustable valves, pressure regulators and flowmeters. The mainstream flow was measured with a Rosemount mass flow meter 3095MV, its velocity was set to 20 m/s. The coolant flow was measured with a rotameter FL-1502A. Its velocity was adjusted upon the BR settings. The coolant loop has an adjustable heater to increase and control the coolant temperature. The DR was considered as unity (0.98). The coolant loop connects the mainstream loop in the test section through a plenum under the bottom. The cross-section dimensions of the test section are 99 mm × 53.5 mm.

The tested geometries were manufactured on a test module, installed on the test plate, which is the bottom of the test section. The lateral width of the slot is 63.5 mm (12.7*D*). Downstream of the test module is a piece of XPS (Extruded Polystyrene), covered with a TLC sheet. The size of the TLC sheet is 203 mm × 89 mm (40.6*D* × 17.8*D*). Considering the end effect, only the central 25% was post-processed. A Toshiba IK-TF7C 3CCD camera is located right above the test section, to capture the TLC images through the transparent test section top. Each test records 300 TLC images at 5 frames/s. They were saved to a workstation with the simultaneous temperature data of the mainstream and the coolant, which were measured with T-type thermocouples. The temperature uncertainty is ±0.2ºC. The post-processing used all these data with in-house programs to calculate the effectiveness η. The averaged uncertainty in η is ±8%. The identical experimental system has accomplished many projects, including [9, 44, 45].

3.2.5 Test Matrix and Parameter Normalization

Four kinds of geometries were included, two new schemes, the cylindrical hole at P = 3D and the simple slot. The roles of the cylindrical hole and the slot were comparisons and validations. The investigated cases are summarized in Table 3.1. The normalized form of effectiveness $\overline{\eta_A}$ is also listed in the table. It was defined to simplify the η performance comparisons among different cases and was written as:

$$\overline{\eta_A} = \frac{1}{3D * 20D} \int_0^{3D} \int_0^{20D} \eta(X,Z)\, dx\, dz \tag{3.7}$$

The definition of $\overline{\eta_L}$ in the present investigations is:

$$\overline{\eta_L} = \frac{1}{3D} \int_0^{3D} \eta\, dz \tag{3.8}$$

The BR definition in the present investigation was modified for the new schemes. The comb scheme has a slot-like exit. Its BR was defined based on the exit conditions. This scheme has an identical mass flow rate with the simple slot. However, the HAR scheme does not have the slot-like exit, therefore its BR would be different if it follows the conventional BR definition. To simplify the investigation, we assumed a virtual slot on the exit of the HAR scheme, and used an identical BR definition to the slot. Hence in the HAR scheme, the present mass flow rate is 2 or 3 times that of a conventional definition when P = 2 or 3t, respectively.

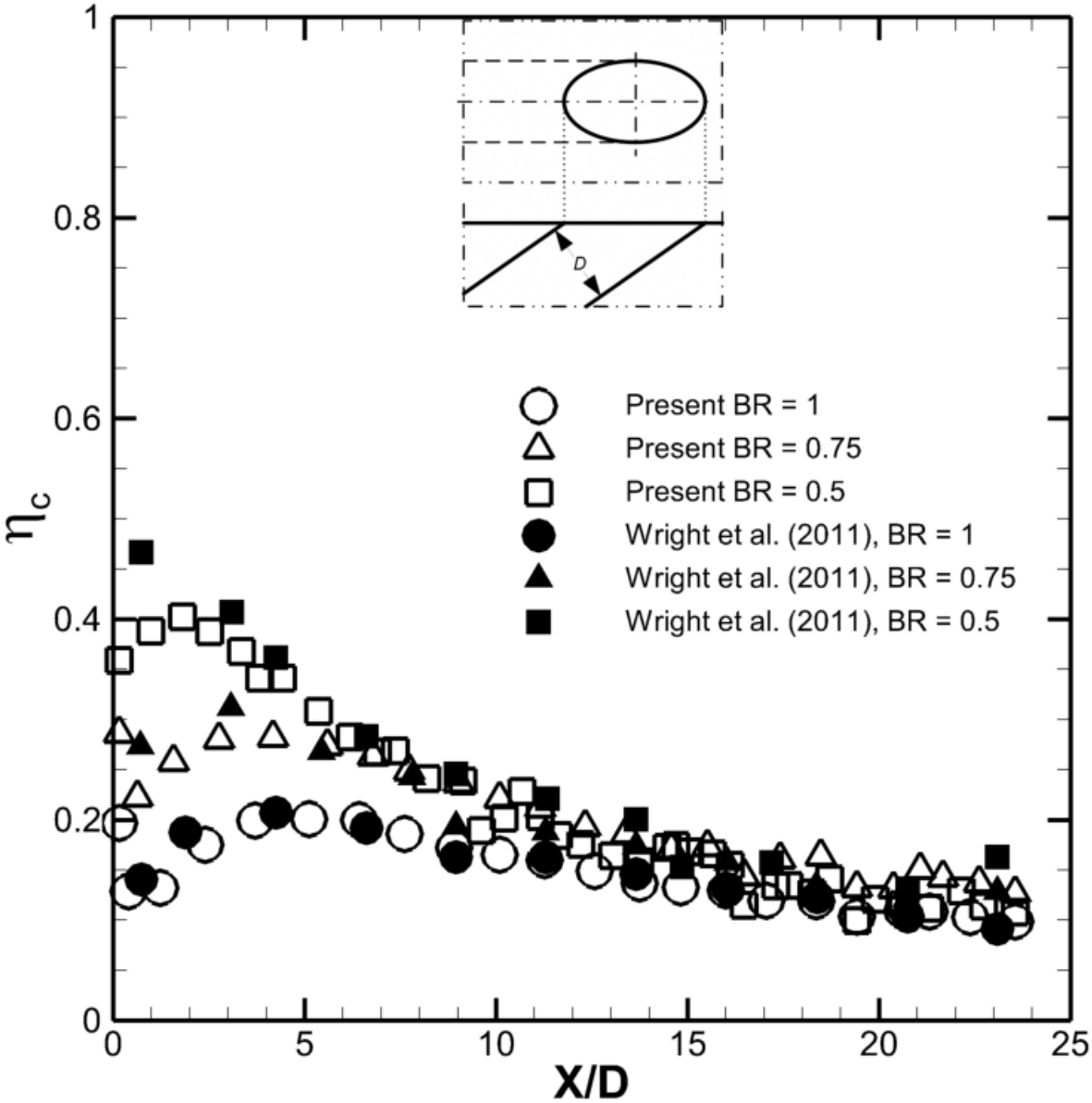

Figure 3.6 Present and published data for the cylindrical hole [48]

3.3 Results and Discussions

The present investigations tested four kinds of geometries, including two classic geometries, the cylindrical hole and the simple slot. They were tested and compared with the published data, to validate the current experimental facilities. Then the performance of two new schemes is presented and compared with the classic geometries.

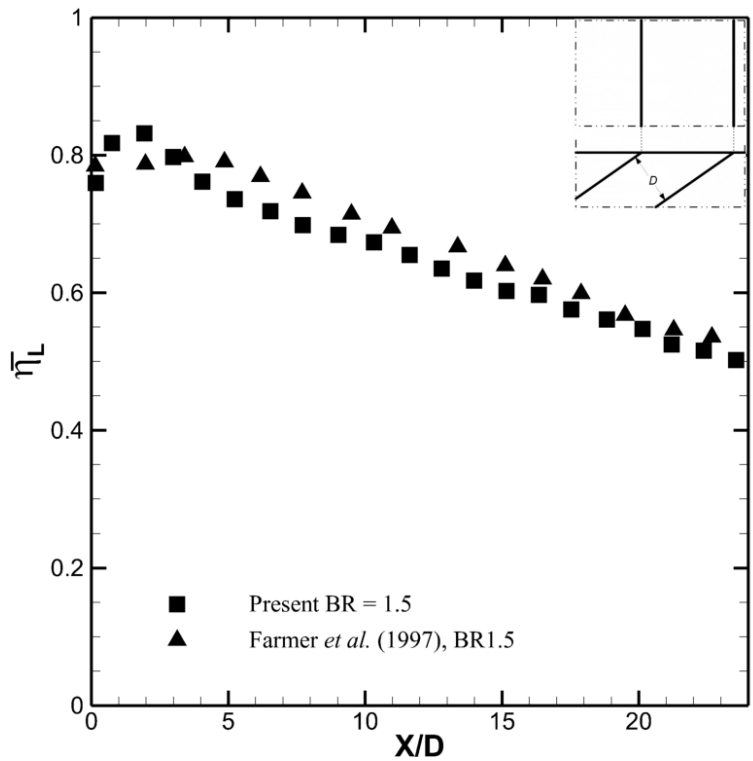

a) BR = 1.5

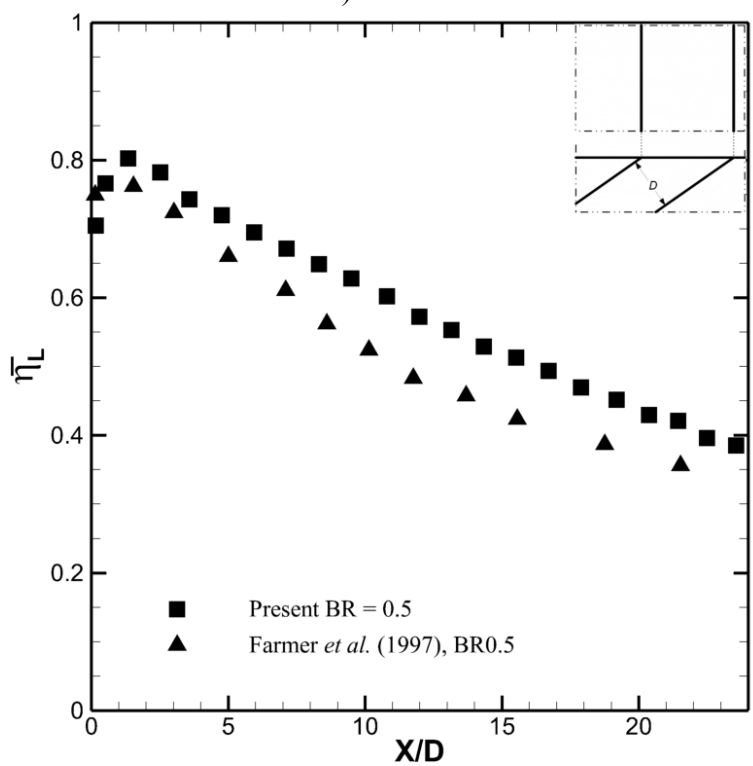

b) BR = 0.5

Figure 3.7 The published data for the simple slot [49]

3.3.1 Validation of the Experimental Facilities

Cylindrical hole is a classic film cooling geometry that has been investigated extensively; Wright *et al.* [48] provides high resolution η distributions of the cylindrical hole with the pressure sensitive paint technique. Its geometry is similar to the present investigation, and the DR is also unity. Its $\overline{\eta_L}$ data is compared with the present test results in Figure 3.6. Only marginal discrepancy is showing at BR = 0.5, the present test has a small liftoff, but the counterpart is attached. Apart from that, high agreements are observed.

The simple slot has ideal η performance. The comb scheme has a slot-like exit. It was aimed to obtain the flow characteristic of the simple slot. The present investigation tested the simple slot from BR = 0.5 to 1.5. Figure 3.7 compares the results with those of Farmer *et al.* [49], which is also an experimental investigation on a simple slot. Figure 3.7a is for the BR = 1.5, at the place immediately downstream of the trailing edge, the present measurement has a slightly bigger liftoff and reattachment than the literature data. After that, high agreement is shown. Figure 3.7b is $\overline{\eta_L}$ distributions at BR = 0.5. They begin at good agreement. Then from X/D = 5, the present measurement is slightly higher than the counterpart. Generally, the discrepancy is acceptable.

The $\overline{\eta_L}$ values in the whole BR range are compared at the positions of X/D = 1 and 5 in Figure 3.8. They show similar distributions and marginal discrepancies. The open published data demonstrates a characteristic that the BR 1 case has the highest $\overline{\eta_L}$, instead of the BR = 1.5 case. The present measurements captured identical trend.

The comparisons with the open published data in Figure 3.6 to Figure 3.8 have demonstrated the acceptable discrepancies completely consistent tendencies. The decent agreements strongly validated the present experimental facilities, proving the reliability of the present results.

3.3.2 Performance of the New Schemes

The $\overline{\eta_L}$ distributions of two new scheme configurations are shown in Figure 3.9, and compared with the cylindrical hole and the simple slot, in which validated η_c is used for cylindrical hole, instead of $\overline{\eta_L}$. Figure 3.9a is for the comb scheme configuration of $H = 1D$, $t_s = 0.1D$ and $P = 2t_s$ at BR = 1. Its performance is much higher than the cylindrical hole, and shows marginal difference with the slot. Figure 3.9b is for the HAR configuration of $t = 0.1D$ and $P = 3t$ at BR = 1. Its performance is also much higher than the cylindrical hole, however, its $\overline{\eta_L}$ is lower than that of the slot on the place immediately downstream of the exit. As moving downstream, it has slower decline rate, and meets the slot from X/D = 20. Moreover, this performance is obviously higher than its *t/P* values.

Among the new scheme configurations, the one in Figure 3.9a has the highest performance, and the one in Figure 3.9b has the lowest. The comb scheme achieving similar performance to the slot indicates the elimination of mainstream entrainment. Meanwhile, the HAR scheme performance much higher than its *t/P* values indicates the coolant expansion. The performance of the new schemes is consistent with the design.

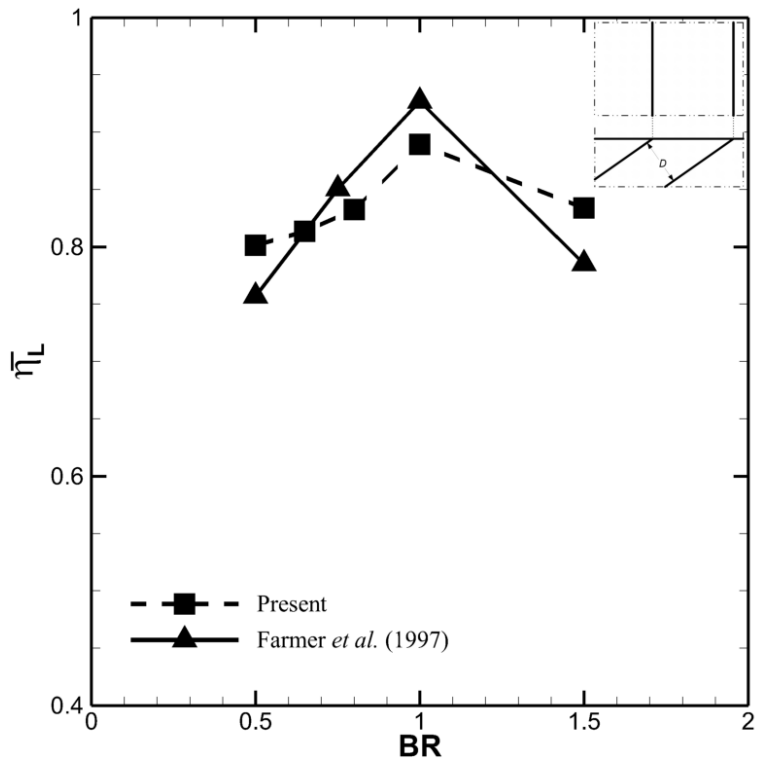

a) X/D = 1

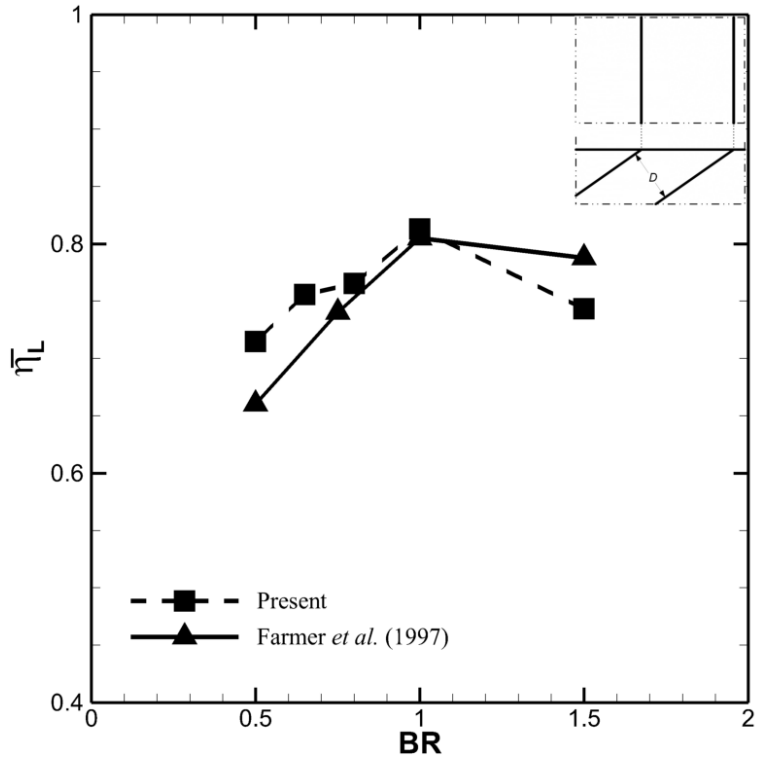

b) X/D = 5

Figure 3.8 The simple slot comparison on blowing ratios with the published data [49]

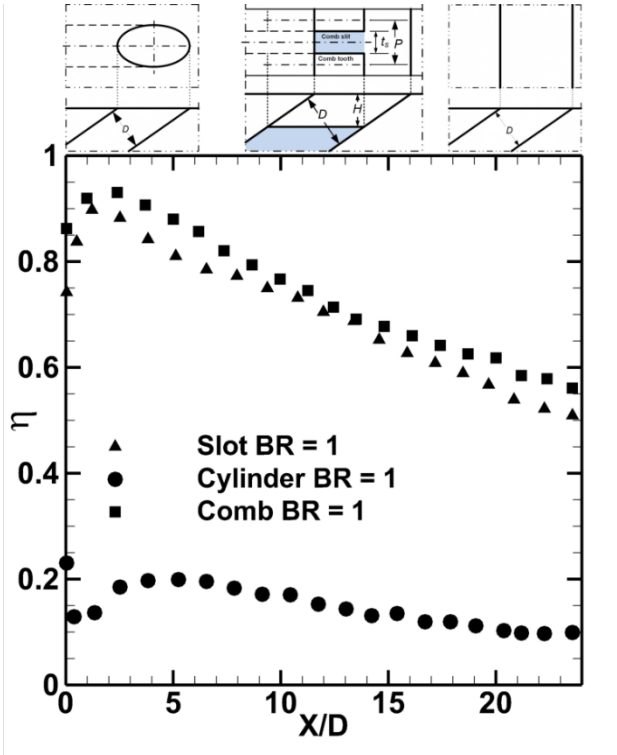

a) The comb configuration at $H = 1D$, $t_s = 0.1D$ and $P = 2t_s$

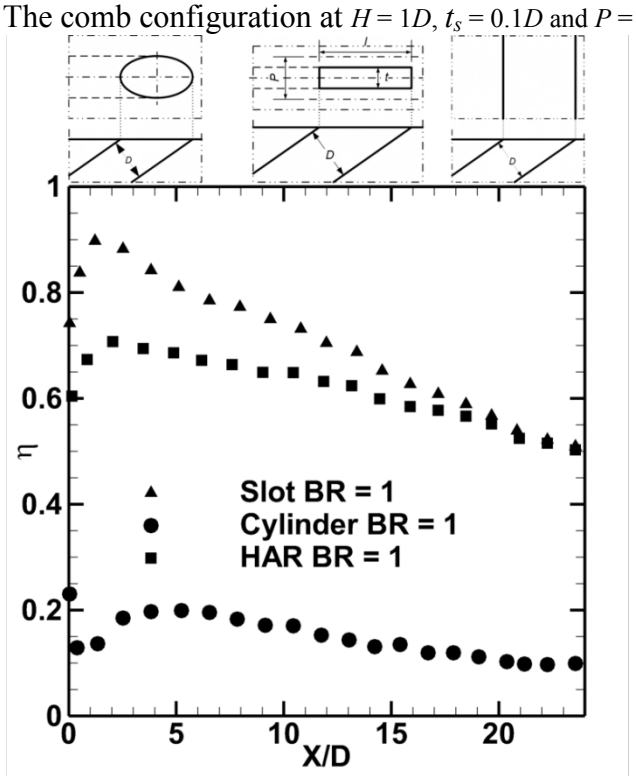

b) The HAR configuration at $t = 0.1D$ and $P = 3t$

Figure 3.9 The new scheme performance at BR = 1

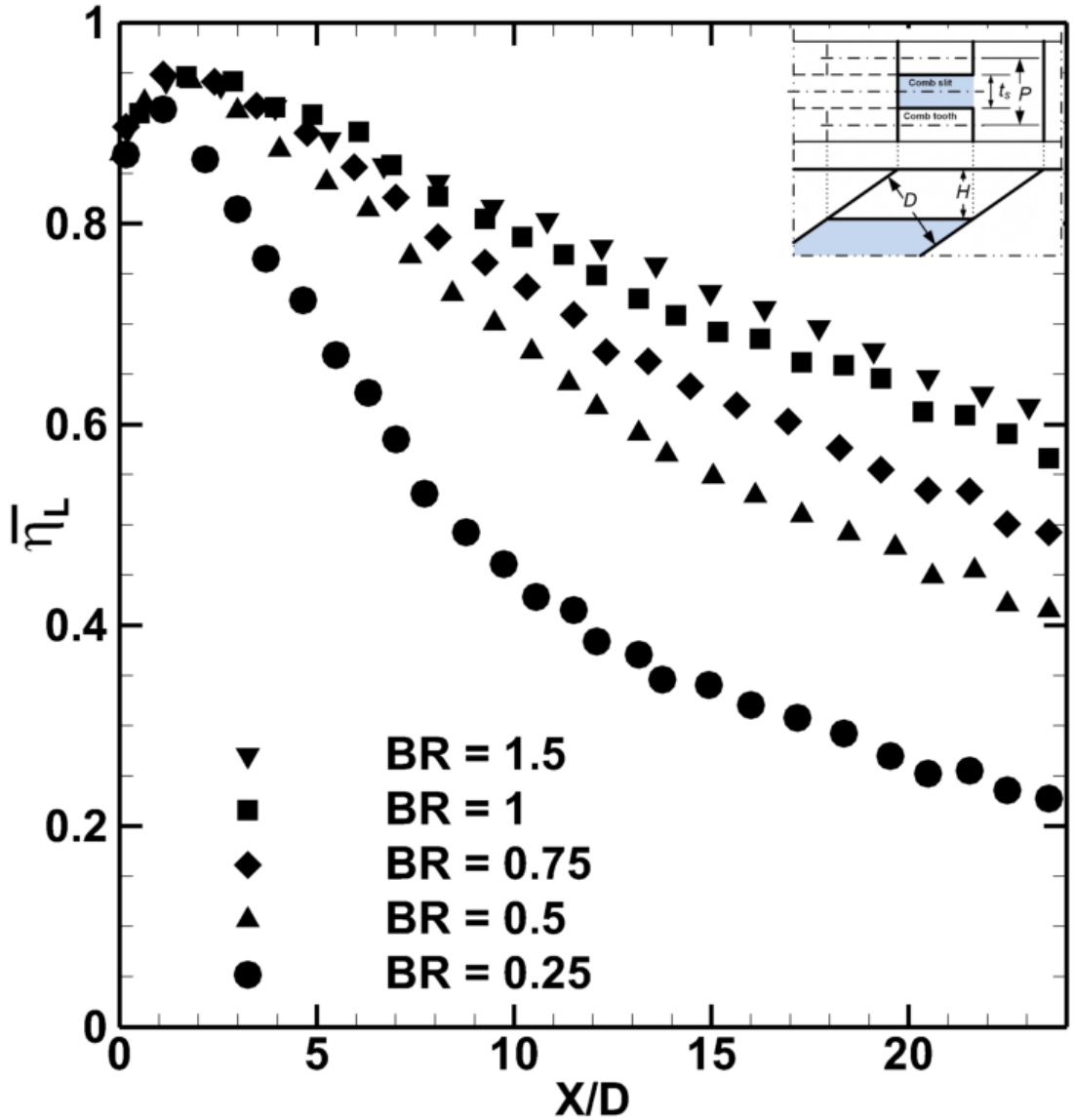

Figure 3.10 The comb scheme performance of the configuration $H = 1D$, $t_s = 0.1D$ and $P = 2t_s$

3.3.3 BR Effect of the New Schemes

The $\overline{\eta_L}$ distributions in the BR range of 0.25 – 1.5 are shown in Figure 3.10. It shows a high performance. The performance increases as the BR increasing. The $\overline{\eta_L}$ distributions of all cases have liftoff-reattachments and similar reattached values of approximate 0.95. The BR shows no significant effect immediate downstream of the exit trailing edge, apart from the low BR case of BR = 0.25 has a 0.03 lower reattached value. However, the BR differentiates the $\overline{\eta_L}$ decline rate further downstream. The case of BR = 0.25 drops the fastest, followed by the case of BR = 0.5, and the BR 1.5 case drops the slowest.

The other new scheme configurations show similar BR effects. Generally, the BR factor has negligible effect on the performance immediately downstream the exit, but has distinct effect on the decrease rate of the $\overline{\eta_L}$ further downstream. This effect is notable at low BR values, while it is

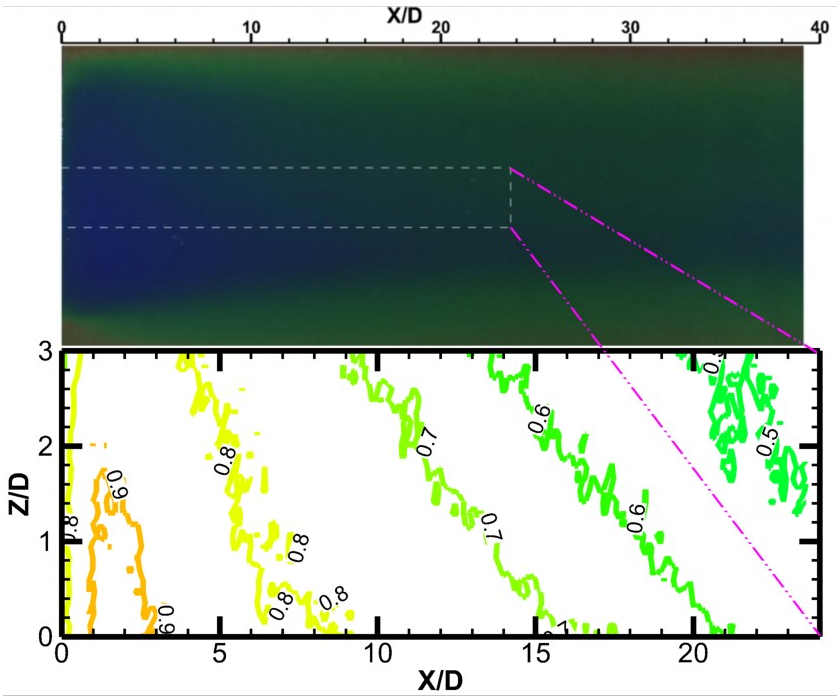

Figure 3.11 The slot η contours at BR = 1

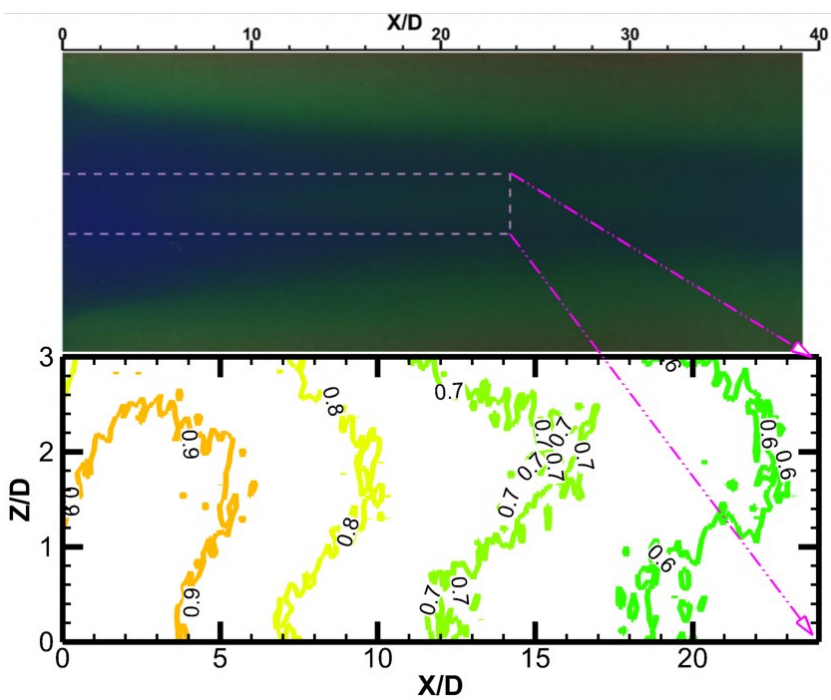

Figure 3.12 The η distribution of the configuration $H = 1D$, $t_s = 0.1D$ and $P = 2t_s$ (cases of 12), BR = 1

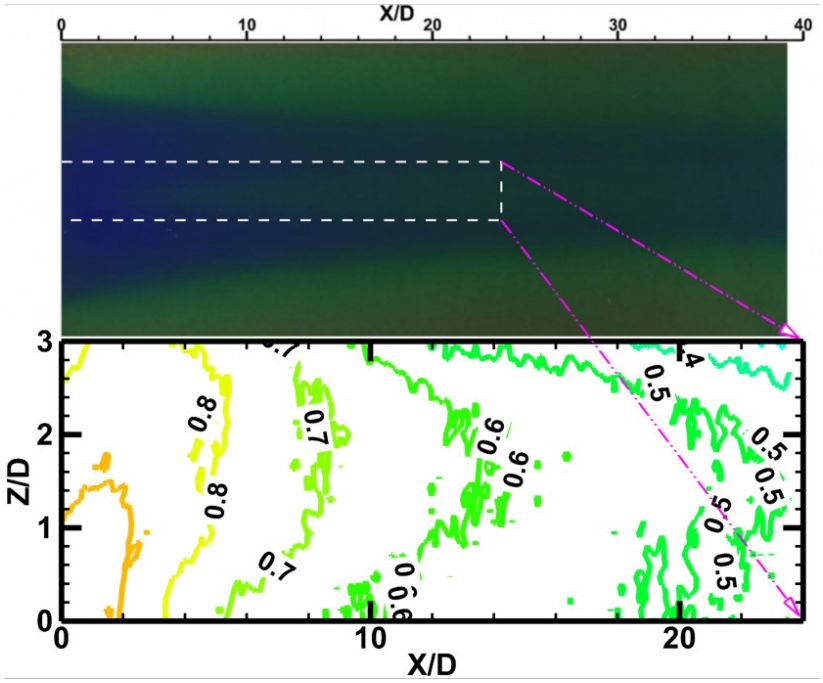

Figure 3.13 The η distribution of the configuration $H = 0.5D$, $t_s = 0.1D$ and $P = 3t_s$ BR = 1

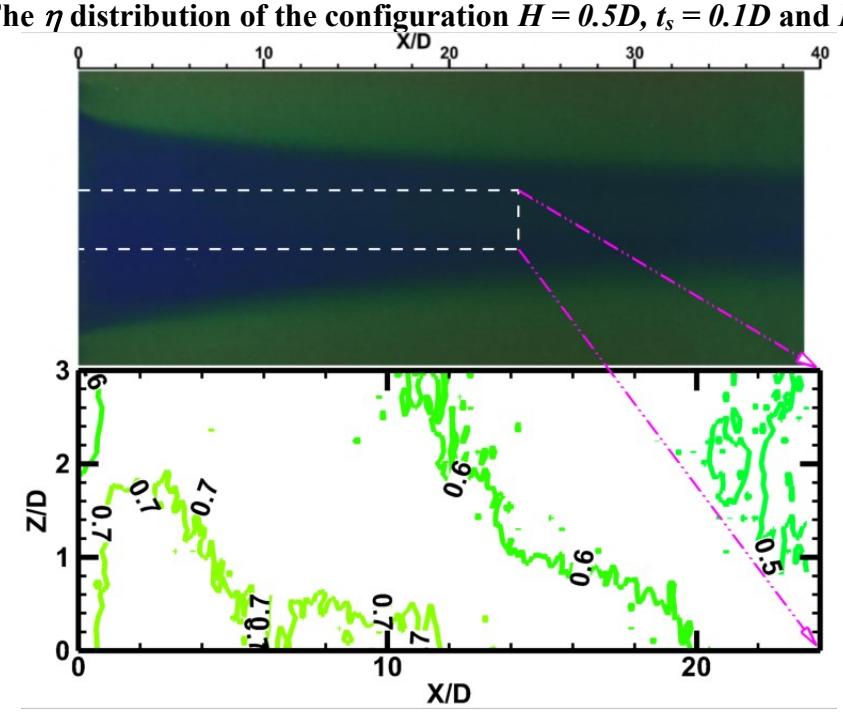

Figure 3.14 The η distribution of the configuration *HAR* $P = 3t$ BR = 1

reduced with BR increasing, and is negligible at high BR values (BR = 1.5).

The present investigations are aimed to focus on the high performance, the performance similar to the slot. In terms of the BR effect, the BR = 1 case demonstrated representative high performance for each new scheme configuration. Hence this case is usually used in the further analysis.

3.3.4 Detail η Distributions

The detail η distributions of four geometries at BR = 1 are shown in Figure 3.11 to Figure 3.14. They are slot, comb configuration of $H = 1D$, $t_s = 0.1D$ and $P = 2t_s$, comb configuration of $H = 0.5D$, $t_s = 0.1D$ and $P = 3t_s$, and HAR configuration of $t = 0.1D$ and $P = 3t$, respectively. In the TLC testing, each test took 300 TLC images to record the color varying. The last image was fairly similar to the η distribution. For this kind of detail η distribution figures in the present paper, the last image of the test case is attached above the η contour chart. In the TLC image, the blue color denotes high η, the green color denotes the lower η, and the red color denotes the lowest. The lateral dimensions of these four geometries were 12.7D. The left side of the image is the exit trailing edge. In each image of these figures, the lateral span of the blue color narrows as moving downstream (the right side), indicates strong end effect. This common phenomenon has been mentioned in the previous research, for example, similar end effect was shown in Bunker [37] (Fig. 6-7, 9-11). Thus, in the present investigation, only the central 25% (3D width) have been post-processed, aimed to reduce the end effect. This region is marked with dashed lines.

The η contour chart in Figure 3.11 is for the slot. It shows a small liftoff-reattachment: the contour line of 0.8 locates at X/D = 0, and the contour lines of 0.9 locates at X/D = 1 and 3, indicates the reattachment at X/D = 2. Then η decreases continuously to 0.5. Similar distributions are shown in Figure 3.12 and Figure 3.13 for the two comb configurations at BR 1, and the η shown in Figure 3.12 is slightly higher, demonstrates that the H value increasing to 0.5D has negligible effect on η. Moreover, the similarity of the comb scheme and the slot denotes the elimination of the mainstream entrainment.

A phenomenon is apparent in Figure 3.13, and is appreciable in Figure 3.11 and Figure 3.12. The central part usually has the highest η values, but it is demonstrated that, the shape of the local η distributions has two branches. The local peak values locate on two sides, a relative low η value occurs in the middle. Saumweber and Schulz [50] discussed this phenomenon in their investigations on fan-shaped hole. They thought it was the result of the in-tube separation leading to a U-shape jet velocity profile. However, our investigations indicate that it is caused by the end effect, because a strong CRVP is produced on two ends. Similar phenomenon was mentioned in [33]. It occurred in the present tests on the slot and the comb scheme, apparently or less apparently. It is an interesting future topic.

Figure 3.14 is for the HAR configuration of $P = 3t$. Its TLC image shows intermittent small green area at the exit trailing, indicates the mainstream penetrates the coolant film. It denotes that the coolant is under expanding, the continuous coolant film has not yet formed. In the η contour chart, a comparatively low η contour line, which is 0.6, shows close to the exit trailing edge. Then η increases to more than 0.7 as moving downstream. After that, η declines continuously to the further downstream. The performance of another HAR configuration, in which $P = 2t$, was similar to Figure 3.11 and Figure 3.12. It showed a high η value, which is close to 1, in the region immediately downstream of the exit trailing edge. It indicates a continuous coolant film has formed, and the coolant has mostly fully expanded. It was demonstrated that increasing P/t does not favor the coolant expansion.

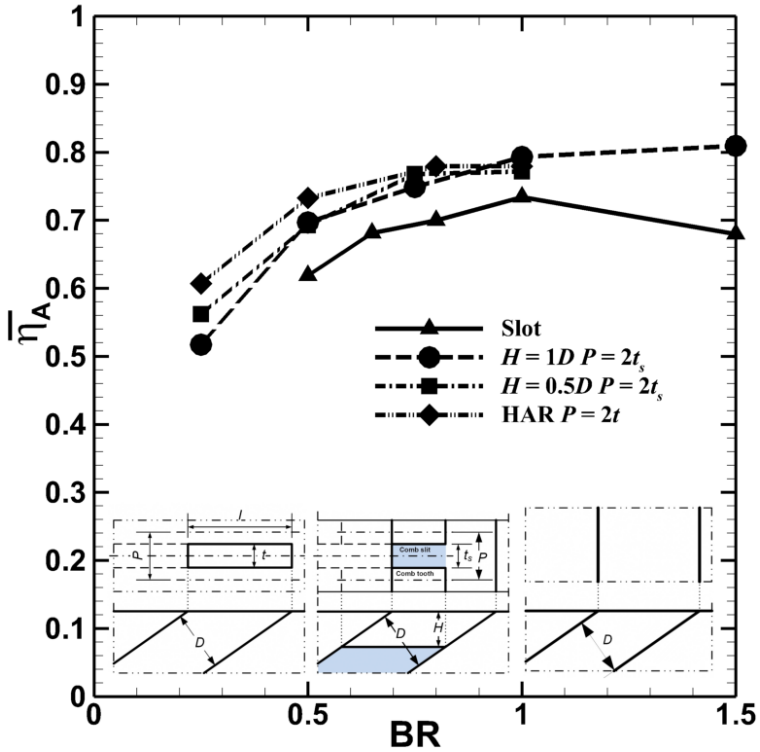

a) Comb configurations at $P = 2t_S$ and HAR at $P = 2t$

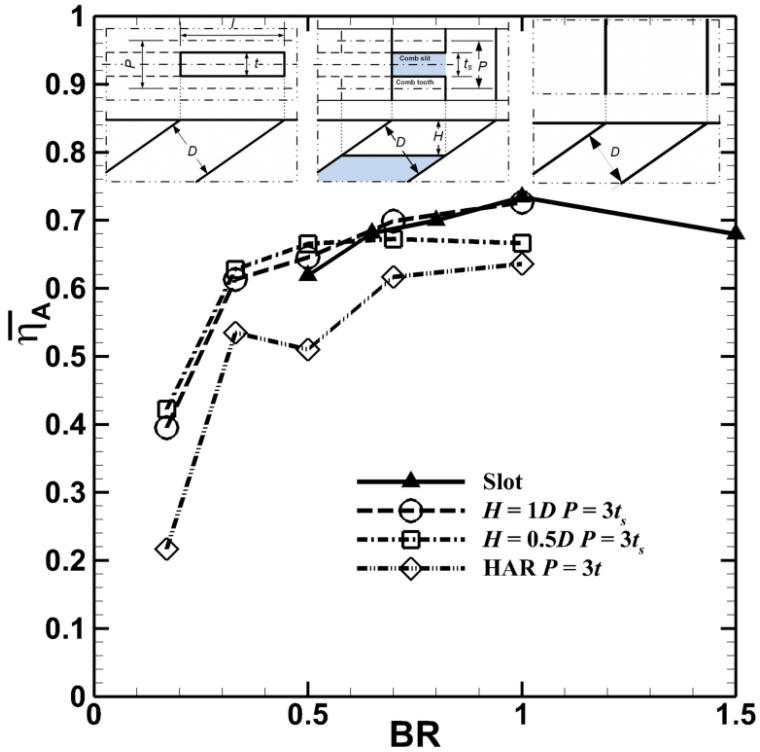

b) Comb configurations at $P = 3t_S$ and HAR at $P = 3t$

Figure 3.15 $\overline{\eta_A}$ performance of the new schemes

3.3.5 The $\overline{\eta_A}$ Performance of the New Schemes

The performance of the new scheme geometries are compared with the slot in Figure 3.15 with their $\overline{\eta_A}$ values. The BR ranges from 0.17 to 1.5. Figure 3.15a shows the comb configurations of $P = 2t_S$ and the HAR configuration of $P = 2t$. All configurations show similar performance, and apparently higher than the slot. Their $\overline{\eta_A}$ distributions increase when their BR increasing. The BR effect is noticeable at low BR values, and reduced at high BR values. This tendency is identical to the aforementioned in Figure 3.10.

Figure 3.15b shows the comb configurations of $P = 3t_S$ and the HAR configuration of $P = 3t$. It shows similar tendency of the BR effect. However, the performance is apparently lower than that in Figure 3.15a, in particular the HAR configuration. It is approximately 0.1 lower than the slot. It demonstrates the higher P/t (or P/t_S) does not favor the high performance.

The design of the comb scheme is aimed to obtain similar flow to the slot, as such to achieve the performance of the slot. The performance in Figure 3.15 indicates this new scheme fully match the design. The $\overline{\eta_L}$ of a traditional film cooling geometry is lower than its *t/P* value. Except the characteristic of the high aspect ratio, the HAR scheme is a simple traditional geometry. The HAR performance shown in Figure 3.15 is much higher than their *t/P* values, convincingly indicates that the coolant expansion is exploited by the new scheme.

3.4 Conclusions

Along the research results of the CRVP effect on η, a mechanism of the film cooling heat transfer has been proposed. The mainstream entrainment and the coolant expansion among this mechanism are applied to develop two new film cooling schemes, the comb scheme and the HAR scheme. The comb scheme is aimed to eliminate the mainstream entrainment, while the HAR scheme is aimed to exploit the coolant expansion.

The new schemes have been experimentally investigated with transient TLC technique. The experimental facilities have been rigidly validated with open published data. The experimental results have shown the high performance of the new schemes. The comb scheme demonstrates comparable performance with the slot, indicates the similar flow uniformity to the slot, and the mainstream entrainment has been eliminated. The HAR scheme demonstrates higher performance than their *t/P* values, indicates the coolant expansion is strongly taking effect. The performance of new schemes matches their design.

The designs of the new schemes were guided by the proposed film cooling heat transfer mechanism. Successfully obtaining the prospective performance convincingly proves the mechanism. It established a solid fundamental of the film cooling research.

Chapter 4 Experimental and Computational Investigations of a Comb-Like Film-Cooling Scheme

Accepted by Heat Transfer Engineering Journal [51][1].

A part has been published on the ASME - JSME - KSME Joint Fluids Engineering Conference 2019 as AJKFLUIDS2019-4659: Experimental Investigations of a Comb-Like Film Cooling Scheme

A part was published in Joint Canadian Society for Mechanical Engineering and CFD Society of Canada International Congress 2019 as: Numerical Investigations of a Comb-Like Film-Cooling Scheme

Abstract

Film-cooling hole-geometry research needs a better understanding in the mechanism of film cooling effectiveness, which was recently shown to depend rather strongly on the counter-rotating vortex pair (CRVP); in this work, a mechanism of the film-cooling heat transfer is proposed. Its mainstream entrainment was aimed to be eliminated by developing a new scheme named comb scheme, which was intended to moving CRVP away from mainstream-coolant interface, rather than suppressing CRVP itself. It is investigated experimentally and numerically in this work. The transient thermochromic liquid crystal technique was used in the experimental work, while the Reynolds-averaged Navier-Stokes equations coupled with a realizable κ-ε turbulence model was used to simulate the flow numerically. The results were assessed against open published results hence demonstrating the so called 'ideal' performance (film cooling effectiveness = 1) of the new scheme, but with practical structural integrity. The geometric parameter analysis showed that the visualized strong CRVP, where intensity is more than 20, is trapped in the blind slot, hence its impact on mainstream-coolant interface is dropped to approximately 3, and mainstream entrainment is eliminated. It confirms the success of the comb scheme in achieving the high performance of the film-cooling heat transfer mechanism.

[1] Co-authors: Wahid Ghaly, Ibrahim Hassan

4.1 Introduction

Cooling technologies are necessary for any advanced gas turbine, in which film cooling is the mainstay. Several decades ago, discovering the superior performance of the shaped hole for film cooling geometries, by Goldstein and Eckert. [4] was considered a revolutionary progress, while, Bunker [2] in his review noted that no further improvement has been achieved. More recently, fundamentals of the film cooling heat transfer have become of much greater urgency.

Bogard and Thole [3] summarized the factors affecting the film cooling effectiveness (η), such as the blowing ratio (BR), density ratio (DR), and turbulence, to list a few. The well-established opinion is that factors involving velocity such as the momentum flux ratio (I) have a crucial effect on η [1, 3, 4]. Sinha *et al.* [5] classified the film cooling flow locally into attached, detached and reattached flows, which were controlled by the momentum flux ratio I. Goldstein and Eckert [4] thought the improved performance of the shaped holes was due to the expanded exit reducing the jet velocity. However, Gritsch *et al.* [6] demonstrated that the area ratio had no significant effect on η.

Models were built to predict η with pertaining parameters, in which the prospective crucial factors were included. The correlation of Baldauf *et al.* [29] included important parameters such as DR, BR, and hole pitch (P), to list a few. The lateral coverage ratio (t/P) and BR were included in the correlation of Colban *et al.* [7], which is based on the shaped hole data. They concluded a regularity about the distribution of the laterally averaged η ($\overline{\eta_L}$): the maximum $\overline{\eta_L}$ is equal to t/P, occurs at the exit trailing edge, then $\overline{\eta_L}$ decreases monotonously when moving downstream.

Fric and Roshko [11] illustrated a vortical structure, the counter-rotating vortex pair (CRVP). Haven *et al.* [13] and Hyams and Leylek [16] thought the superior performance of the shaped holes was due to the weak CRVP. Along with this conclusion, novel film cooling schemes have been developed to improve η by weakening the CRVP [23, 25, 31, 32].

Li and Hassan [7] showed that CRVP strength was the most crucial factor affecting η. They proposed a correlation in the form: $\overline{\eta_A} = t/P + a\overline{\omega_x}$. Here, $\overline{\eta_A}$ is the space averaged η; a is a constant; $\overline{\omega_x}$ is the streamwise CRVP intensity. The simple slot conforms to the correlation, in which t/P is 1, when the CRVP intensity is negligible. So the simple slot has the perfect (or ideal) effectiveness $\eta = 1$ [3]. However, its structural integrity restricts the application. The objective in film cooling geometry research is to obtain the slot performance and resolve the structural integrity issue [2]. Sargison *et al.* [34] developed a scheme named Console, where they used a parameter named minimum cross-section area (MCSA) to quantify the structural integrity. In their paper, the MCSA values of the cylindrical hole, shaped hole, and the Console were 0.67, 0.52 and 0.25, respectively. Bunker [35] proposed a trench scheme, which possesses a slot-like exit. Bunker [37] proposed a scheme named Mesh-Fed Slot. The MCSA values of its two configurations are estimated to be 0.16 and 0.27. Tan *et al.* [52] extended the investigations experimentally and numerically. Similar geometry applied on a vane was investigated [53–55]. Davidson *et al.* [38] and Bruce-Black *et al.* [39] developed a practical slot configuration, in which a blind slot is fed by impinging holes.

Owing to the crucial effect of CRVP, further investigations were performed. Li *et al.* [33] analyzed the CRVP formation in the film cooling flow of the cylindrical hole. The only essential

source was the velocity gradients on the mainstream-jet shear layer. Rather than the *I* effect suggested in [5], the cause of the liftoff-reattachment of the film cooling flow is the CRVP entrainment. When a mass of mainstream gas is entrained into the jet flow by the CRVP, depending on the CRVP intensity, the film cooling flow behaves as attached, liftoff-reattached

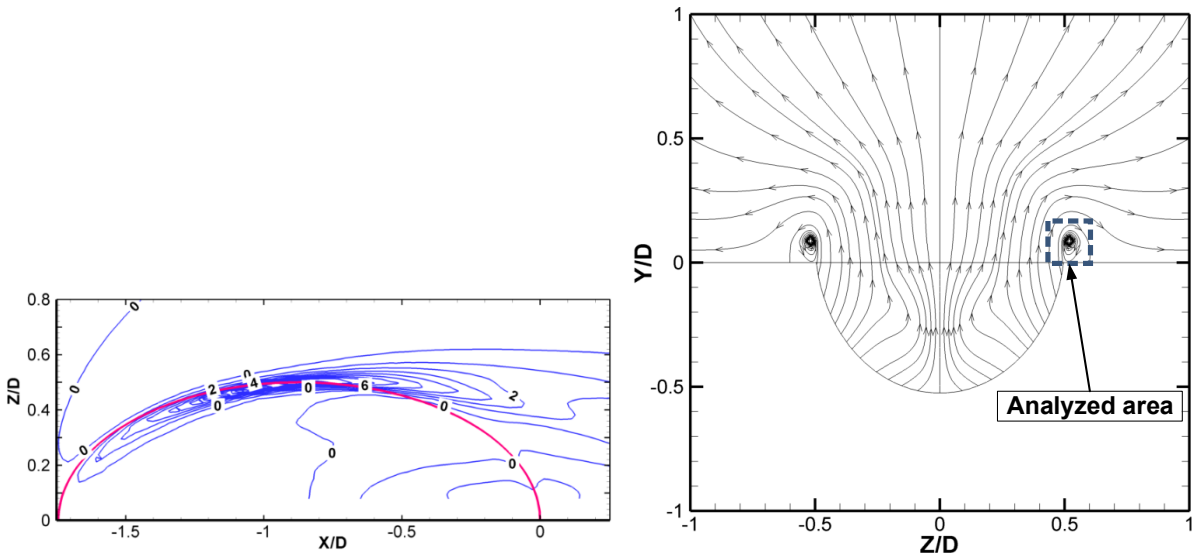

a) Detailed $\partial v/\partial z$ distributions, from [33]

b) CRVP at X/D = -0.75 from [33]

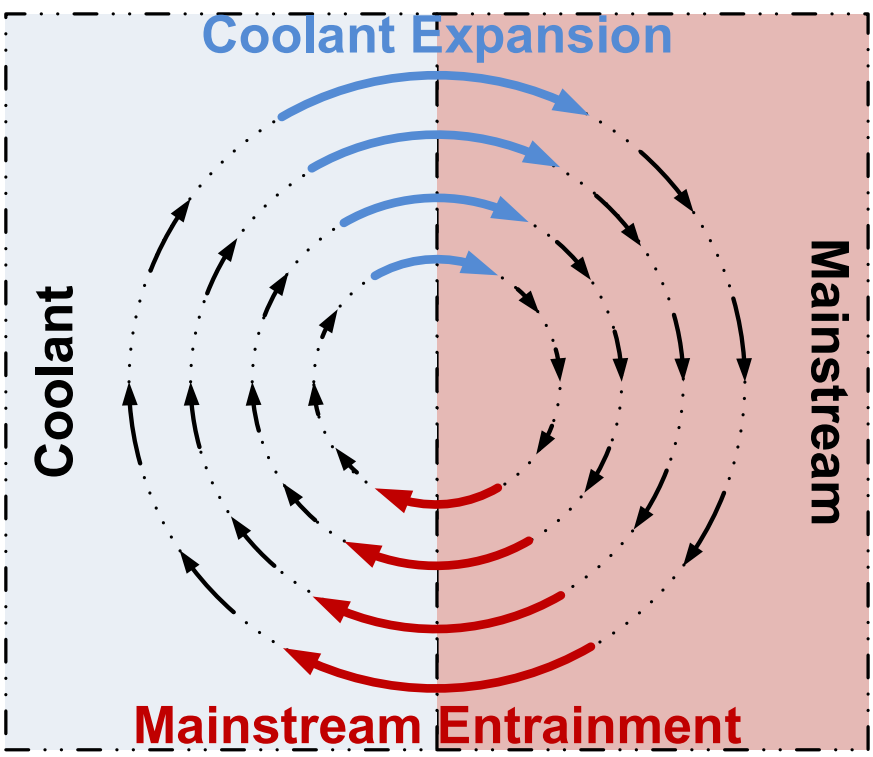

c) Mechanism of the film cooling heat transfer

Figure 4.1 The mechanism of film cooling heat transfer

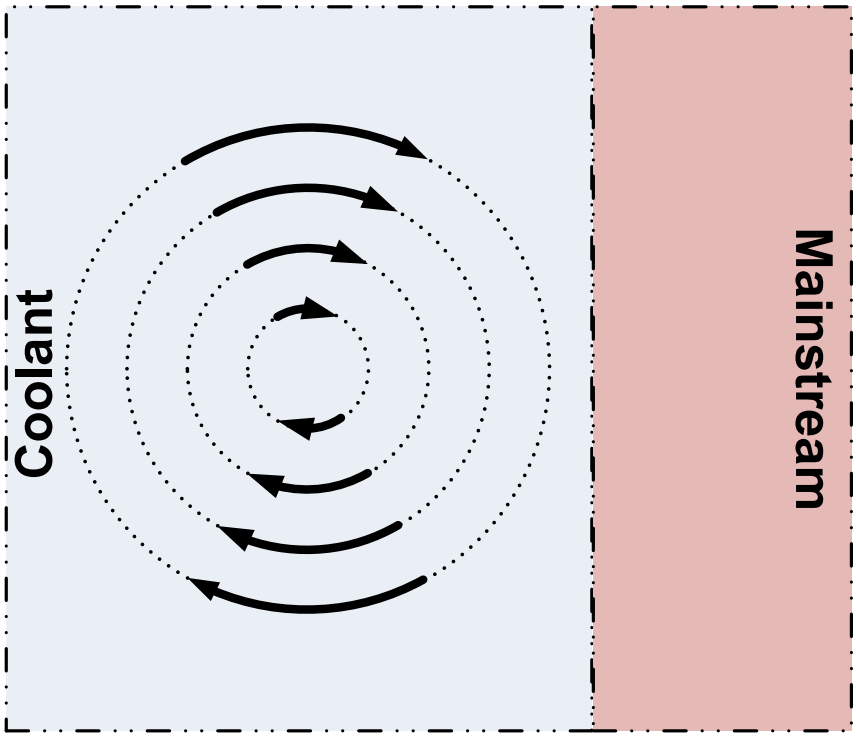

Figure 4.2 Elimination of the mainstream entrainment

and detached. The bulk of the entrained mainstream gas, which has a higher temperature, arriving at the central line becomes the liftoff. The edge of the entrainment, which had a lower temperature, arriving at the center line appears to be the reattachment. In the case of a weaker CRVP, the negligible entrainment leads to the attached. In the case of a stronger CRVP, large entrainment leads to the detached. The mixing of the entrainment commonly appears to be the kidney shape.

Along with the discovery of the CRVP crucial effect [7, 33], the present paper dissects the mechanism underlying this effect. A film cooling heat transfer mechanism is proposed. The mainstream entrainment in this mechanism is aimed to be eliminated by developing a new film-cooling scheme with a slot-like exit and a comb-like structure. Accordingly, its t/P is 1, with a practical structural integrity. This new scheme pushes the CRVP away from the mainstream-coolant interface, thus approaching the ideal performance, namely, a film cooling effectiveness η of one.

4.2 Methodologies and Models

A mechanism of film cooling heat transfer was proposed based on analyzing the crucial effect of CRVP on η. Applying this mechanism, an advanced film cooling scheme named comb scheme was developed. The new scheme was investigated experimentally and was tested numerically. The experiments were performed on a two-loop wind tunnel, with a thermographic technique, the **T**hermochromic **L**iquid **C**rystal (TLC) technique. Steady Reynolds-averaged

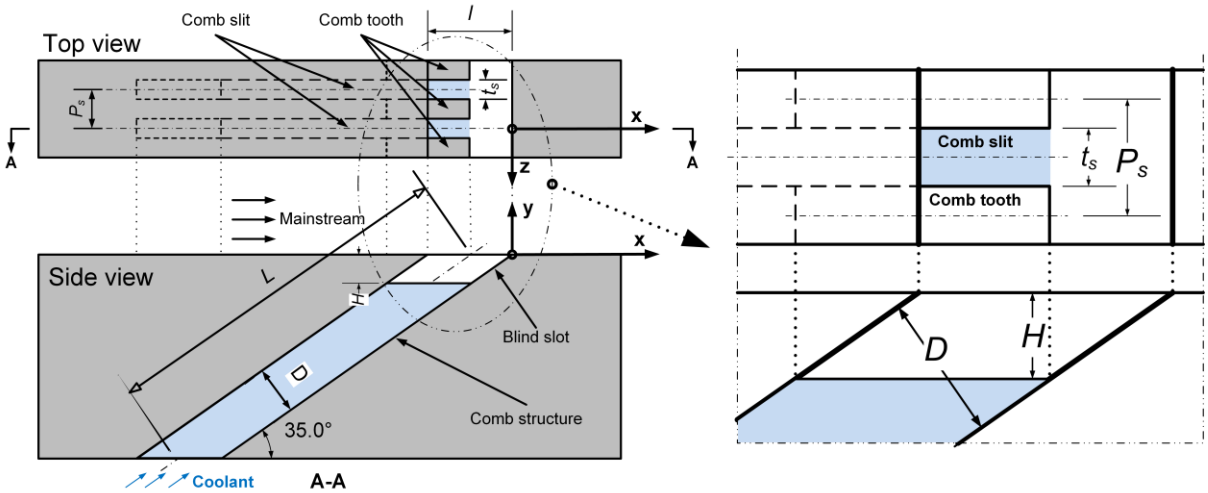

Figure 4.3 Comb scheme configuration

Navier-Stokes (RANS) simulations were performed with the realizable κ-ε (RKE) turbulence model.

4.2.1 Mechanism Underlying the CRVP Crucial Effect

The crucial effect of the CRVP intensity was discovered by Li and Hassan [7], and the vortical structure was further analyzed by Li *et al* [33] who concluded that the secondary flow at the mainstream-coolant interface were the essential source of the CRVP. Figure 4.1(a) taken from [33], shows the detailed distributions of $\partial v/\partial z$, where the edge of the cooling hole exit is shown in the background. The figure demonstrates that the local peak of $\partial v/\partial z$ is right above the edge of the hole exit. Inside the edge is mostly coolant, which jets out with velocity v. Outside the edge is mostly mainstream, where v is deemed to be 0. Hence severe velocity gradients occur at the mainstream-coolant interface where $\partial v/\partial z$ and $\partial w/\partial y$ generate secondary flow which drives the CRVP.

Figure 4.1(b)taken from [33] described the forming process of its CRVP with 2D streamlines. The enlarged form of Figure 4.1(b) is shown as Figure 4.1(c). To simplify the situation, the mainstream-coolant interface thickness is taken to be 0, the CRVP size is ignored, and the offset between the CRVP position and the mainstream-coolant interface is also ignored. Figure 4.1(c) illustrates the mechanism of the film cooling heat transfer: its middle plane is the mainstream-coolant interface, with the coolant to its left and the mainstream to its right. In the vicinity of the interface, severe velocity gradients occur, and lead to rotation ω on the interface which produces penetrations and drastically increases the heat transfer. The penetration from the mainstream to the coolant is the mainstream entrainment, which wedges the mainstream into the coolant and decays η drastically.

The film cooling convection is mostly by advection while the diffusion is neglected [33]. So without advection (CRVP intensity is 0), the mainstream-coolant interface is steady. In this case, the outermost position of the interface is *t/P*. It is the reason under the correlation proposed in [7], $\overline{\eta_A} = t/P + a\overline{\omega_x}$. To obtain the highest available performance, *t/P*, the CRVP effect has to be decreased to 0. However, in a discrete film cooling geometry, velocity gradients naturally

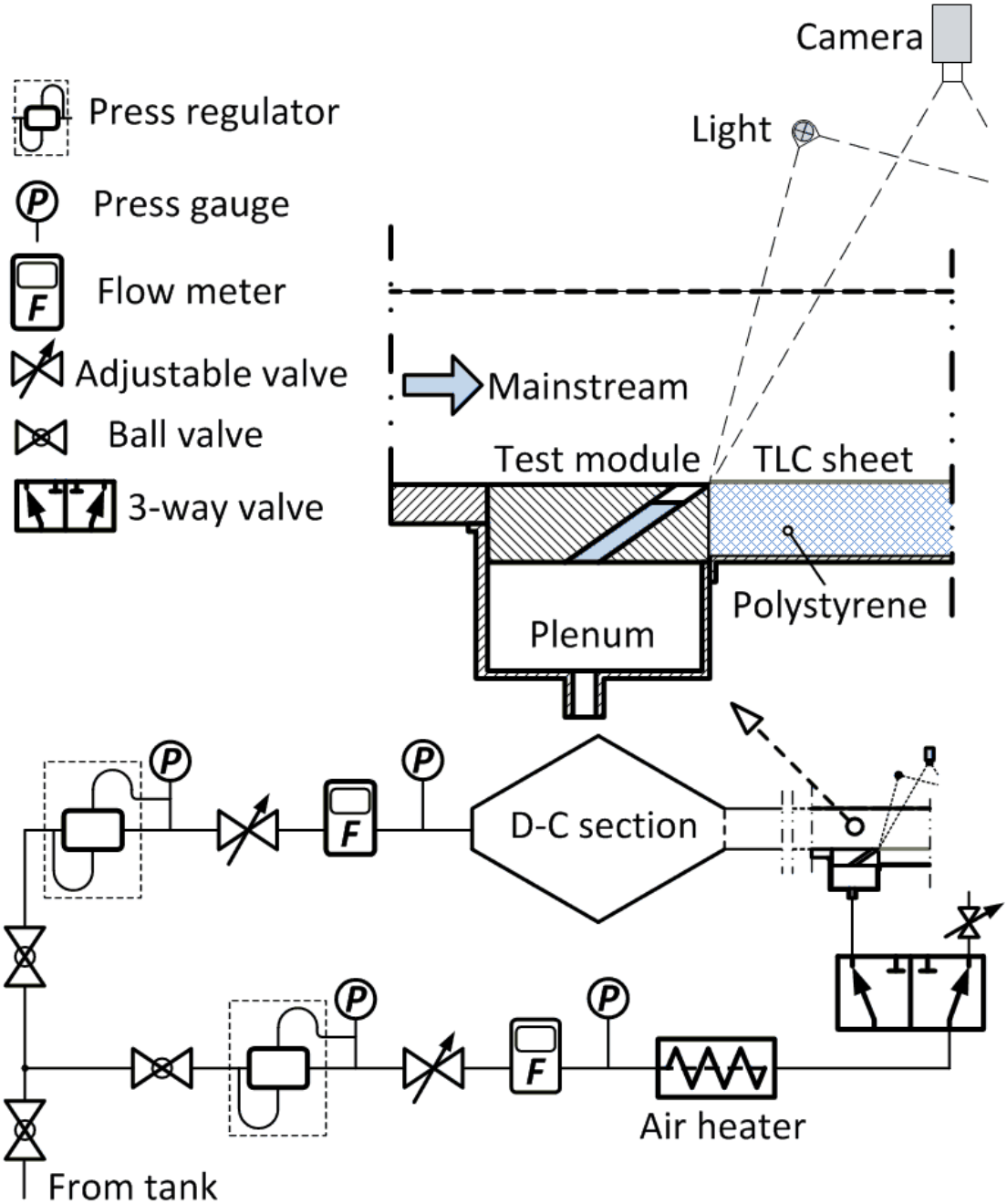

Figure 4.4. Schematic diagram of the experimental setup

occur as the coolant jets out and lead to CRVP. Therefore, instead of suppressing the CRVP itself, we sought to move this vortical structure away from the mainstream-coolant interface, as illustrated in Figure 4.2. If CRVP were far away enough from the interface, the mainstream entrainment would be decreased or eliminated regardless of the CRVP intensity. In other words, the approach of developing the new scheme is not to curb the CRVP intensity, but to manipulate its impact on the interface.

4.2.2 Comb Scheme Configuration

Along with the analysis on the film cooling heat transfer mechanism, a film cooling scheme was developed, its structure is shown in Figure 4.3. It is composed of an inclined blind slot fed by a comb-like structure. The inclined angle is 35°. Due to the blind slot exit, *t/P* is 1. In the comb-like structure, the coolant gets out through the comb slits, and the comb teeth provide the material structural integrity. The new scheme was named comb scheme because of the characteristic comb-like structure. The blind slot width is *D*, it was set to 5 mm in the experiment, and 12.7 mm in the numerical simulations. The exit longitudinal dimension is *l*, and the vertical depth is *H*. The axial length of the geometry, *L*, is 7*D*. For the comb structure, the lateral dimension of the comb slit is t_s, and the lateral space between the two comb slits is P_s.

The Cartesian coordinates for this investigation are also shown in Figure 4.3. The origin is located on the central plane of the comb slit crossing the exit trailing edge. The x-, y- and z-axes are aligned with the mainstream, vertical, and span-wise directions.

As the coolant jets out of the comb slits, severe velocity gradients occur, leads to secondary flow and the CRVP which, in this geometry, is expected to be close to the bottom of the blind slot. Meanwhile, the mainstream-coolant interface is usually located at a Y-value higher than Y =

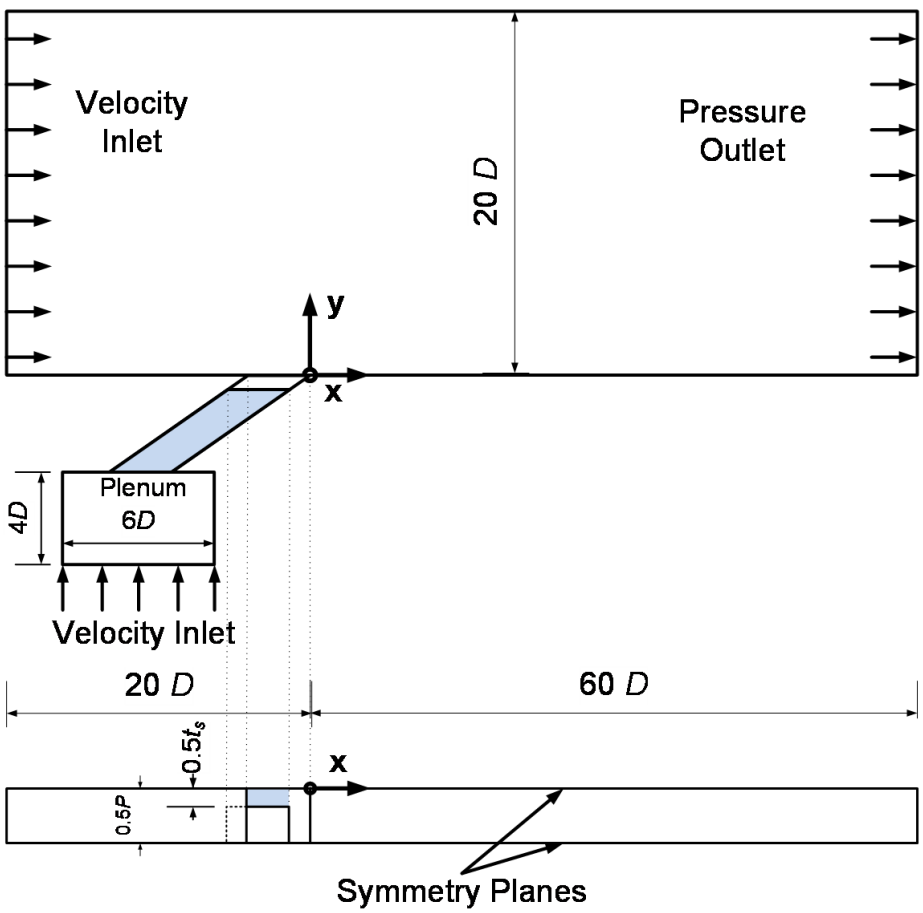

Figure 4.5 Computational flow simulation domain

0. The distance between the CRVP and the interface is approximately H. The CRVP effect on the interface, which will be presented as ω_x on mainstream-coolant interface, is expected to be manipulated mostly by changing the H values.

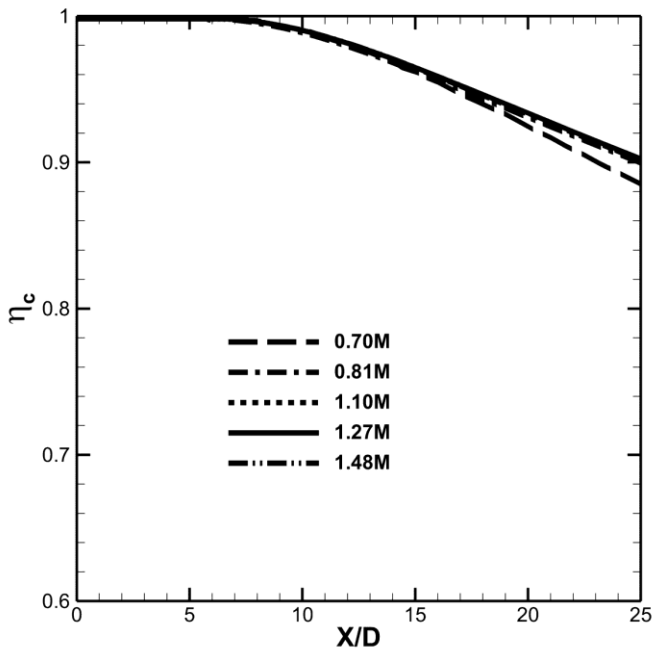

(a) Grid independency test

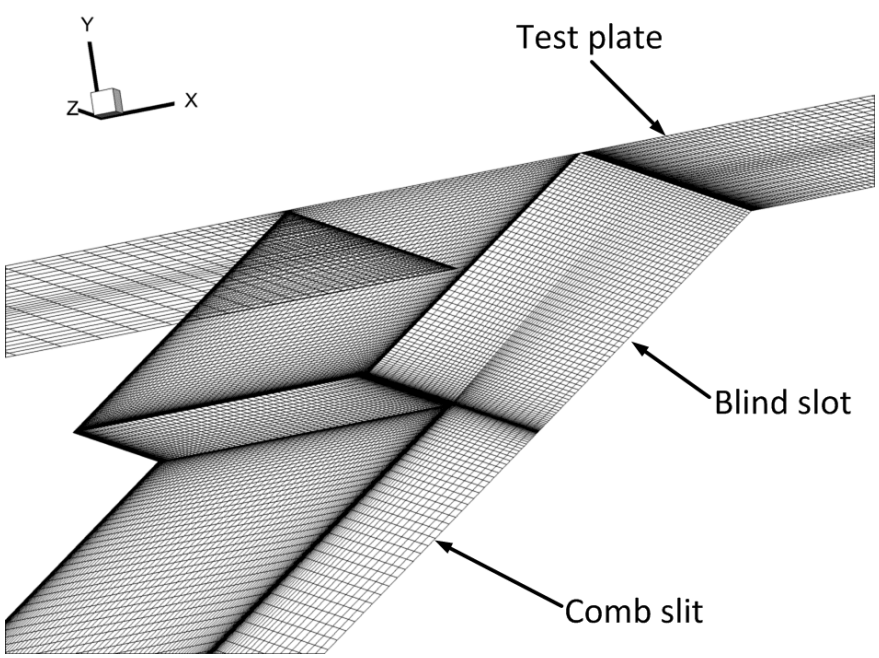

(b) A close look of mesh near the exit

Figure 4.6 Simulation grids

4.2.3 Experimental Facility

The transient TLC technique was used in the present investigations where its color varies with temperature. The transient TLC technique considers the film cooling heat transfer as a transient conduction case, namely the semi-infinite solid case which has the following analytical solution,

$$\left.\begin{aligned} T_w - T_i &= \left[1 - \exp(\beta^2)\, erfc(\beta)\right]\left[\eta\left(T_j - T_m\right) - T_m - T_i\right] \\ \beta &= \frac{h\sqrt{a\tau}}{k} \end{aligned}\right\} \tag{4.1}$$

where η is the film cooling effectiveness, T_m is the mainstream temperature, T_j is the coolant temperature measured at jet state, and T_i is the temperature at the initial state. They were measured with thermocouples. T_w is the temperature on the test plate, which was measured with the TLC technique. So only η and h are unknown in this equation, they were solved in the post-process with our in-house programs. Wang *et al* [40, 41] introduced the TLC technique into the film cooling investigations. Since then, it has been widely used in the film cooling research, to list a few [8, 9, 42–47].

The experiments have been performed in a two-loop wind tunnel, which is shown in Figure 4.4. Its first loop is for the mainstream flow, and the second loop is for the coolant flow. Both loops have adjustable valves, pressure regulators and flowmeters. The coolant loop has a heater to increase the coolant temperature. The DR was considered as unity (0.98). The coolant loop connects the mainstream loop in the test section through a plenum under the bottom. The cross-section dimensions of the test section are 99 mm × 53.5 mm. Its mainstream velocity was set to 20 m/s. The coolant velocity was adjusted upon the BR settings.

The comb scheme geometry was manufactured on a test module, installed on the test plate, which is the bottom of the test section. The lateral width of blind slot is 63.5 mm (12.7*D*). Downstream of the test module is a piece of extruded polystyrene, covered with a TLC sheet. The size of the TLC sheet is 203 mm × 89 mm (40.6*D* × 17.8*D*). To decrease the end effect, only the central 25% was post-processed. A 3CCD camera is located right above the test section, to capture the TLC images through the transparent top of the test section. Each test records 300 TLC images at 5 frames/s. They were saved to a workstation with the simultaneous temperature data of the mainstream and the coolant, which were measured with thermocouples. The temperature uncertainty is ± 0.2K. An in situ TLC calibration was performed, in which calibrated temperature ranged from 22.1°C to 28.3°C. The post-processing used all these data with in-house programs to calculate η. The identical experimental system has accomplished massive projects, including [9, 44, 45], to list a few.

As two unknowns are in Eq. (4.1), two sets of data are needed to solve it. However, a practical experiment has more or less deviations from the assumptions of the semi-infinite conduction model, for example, the step temperature change, and leads to the conceptual uncertainties. Therefore, the multi-sample tests were performed to decrease the uncertainty [56]. In a single test, 300 TLC images, from which T_w is converted, were recorded, and other temperatures were recorded at higher frequency (500Hz). These data were processed with least squares regression method to calculate η. In addition, the tests of each case were repeated to ensure the repeatability.

Table 4.1 Test matrix

Case No.	Geometry	Method	MCSA	DR	BR
1					0.5
2	Cylinder, D = 5mm	Measurement	0.67	1	0.75
3					1
4	Cylinder, D = 12.7mm	Simulation	0.67	2	1
5					0.5
6	Slot, D = 5mm	Measurement	0	1	1
7					1.5
8	Slot, D = 12.7mm	Simulation	0	2	0.5
9					0.25
10	Comb, D = 5mm, $H = D$, t_s= 0.1D, $P_s = 2t_s$	Measurement	0.38	1	0.5
11					1
12					1.5
13	Comb, D = 12.7mm, $H = D$, t_s= 0.1D, $P_s = 2t_s$	Simulation	0.38	2	0.5
14[a]					1
15	Comb, D = 5mm, $H = D$, t_s = 0.1D, $P_s = 3t_s$	Measurement	0.5	1	1
16	Comb, D = 12.7mm, $H = D$, t_s = 0.1D, $P_s = 3t_s$	Simulation	0.5	2	1
17	Comb, D = 12.7mm, $H = D$, t_s = 0.15D, $P_s = 2t_s$	Simulation	0.38	2	1
18	Comb, D = 12.7mm, $H = D$, t_s = 0.15D, $P_s = 3t_s$	Simulation	0.5	2	1
19	Comb, D = 12.7mm, $H = D$, t_s = 0.2D, $P_s = 2t_s$	Simulation	0.38	2	1
20	Comb, D = 12.7mm, H = 0.5D, t_s = 0.1D, $P_s = 2t_s$	Simulation	0.44	2	1
21	Comb, D = 12.7mm, H = 0.5D, t_s = 0.1D, $P_s = 3t_s$	Simulation	0.58	2	1
22	Comb, D = 12.7mm, H = 0.5D, t_s = 0.15D, $P_s = 2t_s$	Simulation	0.44	2	1
23	Comb, D = 12.7mm, H = 0.5D, t_s = 0.15D, $P_s = 3t_s$	Simulation	0.58	2	1
24	Comb, D = 12.7mm, H = 0.5D, t_s = 0.2D, $P_s = 3t_s$	Simulation	0.58	2	1
25	Comb, D = 12.7mm, H = 0.2D, t_s = 0.1D, $P_s = 2t_s$	Simulation	0.48	2	1
26[b]	Comb, D = 12.7mm, H = 0.2D, t_s = 0.1D, $P_s = 3t_s$	Simulation	0.63	2	1

[a] Also named Case A, as a selected case with typical high performance.
[b] Also named Case B, as a selected case with typical low performance.

Due to the complexity on getting the partial derivatives of Eq. (4.1) on T_i, T_j, T_m and T_w, a direct uncertainty analysis on η is unpractical, and the computerized uncertainty analysis was used [56]. Perturbing values of temperature uncertainties were input in an in-house program, their contributions to η were accumulated. With 95% confidence, the averaged uncertainty in η is approximately ±8% near the exit, however, the uncertainty increases with decreasing η. It is approximately ±16% in the further downstream place.

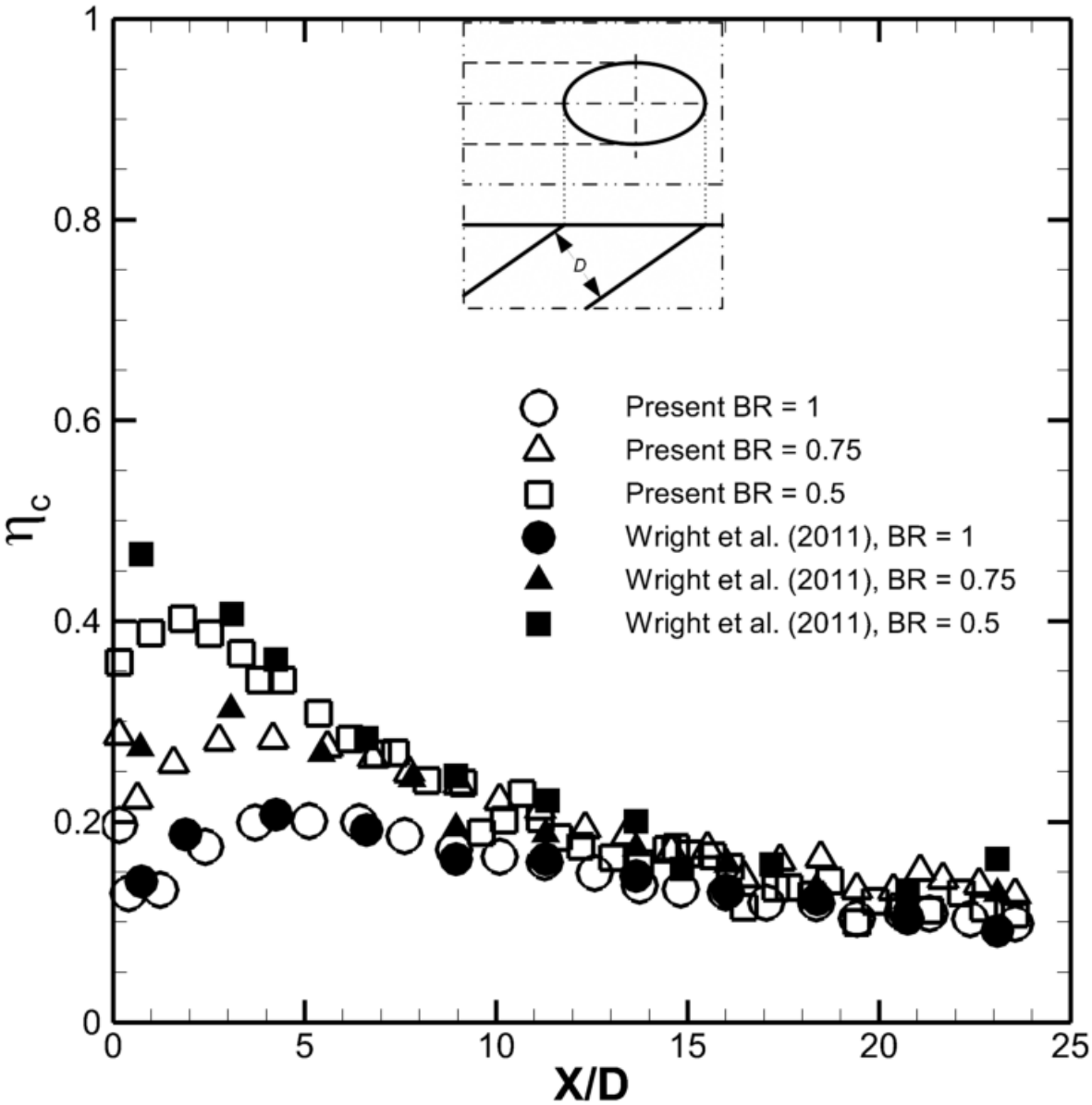

Figure 4.7 Comparisons of measurements for a cylindrical hole (Cases 1-3 of Table 4.1 with [48])

4.2.4 Computational Setup

The computational domain, shown in Figure 4.5, is composed of the wind tunnel and the plenum. The wind tunnel's bottom surface falls on the x-z plane where the test plate is located. The wind tunnel connects the plenum through the film-cooling geometry, which is inclined at 35° to the flow direction x. The geometry axial length is 7*D*. For all simulated geometries, *D* is 12.7 mm. A half-domain is used for the steady flow simulation, so its span-wise width is 0.5*P*. The two lateral domain end planes, the center-plane of the comb slit, and the mid-plane of the comb tooth, were set as symmetry planes. The inlet velocity was set at 20 m/s at the wind tunnel inlet, along with an inlet temperature of 300 K. A velocity inlet at the plenum inlet along with a temperature of 150 K was specified. The DR value is 2 for all simulations. A pressure outlet with a zero gage pressure was applied at the wind tunnel exit. The remaining walls were defined as adiabatic walls with no slip boundary condition, except the wind tunnel top wall that was set as a slip wall. The definition of the Cartesian coordinates is also shown in the figure. The origin is located on the symmetry plane at the exit trailing edge. The x-, y- and z-axes are aligned with the mainstream, the vertical, and the span-wise directions, respectively.

ANSYS-ICEM-CFD was used to generate the mesh. To test grid independence, five grids were generated for the simulation of a comb scheme configuration, in which $H = D$, $t_s = 0.1D$ and $P = 2t_s$. Their sizes ranged from approximately 0.70 to 1.48 million cells. The results of the film-cooling centerline effectiveness (η_c) shown in Figure 4.6(a), indicates slight changes for grid sizes larger than 0.81 million cells. A grid containing 1.27M cells was considered adequate. The identical criterion was adopted in the mesh generation of the new scheme geometries. Figure 4.6(b) shows a close look of the near field mesh.

Zhang and Hassan [10] performed a detailed simulation of the film cooling flow using ANSYS-FLUENT, a steady RANS CFD solver included in the ANSYS package, coupled with a RKE turbulence model. The Enhanced Wall Treatment was selected. In the region near the exit, y+ has been checked to be less than 1. With the ANSYS-CFD computational model constructed as such, reliable results were obtained, such as Figure 4.6(a).

According to [10], ANSYS-FLUENT has been used, and the second order upwind was selected in spatial discretizations. A conservative convergent criterion has been used in calculations, in which the residuals of the mass and the energy have to level off. A typical case took approximately 2×10^5 iterations to reach convergence, the residuals of the mass and the energy were 1×10^{-8} and 1×10^{-10}, respectively.

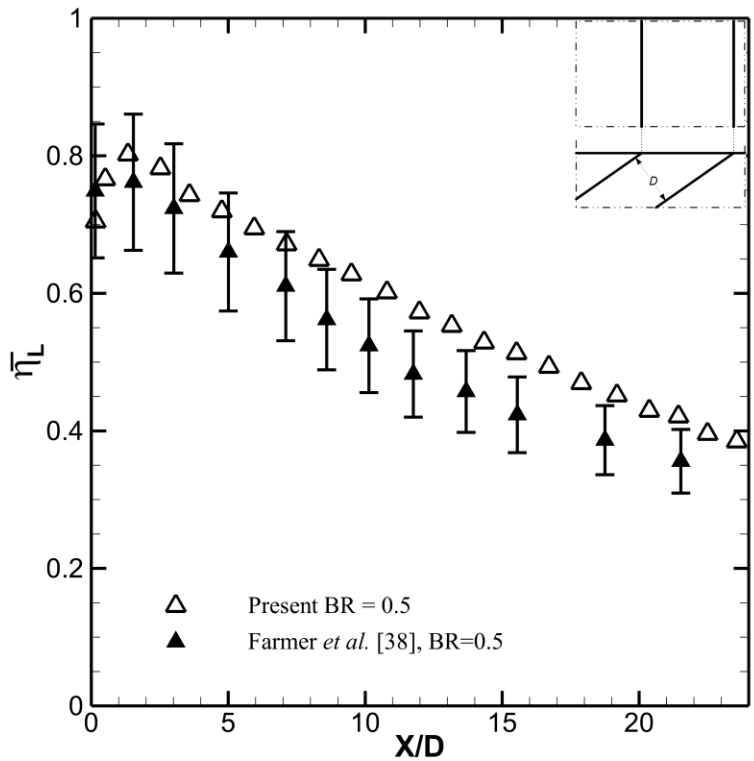

(c) BR = 0.5

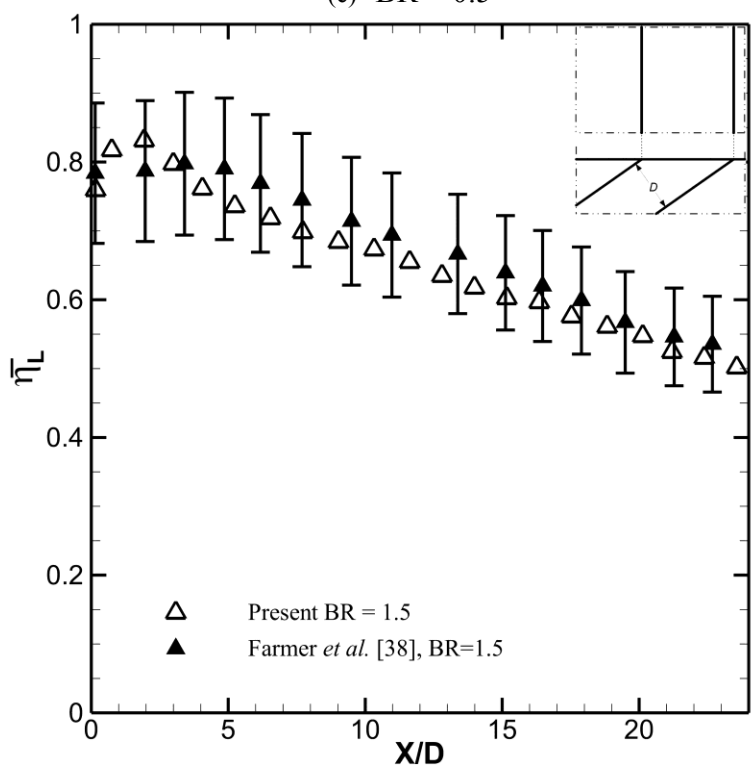

b) BR = 1.5

Figure 4.8 Comparisons of measurements for a simple slot (Cases 5 and 7 of Table 4.1 with [49])

4.2.5 Test Matrix and Parameters Normalization

The investigated cases are summarized in Table 4.1. Three kinds of geometries were included: the cylindrical hole at $P = 3D$, the simple slot and the comb scheme. They were investigated experimentally and numerically, including two comb configurations were measured and twelve comb configurations were simulated. The roles of the cylindrical hole and the slot were comparisons and validations. The experimental results of the comb scheme were also used to validate the simulations. For the experiments, $D = 5$ mm and DR = 1. For the simulations, $D = 12.7$ mm and DR = 2. D was characteristic length in our parameter normalization. Results were presented in a dimensionless format like X/D. Cases 9-12 were measurements of a comb scheme configuration of $H = D$, $t_s = 0.1D$, $P_s = 2t_s$ at BR range of 0.25-1.5. The current paper defined BR at the exit, so the mass flow rate of comb scheme is identical to simple slot at the same BR value, but is 3.8 times of the cylindrical hole. The mass flow rates of Cases 9-12 are equal to cylindrical hole at BR = 0.9-5.7. The current paper was aimed to demonstrate the realization of so-called 'ideal' performance and the approach. Other factors, such as BR effect and geometric optimization, are interesting future topics, but were not studied in the current paper. Therefore, the BR effect of only one configuration is presented as Cases 9-12. For other configurations, only their BR = 1 results are presented as their representative performance. The case numbers in this table will be used when presenting the results. Cases 14 and 26, also named Cases A and B, were selected as typical high or low performance case in the further analysis.

In the present investigations, the temperature is normalized into θ. It is similar to η, however, rather than η being only valid at the test plate, θ is defined and is valid over the whole domain

$$\theta = \frac{T - T_m}{T_j - T_m} \tag{4.2}$$

where T_m and T_j are the mainstream and the coolant temperatures, respectively.

The x-component of the CRVP strength, ω_x, is the main component of the CRVP intensity [33]. It was normalized with the mainstream velocity $U = 20$m/s and $D = 12.7$mm, as this parameter was only used in the numerical results:

$$\omega_x = \frac{\omega_x^*}{U_m / D} \tag{4.3}$$

The definition of $\overline{\eta_L}$ in the experimental results was:

$$\overline{\eta_L} = \frac{1}{3D} \int_0^{3D} \eta \, dz \tag{4.4}$$

In the numerical results, the definition of $\overline{\eta_L}$ was:

$$\overline{\eta_L} = \frac{1}{0.5P_s} \int_0^{0.5P_s} \eta \, dz \tag{4.4b}$$

The present investigations used the parameter of MCSA to quantify the structural integrity, which is important for the practical application of a film cooling scheme. The following equation calculated the MCSA of the new scheme with the geometrical parameters of L, H, t_s, and P_s.

$$MCSA = \left(1 - \frac{t_s}{P_s}\right) * \left(1 - \frac{H}{L * \sin 35°}\right) \tag{4.5}$$

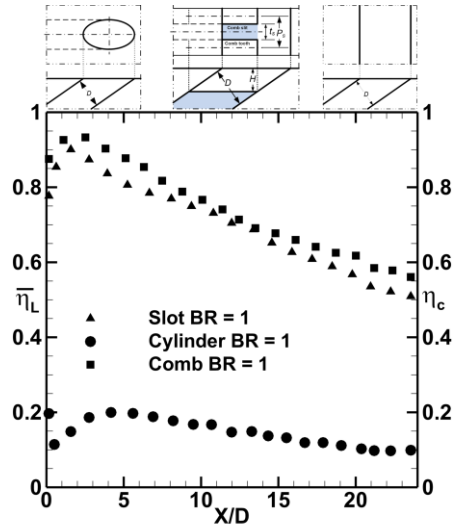

a) $H = D$, $t_s = 0.1D$ and $P = 2t_s$ at BR = 1 (Cases 3, 6 and 11 of Table 4.1)

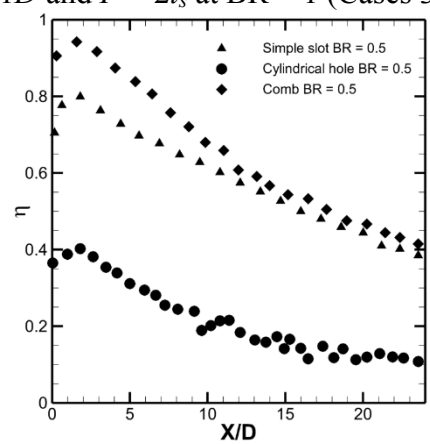

b) $H = D$, $t_s = 0.1D$ and $P = 2t_s$ at BR = 0.5 (Cases 1, 5 and 10 of Table 4.1)

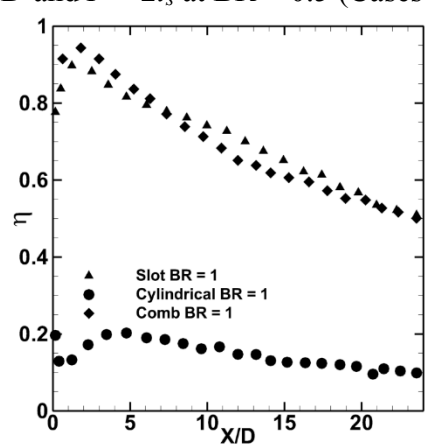

c) $H = D$, $t_s = 0.1D$ and $P = 3t_s$ at BR = 1 (Cases 3, 6 and 15 of Table 4.1)

Figure 4.9 The Comb Scheme performance (Cases 10, 11 and 15 of Table 4.1)

4.3 Results and Discussion

Experimental and numerical investigations have been performed. The experimental results are presented first, in the first three subsections, showing the validations, the performance of two tested comb scheme geometries and the BR effects. Then the numerical results are presented in the rest of subsections. The validated results demonstrate the high performance of the comb scheme. Based on the numerical results, the effect of the geometrical parameters on $\overline{\eta_L}$ and the ω_x on mainstream-coolant interface are analyzed. Finally, further analysis is performed on two selected typical cases.

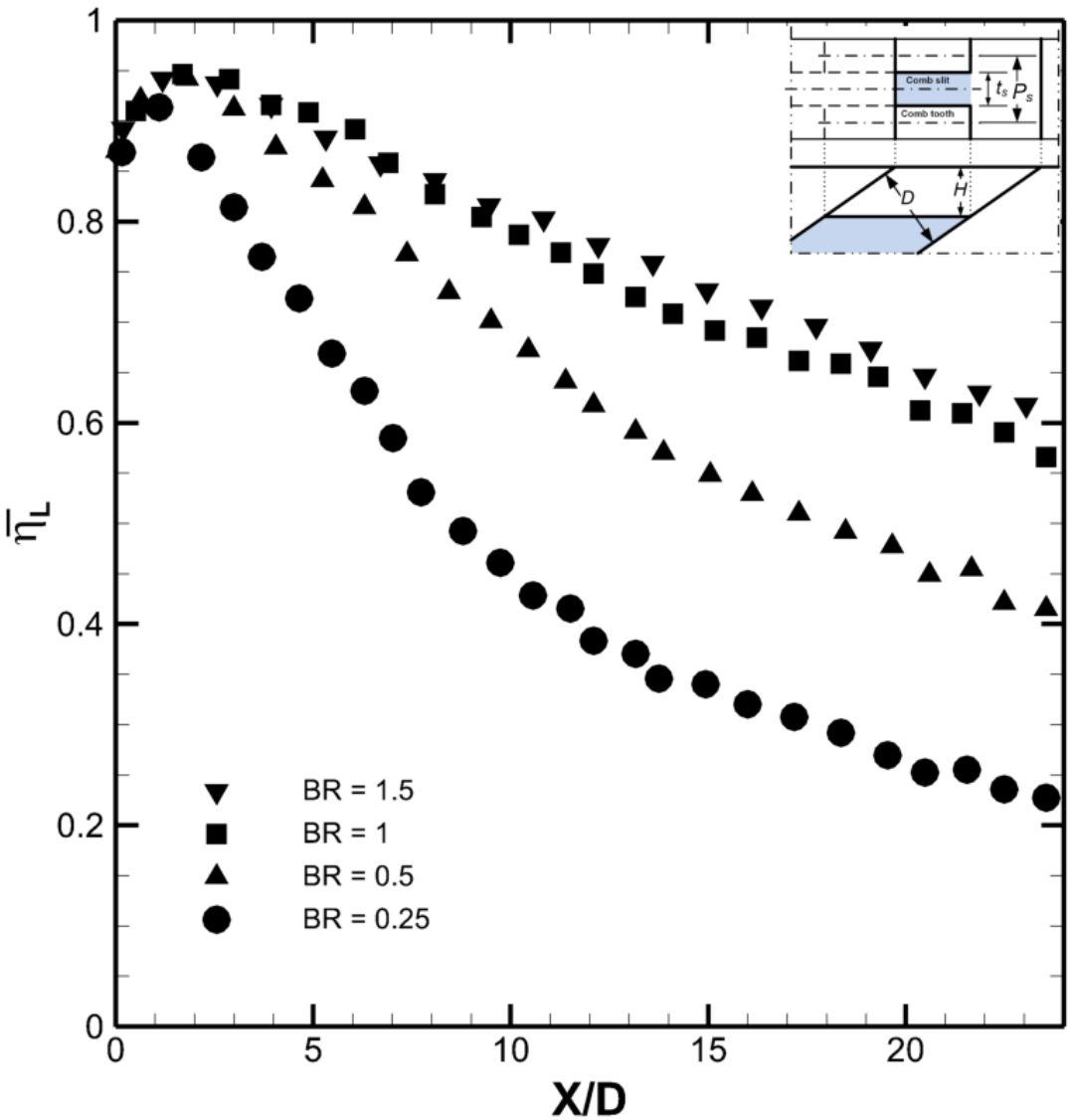

Figure 4.10 BR effect while $H = D$, $t_s = 0.1D$ and $P_s = 2t_s$ (Cases 9-12 of Table 4.1)

4.3.1 Validation of the Experimental Facility

Two traditional geometries, the cylindrical and the slot holes, were tested in the present facility. The results were compared with published open data. Wright *et al.* [48] presented high-resolution η results with the pressure-sensitive painting technique, where its uncertainty was approximately ±4%. It had similar cylindrical hole and its DR was unity. Figure 4.7 shows the comparisons of its data with Cases 1-3 in Table 4.1 for η_c at BR 0.5, 0.75 and 1. For the cases of BR = 0.5, the present results show a small liftoff-reattachment, but the counterpart does not. Apart from that, the discrepancies are less than 0.03, good agreement is shown.

Farmer *et al.* [49] experimentally investigated the simple slot in η uncertainty of ±13%. Its data are compared with the present experiments of Cases 5 and 7 in Figure 4.8, which compares $\overline{\eta_L}$ at two BR values. Figure 4.8a gives $\overline{\eta_L}$ at BR = 0.5 (Case 5), both have liftoff-reattachment and identical tendency. The present measurements are slightly higher in less than 0.1. Figure 4.8b, comparing $\overline{\eta_L}$ at BR = 1.5 (Case 7), shows very similar distribution, and the discrepancy is in the range of the uncertainty. The agreement demonstrated in Figure 4.7 and Figure 4.8 confirms that the present experiment is trustworthy.

4.3.2 Experimental Performance of the Comb Scheme

Two comb scheme configurations were measured and the results are shown in Figure 4.9 and Figure 4.10. Figure 4.9 compares the performance of the comb scheme, Cases 10, 11 and 15, with the slot and the cylindrical hole. The cylindrical hole performance is the validated η_c, while the slot hole is the validated $\overline{\eta_L}$. Figure 4.9a shows $\overline{\eta_L}$ distribution of a comb scheme configuration at BR = 1 (Case 11), in which $H = D$, $t_s = 0.1D$ and $P_s = 2t_s$. Data of three geometries at this value of BR, Cases 3, 6 and 11, show liftoff-reattachment. The comb scheme performance shows to be very similar and slightly superior to the slot at 0.05, and it is several times higher than the cylindrical hole. Figure 4.9(b) shows the comparison at BR = 0.5 for this comb scheme configuration (Case 10). Three geometries, Cases 3, 6 and 11, show liftoff-reattachment. The comb scheme performance is much higher than the cylindrical hole, and higher than the slot at approximately 0.1 the place immediately downstream of the exit. The superiority decreases as moving downstream. It is negligible after X/D = 12. Figure 4.9(c) shows the $\overline{\eta_L}$ of the 2nd tested comb scheme configuration at BR = 1, of which $H = D$, $t_s = 0.1D$ and $P_s = 3t_s$ (Case 15). Data of three geometries, Cases 3, 6 and 15, show liftoff-reattachment. The comb scheme performance is very similar and slightly superior to the slot at less than 0.05, and it is several times higher than the cylindrical hole.

Some more cases of the comb scheme are not shown, as they are similar. The comparisons in Figure 4.9 demonstrated the high performance of the comb scheme. It is several times higher than the cylindrical hole and similar to the slot, . It is widely accepted that the slot has the highest thermal performance in all existing geometries, and the slot is deemed to have ideal performance. One of the objectives in film cooling geometry research is to obtain this so-called ideal performance [2, 3, 37]. This performance is demonstrated to be successfully obtained by the comb scheme, which has practical structural integrity. Furthermore, the $\overline{\eta_L}$ distributions are similar in Figure 4.9(a) and (c), indicated P_s/t_s = 2 or 3has negligible effect at these H and t_s values.

Figure 4.10 shows BR effect at BR = 0.25, 0.5, 1 and 1.5 for the comb geometry of $H = D$, $t_s = 0.1D$ and $P_s = 2t_s$. They are Cases 9-12 in Table 4.1, which shows a performance even better than a simple slot. The $\overline{\eta_L}$ distributions of all cases have a liftoff-reattachment at approximate $\overline{\eta_L}$ = 0.95. It also demonstrates that the BR shows no significant effect immediately downstream of the exit trailing edge, except for a slightly lower reattachment value for the low BR case at BR = 0.25. However, the BR shows a different $\overline{\eta_L}$ decline rate further downstream. A similar BR effect is observed for the 2nd tested comb scheme configuration, the identical configuration to Case 15, in the BR range from 0.35 to 1. But this figure was not repeatedly presented here because of the similar scenario to Figure 4.10. Generally, the BR factor has a negligible effect on the performance immediately downstream of the exit but has a distinct effect on the decrease rate of $\overline{\eta_L}$ further downstream. This effect is notable at low BR values, while it is reduced with increasing BR and is negligible at high BR values (BR = 1.5).

4.3.3 Experimental η Profiles

A slot of infinite width in the z-direction will always have an ideal performance η = 1, however, it is structurally unfeasible. It will be shown that the proposed comb scheme can provide comparable thermal performance with structural stability. Figure 4.9 has shown that $\overline{\eta_L}$ of the two tested comb configurations is similar to the slot configuration. For further comparisons, maps of η for three cases, Cases 6, 11 and 15, are shown in Figure 4.11. In the present TLC testing, each test required processing 300 TLC images when recording accurately the color variation and the last image was shown above the η contour in Figure 4.11. In the TLC image, the blue color denotes high η, the green color denotes lower η, and the red color denotes the lowest. The lateral row length of the slot or the blind slot was 12.7*D*. The left side of the image is the exit trailing edge. Figure 4.11(a) shows the slot detailed η at BR = 1 (Case 6). In the image, the lateral span of the blue color narrows moving downstream (moving to the right), indicating a strong end effect which is common and appeared in previous opened publications. Bunker [37] showed a similar phenomenon in his figures. Hence, to eliminate the end effect in the present investigation, only the central 25% (3*D* width) have been post-processed. This region is framed with dashed lines. It is worth noting that the end effect has not been included in the present numerical simulations. The η contour chart shows high η values for the slot, starting at 0.8 and ending at 0.5. The local peak at approximately X/D = 2 denotes a liftoff-reattachment, the reattached value is 0.9.

Figure 4.11(b) is for the 1st tested comb configuration at BR = 1 (Case 11). In addition to showing the narrowing blue area like the last figure, an interesting phenomenon is more distinct. The central part usually has the highest η values, but the images demonstrate that the shape of the local η distributions has two branches. The central part shows slightly lower η than its two sides. This phenomenon is clearer in the Case 15 η distribution shown in Figure 4.11(c), but less distinct for the slot case shown in Figure 4.11(a). Saumweber and Schulz [50] discussed this phenomenon in their investigations on a fan-shaped hole. They thought of it as the result of an in-tube separation leading to a U-shape jet velocity profile. However, our investigations indicate that it is caused by the end effect because a strong CRVP is produced at the two ends. A similar phenomenon was mentioned in [33]. It is an interesting topic for future research.

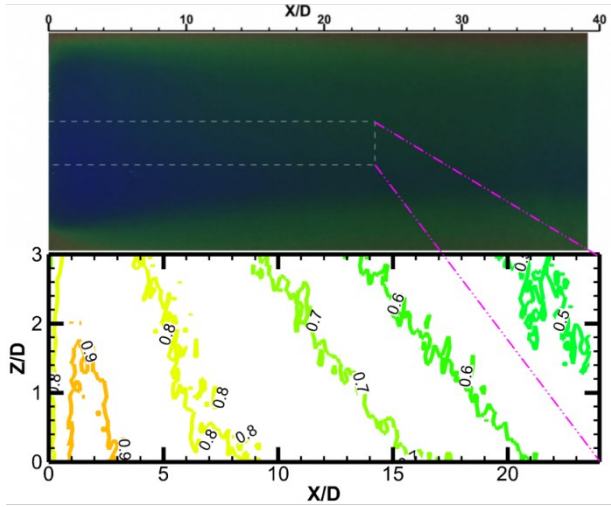

a) Slot (case 6 of Table 4.1)

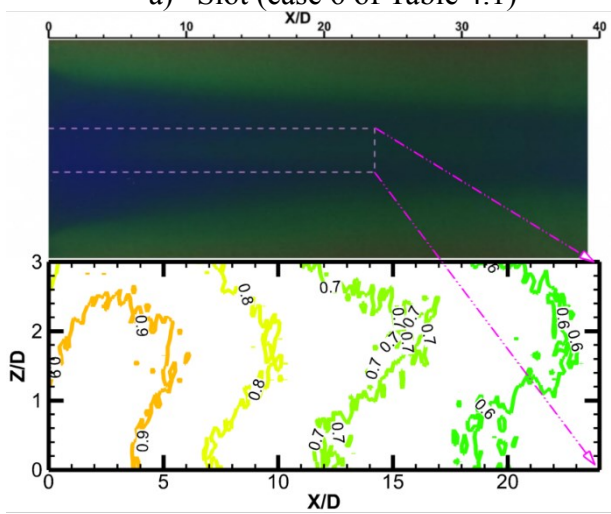

b) Comb configuration $H = D$, $t_s = 0.1D$ and $P = 2t_s$ (case 11 of Table 4.1)

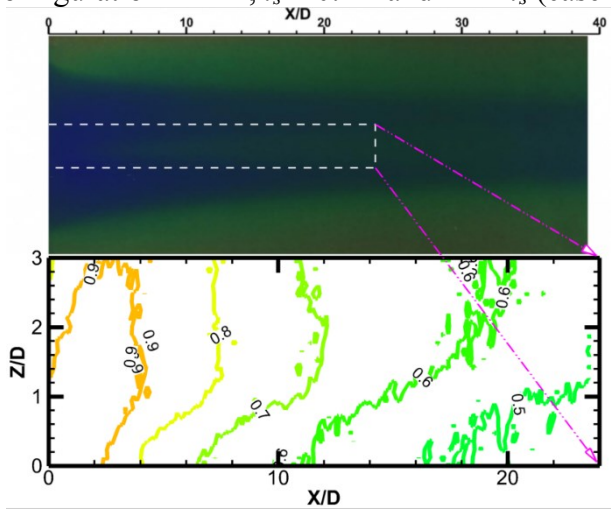

c) Comb configuration $H = D$, $t_s = 0.1D$ and $P = 3t_s$ (case 15 of Table 4.1)

Figure 4.11 The η distribution at BR = 1 (Case 6, 11 and 15 of Table 4.1)

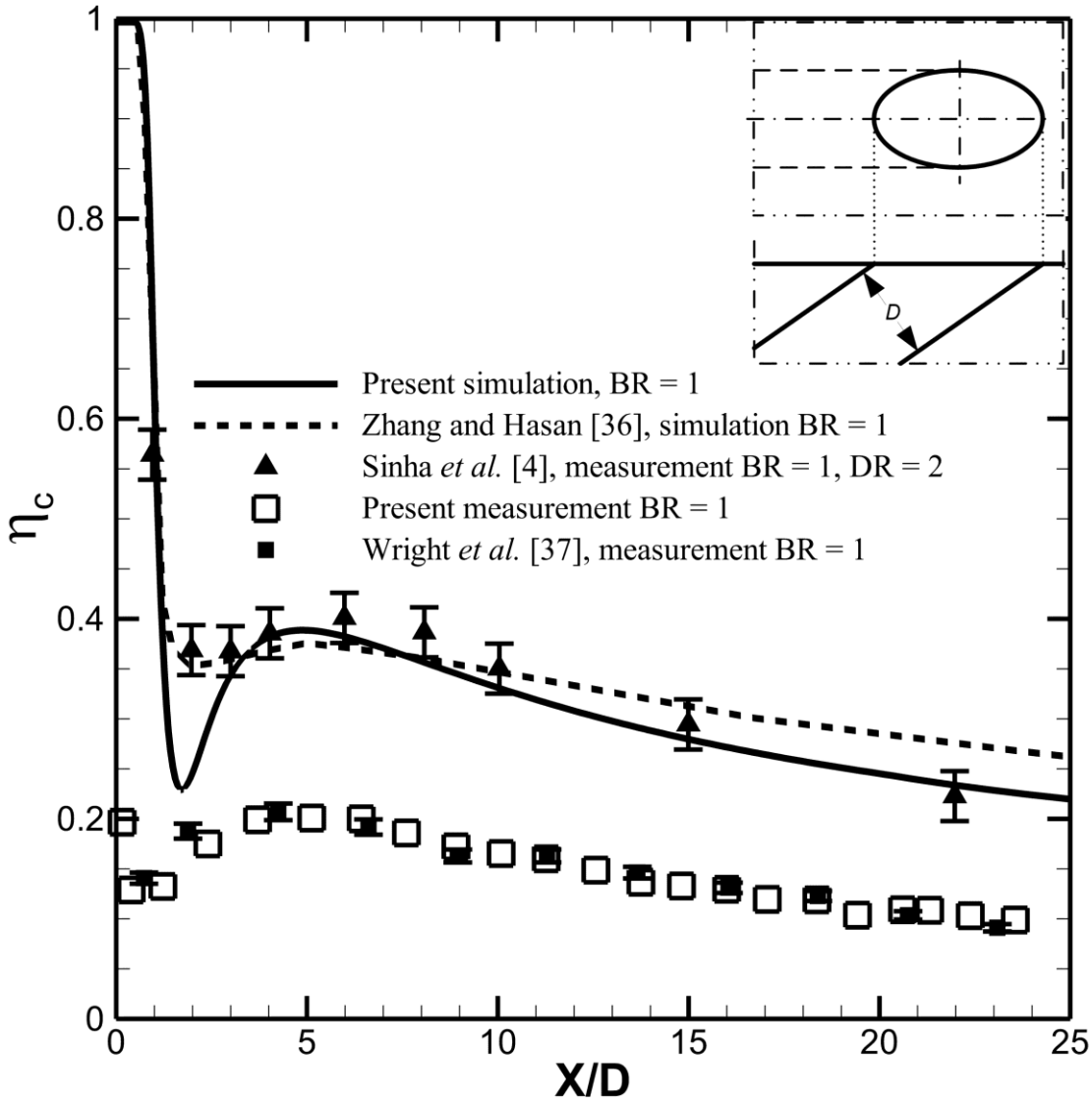

Figure 4.12 Comparison of cylindrical hole at BR = 1 (cases 3 and 4 of Table 4.1 with [5, 10, 48])

In Figure 4.11(b), the contour chart shows η profiles similar to those given in Figure 4.11(a): It starts at a value between 0.8 and 0.9, ends at a value between 0.5 and 0.6; There is a liftoff-reattachment immediately downstream of the exit, where, the reattached value is approximately 0.9.

Figure 4.11(c) is for the second tested comb configuration at BR = 1, (Case 15). Its TLC image shows the most distinct 2-branch η distribution among these three figures. The contour chart shows η contributions similar to the last two figures: It starts at a value between 0.8 and 0.9, ends at a value between 0.5 and 0.6; there is a liftoff-reattachment immediately downstream of the exit, the reattached value is approximately 0.9.

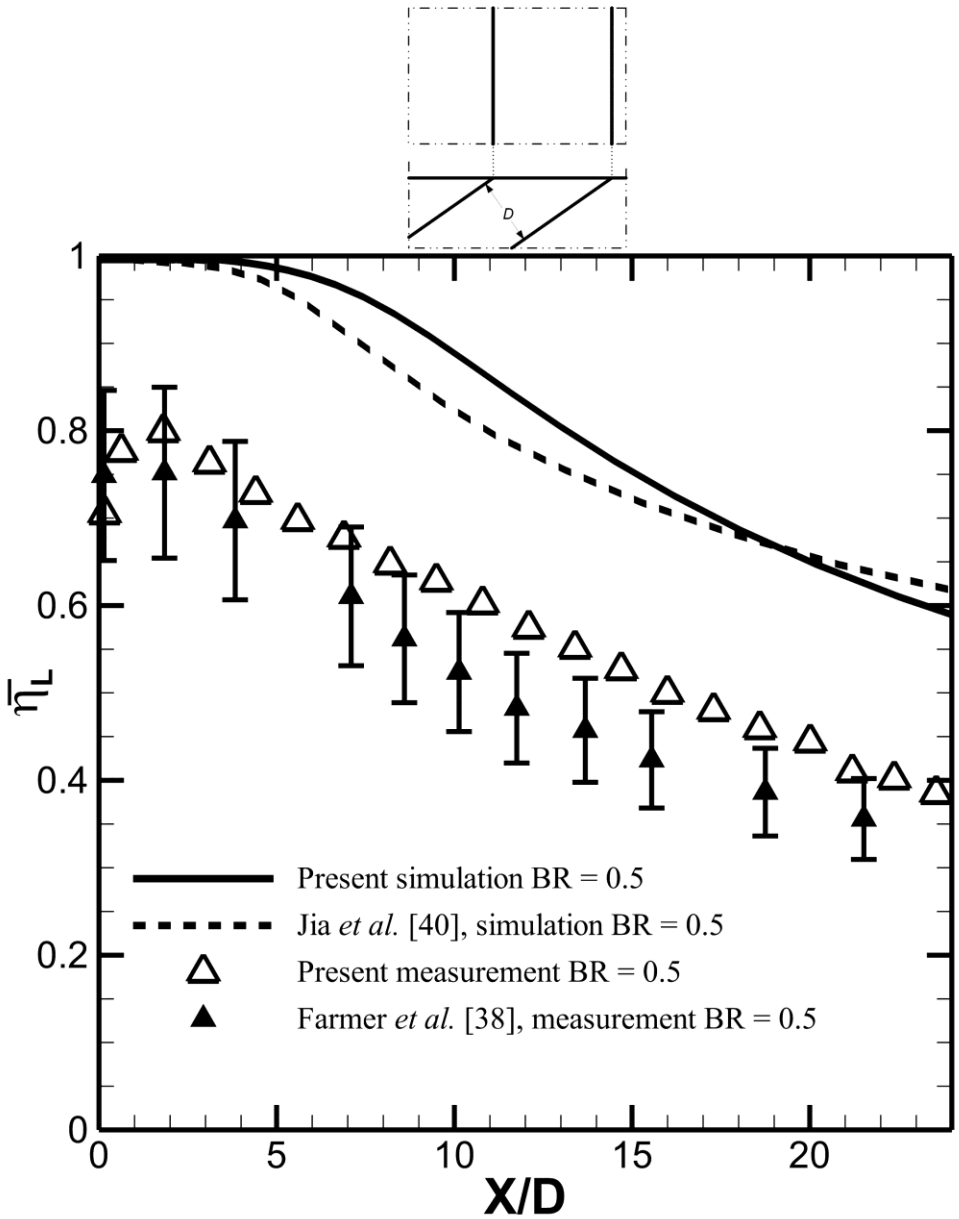

Figure 4.13 Comparison of slot at BR = 0.5 (Cases 5 and 8 of Table 4.1 with [49, 56])

Figure 4.9 and Figure 4.11 have demonstrated that these two comb configurations have η performance similar to the slot that possesses the so called ideal performance. The comparison of these two comb configurations shows P_s varying from 2 t_s to 3 t_s has a marginal effect on the η performance at $H = 1D$ and $t_s = 0.1D$.

4.3.4 Validation of the Numerical Simulation

The present simulations were validated with the results published for traditional geometries namely, the cylindrical hole and the slot. Figure 4.12 compares the cylindrical hole results, in which Cases 3 and 4 are compared with results in [10, 48][1]. Both the measurement and the

[1] Reference numbers are different in the manuscript and the current thesis.

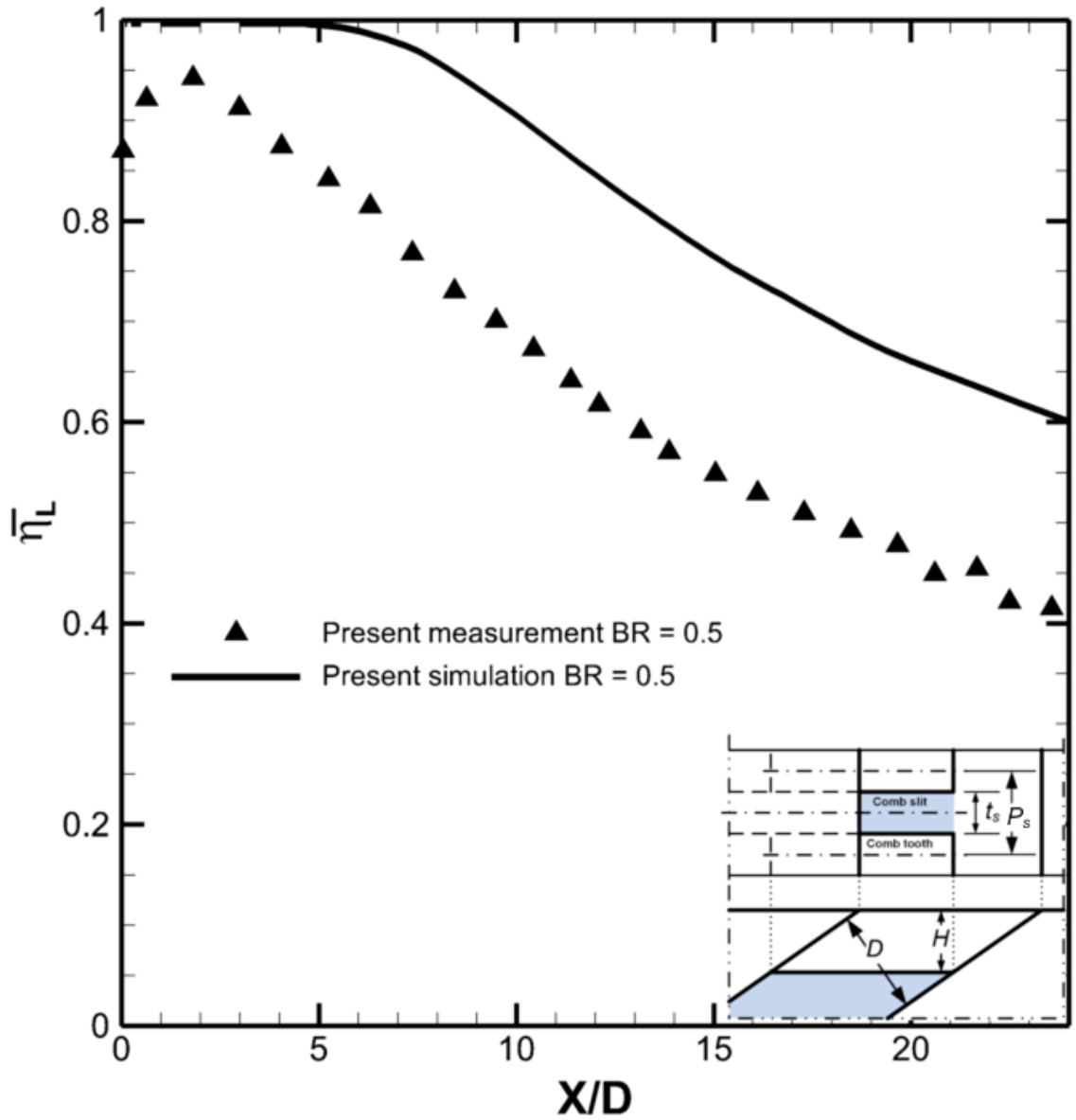

Figure 4.14 Comparison for the case $H = D$, $t_s = 0.1D$ and $P_s = 2t_s$ (Cases 10 and 13 of Table 4.1)

simulation show high agreement with the published results. However, there is a discrepancy between the simulations and the measurements. It is mainly because of the DR difference. DR is 1 in the experiments, while it is 2 in the simulations. This geometry has been known to be sensitive to DR values. Generally, the simulations are deemed to qualitatively agree with the measurements. By contrast, the experimental results of Sinha *et al.* [5] are also presented in this figure, in which DR is 2 and the η uncertainty is approximately ±0.025. In this DR value, the simulation under predicts the liftoff, other than that, the difference is in the range of the accuracy. It indicts that the aforementioned discrepancy between Cases 3 and 4 is due to the DR difference.

The current new scheme is aimed to obtain the so called ideal η performance like the slot. The experimental results have demonstrated a comparable performance with the slot. Its flow

was reckoned similar to the slot. The prediction on the slot is significant for the new scheme predictions. Jia *et al* [57], presented a slot simulation at an inclined angle of 30°, smaller than the present 35°. Figure 4.13 compares Cases 5 and 8 and results in [49, 57][1] at BR = 0.5. Both measurement and simulation show high agreement with their published results. However, there is a discrepancy between the simulations and the measurements, and the simulations do not capture the reattachment observed in the measurements. Similar to this relative low BR case, comparisons at higher BR values showed identical situations: the measurement and simulation agree well with their published results, but the simulations do not capture the reattachment in the measurements, and discrepancies are shown between the simulations and the measurements. The main reason for these discrepancies is mostly due to the end effect: the simulations did not include the end effect, which was strong in the experiments. Theoretically, a uniform coolant film would form when it jets out from a laterally infinite slot, where lateral velocity w and velocity lateral gradients $\partial u/\partial z$, $\partial v/\partial z$ are deemed to be 0. Furthermore, its $\overline{\eta_L}$ has to be 1 immediately downstream of the exit. However, end effect occurs at the two ends of a real slot, where no constraint on the aforementioned w, $\partial u/\partial z$ and $\partial v/\partial z$. Three phenomena in Figure 4.11 were speculated to indicate the end effect:

1. The narrowing lateral span of the blue color indicates distinct lateral movements.
2. The two-branch η distribution indicates secondary flow due to strong velocity gradients. Identical phenomenon was discussed in [58], which was due to CRVP entrainment.
3. $\overline{\eta_L}$ less than 1 immediately downstream of the exit means mainstream penetrates the coolant film. It is most possibly due to the end effect.

End effect is a very interesting future topic. In general, these simulations are also deemed to qualitatively agree with the measurements.

The present measurements have been validated and proven reliable. The comb experimental results, shown in Figure 4.14, provide an acceptable validation of the numerical simulations. It is produced for the comb configuration of $H = D$, $t_s = 0.1D$ and $P_s = 2t_s$ at BR = 0.5 (Case 10 and 13). Like the comparison of the slot, the simulation misses the liftoff-reattachment, and over-predicts the measurements. However, it reflects the tendency, and the difference is constantly at approximately 0.2. The same scenario occurs in the comparisons of the higher BR values and the configuration of $H = D$, $t_s = 0.1D$ and $P_s = 3t_s$. Identical to the slot, the discrepancy is reckoned to be due to the end effect.

The simulation results of these two comb geometries were also compared for the BR effect. Identical to the experimental scenario, they showed a negligible effect on the region immediately downstream of the exit, but a distinct effect on the decrease rate of $\overline{\eta_L}$ further downstream. This effect is notable at low BR values. It is reduced with BR increasing, and is negligible at higher BR values. The present research objective focuses on the mechanism underlying high performance, and the BR = 1 case of each comb configuartion is deemed to have typical high performance. Generally, the numerical agreements on the geometries of the cylindrical hole, the slot, and the comb scheme have demonstrated the reliability of the numerical results. The following analysis is mostly based on the simulations at BR = 1, for all comb configurations.

[1] Reference numbers are different in the manuscript and the current thesis.

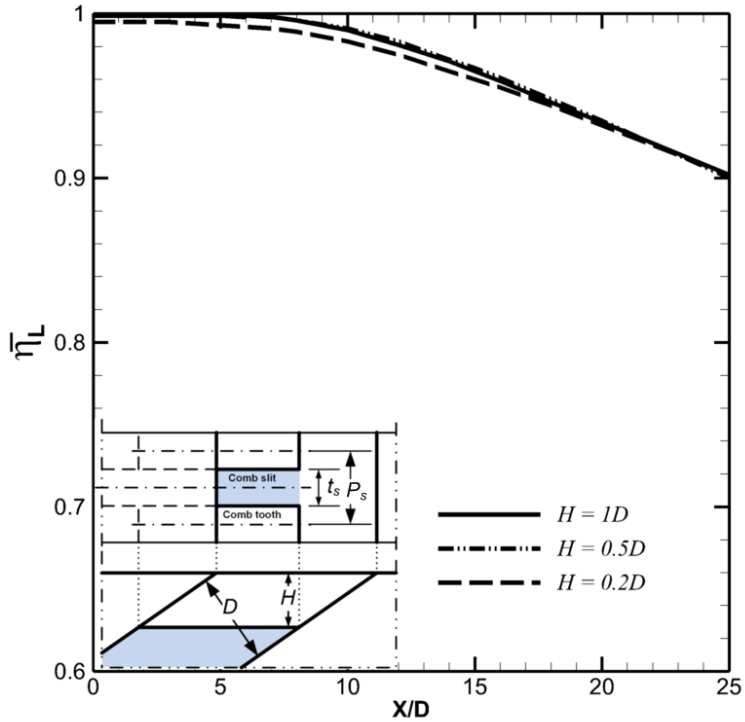

a) Configurations of H = 0.2-1D, t_s = 0.1D and P_s = 2t_s (Cases 14, 20 and 25 of Table 4.1)

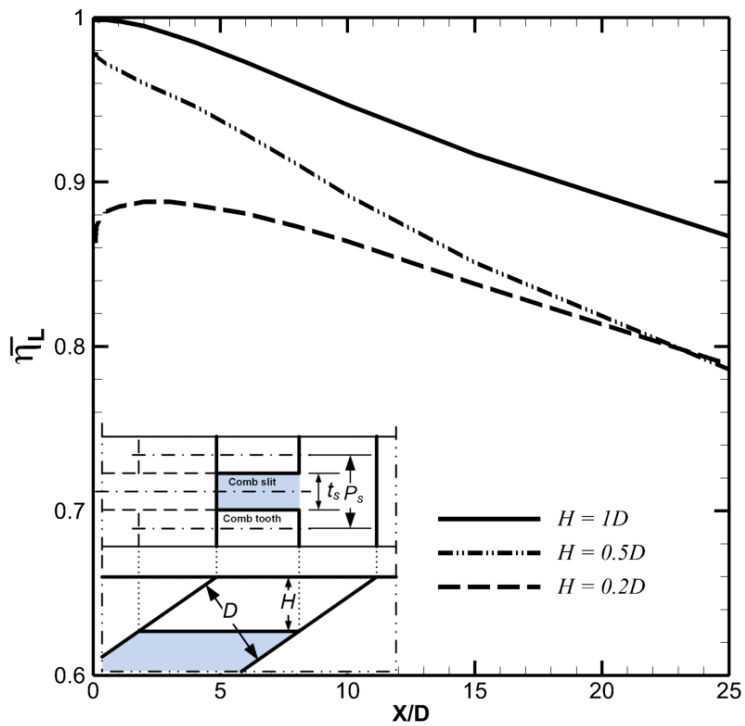

b) Configurations of H = 0.2D, 0.5D and D, t_s = 0.1D and P_s = 3t_s (Cases 16, 21 and 26 of Table 4.1)

Figure 4.15 Effect of *H* on $\overline{\eta_L}$

4.3.5 Geometric Effect of the Comb (New) Scheme

The experimental and computational results presented in the previous sections have demonstrated that the comb scheme performance is comparable with that of the slot, but with practical structural integrity. The comb scheme is characterized by three main geometric parameters: H, t_s and P_s. Their effects on $\overline{\eta_L}$ and the $\omega_x$on mainstream-coolant interface have been investigated.

Three values of H: 0.2D, 0.5D and D, are investigated and the results are shown in Figure 4.15 where Figure 4.15(a) is for Cases 14, 20 and 25, where H = 0.2D, 0.5D and D, t_s = 0.1D and P_s/t_s = 2. $\overline{\eta_L}$ distributions are very similar, except for H = 0.2D case where $\overline{\eta_L}$ starts at a value slightly less than 1, indicating inconspicuous mainstream penetration, demonstrating that the effect of H is negligible at t_s = 0.1D and P_s/t_s = 2.

By contrast, a stronger effect of H is shown at P_s/t_s = 3. Figure 4.15(b) shows Cases 16, 21 and 26, where H = 0.2D, 0.5D and D, t_s = 0.1D and P_s/t_s = 3. Case 16, where $H = D$ still has high performance. $\overline{\eta_L}$ starts at 1, while H = 0.2D case (Case 26) shows a large performance decay, and liftoff-reattachment. Case 21, the case of H = 0.5D shows intermediate results for $\overline{\eta_L}$ distributions. Generally, Figure 4.15 indicates a performance increase with an increase in H.

Three t_s values, 0.1D, 0.15D and 0.2D are investigated and their effect is given in Figure 4.16. Figure 4.16(a) is for Cases 14, 17 and 19, where $H = D$, t_s = 0.1D, 0.15D, 0.2D and P_s/t_s = 2. They all show high performance. At these H and P_s values, t_s demonstrates no effect immediately downstream of the exit trailing edge, where all $\overline{\eta_L}$ are 1. Nevertheless, it has a distinct effect further downstream: $\overline{\eta_L}$ declines faster as t_s increases.

At lower H and higher P_s values, t_s shows a stronger effect. Figure 4.16(b) is for Cases 21, 23 and 24, where H = 0.5D, t_s = 0.1D, 0.15D, 0.2D and P_s/t_s = 3. Case 21, in which t_s = 0.1D, has the best performance. It starts at 0.95, very close to 1. The others start at much lower values. It indicates that the mainstream has (more or less) penetrated the coolant film in these three cases. As the present research objective is focused on the so called ideal performance, they are deemed not so ideal. Generally, identical to Figure 4.16(a), the performance declines as t_s increases.

The parameter P_s was investigated in the form of P_s/t_s, for P_s/t_s = 2 and 3. The aforementioned results, Cases 14 and 16 in Figure 4.15, have revealed that P_s/t_s has a rather negligible effect on $\overline{\eta_L}$ at $H = D$ and t_s = 0.1D, however, it has a distinct effect when H decreases or t_s increases. In Figure 4.17(a), t_s of Cases 17 and 18 increases to 0.15D. Case 17, in which P_s/t_s = 2, has high performance, and its $\overline{\eta_L}$ starts at 1. While Case 18 (P_s/t_s = 3) has clearly lower performance, in which $\overline{\eta_L}$ starts at 0.98, dropping at a faster rate downstream, and lower than the P_s/t_s = 2 case at approximately 0.07. The H values of Cases 22 and 23 decrease to 0.5D in Figure 4.17(b). Also, Case 22, in which P_s/t_s = 2, has high performance, and its $\overline{\eta_L}$ starts at 1. While the performance of the P_s/t_s = 3 case (Case 23) is distinctly lower, in which $\overline{\eta_L}$ starts at 0.84, lower than the P_s/t_s = 2 case at approximately 0.15, demonstrating stronger P_s/t_s effect. In general, as P_s/t_s increases, the performance declines; this effect is reduced when H increases or t_s decreases.

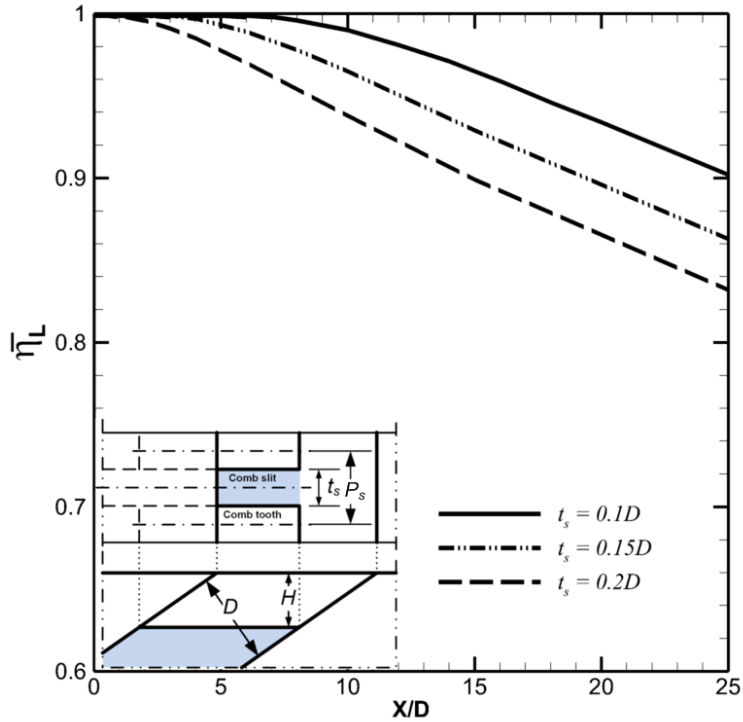

(a) Configurations of $H = D$, $t_s = 0.1D$, $0.15D$ and $0.2D$, and $P_s = 2t_s$ (Cases 14, 17 and 19 of Table 4.1)

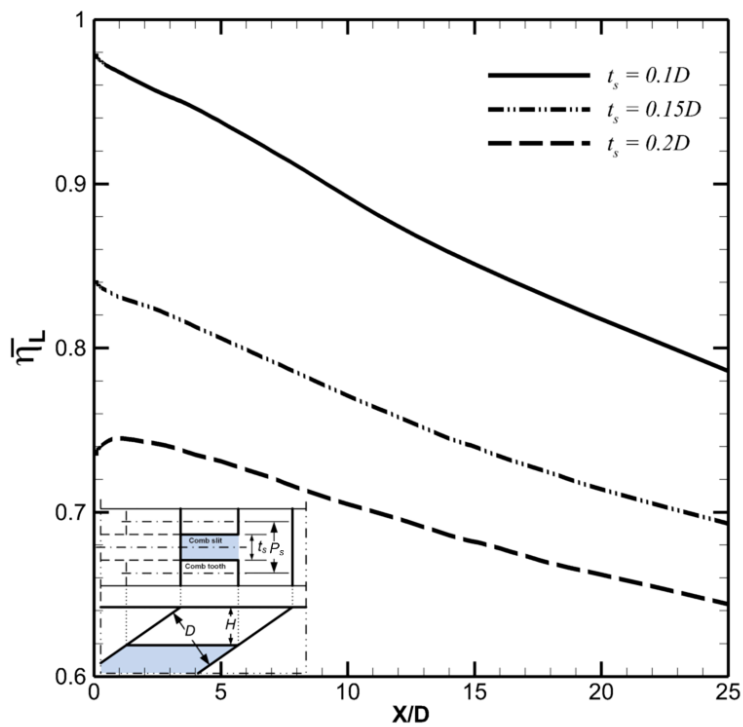

(b) Configurations of $H = 0.5D$, $t_s = 0.1D$, $0.15D$ and $0.2D$, and $P_s = 3t_s$ (Cases 21, 23 and 24 of Table 4.1)

Figure 4.16 Effect of t_s on $\overline{\eta_L}$

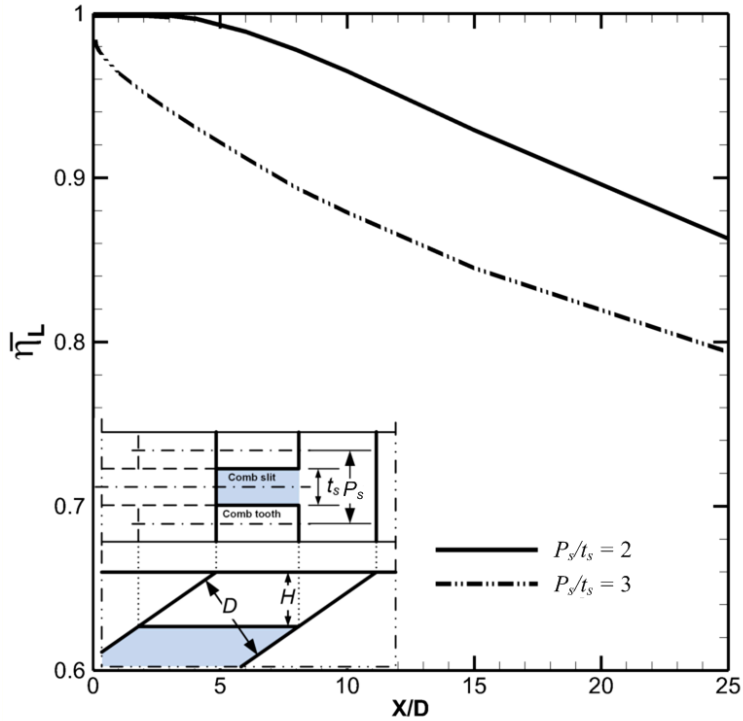

a) Configurations of $H = D$, $t_s = 0.15D$ and $P_s = 2t_s$ and $3t_s$ (Cases 17 and 18 of Table 4.1)

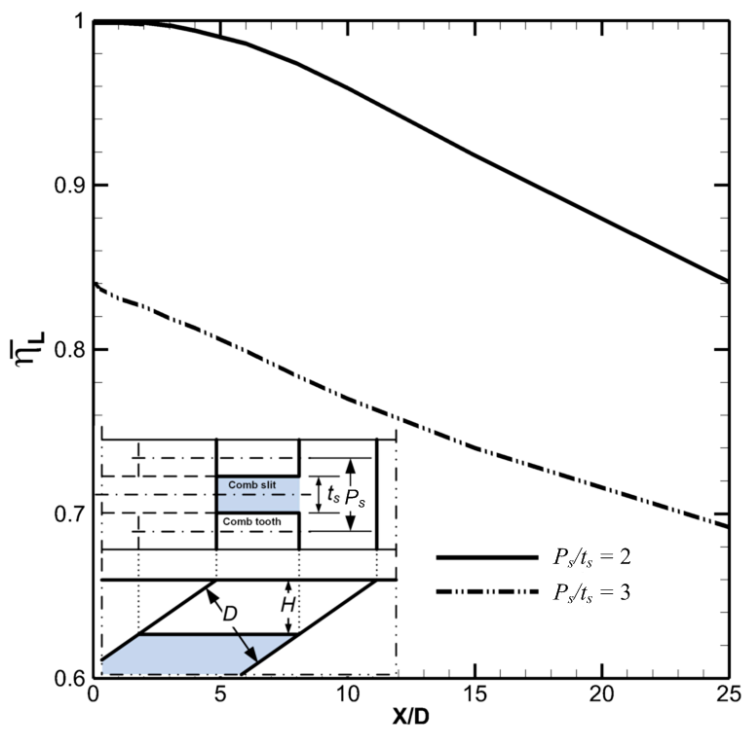

b) Configurations of $H = 0.5D$, $t_s = 0.15D$ and $P_s = 2t_s$ and $3t_s$ (Cases 22 and 23 of Table 4.1)

Figure 4.17 P_s /t_s effect on $\overline{\eta_L}$

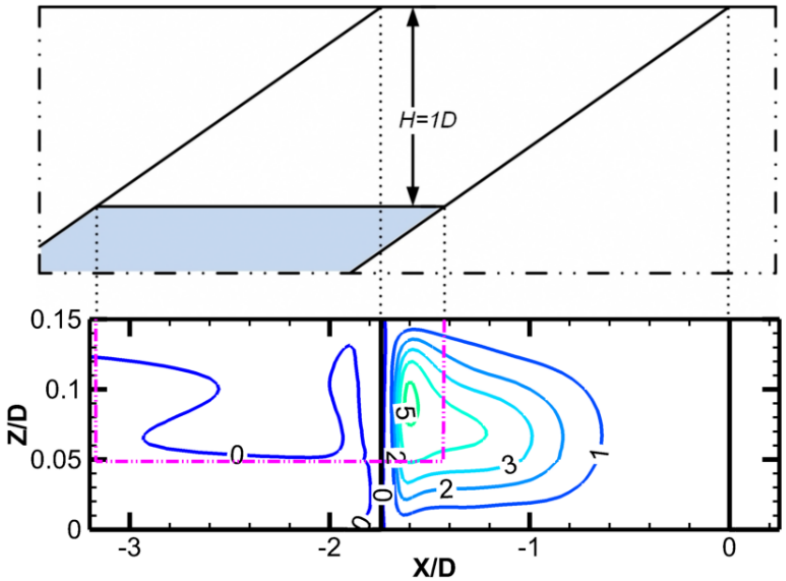

a) Configuration of $H = D$, $t_s = 0.1\ D$ and $P_s = 3t_s$ (Cases 16 of Table 4.1)

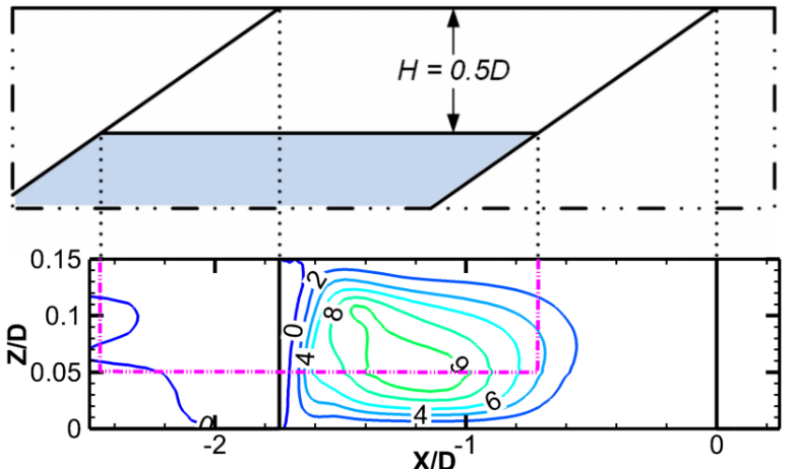

b) Configuration of $H = 0.5D$, $t_s = 0.1\ D$ and $P_s = 3t_s$ (Cases 21 of Table 4.1)

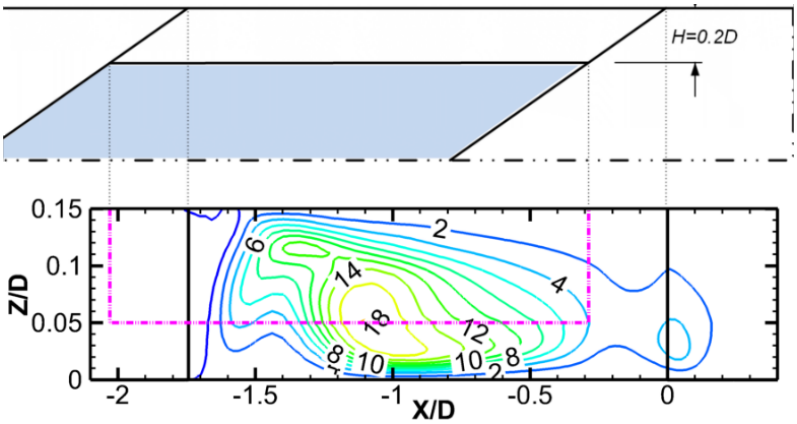

c) Configuration of $H = 0.2D$, $t_s = 0.1\ D$ and $P_s = 3t_s$ (Cases 26 of Table 4.1)

Figure 4.18 *H* effect on interface ω_x (Cases 16, 21 and 26 Table 4.1)

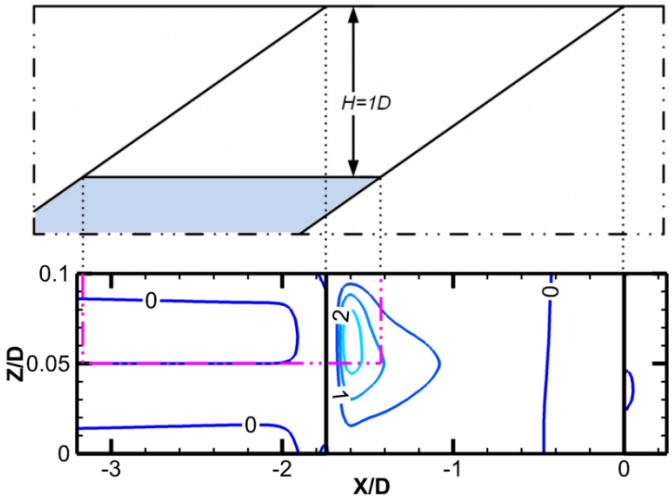

(d) Configuration of $t_s = 0.1D$ (maximum ω_x 3.81, Case 14 of Table 4.1)

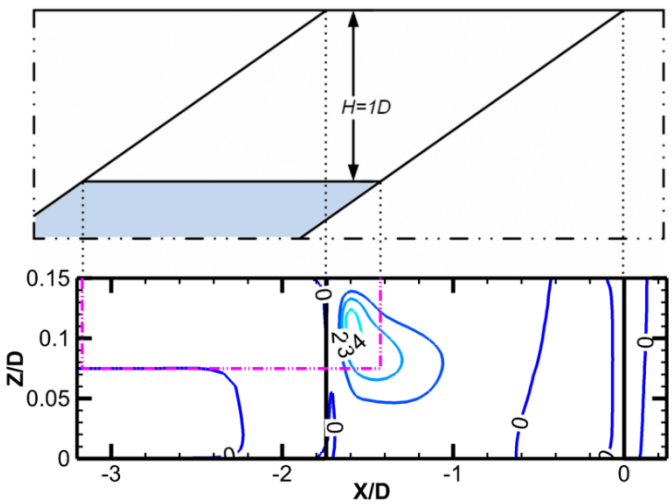

(e) Configuration of $t_s = 0.15D$ (maximum ω_x 4.43, Case 17 of Table 4.1)

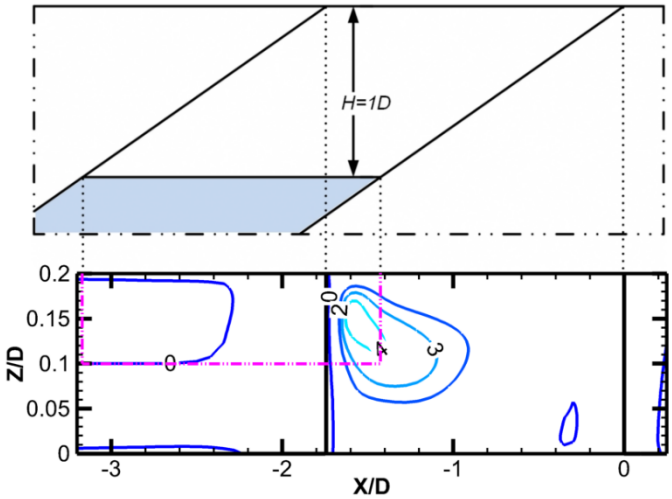

(f) Configuration of $t_s = 0.2D$ (maximum ω_x 4.62, Case 19 of Table 4.1)

Figure 4.19 t_s effect on interface ω_x while $H = D$, $P_s = 2t_s$ (cases 14, 17 and 19 of Table 4.1)

The design of the comb scheme was intended to obtain high performance by eliminating mainstream entrainment. The comb scheme is intended to achieve high performance which has been hereby demonstrated. And the effect of the geometric parameters has been presented in terms of $\overline{\eta_L}$. Moreover, the effects of identical geometric parameters were investigated in terms of ω_x on mainstream-coolant interface, to demonstrate the impact of the CRVP, and its link with $\overline{\eta_L}$, hence to show the approach of obtaining the high performance.

Cases 16, 21 and 26 in Figure 4.18 shows the effect of H on interface ω_x, where H varies from $0.2D$ to $0.5D$ to D, while $t_s = 0.1D$ and $P_s = 3t_s$. The corresponding $\overline{\eta_L}$ distributions were presented in Figure 4.15(b). ω_x is visualized with contour lines in the vicinity of the exit. The background shows the exit leading and trailing edges, and the comb-tooth edges on the blind slot bottom. Section 4.2.1 has indicated that the most important region is the mainstream-coolant interface. However, its location is not fixed. The present figures show a plane at $Y/D = 0.05$. It was deemed to be close to the interface. Case 16, in which $H = D$, is shown in Figure 4.18(a). The highest value of the contour line is 5. The local peak is located near the exit leading edge, but shifts away from the comb-slit edge. The shifting also indicates a slight impact of the CRVP, as the strong CRVP is right above the comb-slit edge. The slight CRVP impact corresponds to the high $\overline{\eta_L}$ distribution in Figure 4.15(b). Figure 4.18(b) shows Case 21, in which $H = 0.5D$. The highest contour line value is 9, and the local peak locates right above the comb-slit edge. It denotes a stronger CRVP impact. The $\overline{\eta_L}$ of Case 21 in Figure 4.15(b) shows that the performance decayed slightly. Case 26, in which $H = 0.2D$, has a strong CRVP impact is shown in Figure 4.18(c): The highest contour line value is 18; the local peak right above the comb-slit edge; and high ω_x covers most of the area above the exit, indicating the domination. It corresponds to the decayed performance of Case 26 in Figure 4.15(b).

Figure 4.18 demonstrates that ω_x on mainstream-coolant interface increases as H decreases. It matches the design of the comb scheme, which aimed to manipulate the distance between CRVP and the mainstream-coolant interface by increasing the H value, hence, decreasing the CRVP impact on the interface, and eliminating the mainstream entrainment. Figure 4.15(b) demonstrated the performance improvement associated with the interface ω_x decline. It ends up with a small ω_x on the interface in Figure 4.18(a), and its achievement of an ideal performance shown in Figure 4.15(b).

In contrast with the distinct geometric effects on the interface ω_x and $\overline{\eta_L}$ shown in Figure 4.18 and Figure 4.15(b), Cases 14, 17 and 19 in Figure 4.19 show the effect of t_s on interface ω_x, in which the results correspond to t_s/D= 0.1, 0.15 and 0.2, while $H = D$, and $P_s = 2t_s$. The corresponding $\overline{\eta_L}$ distributions were shown in Figure 4.16(a). All the local peaks in this figure shift away from the place right above the comb-slit edge. Their maxima are 3.81, 4.43 and 4.62 for $t_s/D = 0.1$, 0.15 and 0.2, respectively. It indicates the marginal CRVP impact on the interface. Figure 4.16(a) demonstrates their high performance. They match the design prospect.

Figure 4.20 shows the effect of P_s/t_s on interface ω_x with Cases 14 and 16, in which $H = D$ and $t_s = 0.1D$. Under these H and t_s values, the P_s/t_s effect is slight. Their ω_x maxima are 3.81 and 5.24, the local peaks shift away from the place right above the comb-slit edge. Comparatively,

Case 16 (P_s/t_s = 3) has stronger interface ω_x. Figure 4.15 showed their $\overline{\eta_L}$. They both had high performance, and the $\overline{\eta_L}$ of the P_s/t_s = 3 case declined faster.

Figure 4.15 to Figure 4.20 demonstrated the geometric effects on $\overline{\eta_L}$ and the ω_x on mainstream-coolant interface, respectively. In addition, they revealed the correspondence between them. This correspondence matches the design of the new scheme, confirming the proposed film cooling heat transfer mechanism.

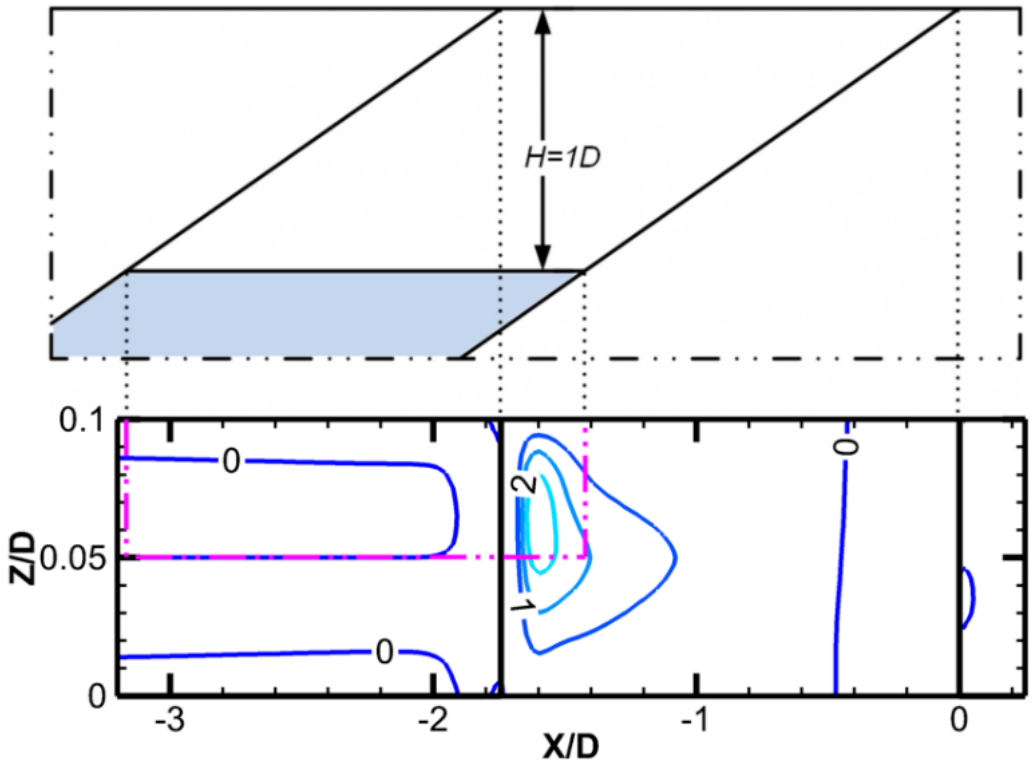

a) Case $H = D$, $t_s = 0.1D$ and $P_s = 2t_s$ (maximum ω_x 3.81, Case 14 of Table 4.1)

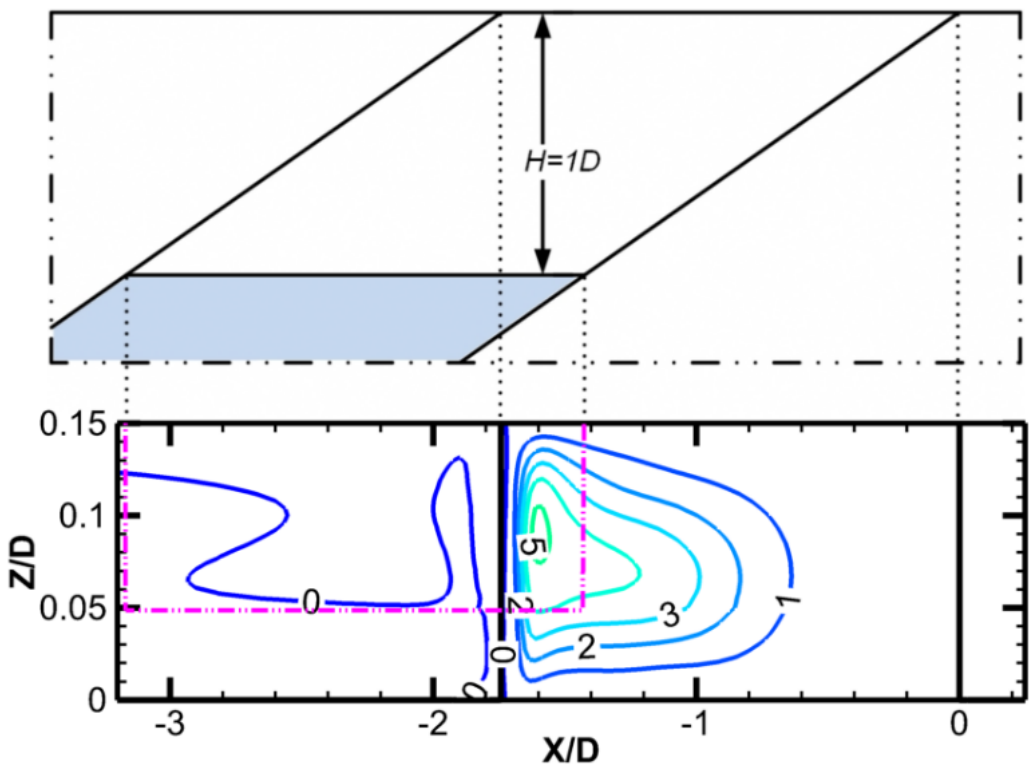

b) Case $H = D$, $t_s = 0.1D$ and $P_s = 3t_s$ (maximum ω_x 5.24, Case 16 of Table 4.1)

Figure 4.20 P_s/t_s effect on interface ω_x while $H = D$, $t_s = 0.1D$ (Cases 14 and 16 of Table 4.1)

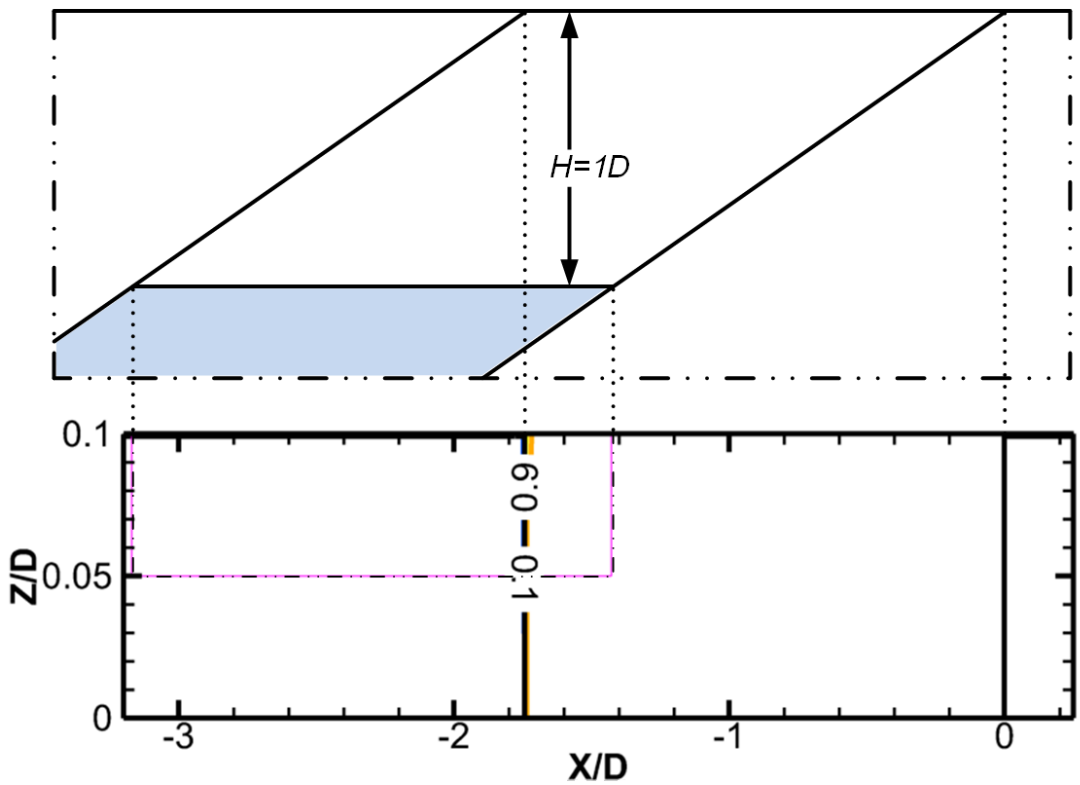

(a) Case A, high performance (Case 14 of Table 4.1)

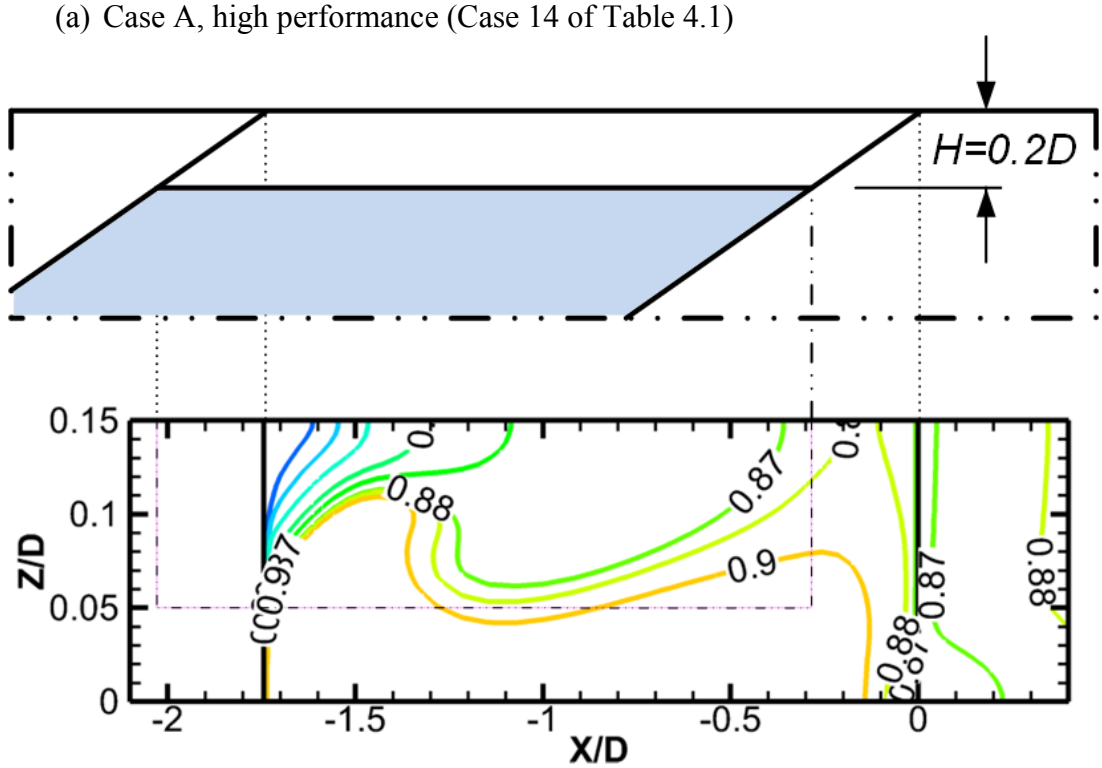

(b) Case B, low performance (Case 26 of Table 4.1)

Figure 4.21 θ contours for Cases A and B at Y=0 (Cases 14 and 26 of Table 4.1)

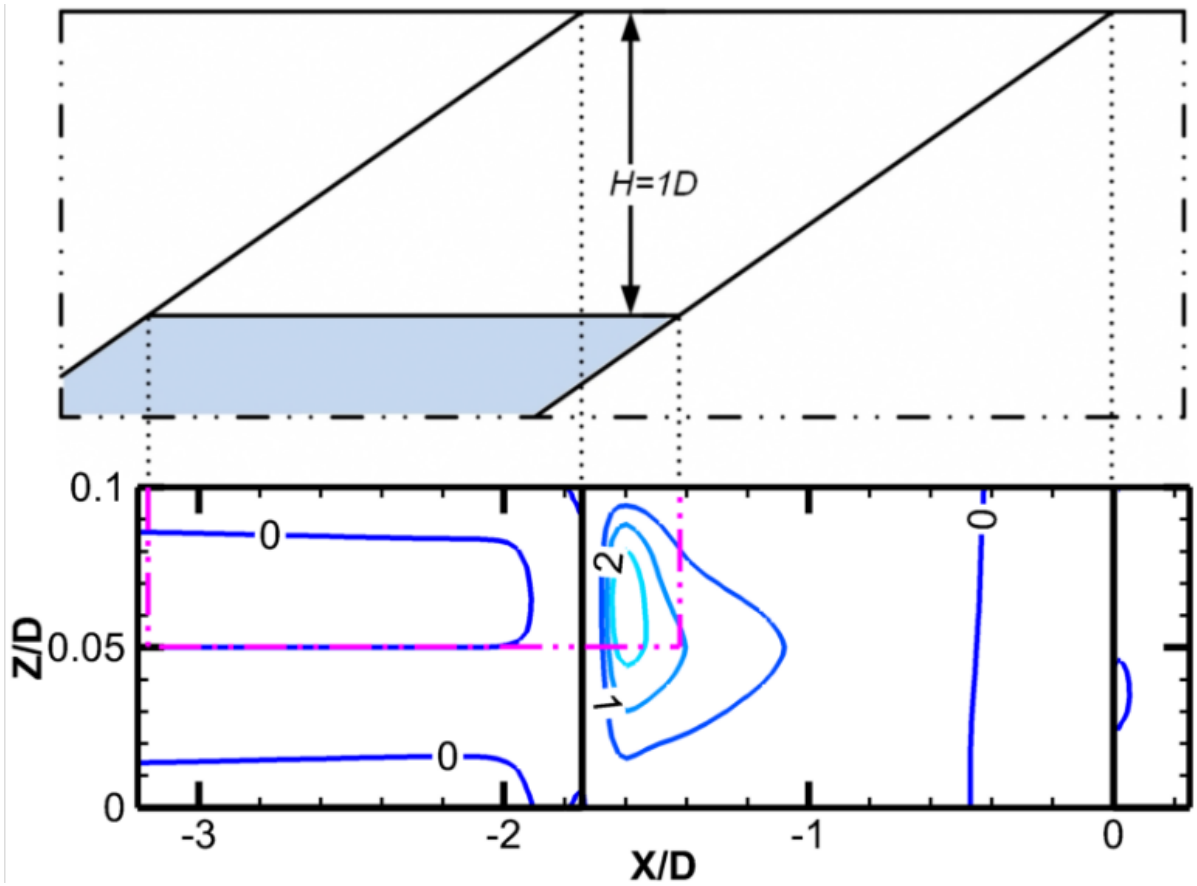

a) Case A, high performance (case 14 of Table 4.1)

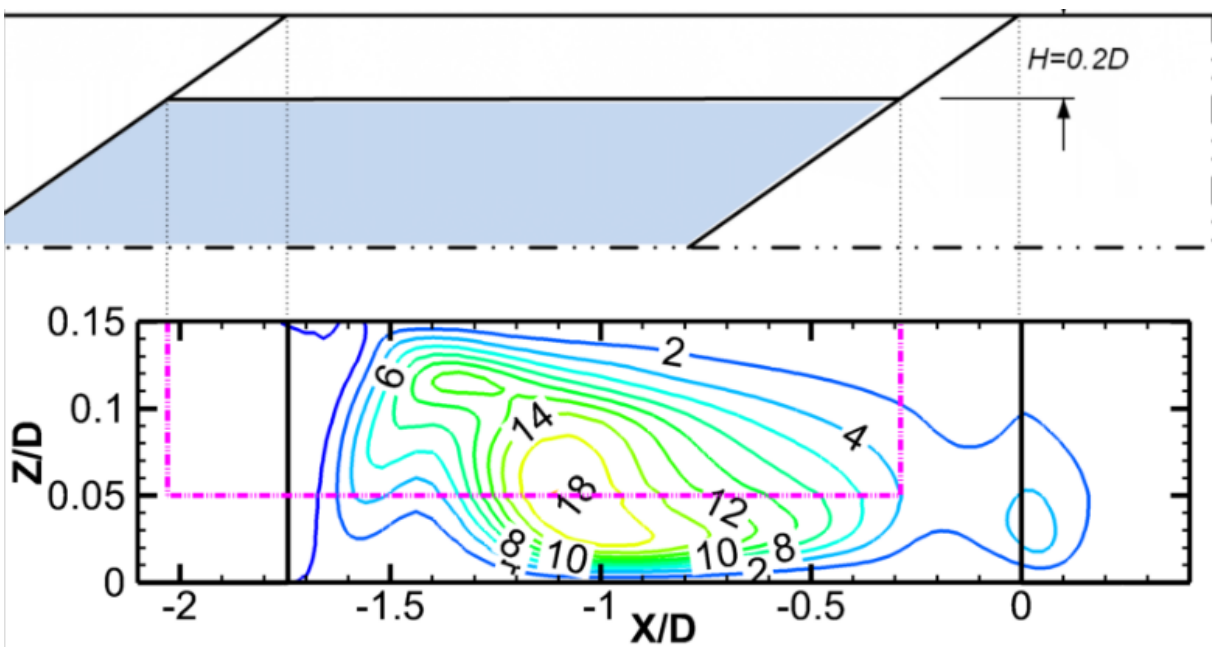

b) Case B, low performance (case 26 of Table 4.1)

Figure 4.22 Interface ω_x distributions for Cases A and B, at Y=0 (Cases 14 and 26 of Table 4.1)

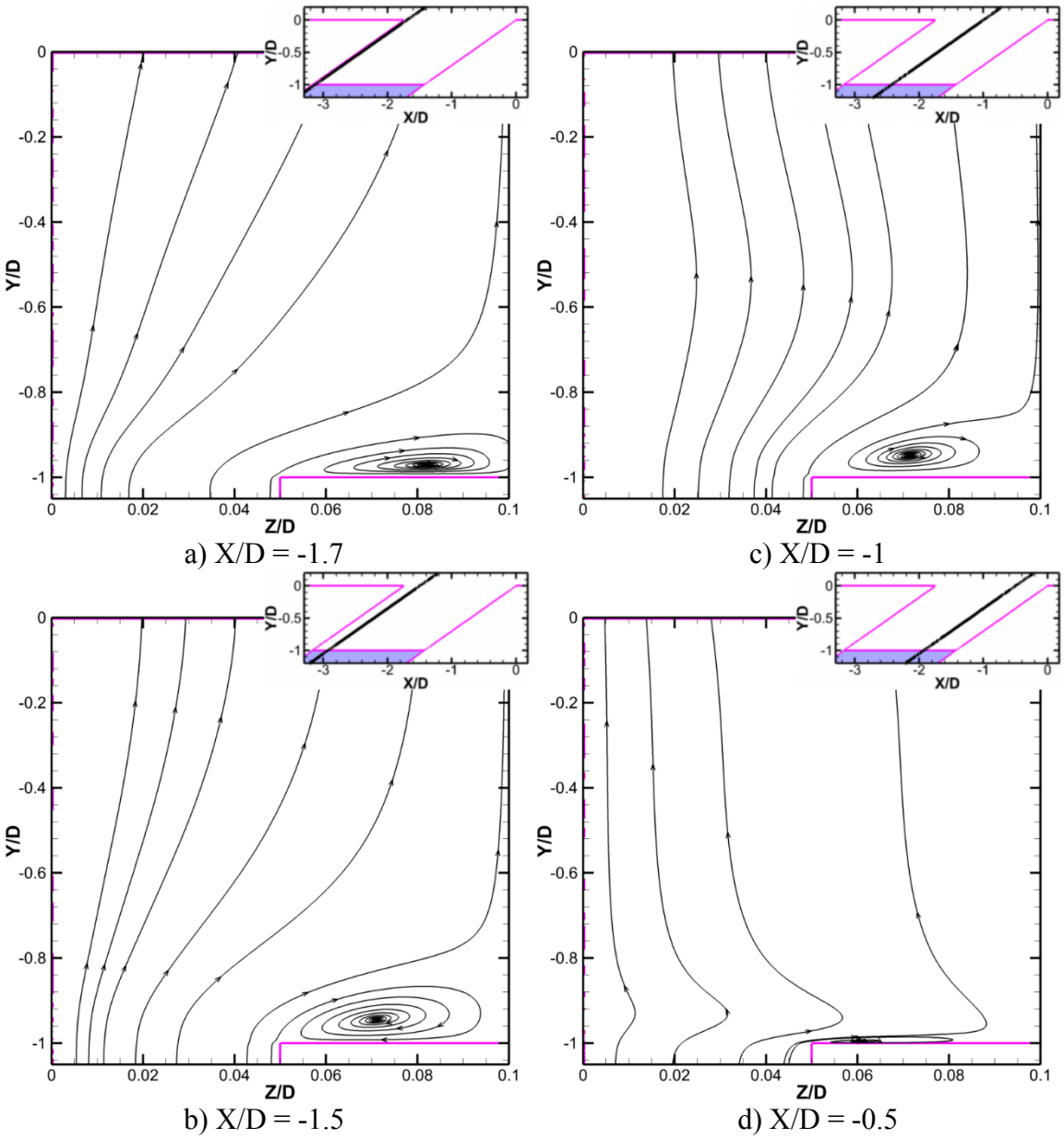

Figure 4.23 CRVP for Case A (Case 14 of Table 4.1)

4.3.6 Detailed η and CRVP Distributions

Cases 14 and 26, also named Cases A and B in Table 4.1 were further investigated due to their typical performance: Case A, where $H = D$, $t_s = 0.1D$ and $P_s = 2t_s$ at BR = 1, deemed to have typical high performance; and Case B: where $H = 0.2D$, $t_s = 0.1D$ and $P_s = 3t_s$ at BR = 1, deemed to have typical low performance. The detailed contours of η, ω_x on mainstream-coolant interface are demonstrated, and CRVP are visualized hereafter.

The θ contours on the exit plane, Y = 0, are given in Figure 4.21. Figure 4.21(a) shows the typical high performance Case A, where the θ-contour lines between 0.1 and 0.9 collapse on the slot leading edge, implying that the coolant covers the exit fully. In Figure 4.21(b), showing the

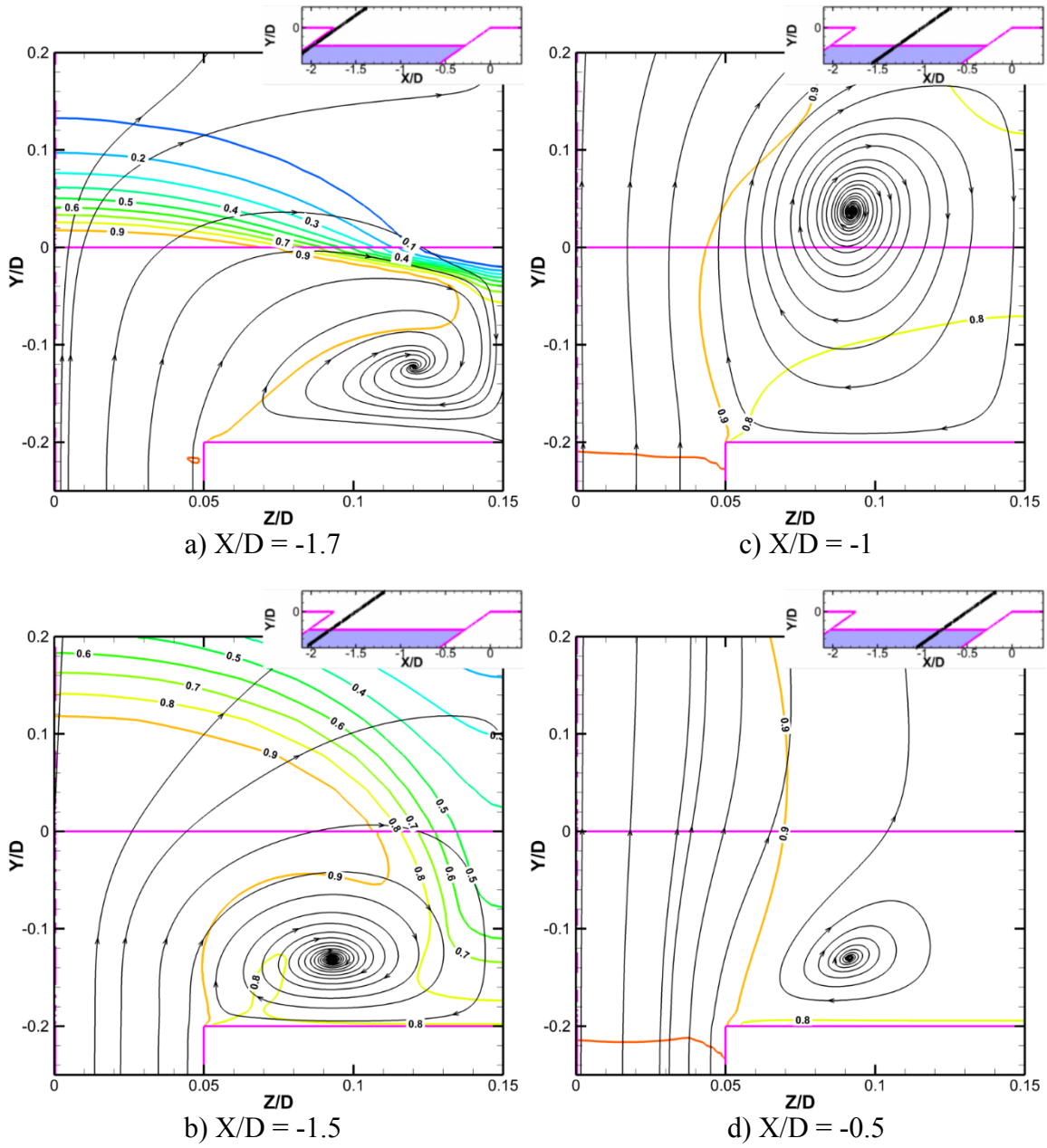

Figure 4.24 CRVP for Case B (Case 26 of Table 4.1)

typical low performance Case B, the θ contours at the exit plane show that the mainstream is mixed out with the coolant. The sequence of the contour lines and the slot trailing edge is 0.9, 0.88, 0.87, slot trailing edge line, 0.87 and 0.88, denotes a small liftoff-reattachment.

Figure 4.22 compares ω_x on mainstream-coolant interface of Cases A and B, plotted at the plane Y/D = 0.05. For Case A, Figure 4.22(a) shows a negligible CRVP impact, denotes a uniform flow and a thick smooth coolant film, it corresponds to the temperature distribution depicted in Figure 4.21(a). By contrast, strong CRVP impact is shown in Figure 4.22(b) for Case B. In this figure, the highest line value is 18 and the local peak is located exactly above the edge

of the comb-slit. Strong ω_x covers most of the exit which indicates a strong mainstream entrainment and leads to the decayed performance depicted in Figure 4.21(b).

To show the CRVP details for these two typical cases, their CRVPs have been visualized with streamlines on inclined cut planes, overlapping with the θ contours, which were intended to point out the mainstream-coolant interface. The inclined angle is 35°, parallel with the slot axial direction. The nominal position of the plane is their X value at Y = 0. For example, the cut plane of the nominal X/D = -0.5 is the plane in which X = -0.5D when Y = 0. Figure 4.23 shows the CRVP of Case A on the cut planes of X/D= -1.7, -1.5, -1 and -0.5. On the top right of the figure, a sketch indicates the cut plane position. On the bottom right of the figure, the edges of the comb-tooth are shown in the background. Figure 4.23(a) is the cut plane X/D= -1.7, and the X/D of the exit leading edge is -1.74, so this plane is very close to the leading edge. The CRVP core locates at (0.08, -0.97), where ω_x is 10. The impact of the CRVP seems lower than Y/D = -0.8. No θ contour line appears in this figure because the mainstream-coolant interface is higher than the figure range. In fact, the θ contour line value is 0.9 and is located at around Y/D = 0.02. The CRVP is far from the interface, no hot gas is entrained into the coolant by this vortical structure.

The remaining cut planes are similar. At the plane X/D = -1.5, Figure 4.23(b), the CRVP core is located at (0.07, -0.95), where ω_x is 23. The θ contour line value is 0.9 and is located at around Y/D = 0.2, higher than the figure range. The CRVP impact is lower than that for Y/D = -0.8, far from the interface. At the plane of X/D = -1, Figure 4.23(c), the CRVP core is located at (0.07, -0.95), where ω_x value is 13. The CRVP impact is far from the interface. The last cut plane, the plane X/D = -0.5, shown in Figure 4.23(d). ω_x is 4 at the CRVP core which is fading away.

This case has already demonstrated high performance, and Figure 4.23 has shown that its CRVP intensity is not small, but in the slot. For example, on the plane of X/D = -1.5, the ω_x of the CRVP core is 23. The reason for the high performance under strong CRVP is the long distance between CRVP and the mainstream-coolant interface. It leads to the negligible CRVP effect on the mainstream-coolant interface inFigure 4.22(a), showing no mainstream entrainment.

Another characteristic of the new scheme is worth noting. Rather than the velocity gradients of the mainstream-coolant shear layer in the film cooling flow of the cylindrical hole, in the current geometry, the velocity gradients of the coolant itself are the source of the CRVP. It is driven by the relevant velocity differences between the coolant jetting out the comb-slit and the coolant above the comb-tooth. Therefore, the CRVP strongly links to the geometrical parameters. However, the comb structure used in the present investigation is merely to simplify the simulation, because of its simple shape. Otherwise, any geometry providing both structural integrity and high uniformity could be chosen.

Table 4.1 CRVP intensity and the core positions

Nominal Position at Y=0		X/D=-1.7	X/D=-1.5	X/D=-1.0	X/D=-0.5
Typical high performance	CRVP Core Position (Z/D, Y/D)	0.08, -0.97	0.07, -0.95	0.07, -0.95	0.06, -0.99
	ω_x	10	23	13	4
Typical low performance	CRVP Core Position (Z/D, Y/D)	0.12, -0.12	0.09, -0.13	0.09, 0.04	0.09, -0.13
	ω_x	11	32	12	4

The CRVP of Case B is visualized in Figure 4.24. Additionally, for the comparison with Case B, their positions of the right side CRVP core, and in which the core $\omega_x$values, are also listed in Table 4.2. Figure 4.24 (a) and (b) show the two cut planes at X/D = -1.7 and -1.5. The mainstream entrainment is clearly observed: some mainstream has clearly entrained into the coolant. The kidney shape is distinct, in particular the θ 0.9 contour line in Figure 4.24(b). Figure 4.24 (c) and (d) show that the blind slot is full of mainstream-coolant mixture. The mainstream entrainment causes the liftoff-reattachment as shown in Figure 4.15(b) and Figure 4.21(b).

The performance of Case B is comparatively poor. Figure 4.24 has demonstrated that the main reason for the lower performance is mostly the CRVP position. The CRVP is close to the mainstream-coolant interface and produces mainstream entrainment.

The previous researches on the CRVP effect highlighted the CRVP intensity but overlooked its position, because when the CRVP is naturally close to the mainstream-coolant interface, the offset between the CRVP and the interface is neglected. However, in the comb scheme, the CRVP effect is not inevitable anymore. The special structure makes the CRVP away from the mainstream-coolant interface. Under this situation, the CRVP effect has to count two factors: intensity and position. First, the CRVP intensity has to be strong enough to entrain the mainstream. Also, the CRVP has to locate near the mainstream-coolant interface, hence the rotating velocity penetrates the interface. Figure 4.23 demonstrates that the CRVP of Case A occurs on the bottom of the blind slot. The impact of its CRVP is lower than Y/D = -0.8. The mainstream-coolant interface is higher than Y = 0, where the interface ω_x is negligible, as shown in Figure 4.22(a). The CRVP is completely trapped in the blind slot, leading to the high performance of this case.

Figure 4.25 shows the extracted CRVP core positions of these two cases. The distance between the CRVP and the mainstream-coolant interface is distinct. The mainstream-coolant interface is usually higher than Y = 0. For Case B, its core positions of Y/D range from -0.13 to 0.404, the mainstream entrainment is likely to occur. For Case A, its core positions of Y/D are lower than -0.95, the CRVP is so far away from the mainstream-coolant interface that it is unlikely to impact the interface.

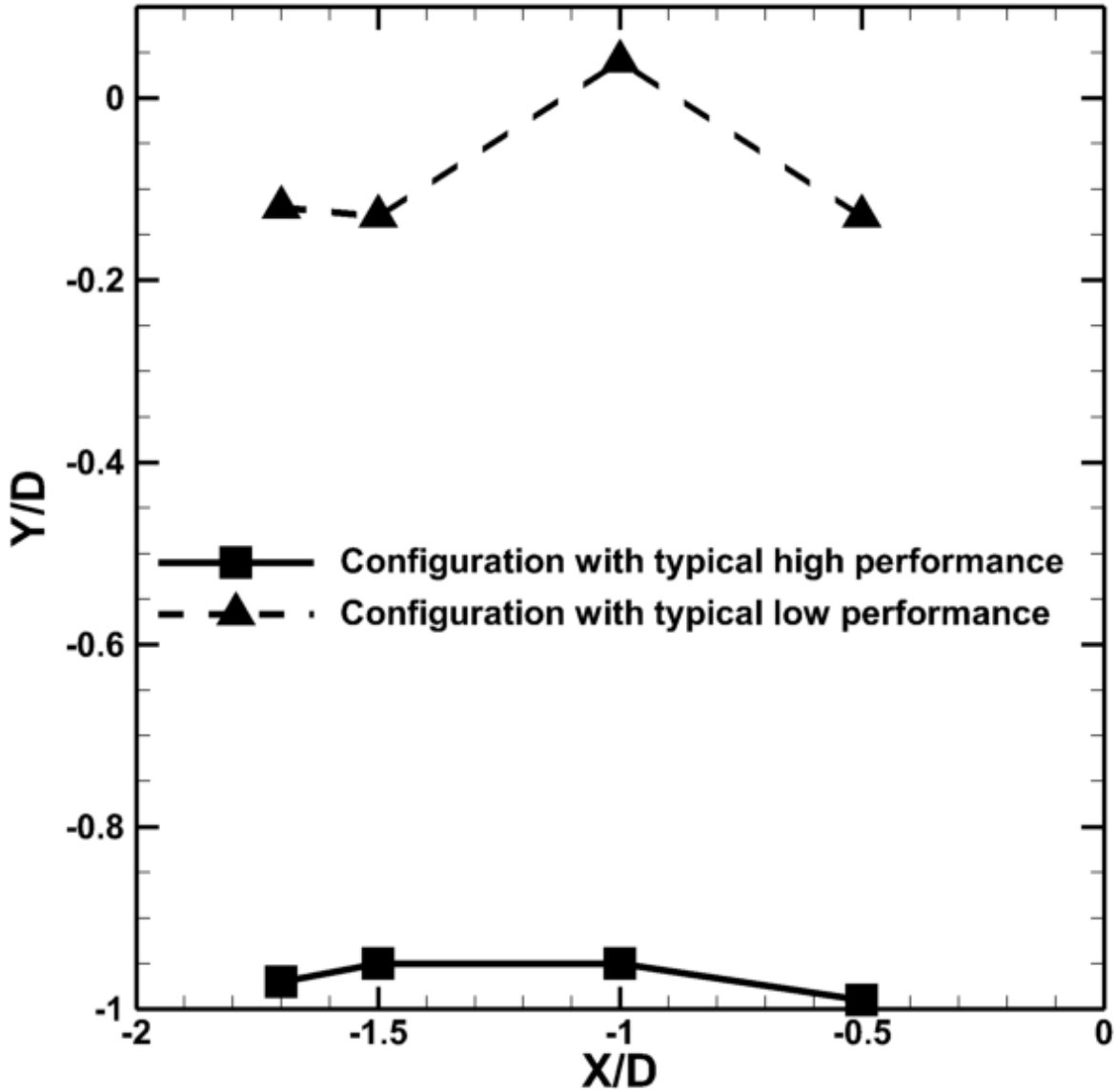

Figure 4.25 The CRVP core positions for Case A and Case B of Table 4.1

Comparison of Cases A and B given in Figure 4.21 to Figure 4.25 demonstrates that the CRVP starts developing at the bottom of the blind slot, not at the mainstream-coolant interface, so that the deeper the blind slot is the better it is. In other words, the comb scheme traps the CRVP within the blind slot. In addition, it reveals that the distance between the CRVP and the mainstream-coolant interface is mostly linked to *H*, which is consistent with the aforementioned parameter analysis, and matches the idea of the new scheme design shown in Figure 4.2.

4.4 Conclusions

A mechanism of the film cooling heat transfer has been proposed based on the relations discovered earlier between the CRVP and η, where strong velocity gradients on the mainstream-

coolant interface produce secondary flows penetrating the interface. The mainstream entrainment refers to the penetration of hot gases from the mainstream into the coolant. It enhances the heat transfer, hence decaying η drastically. Conventionally, the mainstream entrainment is inevitable in discrete film cooling geometries like the cylindrical hole. The present paper eliminated the mainstream entrainment by developing the comb scheme where the CRVP is trapped in a blind slot.

The comb scheme has been investigated experimentally and computationally. The transient TLC technique was used in the experimental investigation, and the steady RANS momentum equations with RKE turbulence model were used in the numerical simulations. The experimental and computational schemes were assessed and proved to be reliable. Both experimental and computational results demonstrated the so-called 'ideal performance' of the comb scheme, i.e. where $\eta = 1$, while its material structure is practical.

The effect of the geometric parameters: H, t_s and P_s on $\overline{\eta_L}$ and the interface ω_x has been analyzed. In addition to demonstrating their parametric effect on the high performance, it also stressed the fact that increasing ω_x on mainstream-coolant interface resulted in decreasing $\overline{\eta_L}$, hence supporting the present proposed film cooling heat transfer mechanism.

Two typical high and low performance Cases, A and B, were selected as samples. The distance between the CRVP and the gas-coolant interface being $H/D = 1$ and 0.2; η and ω_x distributions above the exit exhibited the blind slot fully traps of the CRVP for Case A but not for Case B, leading to the decrease or elimination of the mainstream entrainment. In addition, it revealed the importance of H, the depth of the blind slot. It also matches the comb scheme design.

The visualization of the CRVP in the blind slot reveals a characteristic of the comb scheme distinct from the traditional geometry: the source of the CRVP in the comb scheme is the coolant velocity gradients rather than the velocity gradients at the mainstream-coolant shear layer in a traditional geometry like the cylindrical hole.

The comb scheme was developed along with the proposed mechanism of the film cooling heat transfer. In addition to providing a trail to develop high performance film cooling geometry, the successful achievement of the high performance presented a solid proof of the proposed mechanism. The clarification of the film cooling heat transfer mechanism has established a solid base for the film cooling heat transfer research.

Chapter 5 On The Use of High-Aspect-Ratio Film Cooling Scheme

Accepted by Heat Transfer Engineering Journal [59][1].

A part has been published on ASME 2017 Summer Heat Transfer Conference HT2017 as HT2017-4796: Analysis of Film Cooling with High-Aspect-Ratio Holes: Heat Transfer Mechanisms

Abstract

Current film-cooling hole-geometry research is attempting to clarify the mechanism of film cooling effectiveness and its relation to the counter-rotating vortex pair (CRVP), in this paper a mechanism of film cooling heat transfer has been proposed. The coolant expansion in this mechanism is likely to improve film cooling effectiveness. It was characterized by developing a high aspect ratio (AR), hence named high-aspect-ratio (HAR) scheme. Typical AR values investigated experimentally and numerically in this work were 17.5 and 35. The transient thermochromic liquid crystal technique and the steady Reynolds-Averaged Navier-Stokes simulation with realizable *κ-epsilon* turbulence model were used. The results were assessed against available data hence demonstrating the high performance of the new scheme. The film cooling effectiveness of the full expansion cases is close to 1, achieved the so call 'ideal' performance. Meanwhile, CRVP was still very strong, demonstrating that the CRVP did not result in decaying performance in the new scheme. Consequently, the HAR scheme achieved successfully the high performance of the proposed film cooling heat transfer mechanism.

[1] Co-authors: Wahid Ghaly, Ibrahim Hassan

5.1 Introduction

Given the direct relationship between the turbine inlet temperature and its thermodynamic efficiency, all advanced gas turbines are operating at extremely high temperatures, making film cooling indispensable to ensure the durability of the turbine components. Nowadays, one of the turbine developing directions is the turbine cooling technology [3, 60] and, in particular, film cooling in all of its various formats has become a mainstay [28, 61–63].

A slot has high film cooling performance; however, because of its structural rigidity, it was rarely used, despite the fact that its film cooling effectiveness (η) is ideal (or perfect) performance [3]. In a real engine, discrete film cooling holes, such as a cylinder hole and a shaped hole, are generally used [28, 62, 64]. Compared with a cylindrical hole, Goldstein and Eckert [4] found that a shaped hole improved the performance drastically. The finding of the shaped holes is revolutionary progress. Over the past decades after this revolution, considerable research efforts have been dedicated, no equivalent improvement has been achieved. It is also true that the gas turbine heat transfer and thermal management technology has reached a plateau [2, 62, 64]. It is much needed to clarify the complex film cooling heat transfer mechanisms, to guide the research on the film cooling geometries.

Conventionally, the most crucial factor on η is thought of as the velocity relevant factors like the momentum flux ratio (I) and the blowing ratio (BR) [3–5]. Sinha *et al.* [5] investigated the η values of the cylinder hole. The film-cooling flow was classified into three types: attached, detached and reattached flow. The liftoff-reattachment mechanism was thought to be a function of the momentum flux ratio I. The performance improvement of the shaped holes was attributed to the decrease of the jet mean velocity by Goldstein and Eckert [4]. This opinion misdirected the research on the advanced film cooling scheme to expand the exit as large as possible to decrease the momentum flux ratio [10].

Investigating the correlation between η and the related variables is an important approach to analyze the mechanism of the film cooling heat transfer. The factors considered to have the most significant effect on η must be included in these correlations. Baldauf *et al.* [29] analyzed enormous experimental data of the cylinder hole, and the correlation included the parameters of inclined angle, turbulence intensity, hole pitch (P), density ratio (DR) and blowing ratio. Colban *et al.* [30] analyzed the shaped hole data. The main parameters in the correlation are the lateral coverage ratio (t/P) and BR. The characteristics of the shaped hole η distributions were also summarized: the maximum lateral averaged film cooling effectiveness ($\overline{\eta_L}$) is equal to t/P, occurs at position X = 0; then, the $\overline{\eta_L}$ value decreases monotonously along with X/D. The maximal characteristic $\overline{\eta_L}$ less than t/P was generalized with shaped holes, but all existing geometries have compliance with it.

Fric and Roshko [11] depicted the near field vortical structures of jet in cross flow, including the counter-rotating vortex pair (CRVP), which is the main vortical structure in the film cooling flow. This vortical structure has also been considered an essential factor on η. Haven and Kurosaka [12] observed two vortical structures, the kidney vortices (CRVP) and the anti-kidney vortices. The anti-kidney vortices were supposed to decrease the intensity of the kidney vortices. Correspondingly, Haven *et al.* [13] attributed the superior performance of the shaped holes to the anti-kidney vortices cancelling out the effect of the kidney vortices. Hyams and Leylek [16] proposed a similar conclusion. Related new film cooling schemes have been introduced by [23,

25, 31, 32]. They attributed the increased cooling performance to the decrease of the CRVP strength.

Li and Hassan [7] designed a unique geometry to separate the momentum flux ratio and the CRVP strength. It was found that the CRVP strength, instead of the momentum flux ratio, is the most critical factor influencing η, and a correlation between the CRVP intensity and η was proposed. This flow structure was further investigated by Li *et al.* [58], in which its essential source, its main components and its relations with the reattachment and the kidney shape of the jet flow were analyzed.

For the ambiguity on the film cooling heat transfer, the film cooling geometry research remains sluggish, at the η far less than perfect. Along the discovering of the CRVP crucial effect and the analysis underlying this effect on film cooling flow, the present paper proposes a mechanism of the film cooling heat transfer. The coolant expansion among the CRVP effect is revealed by dissecting this mechanism. Furthermore, a new advanced film-cooling scheme is developed to exploit the coolant expansion, aimed to obtain the 'ideal' performance.

5.2 Methodologies and Models

A mechanism of the film cooling heat transfer was proposed based on analyzing the crucial effect of CRVP on η. By applying this mechanism, an advanced film cooling scheme named high-aspect-ratio (HAR) scheme was developed and investigated experimentally and numerically. The experiments were performed on a two-loop wind tunnel, with a thermographic technique, i.e., the thermochromic liquid crystal (TLC). The steady flow Reynolds-averaged Navier-Stokes (RANS) simulations were performed with the realizable κ-ε model (RKE) turbulence model.

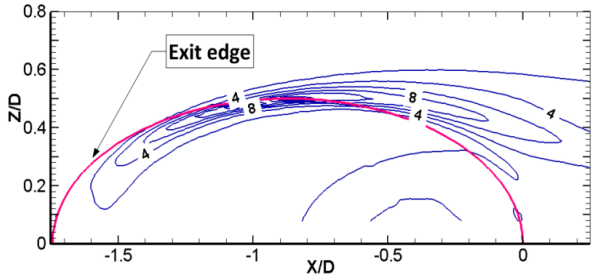

a) ω Distribution from [57]

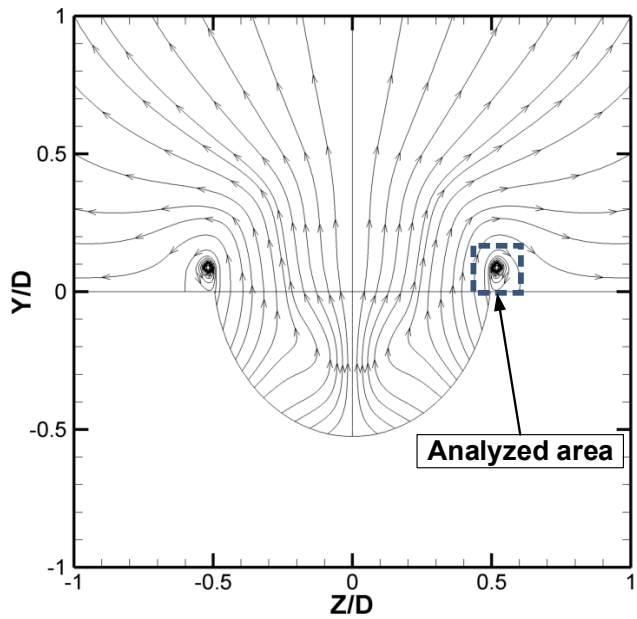

b) CRVP at X/D = -0.75 from [57]

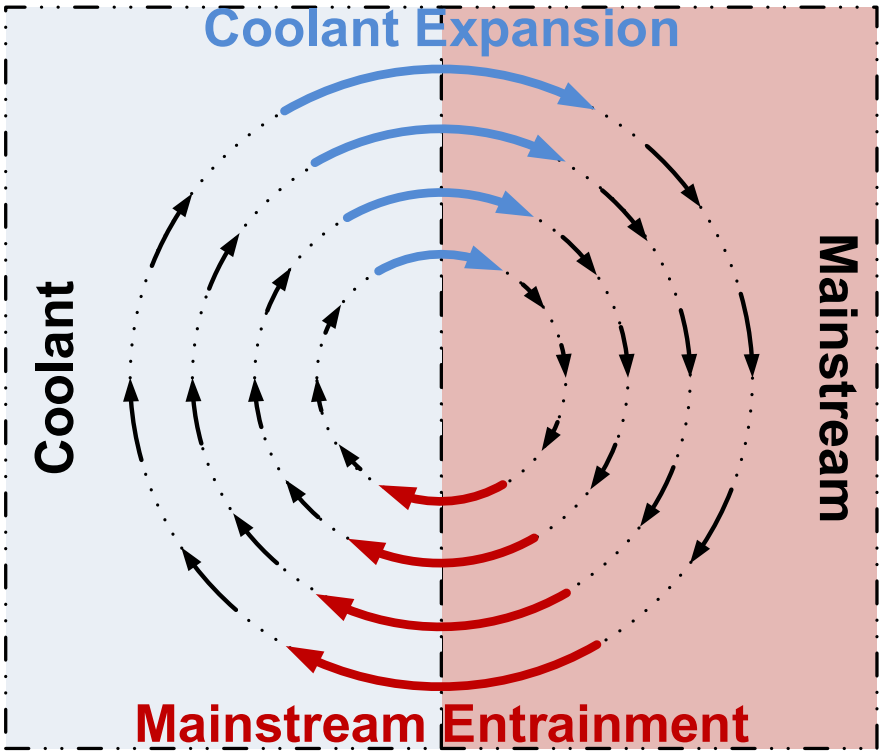

c) Mechanism of the film cooling heat transfer

Figure 5.1 Film cooling heat transfer mechanism

5.2.1 The Mechanism Underlying the CRVP Crucial Effect

Li and Hassan [7] first reported the crucial effect of the CRVP intensity and the vortical structure was further analyzed by Li *et al.* [58]. It concluded that the essential source of the CRVP is the vorticity sheet formed at the mainstream-coolant interface. Figure 6 in [58] presents the detailed distributions of vorticity and velocity gradients. Figure 6(a) in [58], showing the magnitude of vorticity ω, is displayed in this paper as Figure 5.1(a). The edge of the cooling hole exit is shown in the background. It demonstrates that the local peak vorticity is right above the edge of the exit while inside the edge is mostly coolant that jets out with a velocity v. Outside the edge is mostly the mainstream, where v is deemed to be 0, hence strong vorticity accompanied with large velocity gradients occur in the mainstream-coolant interface and mostly drive the CRVP.

Figure 4 in [58] describes the CRVP forming process with 2D streamlines. Figure 4(b) in [58] is displayed in this paper as Figure 5.1(b), where the area around the CRVP is framed with dash lines and is depicted as Figure 5.1(c). The situation in the sketch has been simplified: 1. the mainstream-coolant interface thickness is deemed to be 0; 2. the CRVP size is ignored; 3. the offset between the CRVP position and the mainstream-coolant interface is also ignored. Figure 5.1 (c) illustrates the mechanism of the film cooling heat transfer. Its midline is the mainstream-coolant interface and is simplified into a line where the coolant flows to its left and the

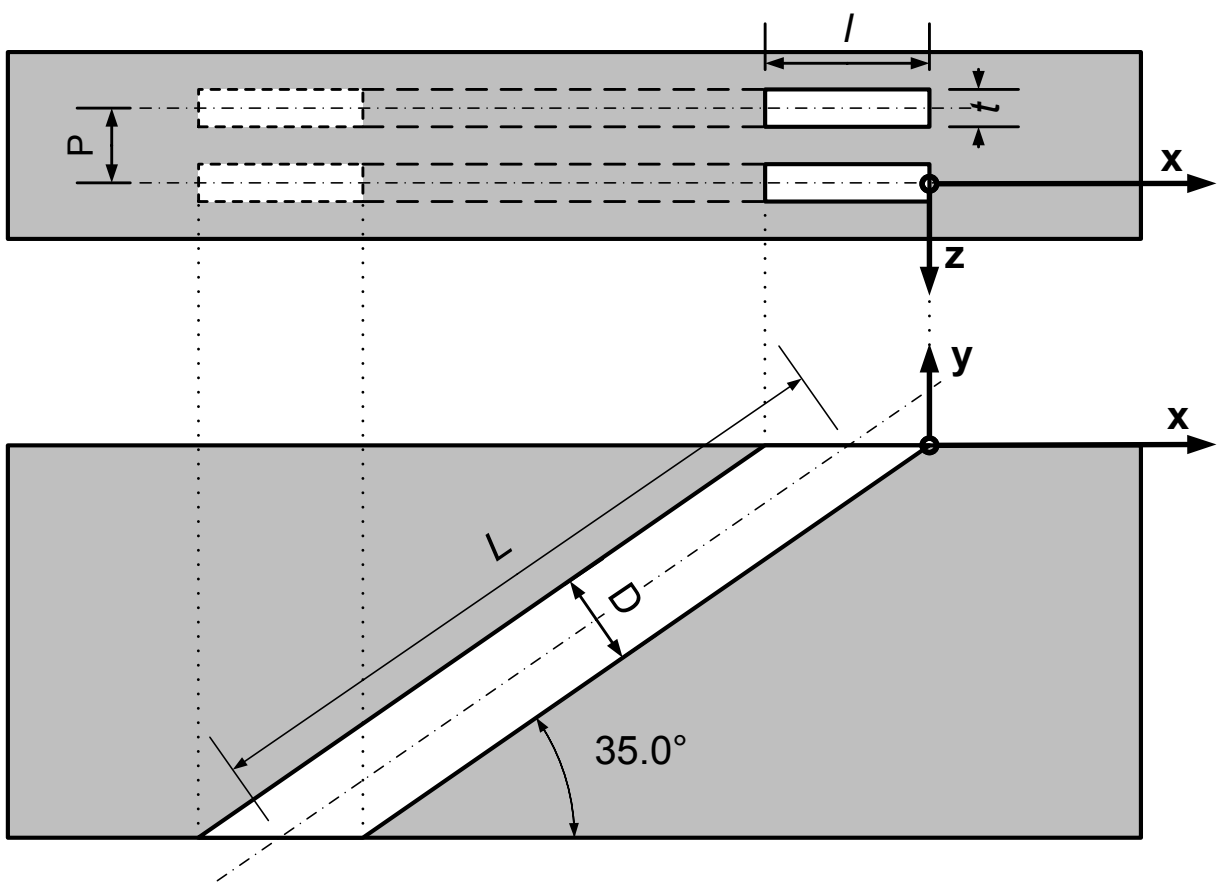

Figure 5.2 High-Aspect-Ratio scheme configuration

mainstream to its right. In the vicinity of the interface, large vorticity and associated velocity gradients occur, and lead to flow rotation. The vorticity ω on the interface produces mainstream flow penetration into the coolant side, which drastically increases the heat transfer between these two streams so that further downstream the mainstream flow is colder. The penetration from the mainstream into the coolant is referred to as the mainstream entrainment. Meanwhile, the coolant penetration into the mainstream is the coolant expansion, which expands the coolant into the mainstream, likely to improve η. The mainstream entrainment is notable, in the conventional film cooling research, it has been the only appreciable CRVP effect on η while the coolant expansion is fully ignored.

The film cooling convection is mostly by advection while the diffusion is neglected [58]. So without advection (CRVP intensity is 0), the mainstream-coolant interface is steady, and the outermost position of the interface is *t/P*. It is the reason under the correlation proposed in [7], $\overline{\eta_A} = t/P + a\overline{\omega_x}$, where $\overline{\eta_A}$ is area averaged η. In the case of highlighting the mainstream entrainment, which immediately impacts η, the highest available performance is *t/P*, on the condition that ω_x is 0. Li *et al.* [65] developed a new scheme along this approach. The perfect high performance has been successfully achieved by eliminating the entrainment.

In contrast to the entrainment, even the coolant expansion favors improving η, its impact on η is hard to be perceived in the conventional film cooling geometries. A new geometry has to be developed to exploit the coolant expansion. In the coolant expansion dominating, the mainstream-coolant interface tends to move outside; thus η breaks the value restriction of the *t/P* and obtains high values.

5.2.2 The HAR Configuration

A film cooling scheme is developed on the configuration given in Figure 5.2. It is formed of a row of rectangular holes of size *D* by *t* and inclined at 35° to the flow direction, x-direction. The hole size *D* is set at 5 mm in the experiment and 12.7 mm in the computations. The axial length of the coolant passage, *L*, is set to 7*D*. The lateral width is set to *t*, and the longitudinal dimension at exit is set to *l*. The lateral spacing is referred to as pitch, *P*. The Cartesian coordinates for this investigation are also shown in Figure 5.2. The origin is located at the center of the trailing edge exit. The x-, y- and z-axes are aligned with the main flow stream, the vertical, and span-wise directions, respectively.

The coolant expansion occurs at a place further away from the protected surface (the wall). The new scheme has to provide enough time for it to take effect. The geometrical characteristic of the new scheme is its exit aspect ratio (AR), defined as AR = *l/t*. To exploit the coolant expansion, the longitudinal length, *l*, was drastically extended. The AR values of the new scheme were 17.5 and 35 in the present investigations, which is much higher than the conventional film cooling geometries, which are usually less than 2. Therefore, the new scheme was named high-aspect-ratio (HAR) scheme.

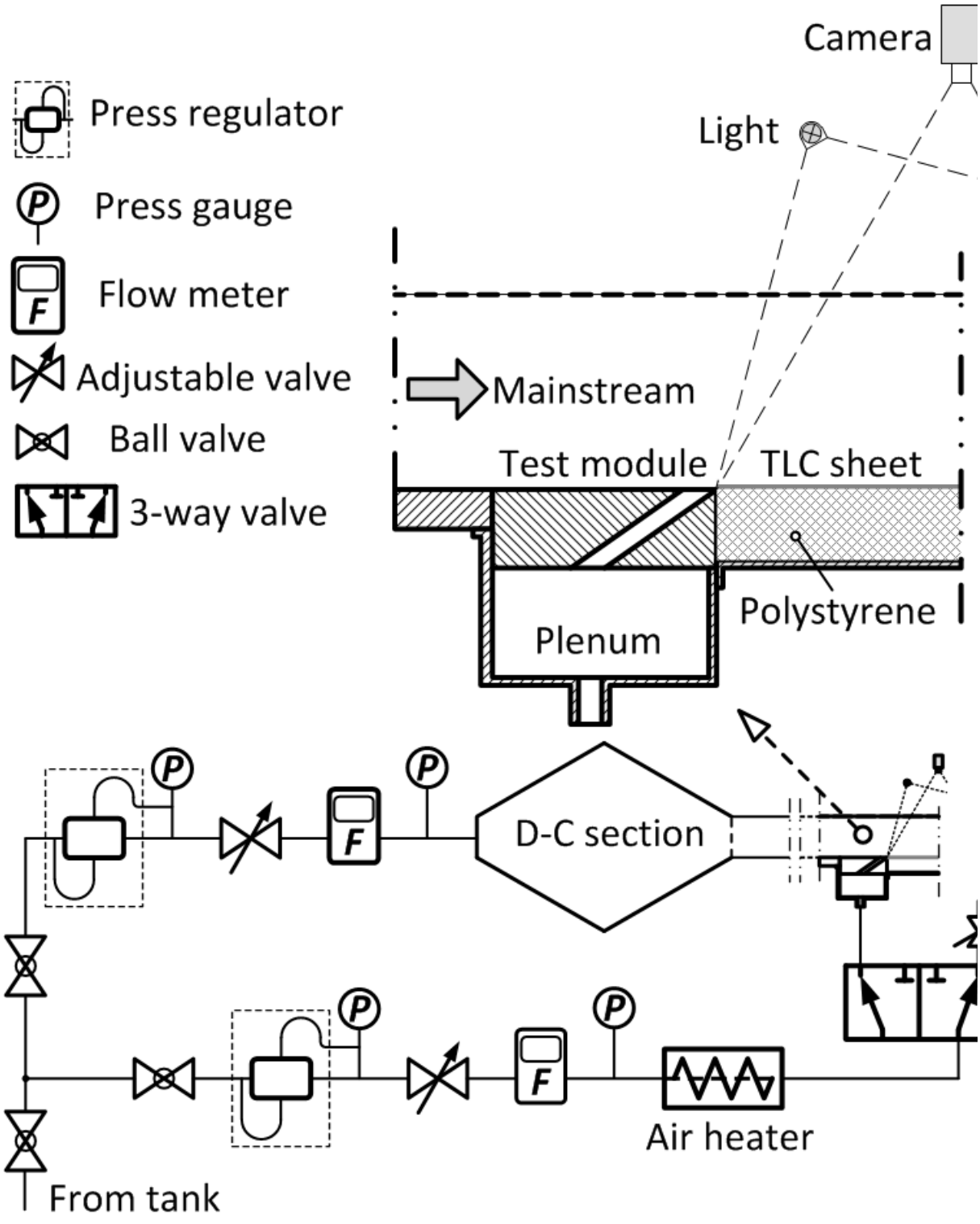

Figure 5.3 Schematic diagram of the experimental system

5.2.3 Experimental Facilities

The present paper used identical experimental method to [9, 44, 45]. The transient TLC technique was used to measure η, and experiments were performed with a two-loop wind tunnel. They are briefly introduced in this subsection.

The experiments have been performed in a two-loop wind tunnel, which is shown in

Figure 5.3. Its first loop is for the mainstream flow, and the second loop is for the coolant flow. Both loops have adjustable valves, pressure regulators and flowmeters. The coolant loop has a heater to increase the coolant temperature. The DR was considered as unity. The coolant loop connects the mainstream loop in the test section through a plenum under the bottom. The cross-section dimensions of the test section are 99 mm × 53.5 mm. Its mainstream velocity was set to 20 m/s. The coolant velocity was adjusted upon the BR settings.

A row of HAR holes was manufactured on a test module, installed on the test plate, which is the bottom of the test section. The lateral width of this row is 63.5 mm (12.7*D*). Downstream of the test module is a piece of extruded Polystyrene, covered with a TLC sheet. The size of the

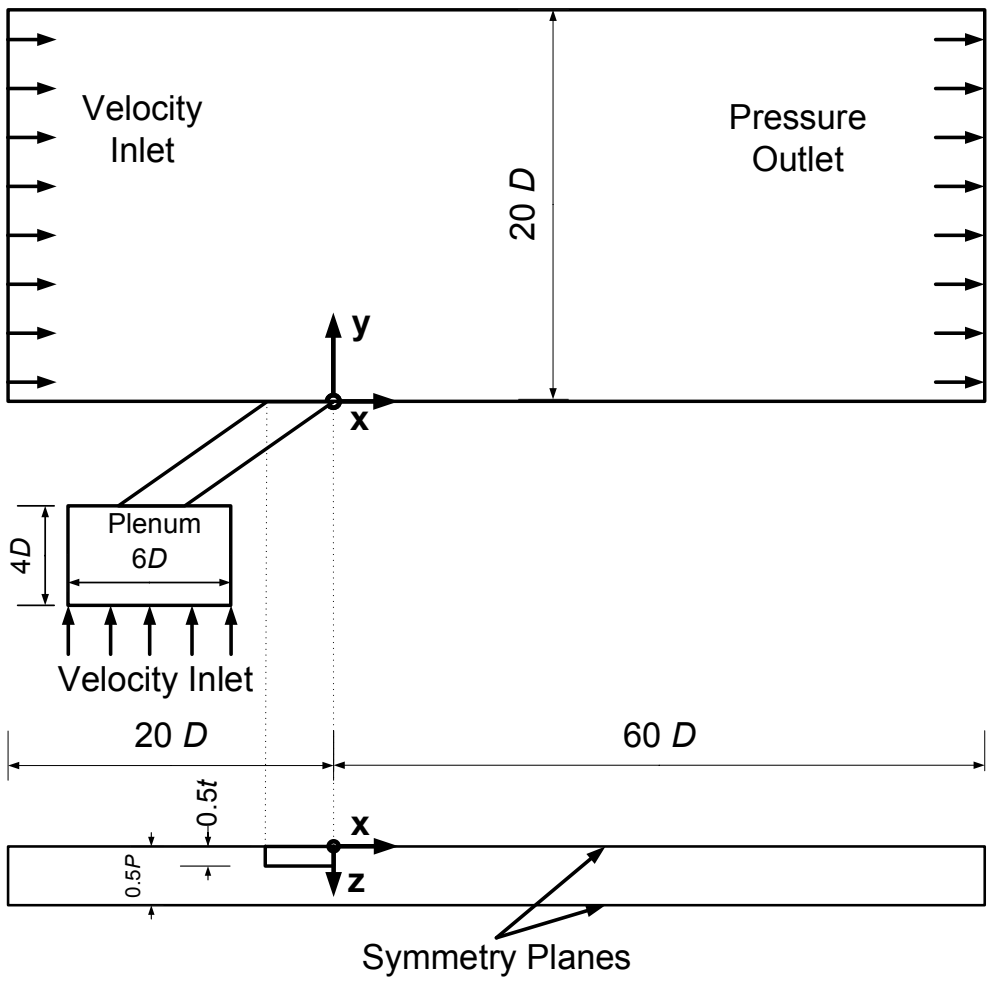

Figure 5.4 The computational domain

TLC sheet is 203 mm × 89 mm (40.6D × 17.8D). Considering the end effect, only the central 25% was post-processed. A 3CCD camera is located right above the test section to capture the TLC images through the transparent test section top. Each test records 300 TLC images at 5 frames/s. They were saved to a workstation with the simultaneous temperature data of the mainstream and the coolant, which were measured with thermocouples.

The transient TLC technique was used in the present investigations where its color varies with temperature. Wang *et al.* [66, 67] introduced the TLC technique into the film cooling investigations. Since then, it has been widely used in the film cooling research, to list a few [8, 9, 43–45, 47, 68, 69]. The transient TLC technique considers the film cooling heat transfer as a transient conduction case, namely the semi-infinite solid case which has the following analytical solution

$$\left.\begin{aligned} \frac{T_w - T_i}{T_f - T_i} &= 1 - \exp(\beta^2)\, erfc(\beta) \\ \beta &= \frac{h\sqrt{a\tau}}{k} \end{aligned}\right\} \tag{5.1}$$

where T_w, T_f and T_i are the temperatures of test plate surface, film and the initial state, respectively. At the initial moment, the entire test plate has a uniform temperature of T_i, and suddenly exposed to a convection boundary condition, in which the fluid temperature is T_f, and heat transfer coefficient is h. The test plate that is covered with a TLC sheet produces transient response T_w, which is recorded by a CCD camera. In film cooling flow, T_f is the film temperature. It is replaced by η, which is defined as

$$\eta = \frac{T_f - T_m}{T_j - T_m} \tag{5.2}$$

where T_m, and T_j are the temperatures of mainstream and coolant, respectively. So the solution becomes

$$T_w - T_i = \left[1 - \exp(\beta^2)\, erfc(\beta)\right]\left[\eta\left(T_j - T_m\right) - T_m - T_i\right] \tag{5.3}$$

In the experiments, the temperatures of T_i, T_j, and T_m were measured with thermocouples. T_w was measured with the TLC technique. This equation has two unknowns, η and h, only data of two instants is necessary to solve it. However, the semi-infinite solid conduction model assumes a step T_f change that is unrealizable in an experiment. It is considered to be a conceptual uncertainty [56]. Therefore, the present experiments performed multi-sample tests to decrease the uncertainty. Each test recorded 300 TLC images at 5 frames/s, and other temperatures were measured at 500 Hz. They were used to calculate η in the equation with less square regression method. All experimental cases were repeatedly tested to ensure the repeatability.

Directly analyzing the uncertainty in η is unpractical because Eq. (3) is too complex to get all partial derivatives for temperatures of T_i, T_j, T_m and T_w. The present investigation estimated the uncertainty in η with computerized uncertainty analysis [56]. Perturbing values of the temperatures were input in an in-house program, their contributions to the uncertainty were accumulated. The uncertainty in temperature measurements is ±0.2K. With 95% confidence, the averaged uncertainty in η is approximately ±8% near the exit, however, the uncertainty increases

where η decreases. It is approximately ±16% in the further downstream place. More details of the experimental facilities and the uncertainties of other parameters are available in [9, 44, 45].

5.2.4 Numerical Settings

The computational domain is shown in Figure 5.4. The wind tunnel bottom surface is considered as the test plate and the wind tunnel connects to the plenum through the film-cooling hole. The hole is inclined at 35° to the x-axis and the axial hole length is 7*D*. For all simulated geometries, *D* is 12.7 mm. The half domain is used for the steady simulation, so its span-wise width is 0.5*P*. The two lateral end planes of the domain, the center-plane of the cooling hole, and the middle plane between two cooling holes were set to symmetry planes. The inlet velocity was set at 20 m/s at the wind tunnel inlet, along with an inlet temperature of 300 K. A velocity inlet along with a temperature of 150 K was specified at the plenum inlet. The density ratio DR is 2 for all simulated cases. A pressure outlet of zero gage pressure was applied at the wind tunnel exit. The remaining walls were defined as adiabatic and no slip walls boundary conditions, except the wind tunnel top wall set as a free slip wall. The set of Cartesian coordinates is also shown in the figure. The origin is located on the symmetry plane at the downstream edge of the hole exit. The x-, y- and z-axes are aligned with the mainstream, vertical, and span-wise directions, respectively.

Concerning the simulation of the film cooling flow, Zhang and Hassan [10] performed detail comparisons of the computational domain, the boundary conditions, the turbulence model and the near wall treatment. According to their conclusions: ANSYS-FLUENT, a CFD solver

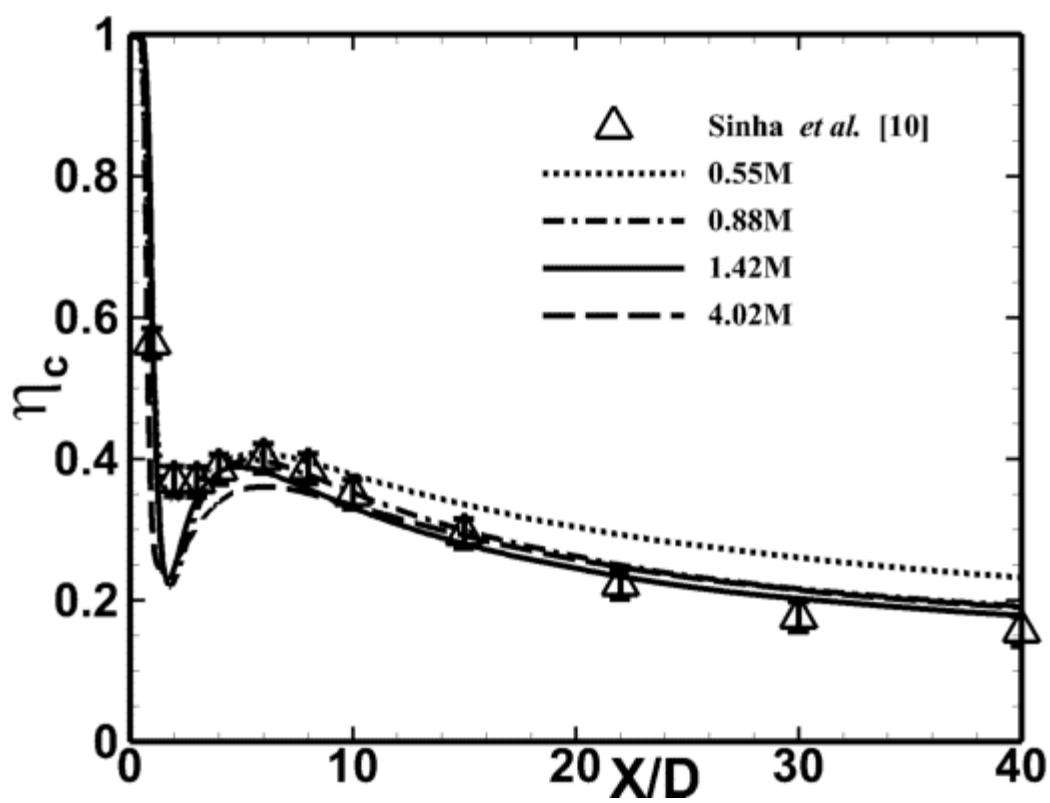

Figure 5.5 Grid independency

included in the ANSYS package, was used to simulate the current flow; a steady RANS simulation was performed and a realizable κ-ε model (RKE) was used as the turbulence model.

ANSYS-ICEM-CFD was used to generate the mesh. To test the grid independence, four grids were created to simulate a row of cylindrical holes. Their sizes ranged from approximately 0.55 million to 4.02 million cells. The boundary conditions are identical to the setting in Sinha *et al.* [5], in which the η uncertainty was estimated at ±0.025. The resulting film-cooling centreline effectiveness (η_c) is compared in Figure 5.5. The main discrepancy is the computations larger than 0.88M under predict the liftoff value, which may be due to the imperfection of the turbulence model. Other than this, they well capture the liftoff-reattachment, and the values approximately overlap the measurements. The high agreements with the experimental data [5] are shown. The grid containing 1.42M cells was considered appropriate. The identical criterion was adopted in the mesh generation of the new scheme geometries. A close look of the near field mesh is shown in Figure 5.6. The present simulations used a conservative convergence criterion:

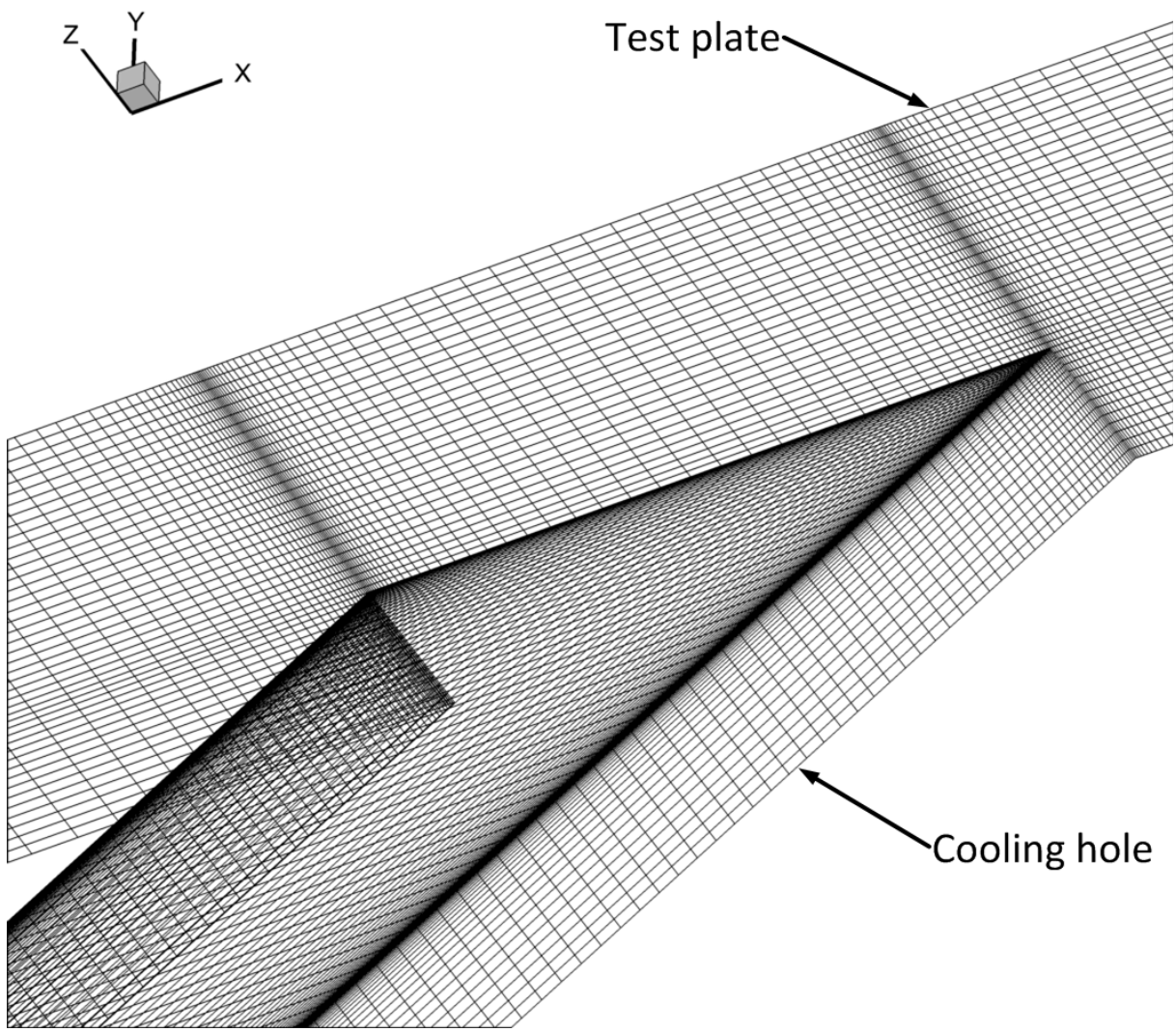

Figure 5.6 A close look of the mesh near the cooling hole exit

the residuals on mass and energy residuals have to reach steady values. A typical case took approximately 2×10^5 iterations to reach convergence; the residuals on mass and energy were 1×10^{-8} and 1×10^{-11}, respectively.

5.2.5 Test Matrix and Parameters Normalization

The investigated cases are summarized in Table 5.1. Three types of geometries were included: the cylindrical hole with $P = 3D$, the simple slot and the HAR geometry. They were investigated experimentally and numerically. In the experiments, $D = 5$ mm and DR = 1. In the computations, $D = 12.7$ mm and DR = 2. The use of a cylindrical hole and a rectangular slot was to allow for a fair comparison of experimental results with available experimental data and assess computational data with the data measured for the HAR geometry.

The temperature is normalized into θ in the present investigations. It is similar to η except that η is only valid at the test plate while θ was defined and is valid over the whole domain.

$$\theta = \frac{T - T_m}{T_j - T_m} \tag{5.4}$$

where T_m and T_j are the temperatures of mainstream and coolant.

The x-component of the CRVP strength, ω_x is the main component of the CRVP intensity [58]. It was normalized with the mainstream velocity $U_m = 20m/s$ and D = 12.7mm, as this parameter was only used in the numerical results:

$$\omega_x = \frac{\omega_x^*}{U_m / D} \tag{5.5}$$

In the experimental results, $\overline{\eta_L}$ is defined as:

$$\overline{\eta_L} = \frac{1}{3D}\int_0^{3D} \eta \, dz \tag{5.6}$$

In the computational results, $\overline{\eta_L}$ is defined as:

$$\overline{\eta_L} = \frac{1}{0.5P}\int_0^{0.5P} \eta \, dz \tag{5.7}$$

5.3 Results and Discussion

Experimental and numerical investigations have been performed. They are reported in this section. In the first two sub-sections, the experimental results are presented, showing the validations/assessments, the performance for two HAR geometries and the BR effects. The numerical results are presented in the rest subsections. The flow computations are then assessed with data and measurements available in the literature. Based on the numerical results, further analysis is performed on the coolant expansion.

Table 5.1 Test matrix

Case No.	Geometry	Method	AR	DR	BR
1	Cylinder, D=5mm	Measurement	1.75	1	0.5
2					0.75
3					1
4	Cylinder, D=12.7mm	Simulation	1.75	2	1
5	Slot, D=5mm	Measurement	0.14	1	0.5
6					1
7					1.5
8	Slot, D=12.7mm	Simulation	0	2	0.5
9	HAR, D = 5mm, t = 0.1D, P = 2t	Measurement	17.5	1	0.5
10					1
11					2
12	HAR, D = 12.7mm, t = 0.1D, P = 2t	Simulation	17.5	2	0.5
13					1
14					2
15					4
16	HAR, D = 5mm, t = 0.1D, P = 3t	Measurement	17.5	1	1
17					2
18					3
19	HAR, D = 12.7mm, t = 0.1D, P = 3t	Simulation	17.5	2	1
20					2
21					3
22	HAR, D = 12.7mm, t = 0.05D, P = 2t	Simulation	35	2	1
23					2
24					4
25	HAR, D = 12.7mm, t = 0.05D, P = 3t	Simulation	35	2	1
26					2
27					3

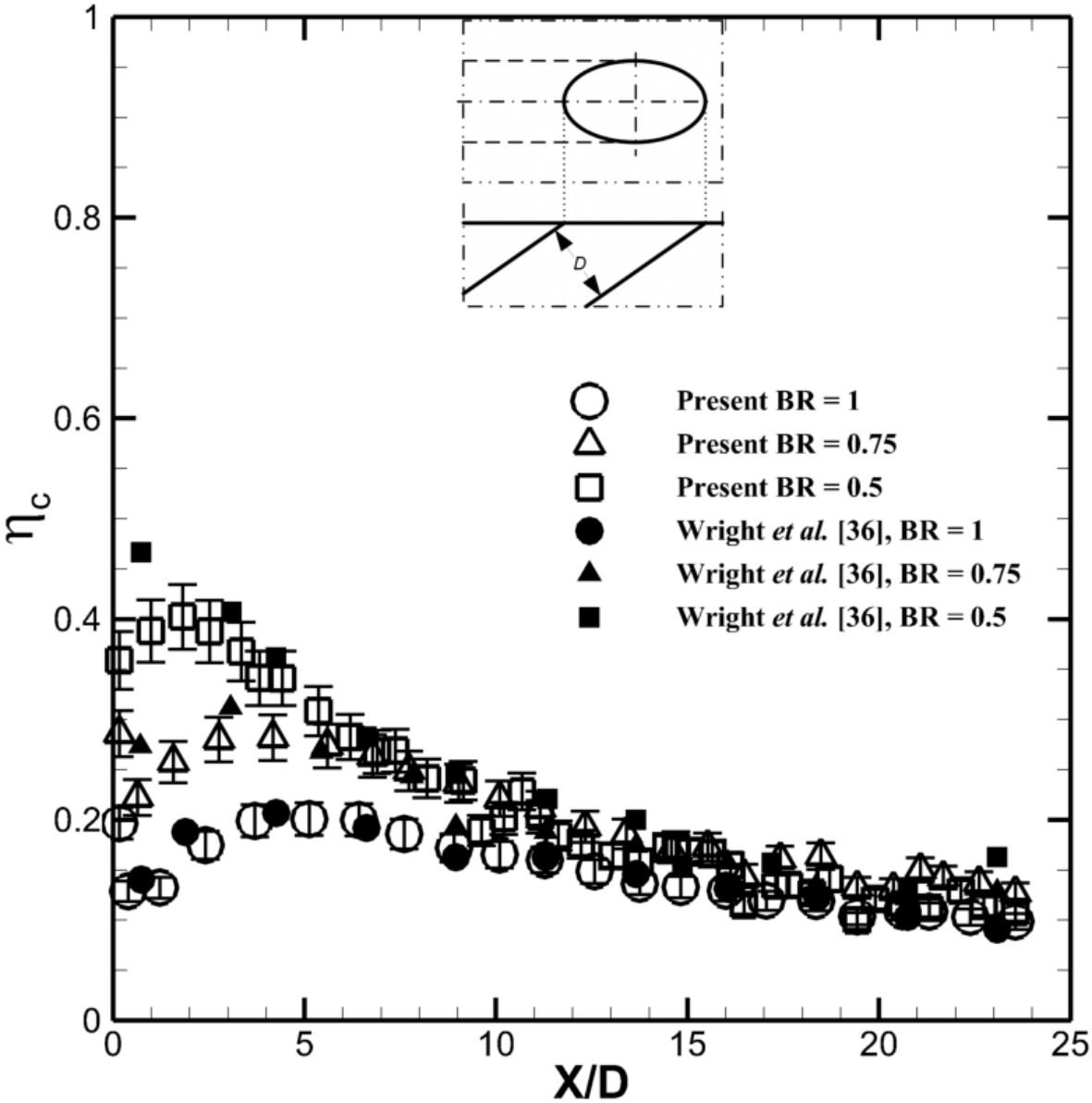

Figure 5.7 Experimental cylindrical hole data compared with published data (Cases 1-3 with [48])

5.3.1 Validation on the Experimental Facility

Two traditional geometries: the cylindrical hole and the slot, were tested in the present facility. The results were compared with published data. Wright *et al*. [48] presented high-resolution η results using the pressure-sensitive painting technique. It had a similar geometry and the density ratio DR was unity. Its uncertainty is approximately 4% at $\eta > 0.65$. Figure 5.7[1] shows a comparison of measured η_c at BR = 0.5, 0.75 and 1with those available in the literature

[1] Reference numbers in the manuscript is [36], but in the current thesis is [48]

[48]. For the case of BR = 0.5, the present results show a small liftoff-reattachment, but the literature results do not show any. Other than that, their difference is less than 0.03, which shows good agreement.

Farmer *et* al. [70] experimentally investigated the simple slot. Its uncertainty in η is 13%. The results are compared with the present experimental ones in Figure 5.8, which compares $\overline{\eta_L}$ at two BR values. Figure 5.8 (a) gives $\overline{\eta_L}$ at BR = 0.5. They begin with an excellent agreement, and then from X/D = 5, the present measurement is slightly higher than the counterpart. The present measurement accurately captured the lift-off, the reattachment and the following tendency, the difference is less than 0.1. Figure 5.8 (b) gives $\overline{\eta_L}$ at BR = 1.5. The distributions are overlapped and showing excellent agreement over the full range. The rather very good agreement with the open literature shown in Figure 5.7 and Figure 5.8 demonstrates the good quality of the present experimental results.

5.3.2 The Performance of the HAR Configuration

Two HAR geometries were tested at BR = 0.5, 1, 2 and 3. The configuration of the 1st geometry is $t = 0.1D$ and $P = 2t$, in which $t/P = 1/2$, and AR = 17.5. Its $\overline{\eta_L}$ distribution at BR = 1 is shown in Figure 5.9 and compared with the slot and the cylindrical holes. The cylindrical hole performance showing here is the validated η_c, instead of $\overline{\eta_L}$. For the slot, $\overline{\eta_L}$ shows a clear liftoff-reattachment at the place immediately downstream of the exit, where the $\overline{\eta_L}$ of the HAR has unnoticeable liftoff-reattachment. It starts at 0.93 at X = 0, and reattaches at 0.96 at X/D = 1. The change in $\overline{\eta_L}$ is only 0.03 otherwise the HAR $\overline{\eta_L}$ distribution is similar to the slot and several times higher than the cylindrical hole. The HAR maximal $\overline{\eta_L}$ is much higher than its t/P = 1/2.

The $\overline{\eta_L}$ distribution at BR = 0.5 is shown in Figure 5.10, and compared with slot and cylindrical hole. The slot $\overline{\eta_L}$ shows a liftoff-reattachment, as the HAR only shows a subtle liftoff-reattachment of 0.02. Similar to the BR=1 case, the HAR presents a high $\overline{\eta_L}$ as close to the exit trailing edge and much higher than its t/P value. However, it decays faster than that of slot, lags behind the slot from X/D = 8 and downstream. Generally, the HAR $\overline{\eta_L}$ is marginally lower than the slot, and much higher than the cylindrical hole.

Figure 5.11 summarizes the HAR performance of this geometry in the tested BR range. The $\overline{\eta_L}$ distributions increase with increasing BR. All cases have modest liftoff-reattachments and similar high values of approximately 0.95 at the place close to the exit trailing edge. The value is much higher than their t/P value. They decline differently as moving downstream. The case of BR = 0.5 drops the fastest with increasing X/D, BR = 2 case drops the slowest, and the BR = 1 case is in-between. It has been shown that the BR factor has a negligible effect on the performance immediately downstream exit but has a distinct impact on the decrease rate of the $\overline{\eta_L}$ along X/D. This effect is notable as BR varies from 0.5 to 1, while it is reduced with BR ranging from 1 to 2.

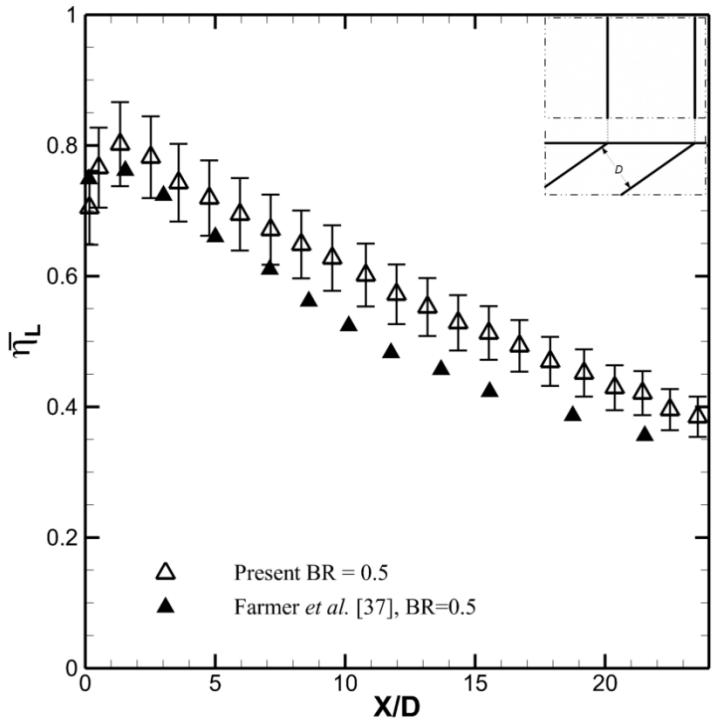

a) BR = 0.5

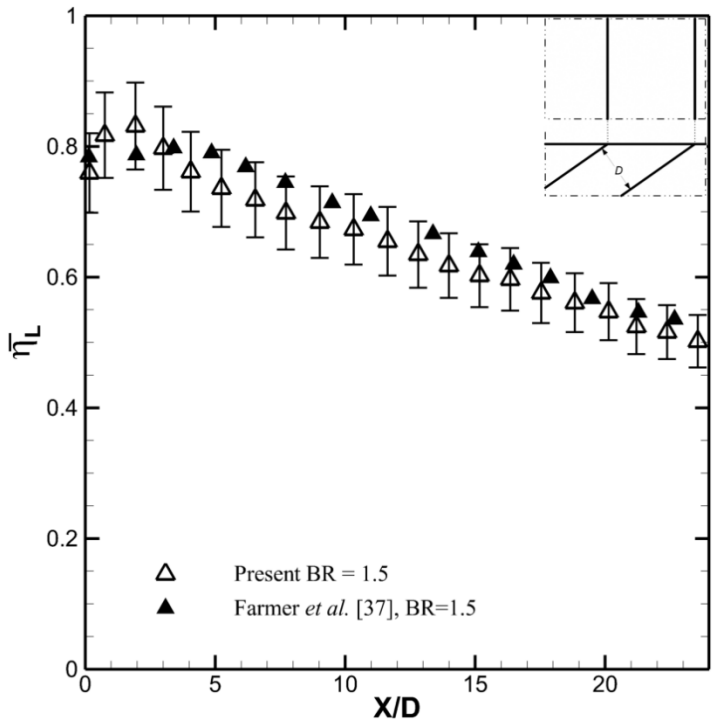

b) BR = 1.5

Figure 5.8 Experimental simple slot data compared with published data [68] (Cases 5 and 7)

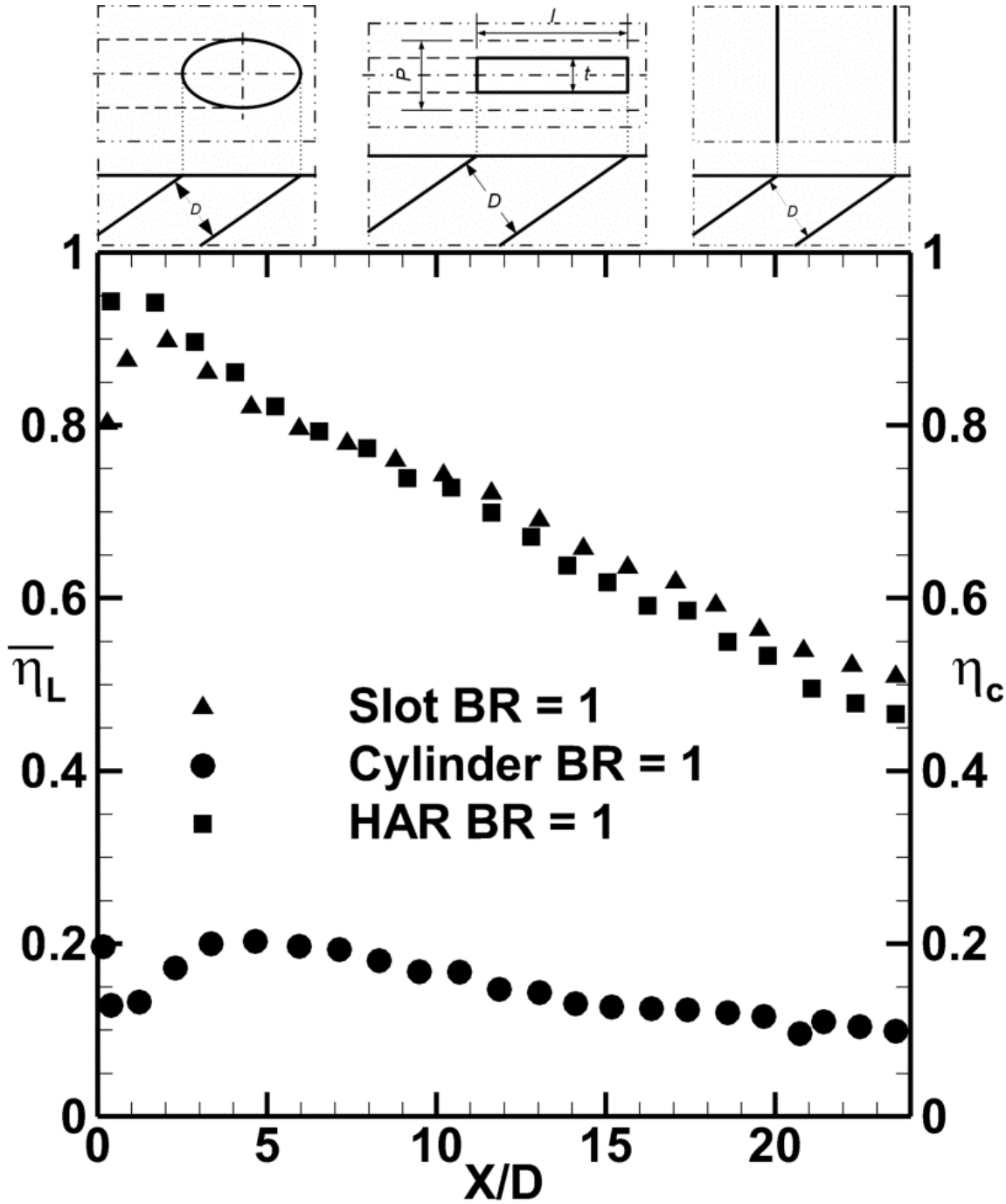

Figure 5.9 Measured HAR performance for the case t = 0.1D and P = 2t at BR = 1 (Cases 3, 6 and 10)

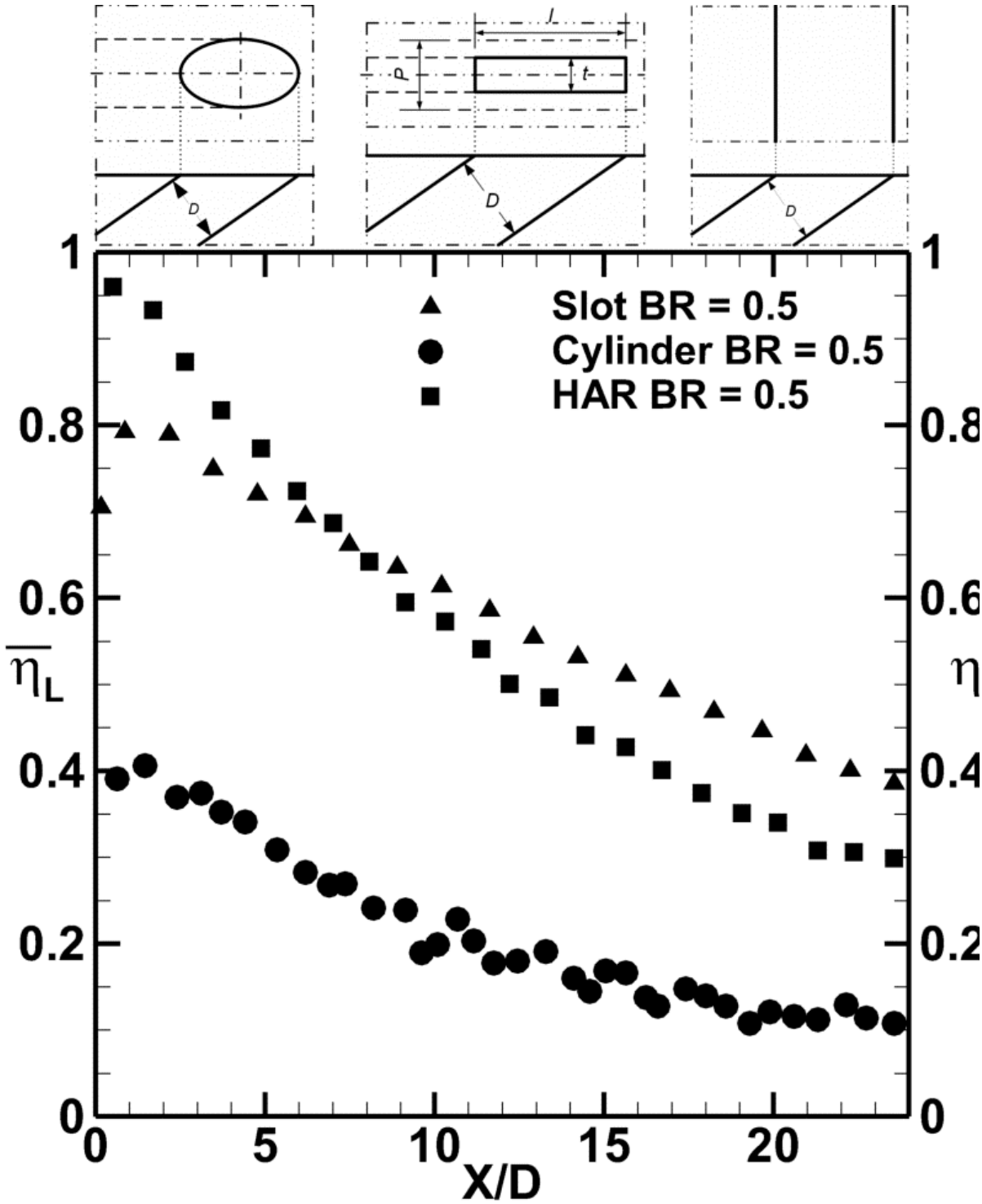

Figure 5.10 Measured HAR performance for the case t = 0.1D and P = 2t at BR = 0.5 (Cases 1, 5 and 9)

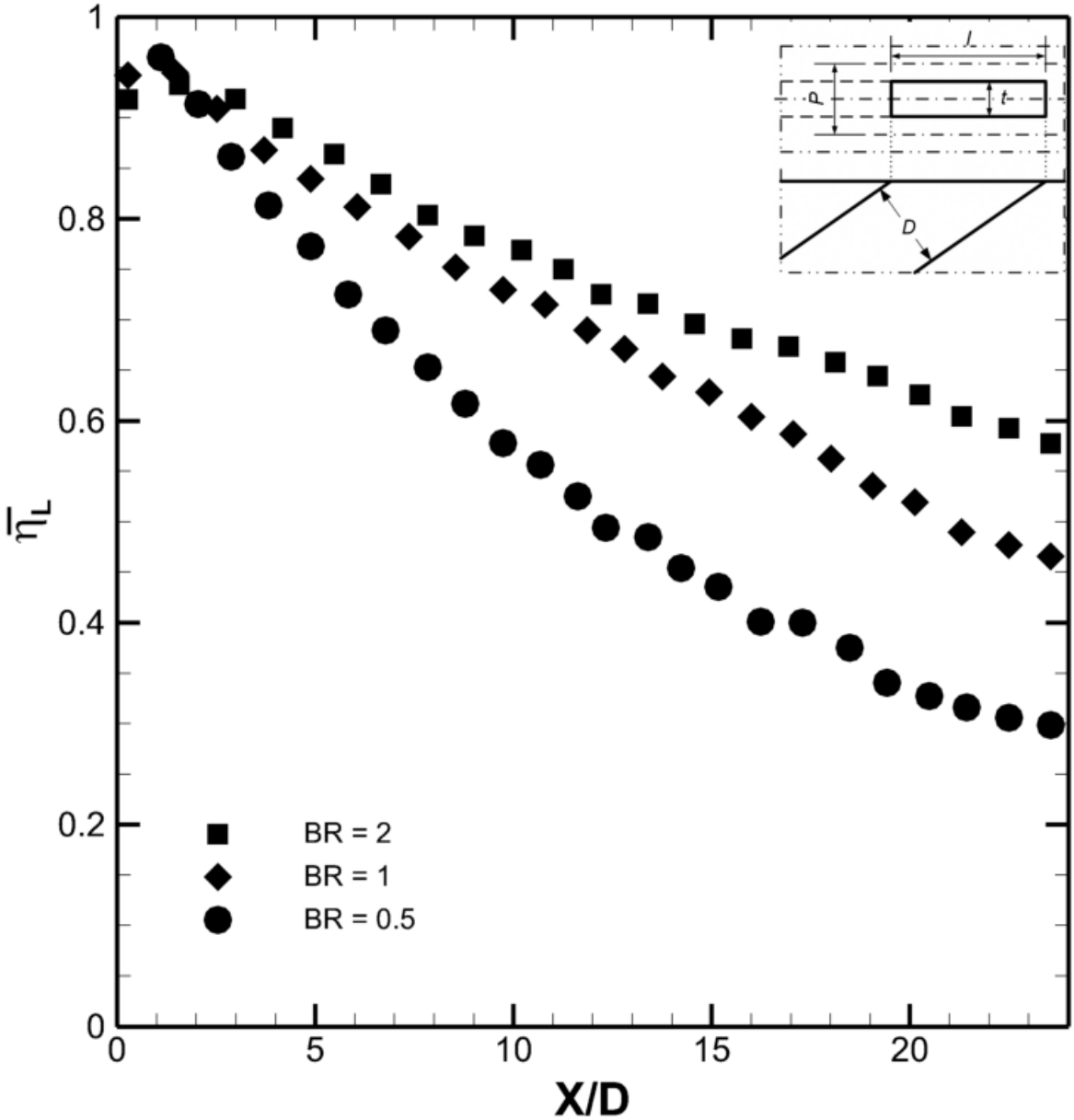

Figure 5.11 Measured HAR performance for the case *t* = 0.1*D* and *P* = 2*t*, (Cases 9-11)

Figure 5.12 and Figure 5.13 show the $\overline{\eta_L}$ of the 2nd HAR tested configuration, of which t = 0.1D and P = 3t, thus for this geometry, the t/P = 1/3, and AR = 17.5. Its $\overline{\eta_L}$ distribution at BR = 1 is shown in Figure 5.12 and compared with the slot and the cylindrical hole. Similar to the slot and the cylindrical hole, the HAR $\overline{\eta_L}$ distribution shows a distinct liftoff-reattachment. It demonstrates much higher values than its t/P = 1/3, and much higher than the cylindrical hole, but lower than the slot.

Figure 5.13 summarizes the HAR performance of this geometry in the tested BR range, and shows the effect of BR. The $\overline{\eta_L}$ of BR=2 case has a clear liftoff-reattachment; it has a trend

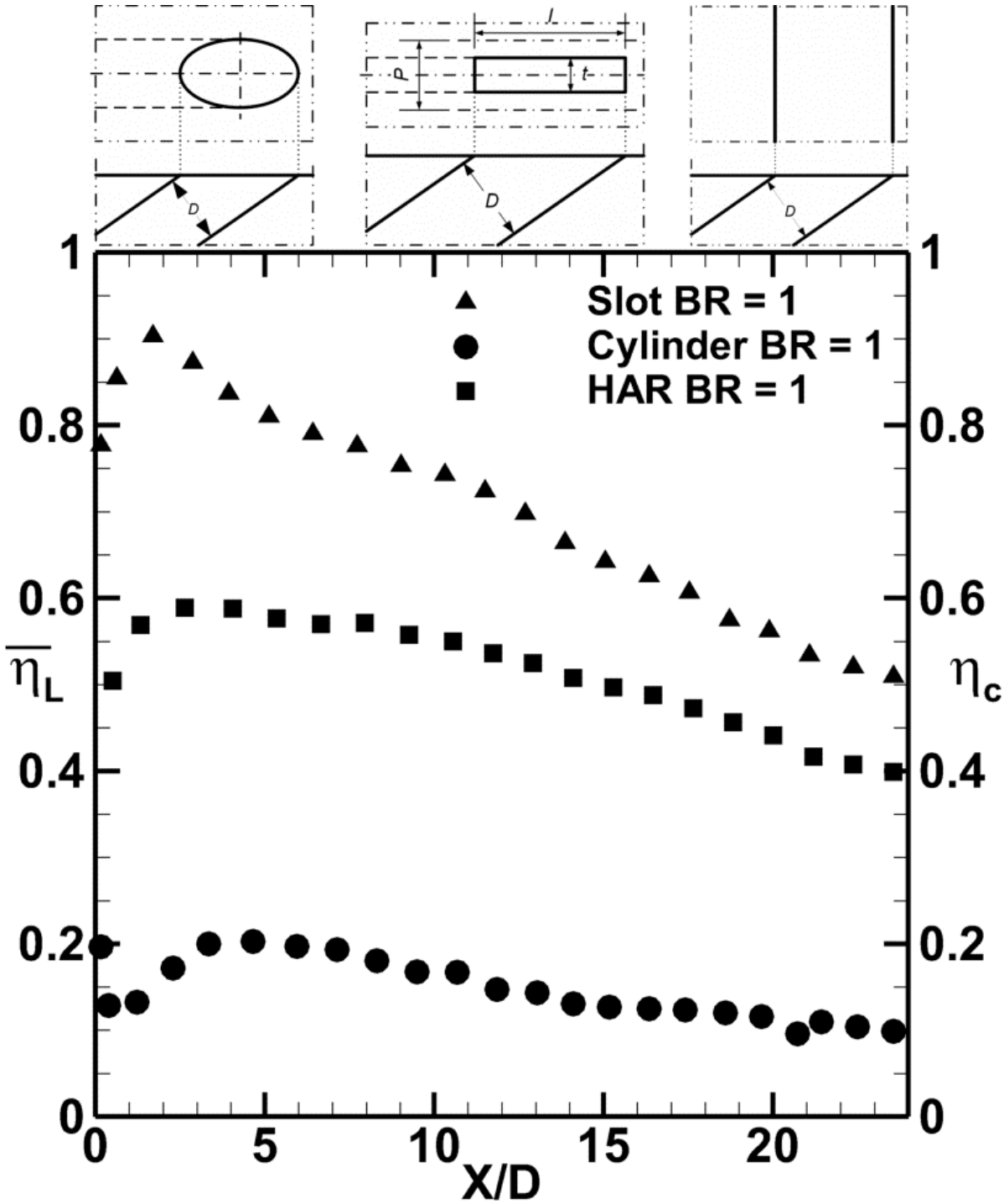

Figure 5.12 Measured HAR performance for the case t = 0.1D and P = 3t at BR = 1, (Cases 3, 6 and 16)

similar to that of BR=1 case, but is superior in value by approximately 0.1. The BR=3 and BR=2 cases show similar trends over the full range of *X/D*. In short, $\overline{\eta_L}$ performance is much more sensitive to BR in the range from 1 to 2, than the range 2 to 3.

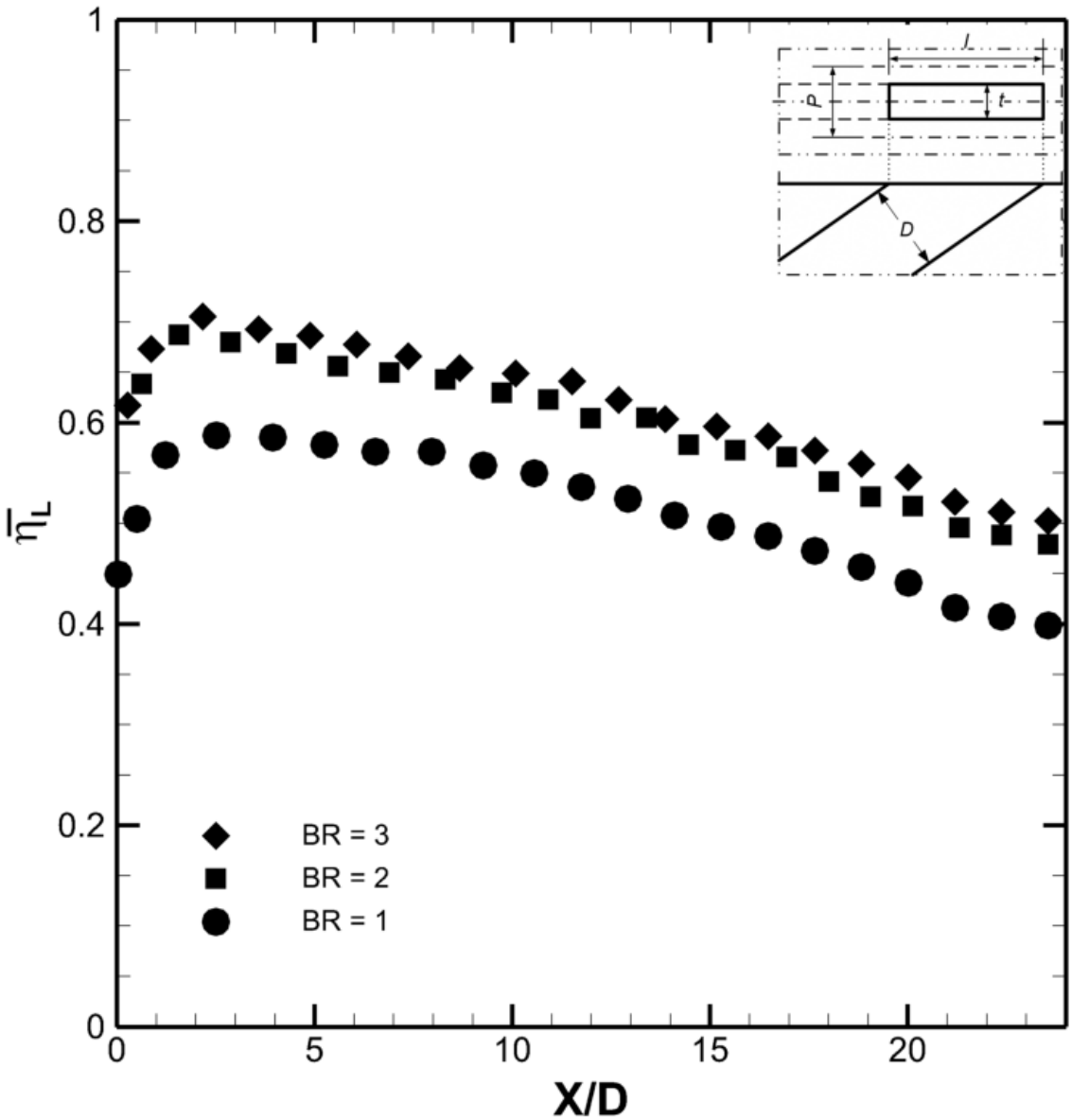

Figure 5.13 Measured HAR performance for the case t = 0.1D and P = 3t, (cases 16-18)

The detailed η distributions of the three cases are selected and shown in Figure 5.14 to Figure 5.16. In the TLC testing, each test took 300 TLC images to record the color varying. The last image was reasonably similar to the η distribution. For this kind of detailed η distribution figures in the present paper, the last image of the test case is attached above the η contour chart. Figure 5.14 shows the detailed η of the 1st geometry at BR = 1. In the TLC image, the blue color denotes high η, the green color denotes the lower η, and the red color denotes the lowest. The lateral row length of the HAR geometries was 12.7D, so there were 64 of this kind of HAR holes. The left side image is the exit trailing edge. In the image, the blue color's lateral span narrows when moving downstream (the right side), indicating a strong end effect. It is common; similar end effect was shown in Bunker [37] (Fig. 6-7, 9-11). Thus, only the central 25% (3D width) have been post-processed in the present investigation, aimed to eliminate the end effect.

This region is marked with dashed lines. The end effect has not been included in the present computations. The η contour chart shows high η values, which are close to 1, in the region immediately downstream of the exit trailing edge, indicates a continuous coolant film has formed, and the coolant has mostly fully expanded. The reattachment in $\overline{\eta_L}$ is smaller than 0.1 (in Figure 5.9). It is not appreciable in this kind of contour charts, so η declines gradually as the flow moves downstream, like the attached flow. Figure 5.15, for the same geometry at BR=0.5, shows similar η distribution, where the highest η locates at the place immediately downstream of the exit trailing edge, then decreases continuously, but at a faster rate. It has been demonstrated that the coolant has mostly fully expanded in this geometry, and high performance has been successfully achieved.

Figure 5.16, which is for the 2nd geometry at BR=1, shows a different η distribution. Its TLC image shows intermittent small green areas at the exit trailing, indicates the mainstream penetrates the coolant film. In other words, the coolant is under expanding, and the continuous coolant film has not yet formed. In the η contour chart, a comparatively low η contour line, which is 0.4, shows close to the exit trailing edge. Then η increases to more than 0.5 as the flow is moving downstream. After that, η declines continuously to the far downstream. It demonstrates a liftoff-reattachment flow, corresponds to the $\overline{\eta_L}$ distribution in Figure 5.13. This geometry has demonstrated the coolant is under expanding, and decreasing *t/P* does not favor the coolant expansion.

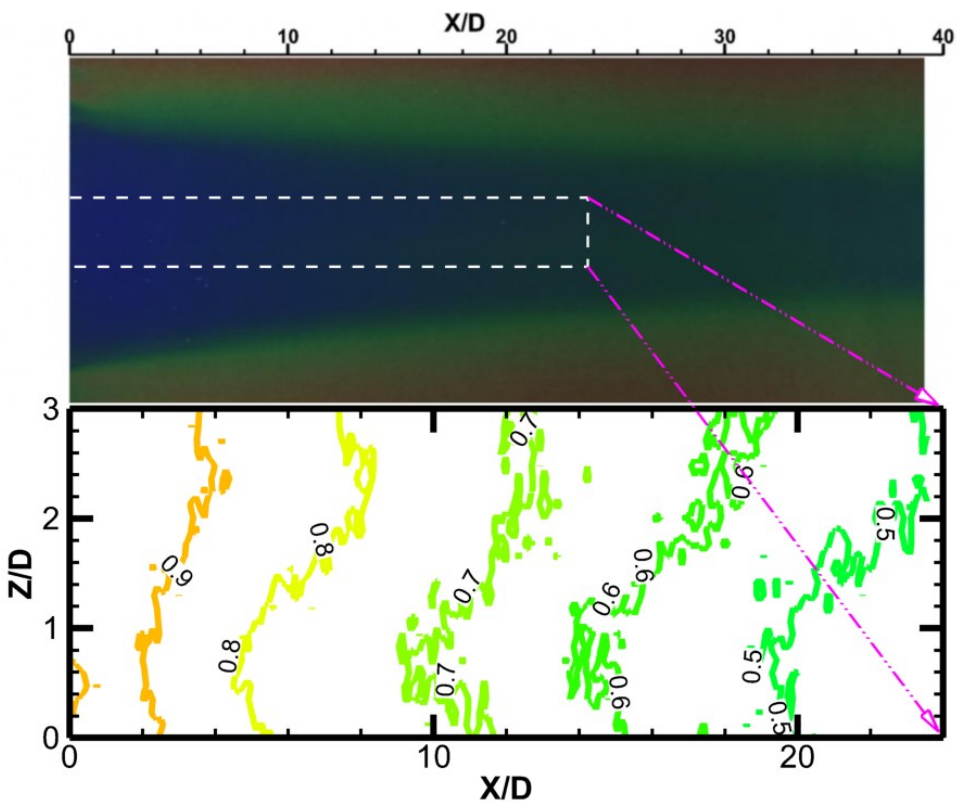

Figure 5.14 η distribution for the case t = 0.1D and P = 2t, at BR = 1 (Case 10)

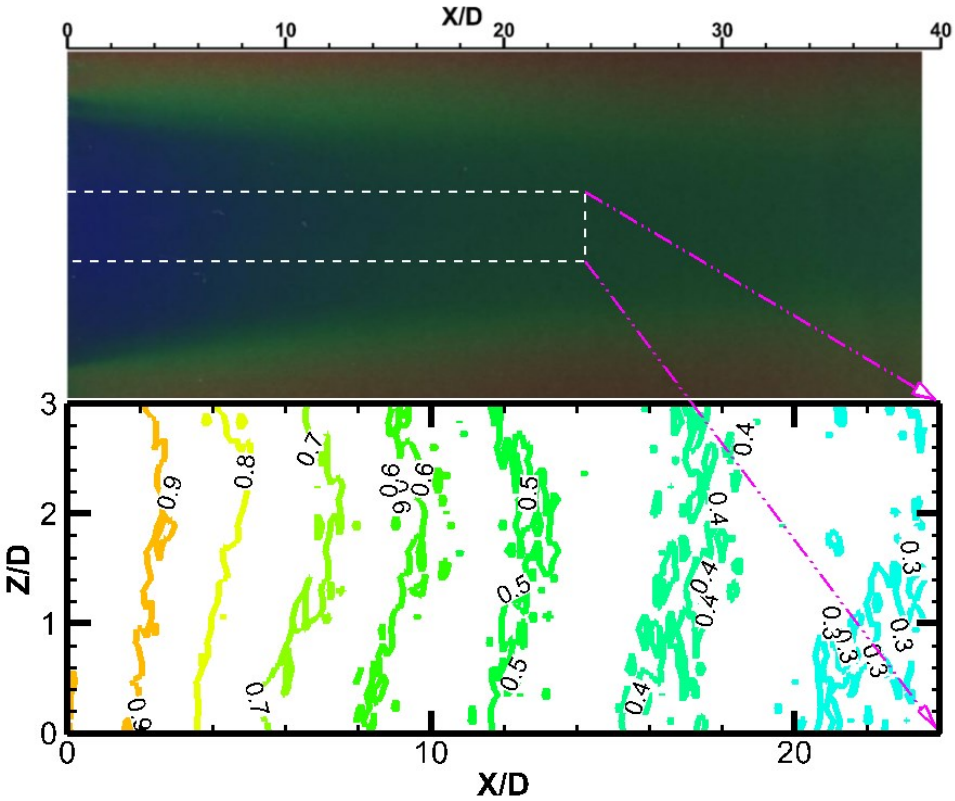

Figure 5.15 η distribution for the case t = 0.1D and P = 2t, at BR = 0.5 (Case 9)

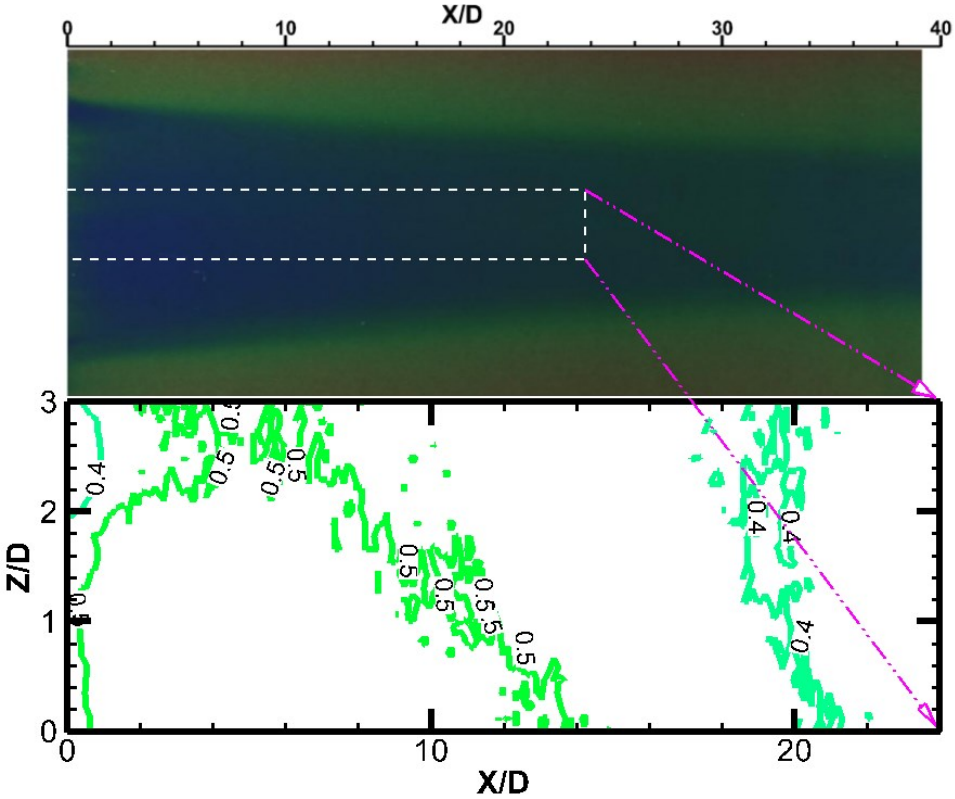

Figure 5.16 The η distribution of the case t = 0.1D and P = 3t, at BR = 1 (Case 16)

5.3.3 Assessment of the Computational Results

The present computations were assessed with the published data of traditional geometries, namely the cylindrical hole and the slot. Figure 5.17 compares the experimental and computational results for the cylindrical hole. The experimental data match very well and the computations show excellent agreement; however, the computational results over-predict the measurements. It is mainly because of the DR difference, which is 1 in the experiment, and 2 in the simulations. This geometry has been known to be sensitive to DR. Generally, the computations are deemed to qualitatively agree with the measurements.

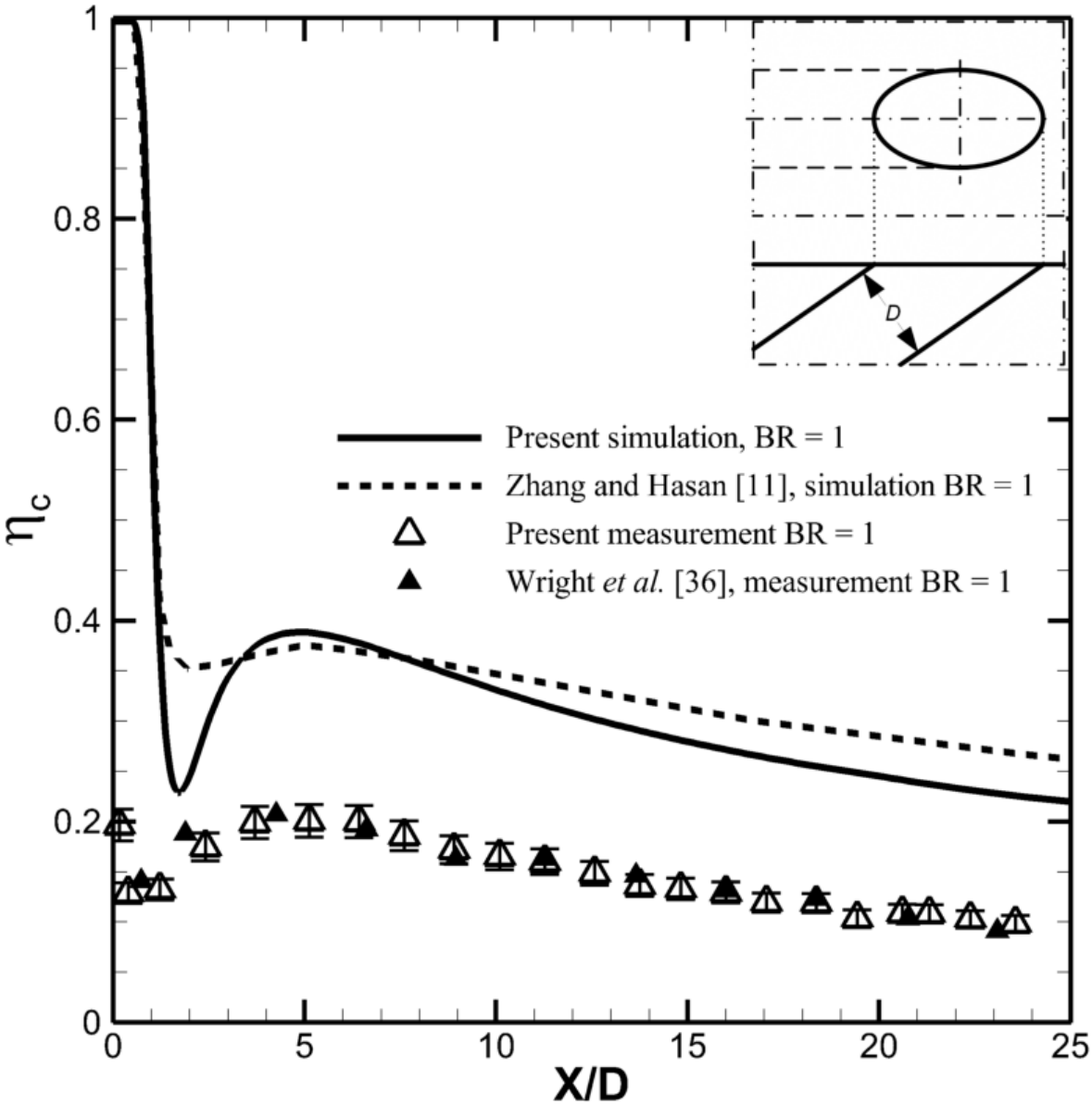

Figure 5.17 Comparison of cylindrical hole results at BR = 1 (Cases 3 and 4 with [10, 48])

Figure 5.18 compares the current experimental and computational slot results at BR = 0.5, with data published in Jia *et al.* [57] and Farmer *et al*. [70], which presented a slot simulation at an inclined angle of 30°, which is smaller than the present angle that is 35°. Both measurement and simulation show perfect agreement with those available in the open literature [57, 70]. However, there is a slight discrepancy between the simulations and the measurements, perhaps due to the simulations' limitation, which cannot capture the reattachment in the measurements. Similar to this relatively low BR case, comparisons of higher BR values showed similar behavior. The measurement and the simulation agree well with the published data, but the simulations do not capture the reattachment observed in the measurements, and over-predict the measurements. The main reason being the end effect, the simulations did not include the end effect, which was strong in the experiments. Similarly, the simulations are deemed to

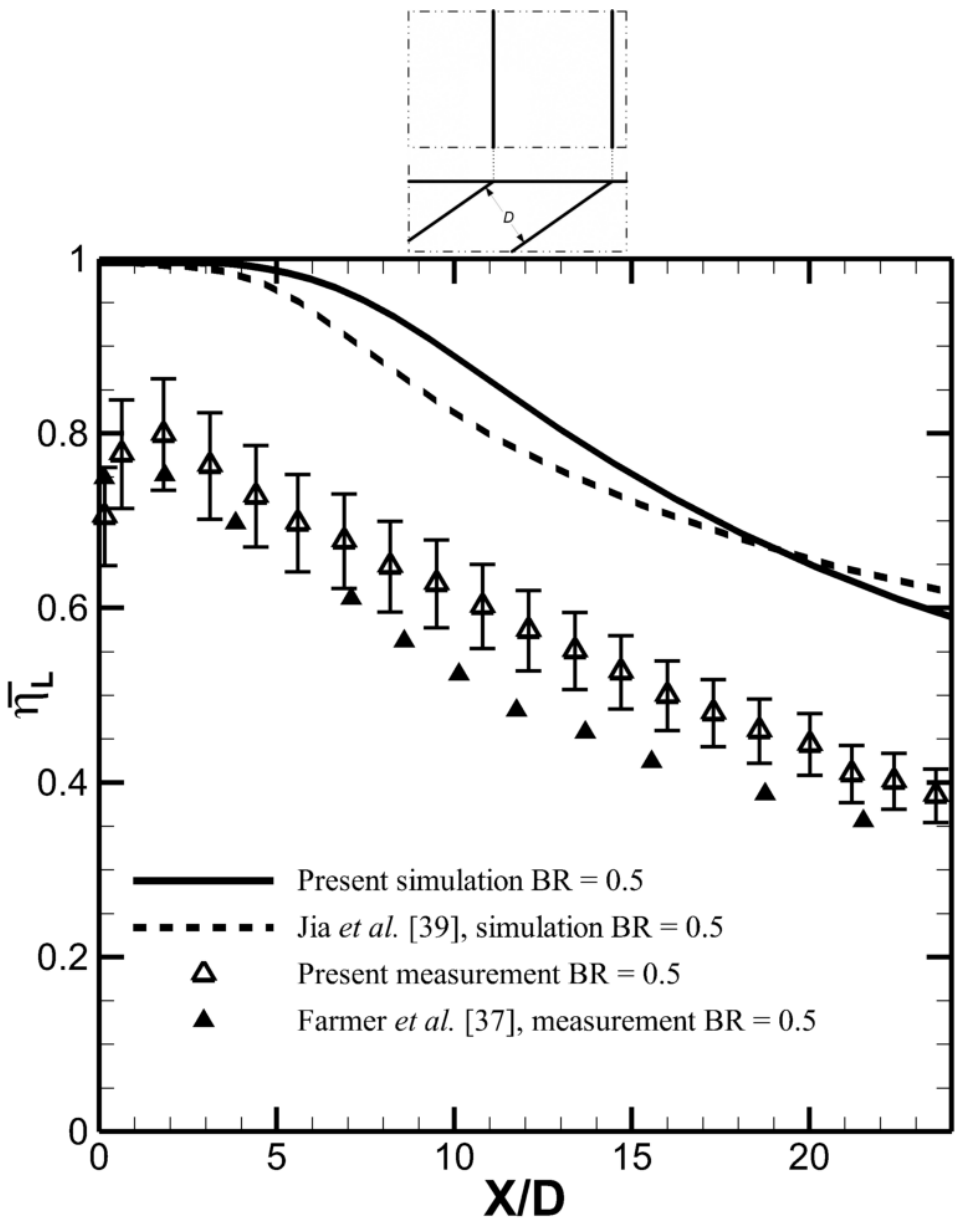

Figure 5.18 Comparison of slot results at BR = 0.5 (Cases 5 and 8 with [37, 39])

qualitatively agree with the measurements.

The experimental results given above provide a good support to use the experimental set up in assessing the computational results obtained for the HAR configurations, see Figure 5.19 and Figure 5.20. Figure 5.19 shows comparison for the HAR configuration of $t = 0.1D$, $P = 2t$ at BR = 0.5. In the region immediately downstream of the exit, where $\overline{\eta_L}$ is much higher than t/P, the computation shows a slightly bigger liftoff-reattachment region. Apart from that, the computation agrees well with the measurement. Figure 5.20 shows a comparison for the HAR configuration

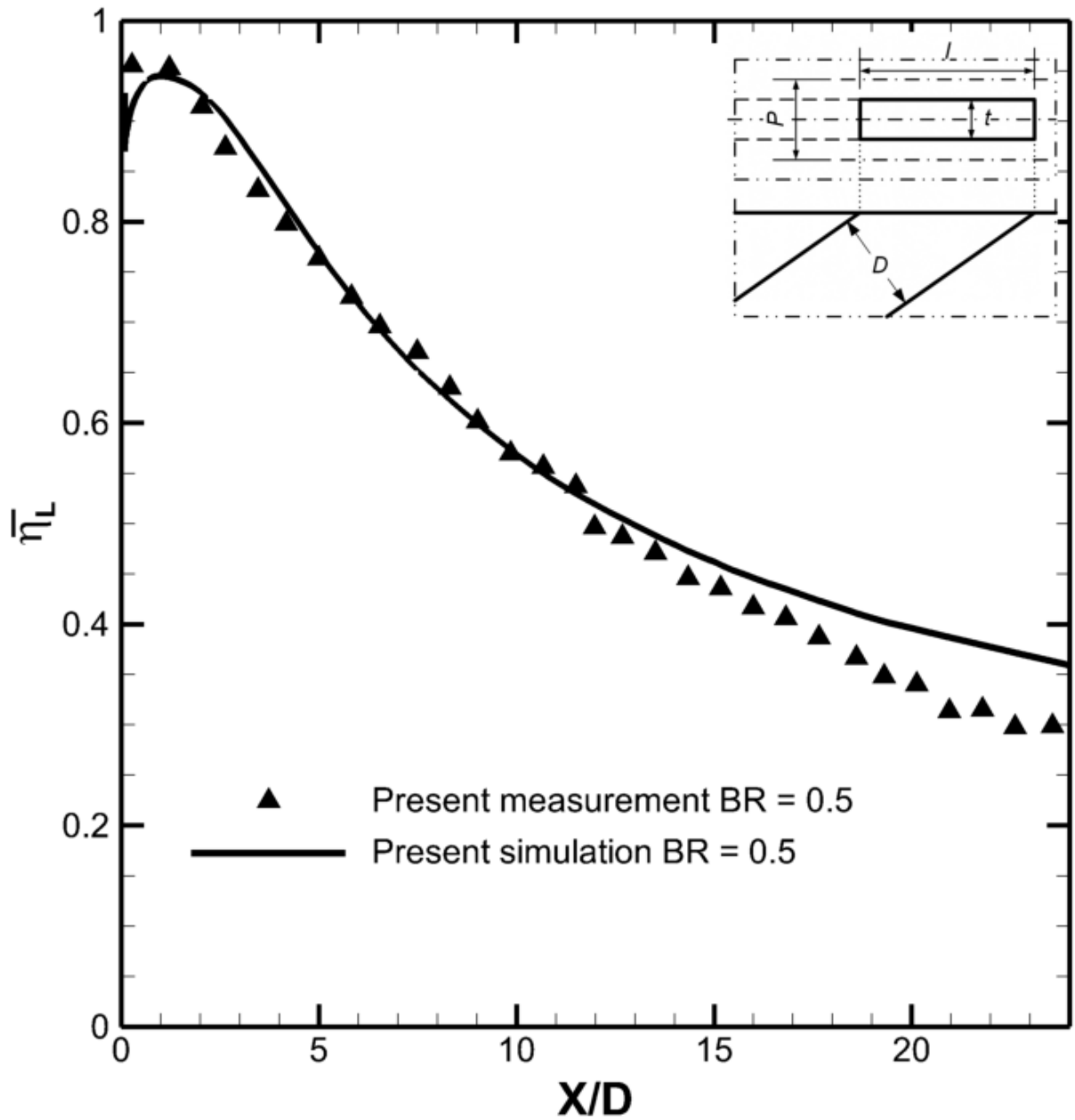

Figure 5.19 Comparison of measured with numerical results for the case of $t = 0.1D$ & $P = 2t$ (Cases 9 & 12)

for t = 0.1D, P = 3t at BR = 1. The simulation predicts approximately 0.15 higher than the measurement in the region immediately downstream of the exit. The over-prediction continuously decreases to approximately 0.05 as the flow moves downstream.

In the cases of higher BR values for these two configurations, the computations capture accurately the liftoff-reattachments but over-predict the measurements further downstream. The discrepancy mainly relates to the DR difference. In general, the computations show acceptable agreement. Hence the numerical results were deemed reliable. The following analysis is mostly based on the computational results.

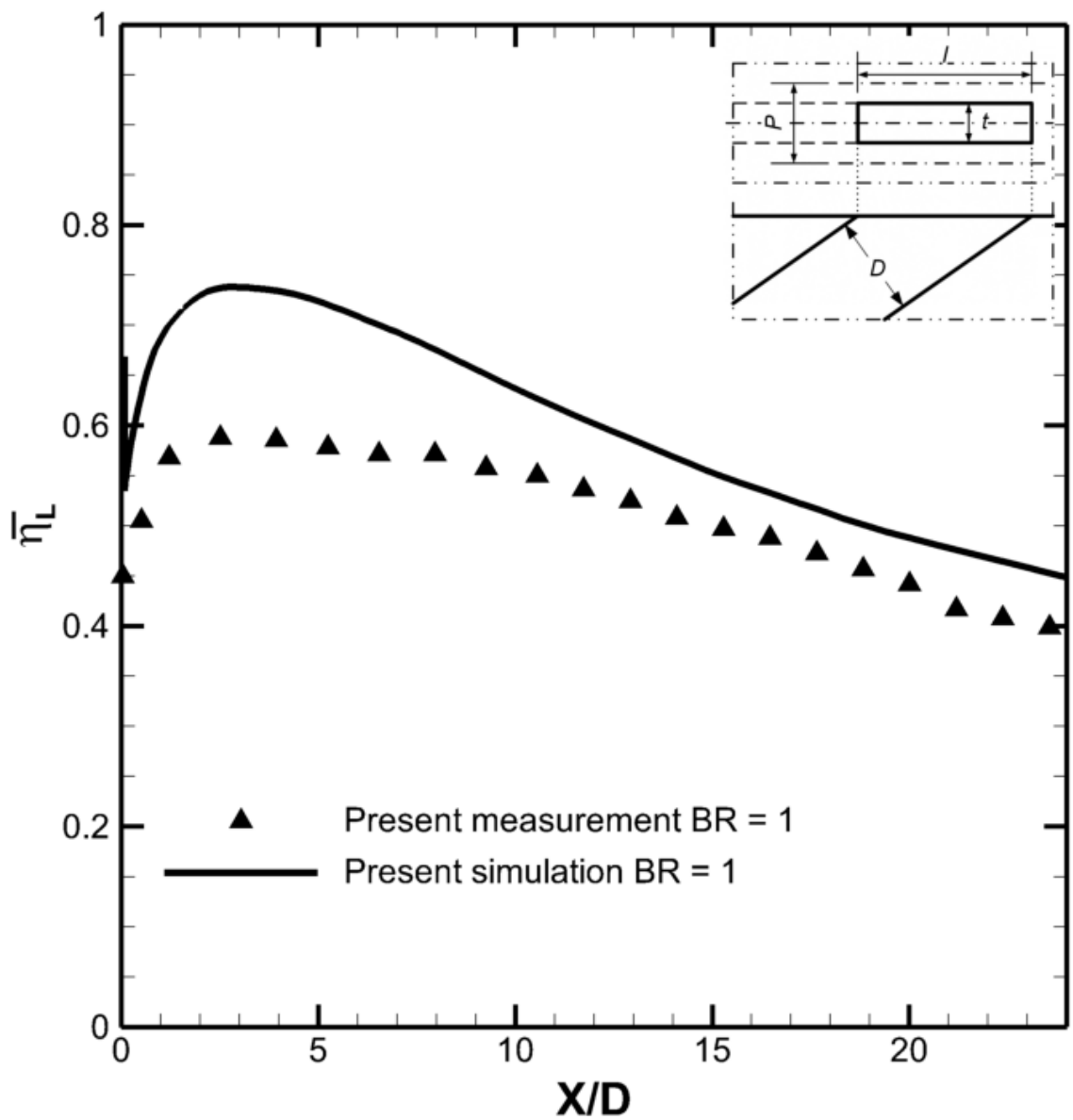

Figure 5.20 Comparison of numerical & measured results for the case of t = 0.1D & P = 3t (Cases 16 & 19)

The BR effect on $\overline{\eta_L}$ of the numerical results are identical to the measurements: the BR demonstrated negligible impact on the region immediately downstream of the exit; and showed evident effect on the $\overline{\eta_L}$ decrease rate as moving downstream, which is more clear at small BR value, but reduced at high BR. In general, the BR = 2 case of each geometry shows the typical high performance. It is used in the following investigations.

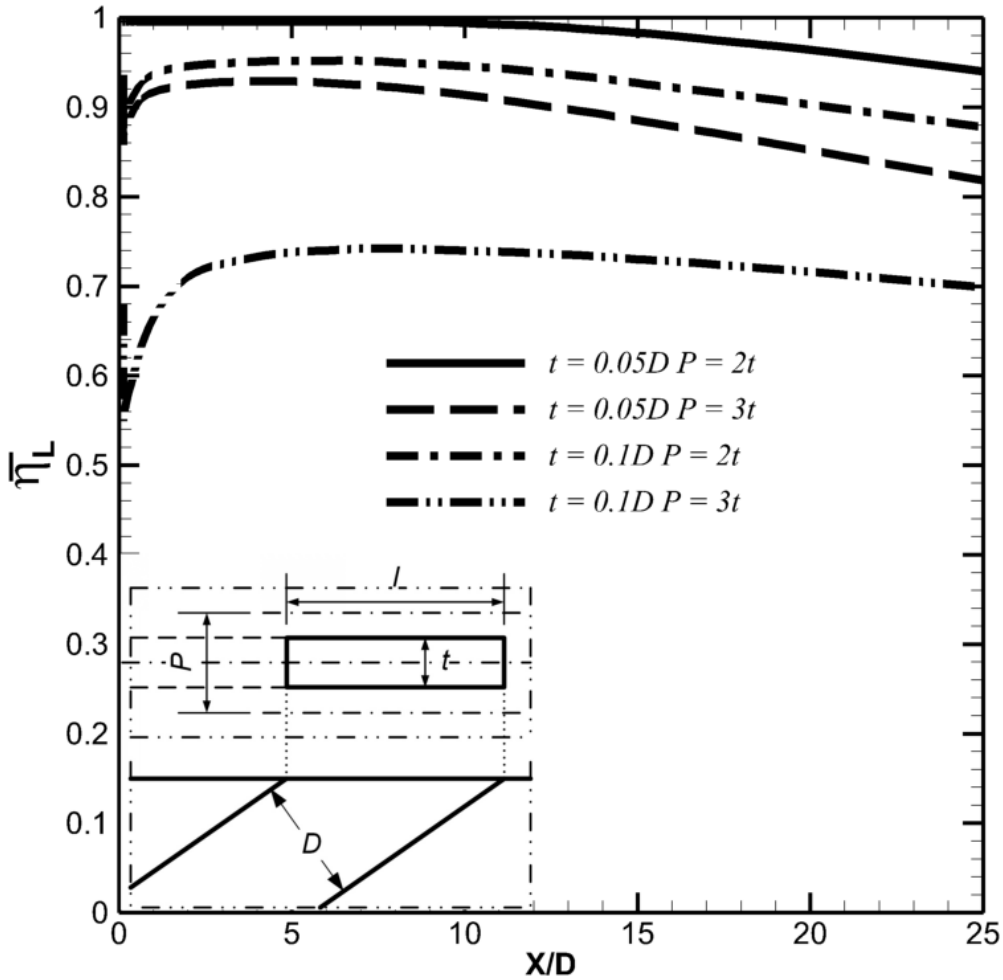

Figure 5.21 The HAR performance at BR = 2 (cases 14, 20, 23, 26)

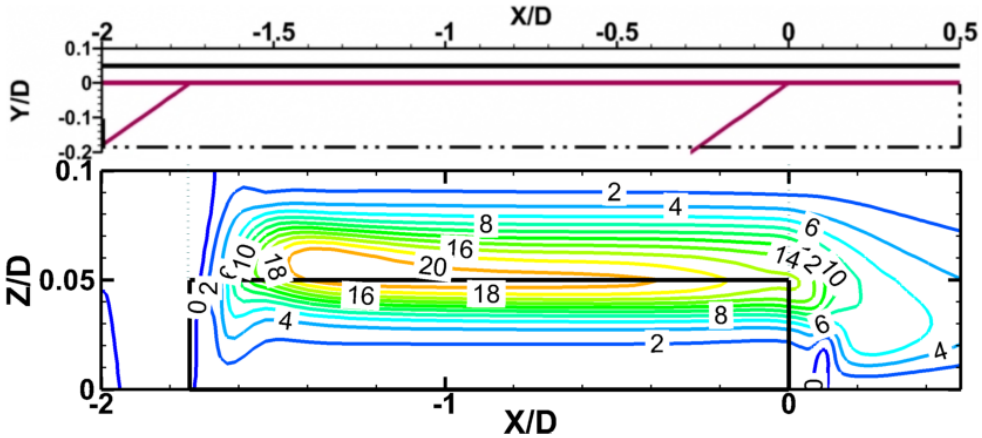

a) $t = 0.1D$ and $P = 2t$ at BR = 2 (Case 14)

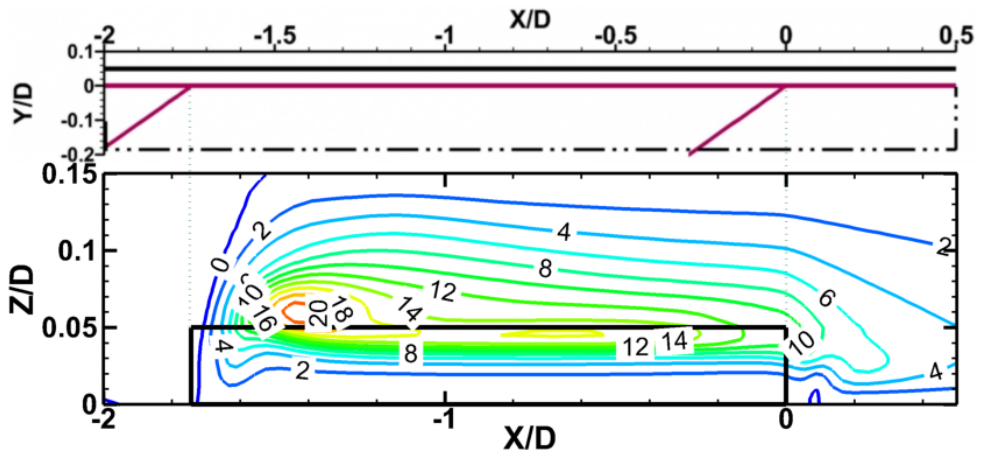

b) $t = 0.1D$ and $P = 3t$ at BR = 2 (Case 20)

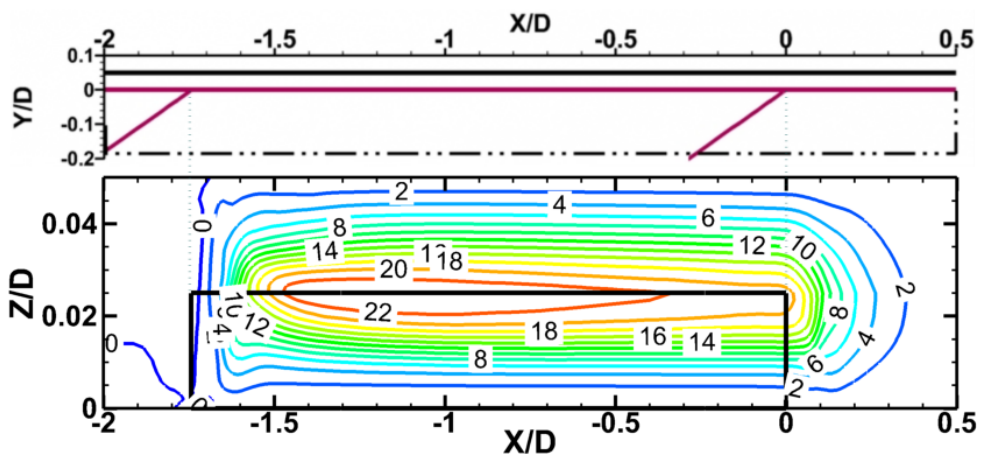

c) $t = 0.05D$ and $P = 2t$ at BR = 2 (Case 23)

Figure 5.22 ω_x contours at the exit plane

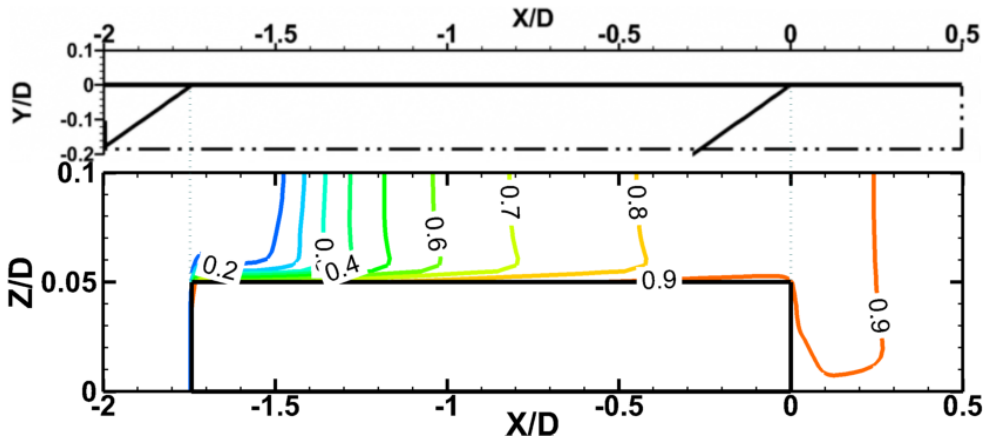

a) $t = 0.1D$ and $P = 2t$ at BR = 2 (Case 14)

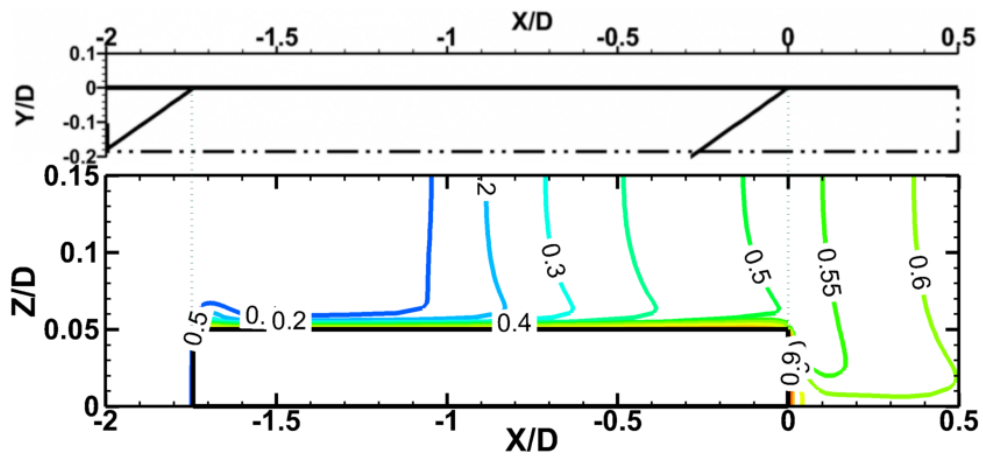

b) $t = 0.1D$ and $P = 3t$ at BR = 2 (Case 20)

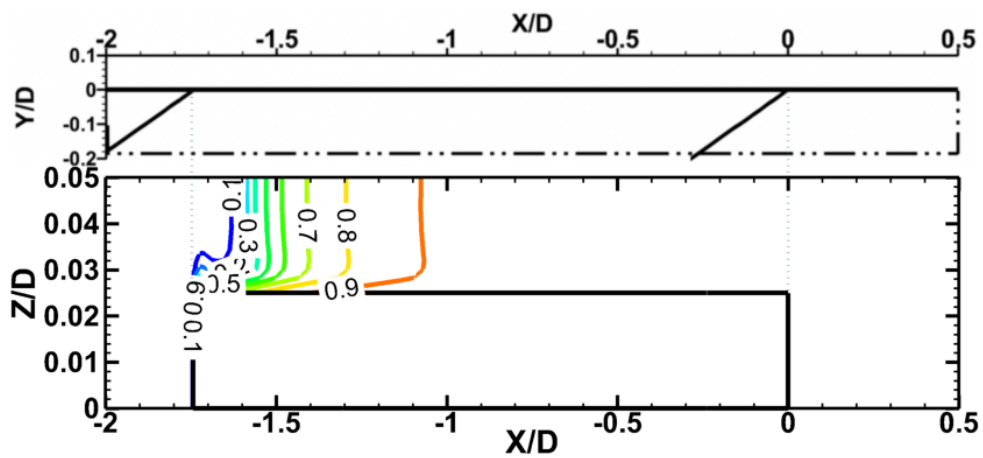

c) $t = 0.05D$ and $P = 2t$ at BR = 2 (Case 23)

Figure 5.23 η contours at the exit plane

5.3.4 HAR Performance

The AR=17.5 in the two HAR mentioned above geometries. Their $\overline{\eta_L}$ distributions were much higher than *t/P*, indicated the strong coolant expansion. However, $\overline{\eta_L}$ was shown to be less than 1, and showed liftoff-reattachment. That indicates that the coolant expansion is incomplete. Hence two HAR geometries, of which AR = 35, have been investigated numerically.

Figure 5.21 shows the $\overline{\eta_L}$ distributions for the four configurations at BR = 2, of which t = 0.05D and 0.1D, P = 2t and 3t. The configuration of t = 0.05D and P = 2t shows perfect performance where $\overline{\eta_L}$ starts at 1. In fact, if we look closely, a tiny liftoff-reattachment immediately downstream of the exit is present. However, for values larger than 0.98, it is deemed to be approximately equal to 1. This liftoff-reattachment is neglected, and the coolant expansion in this geometry is deemed to be complete.

The remaining three cases in this figure shows clearly liftoff-reattachment. The cases where t = 0.05D & P = 3t, and t = 0.1D & P = 2t, show similar performance, and the case where t = 0.1D and P = 3t gives the lowest values of $\overline{\eta_L}$. They indicated their coolant expansions at varying levels, but not completely. Moreover, higher AR (i.e. *t/P*) improves the performance.

5.3.5 Details of ω_x and η near the Hole Exit

According to the previous research results based on the conventional geometries, the potential maximum $\overline{\eta_L}$ is *t/P*, and the increase in CRVP intensity reduces η drastically. The HAR scheme has demonstrated its maximal $\overline{\eta_L}$ at a value much higher than *t/P*. Figure 5.22 shows the CRVP intensity around the exit of the HAR geometries. Three cases, for which BR=2, were selected as samples. The ω_x contour lines on a plane of Y/D = 0.05 are visualized and demonstrate similar distributions, see Figure 5.22. The local peaks are located right above the exit's lateral edges and the highest ω_x value for the three sample cases seen in Figure 5.22(a), (b), and (c) to be 20, 20, and 22. All three cases show a strong CRVP intensity. The geometry in Figure 5.22(c), which has the strongest ω_x, also possesses the best performance. It has been clearly demonstrated that the CRVP does not decrease the HAR performance scheme.

In the conventional geometries, in which AR < 2, the CRVP appears to be mainstream entrainment only. Hence only CRVP decreasing η is observed. The present new scheme has prolonged the longitudinal length of the exit to exploit the coolant expansion. The configuration of t = 0.05D and P = 2t, of which the AR has been extended to 35, has shown a full expansion.

Detailed η distributions of the same cases are shown in Figure 5.23. For the geometry in Figure 5.23 (a), AR = 17, and *t/P* =1/2. The η contour line of 0.1 located at approximate X/D = -1.5, denotes the expansion starts affecting η, where upstream is deemed to be dominated by mainstream. This position is 2.4t downstream of the exit leading edge, larger than the longitudinal dimension of a conventional geometry, of which AR is usually less than 2. Hence the previous research on the conventional geometries would not observe the expansion. The coolant expands continuously as moving downstream. At the position of X/D = 0, where the coolant supply is deemed to be stopped, the η is still a little bit lower than 0.9, denotes the coolant is very close to but not yet fully expanded.

Figure 5.23 (b) shows a geometry of AR = 17.5 and *t/P* =1/3, of which the η contour line of 0.1 locates at approximate X/D = -1.05, approximate 7t downstream of the exit leading edge. At X/D = 0, η is 0.5, denotes the coolant expansion is not fully completed yet. Figure 5.23 (c) shows

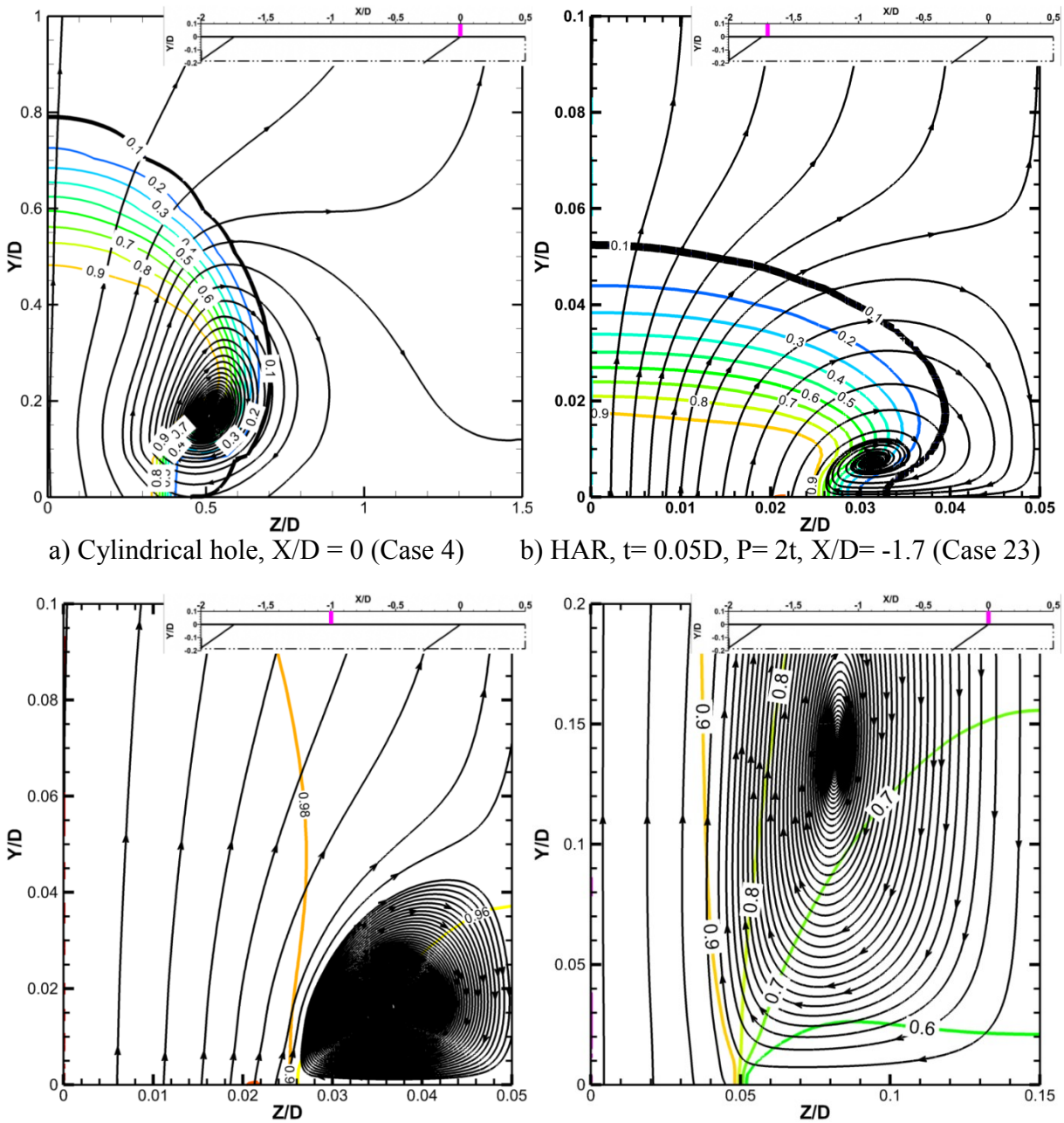

a) Cylindrical hole, X/D = 0 (Case 4) b) HAR, t= 0.05D, P= 2t, X/D= -1.7 (Case 23)

c) HAR, t = 0.05D and P = 2t, X/D = -1 (Case 23) d) HAR, t = 0.1D, P = 3t, X/D= 0 (Case 20)

Figure 5.24 CRVP and expansion

a geometry of AR = 35 and *t/P* =1/2. The coolant expansion starts to be visible at approximate X/D = -1.64, approximate 2*t* downstream of the exit leading edge. The η contour line of 0.9 locates at approximate X/D = -1.05, approximate 14*t* downstream of the exit leading edge. It denotes the coolant is fully expanded. Figure 5.23 also demonstrates that increase in AR or *t/P* is in favor of the coolant expansion.

5.3.6 CRVP and the Coolant Expansion

Figure 5.24 further illustrates the coolant expansion on the Y-Z planes. Surface streamlines were used to visualize the CRVP. Three cases, cases 4, 20 and 23, were selected as samples for comparison purposes. Case 4 is that of a cylindrical hole, the typical conventional geometry.

Figure 5.24 (a) shows its plane at $X/D = 0$, where is $1.74D$ downstream of the leading edge. The θ-contours indicate the mainstream-coolant interface. The CRVP is strong and is located right on the mainstream-coolant interface. The bold contour line of θ=0.1 denotes its right side is dominated by the mainstream. No coolant expansion is observed, and the coolant supply is deemed to be stopped downstream of this position.

Case 23 is the HAR configuration of $t = 0.1D$ and $P = 2t$, the typical case with high performance. Figure 5.24 (b) shows the plane at $X/D = -1.7$, approximately a distance t downstream of the leading edge. Similar to Figure 5.24 (a), CRVP is strong and is located right on the mainstream/coolant interface. The right side of the bold contour line is dominated by the mainstream, and no clear coolant expansion is observed. However, the coolant keeps supplying, and the coolant expansion is continuing. Moving downstream to $X/D = -1$, Figure 5.24 (c) shows the plane $15t$ downstream of the leading edge. CRVP is also strong. As the θ-contour line of 0.9 is not in the figure range, two contour lines of $\theta = 0.96$ and 0.98 were added to denote the coolant has dominated the whole range, the coolant expansion is fully complete.

Case 20 is the HAR configuration of $t = 0.1D$ and $P = 3t$, the typical case with low performance. Figure 5.24 (c) shows the plane at $X/D = 0$, which is located at $17t$ downstream of the leading edge. The CRVP is also strong. The coolant dominates the region of $Z/D < 0.05$, but they are still mainstream-coolant mixture at $Z/D > 0.05$. The coolant supply is deemed to be stopped downstream of this position, hence the coolant expansion is not fully completed. It demonstrated that the longitudinal dimension has to be extended enough to cause the coolant to fully expand.

5.4 Conclusions

Along the previous discovery of the relations between the CRVP and η, a mechanism of film cooling heat transfer has been proposed. The coolant expansion in this mechanism has been exploited by developing a new film cooling scheme named HAR configuration. The new scheme features high AR values namely 17.5 and 35 in the present investigations.

The HAR configuration has been investigated experimentally and numerically. The transient TLC technique was used in the experiments, and the simulation of the steady RANS equations coupled with the RKE turbulence model was performed. They have been rigorously assessed and proven to be reliable. Both experimental and numerical results demonstrated the high performance of the HAR scheme. Some of them have achieved the so-called perfect performance. A characteristic of the HAR performance is much higher than their t/P values, which are thought of as the maximum of the conventional geometries.

Further analysis has demonstrated that a strong CRVP accompanies the HAR configuration scheme. It shows that the CRVP does not decrease η in HAR scheme. In the traditional film cooling geometries research, the mainstream entrainment was emphasized. The action of the coolant expansion on η has never been observed. It led to the conclusion that CRVP is destructive to η, until the current HAR scheme debut.

In addition, the analysis has demonstrated that, in a traditional geometry, where AR < 2, the coolant stops supply before the coolant expansion affects η. By contrast, in the HAR scheme, which has high AR values, the action of the coolant expansion on η is visible in a place enough downstream of the exit leading edge, develops further downstream, then fully expands further downstream, before the coolant supply stops.

The previous research results on the discrete film cooling geometry have shown that *t/P* is the outmost position for the mainstream-coolant interface. When highlighting the mainstream entrainment, the interface is pushed inwards, appears as the $\overline{\eta_L}$ less than *t/P*. The HAR performance much higher than *t/P* under high CRVP intensity indicated the strong coolant expansion. Also, it presented a solid proof of the proposed mechanism of the film cooling heat transfer, built a solid base for further research on the film cooling geometry.

Chapter 6 Conclusions

6.1 A Summary

This research presented a new film cooling heat transfer mechanism. Accordingly, two new film cooling schemes with so-called 'perfect performance' have been developed by applying the new mechanism. The thesis is composed mostly of four papers. The first paper performed a detailed investigation on CRVP. Its results led to the new film cooling heat transfer mechanism, in which two kinds of secondary flows were highlighted. Based on them, two new film cooling schemes, namely the comb scheme and the HAR scheme, were designed, each scheme for one kind of secondary flow, respectively. These two schemes were investigated experimentally and numerically in the remaining three papers. The second paper measured the film cooling effectiveness of the new schemes. The third and fourth papers performed detailed investigations on the comb scheme and the HAR scheme, respectively. The success of the new film cooling schemes presented convinced support to the film cooling heat transfer mechanism.

The first paper performed detailed investigations on CRVP. The main challenge in film cooling research had been the vagueness in film cooling heat transfer mechanism. Motivated by the discovery of the CRVP effect on η, a further investigation has been performed on this flow structure. Taking advantage of CFD, the boundary layer effect on different positions was isolated, and the vortical structures near the cooling hole were visualized. In addition to showing the effect of the CRVP intensity on the liftoff-reattachment phenomenon, the most important result is that the source of this flow structure has been related to the velocity gradients in mainstream-coolant shear layer, particularly in the film cooling flow, it is the gradient of the vertical velocity at lateral direction.

Combining the crucial effect of the CRVP intensity on η and the results in the first paper, a film cooling heat transfer mechanism was identified. In film cooling flow, strong velocity gradients in the mainstream-coolant shear layer produce secondary flows. Some secondary flows penetrate the mainstream-coolant interface, turn into advection. As advection had been found to be the main manner in film cooling heat transfer, these secondary flows dominate the film cooling heat transfer. They were classified into mainstream entrainment and coolant expansion. The mainstream entrainment results in decaying η, which is the only CRVP effect mentioned in the previous film cooling research. By contrast, the coolant expansion is likely to improve η. To the best of my knowledge, the favorable effect of the coolant expansion on η has been discovered for the first time. The new mechanism clearly indicated the direction of developing high performance film cooling schemes.

Two film cooling schemes, named comb scheme and HAR scheme, have been developed according to two kinds of advections in the new mechanism. Each scheme was aimed at one kind of advection, respectively. The comb scheme was aimed to eliminate the mainstream entrainment by moving the CRVP away from the mainstream-coolant interface, while the HAR scheme was aimed to exploit the coolant expansion by prolonging the coolant supply. The first motivation of developing these schemes was to indicate an application of the new mechanism.

They were investigated numerically and experimentally. The experimental investigations were performed in a wind tunnel with transient TLC technique for measuring η. The facility has been well validated, and at least three Ph. D. theses were accomplished directly based on its outputs. The averaged uncertainty in η is ±8%. The present research mainly updated its test section, including a set of test modules and using a lower conductivity material (XPS) for the test

plate. The facility has been double confirmed by the high agreement between the present measurements and the open published data. The numerical investigations performed steady RANS simulation coupled with the RKE turbulence model. A row of cylindrical holes, slot and the new schemes in varied geometrical parameters, more than 20 configurations were simulated at BR ranged 0.5 – 4. In addition to the comparison with open published data on cylindrical hole and slot, the simulation was validated by comparison with the present measurements on the new scheme configurations.

The second paper described the measurements of the present research. Eight test modules, including a simple slot, a row of cylindrical holes and 6 new scheme configurations, have been manufactured and tested at BR ranging between 0.17 – 4. The high performance of the new schemes was demonstrated with the experimental results. For the comb scheme, the high performance, which is comparable to the slot, implied that its flow uniformity would be similar to the slot, and the mainstream entrainment has been eliminated. For the HAR scheme, its performance was much higher than their *t/P* values that had been considered as the maximum η in traditional discrete geometry, implied that the coolant expansion is strongly taking effect. Both of the new schemes matched the design on applying the film cooling heat transfer mechanism.

The third paper described the comb scheme in detail. This scheme was aimed to eliminate the mainstream entrainment by moving CRVP into the interior of the coolant. Its so-called 'ideal performance' has been demonstrated, while its mechanical integrity is practical. The further geometric parameter investigations showed relations among CRVP, its impact on the mainstream-coolant interface and η. As adjusting the geometric parameters, H (depth of the blind slot) in particular, the CRVP was moving away from the mainstream-coolant interface. Reverse trends between the CRVP effect on mainstream-coolant interface and η have been revealed. When CRVP was entirely trapped by the blind slot, its impact on the mainstream-coolant interface was negligible, a continuous coolant film was formed at least on the blind slot trailing edge, and the high performance was obtained. The flow behavior of this new scheme matched the initial design on applying the heat transfer mechanism.

The fourth paper described the HAR scheme in detail. This scheme was aimed to exploit the coolant expansion by prolonging the coolant supply. Its geometry was identical to a conventional discrete geometry except its high AR values. AR is the characteristic parameter of this new scheme. Its high performance has been demonstrated. Its $\overline{\eta_L}$ was much higher than the t/P value that had been considered as the maximum performance in previous research. The coolant expansion has been observed starting at AR value higher than traditional geometries. As the configuration of the new scheme has higher AR value, its performance increased. In the configurations with high AR values, the coolant dominated entire lateral space, including the space between exits, and formed a continuous coolant film. The so-called 'ideal performance' has also been obtained. Moreover, no matter what AR and η value, this scheme had fairly strong CRVP. It has manifested that CRVP in HAR scheme doesn't decrease η. Ultimately; the flow behavior of the HAR scheme also matched the initial design on applying the heat transfer mechanism.

One main objective of developing these two new schemes was to present examples for the application of the new film cooling heat transfer mechanism. To highlight the effect of the secondary flows, their geometries have been simplified rather than optimized. Even so, the so-called 'ideal performance' was obtained by the new schemes. The successful achievement

convincingly support the new mechanism. The clarification of the film cooling heat transfer mechanism would solve the chronic challenge, and established a solid base for the film cooling research.

6.2 Contributions

The current research presented a new film cooling heat transfer mechanism. Many factors on η or film cooling heat transfer were investigated, but no systematic explanation was proposed. The new scheme in current research shows some secondary flows are the main approach in film cooling heat transfer. Their source and their impacts on η have been analyzed. The coolant expansion, in particular, has been discovered for the first time.

Two new film cooling schemes have been developed according to the new mechanism. The high performance of the new schemes has been demonstrated, and the so-called ideal performance has been achieved for the first time. Directions for the future research on film cooling performance are now clearer than before.

6.3 Limitations

The new mechanism is qualitative. The author cannot directly quantify it yet. Main challenges: quantify the impact of the secondary flows on the heat transfer, as well as the impact of the secondary flows on η (the temperature on the protected surface).

The liftoff and reattachment in a simple slot and the new schemes with high performance is an interesting phenomenon. Its underlying reason is still opened. A supposed reason emphasized in current thesis is end effect, which is a main difference between the current simulations and measurements. Theoretically, in film cooling flow of a simple slot that with infinity lateral dimension, the way of mainstream reaching slot trailing edge is unknown. A further investigation would lead to interesting new discover, if it is not caused by end effect.

The current simulation didn't consider the end effects. However, it always exits in a real film cooling geometry. This effect seems to have negative impact on η, needs to be decreased or removed. No matter whether the end effect is the reason leading to the liftoff and reattachment of the high performance new schemes, end effect needs to be further investigated.

References

[1] Koff, B. L. Gas Turbine Technology Evolution: A Designers Perspective. *J. Propuls. Power*, **2004**, *20* (4), 577–595. https://doi.org/10.2514/1.4361.

[2] Bunker, R. S. Gas Turbine Heat Transfer: Ten Remaining Hot Gas Path Challenges. *J. Turbomach.*, **2007**, *129* (2), 193–201. https://doi.org/10.1115/1.2464142.

[3] Bogard, D.; Thole, K. Gas Turbine Film Cooling. *J. Propuls. Power*, **2006**, *22* (2), 249–270. https://doi.org/10.2514/1.18034.

[4] Goldstein, R. J.; Eckert, E. R. G. Effects of Hole Geometry and Density on Three-Dimensional Film Cooling. *Int. J. Heat Mass Transf.*, **1974**, *17* (5), 595–607. https://doi.org/10.1016/0017-9310(74)90007-6.

[5] Sinha, A. K.; Bogard, D. G.; Crawford, M. E. Film-Cooling Effectiveness Downstream of a Single Row of Holes with Variable Density Ratio. *J. Turbomach.*, **1991**, *113* (3), 442–449. https://doi.org/10.1115/1.2927894.

[6] Gritsch, M.; Colban, W.; Schar, H.; Dobbeling, K. Effect of Hole Geometry on the Thermal Performance of Fan-Shaped Film Cooling Holes. *Trans. ASME J. Turbomach.*, **2005**, *127* (4), 718–725. https://doi.org/10.1115/1.2019315.

[7] Li, H. M.; Hassan, I. The Effects of Counterrotating Vortex Pair Intensity on Film-Cooling Effectiveness. *Heat Transf. Eng.*, **2015**, *36* (16), 1360–1370. https://doi.org/10.1080/01457632.2015.1003715.

[8] Yu, Y.; Yen, C.-H.; Shih, T. I.-P.; Chyu, M. K.; Gogineni, S. Film Cooling Effectiveness and Heat Transfer Coefficient Distributions around Diffusion Shaped Holes. *J. Heat Transf.*, **2002**, *124* (5), 820–827. https://doi.org/10.1115/1.1418367.

[9] Ghorab, M. G.; Hassan, I. G.; Lucas, T. An Experimental Investigation of Film Cooling Performance of Louver Scheme. *Int. J. Heat Mass Transf.*, **2011**, *54* (7–8), 1387–1399. https://doi.org/10.1016/j.ijheatmasstransfer.2010.12.002.

[10] Zhang, X. Z.; Hassan, I. Film Cooling Effectiveness of an Advanced-Louver Cooling Scheme for Gas Turbines. *J. Thermophys. Heat Transf.*, **2006**, *20* (4), 754–763. https://doi.org/10.2514/1.18898.

[11] Fric, T. F.; Roshko, A. Vortical Structure in the Wake of a Transverse Jet. *J. Fluid Mech.*, **1994**, *279*, 1–47. https://doi.org/10.1017/S0022112094003800.

[12] Haven, B. A.; Kurosaka, M. Kidney and Anti-Kidney Vortices in Crossflow Jets. *J. Fluid Mech.*, **1997**, *352*, 27–64. https://doi.org/10.1017/S0022112097007271.

[13] Haven, B. A.; Yamagata, D. K.; Kurosaka, M.; Yamawaki, S.; Maya, T. Anti-Kidney Pair of Vortices in Shaped Holes and Their Influence on Film Cooling Effectiveness. In *Proceedings of the ASME GT 1997*; American Society of Mechanical Engineers (ASME): Orlando, FL, United States, 1997; Vol. 3, pp 1–8. https://doi.org/10.1115/97-GT-045.

[14] Leylek, J. H.; Zerkle, R. D. Discrete-Jet Film Cooling: A Comparison of Computational Results with Experiments. *J. Turbomach.*, **1994**, *116* (3), 358–368.

[15] Walters, D. K.; Leylek, J. H. Detailed Analysis of Film-Cooling Physics. Part I: Streamwise Injection with Cylindrical Holes; ASME: 1998173935899, 1997; pp 14p-d]14p.

[16] Hyams, D. G.; Leylek, J. H. A Detailed Analysis of Film Cooling Physics: Part III-Streamwise Injection with Shaped Holes. *J. Turbomach.*, **2000**, *122* (1), 122–132. https://doi.org/10.1115/1.555435.

[17] Kim, S. I.; Hassan, I. Unsteady Simulations of a Film Cooling Flow from an Inclined Cylindrical Jet. *J. Thermophys. Heat Transf.*, **2010**, *24* (1), 145–156. https://doi.org/10.2514/1.33167.
[18] Yuan, L. L.; Street, R. L.; Ferziger, J. H. Large-Eddy Simulations of a Round Jet in Crossflow. *J. Fluid Mech.*, **1999**, *379*, 71–104. https://doi.org/10.1017/S0022112098003346.
[19] Recker, E.; Bosschaerts, W.; Wagemakers, R.; Hendrick, P.; Funke, H.; Börner, S. Experimental Study of a Round Jet in Cross-Flow at Low Momentum Ratio. **2010**, 13.
[20] Guo, X.; Schroder, W.; Meinke, M. Large-Eddy Simulations of Film Cooling Flows. *Comput. Fluids*, **2006**, *35* (6), 587–606. https://doi.org/10.1016/j.compfluid.2005.02.007.
[21] Marzouk, Y. M.; Ghoniem, A. F. Vorticity Structure and Evolution in a Transverse Jet. *J. Fluid Mech.*, **2007**, *575*, 267–305. https://doi.org/10.1017/S0022112006004411.
[22] Schlegel, F.; Wee, D.; Marzouk, Y. M.; Ghoniem, A. F. Contributions of the Wall Boundary Layer to the Formation of the Counter-Rotating Vortex Pair in Transverse Jets. *J. Fluid Mech.*, **2011**, *676*, 461–490. https://doi.org/10.1017/jfm.2011.59.
[23] Kusterer, K.; Bohn, D.; Sugimoto, T.; Tanaka, R. Double-Jet Ejection of Cooling Air for Improved Film Cooling. *J. Turbomach.*, **2007**, *129* (4), 809–815. https://doi.org/10.1115/1.2720508.
[24] Heidmann, J. D.; Ekkad, S. A Novel Antivortex Turbine Film-Cooling Hole Concept. *J. Turbomach.*, **2008**, *130* (3), 031020–031021. https://doi.org/10.1115/1.2777194.
[25] Dhungel, A.; Lu, Y.; Phillips, W.; Ekkad, S. V.; Heidmann, J. Film Cooling from a Row of Holes Supplemented with Antivortex Holes. *J. Turbomach.*, **2009**, *131* (2), 021007 (10 pp.). https://doi.org/10.1115/1.2950059.
[26] Ely, M. J.; Jubran, B. A. A Numerical Evaluation on the Effect of Sister Holes on Film Cooling Effectiveness and the Surrounding Flow Field. *Heat Mass Transf.*, **2009**, *45* (11), 1435–1446. https://doi.org/10.1007/s00231-009-0523-8.
[27] Ely, M. J.; Jubran, B. A. A Numerical Study on Improving Large Angle Film Cooling Performance through the Use of Sister Holes. *Numer. Heat Transf. Part Appl.*, **2009**, *55* (7), 634–653. https://doi.org/10.1080/10407780902821532.
[28] Bunker, R. S. Film Cooling: Breaking the Limits of Diffusion Shaped Holes. *Heat Transf. Res. HTR*, **2010**, *41* (6), 627–650. https://doi.org/10.1615/HeatTransRes.v41.i6.40.
[29] Baldauf, S.; Scheurlen, M.; Schulz, A.; Wittig, S. Correlation of Film-Cooling Effectiveness from Thermographic Measurements at Enginelike Conditions. *J. Turbomach.*, **2002**, *124* (4), 686–698. https://doi.org/10.1115/1.1504443.
[30] Colban, W. F.; Thole, K. A.; Bogard, D. A Film-Cooling Correlation for Shaped Holes on a Flat-Plate Surface. *J. Turbomach.*, **2011**, *133* (1), 011002 (11 pp.). https://doi.org/10.1115/1.4002064.
[31] Yao, J.; Xu, J.; Zhang, K.; Lei, J.; Wright, L. M. Interaction of Flow and Film-Cooling Effectiveness between Double-Jet Film-Cooling Holes with Various Spanwise Distances. *J. Turbomach.*, **2018**, *140* (12), 121011 (8 pages). https://doi.org/10.1115/1.4041809.
[32] Heidmann, J. D.; Ekkad, S. A Novel Anti-Vortex Turbine Film Cooling Hole Concept. In *Proceedings of the ASME Turbo Expo*; American Society of Mechanical Engineers: Montreal, Que., Canada, 2007; Vol. 4 PART A, pp 487–496. https://doi.org/10.1115/GT2007-27528.

[33] Li, H. M.; Ghaly, W.; Hassan, I. The Formation of Counter-Rotating Vortex Pair and the Nature of Liftoff-Reattachment in Film-Cooling Flow. *Fluids*, **2016**, *1* (4), 39. https://doi.org/10.3390/fluids1040039.
[34] Sargison, J. E.; Guo, S. M.; Oldfield, M. L. G.; Lock, G. D.; Rawlinson, A. J. A Converging Slot-Hole Film-Cooling Geometry-Part 1: Low-Speed Flat-Plate Heat Transfer and Loss. *J. Turbomach.*, **2002**, *124* (3), 453–460. https://doi.org/10.1115/1.1459735.
[35] Bunker, R. S. Film Cooling Effectiveness Due to Discrete Holes within a Transverse Surface Slot. In *American Society of Mechanical Engineers, International Gas Turbine Institute, Turbo Expo (Publication) IGTI*; American Society of Mechanical Engineers: Amsterdam, Netherlands, 2002; Vol. 3 A, pp 129–138. https://doi.org/10.1115/GT2002-30178.
[36] Waye, S. K.; Bogard, D. G. High-Resolution Film Cooling Effectiveness Comparison of Axial and Compound Angle Holes on the Suction Side of a Turbine Vane. *J. Turbomach.*, **2007**, *129* (2), 202–211. https://doi.org/10.1115/1.2448016.
[37] Bunker, R. S. A Study of Mesh-Fed Slot Film Cooling. *J. Turbomach.*, **2011**, *133* (1), 011022 (8 pages). https://doi.org/10.1115/1.4000548.
[38] Davidson, F. T.; Bogard, D. G.; Bruce-Black, J.; Johns, D. R. Adiabatic Effectiveness on the Suction Side of a Turbine Vane and the Effects of Curvature at the Point of Film Injection. In *Proceedings of ASME Turbo Expo 2008: Power for Land, Sea, Air*; American Society of Mechanical Engineers (ASME): Berlin, Germany, 2008; Vol. 4, pp 1137–1146. https://doi.org/10.1115/GT2008-51350.
[39] Bruce-Black, J.; Davidson, F. T.; Bogard, D. G.; Johns, D. R. Practical Slot Configurations for Turbine Film Cooling Applications. *J. Turbomach.*, **2011**, *133* (3), 031020 (8 pp.). https://doi.org/10.1115/1.4002413.
[40] Wang, Z.; Ireland, P. T.; Jones, T. V.; Davenport, R. A Colour Image Processing System for Transient Liquid Crystal Heat Transfer Experiments; American Society of Mechanical Engineers (ASME): 20151100634009, 1994; Vol. 4, p International Gas Turbine Institute. https://doi.org/10.1115/94GT290.
[41] Wang, Z.; Ireland, P. T.; Jones, T. V. An Advanced Method of Processing Liquid Crystal Video Signals from Transient Heat Transfer Experiments; American Society of Mechanical Engineers: 20151400701282, 1993; Vol. 3B, p International Gas Turbine Institute. https://doi.org/10.1115/93-GT-282.
[42] Drost, U.; BoIcs, A.; Hoffs, A. Utilization of the Transient Liquid Crystal Technique for Film Cooling Effectiveness and Heat Transfer Investigations on a Flat Plate and a Turbine Airfoil; American Society of Mechanical Engineers (ASME): 20162402499560, 1997; Vol. 3. https://doi.org/10.1115/97-GT-026.
[43] Ekkad, S. V.; Han, J. C.; Du, H. Detailed Film Cooling Measurements on a Cylindrical Leading Edge Model: Effect of Free-Stream Turbulence and Coolant Density. *J. Turbomach.*, **1998**, *120* (4), 799–807. https://doi.org/10.1115/1.2841792.
[44] Hassan, O.; Hassan, I. Experimental Investigations of the Film Cooling Effectiveness of a Micro-Tangential-Jet Scheme on a Gas Turbine Vane. *Int. J. Heat Mass Transf.*, **2013**, *61*, 158–171. https://doi.org/10.1016/j.ijheatmasstransfer.2013.02.001.
[45] Elnady, T.; Hassan, I.; Kadem, L. Experimental Investigation of Louver Cooling Scheme on Gas Turbine Stator. *Heat Transf. Eng.*, **2016**, *37* (1), 82–105. https://doi.org/10.1080/01457632.2015.1042346.

[46] Li, H.-M.; Ghaly, W.; Hassan, I. EXPERIMENTAL INVESTIGATIONS OF A COMB-LIKE FILM-COOLING SCHEME; ASME - JSME - KSME Joint Fluids Engineering Conference 2019, 2019; Vol. AJKFLUIDS2019-4695.
[47] Li, H.; Zhao, G.; Zhou, Z.; Wang, H.; You, R. The Characteristics and Divergence of Fan-Shaped and Cylindrical Holes on the Suction Side of a Turbine Blade under Rotating Conditions. *Int. J. Heat Mass Transf.*, **2019**, *139*, 432–441. https://doi.org/10.1016/j.ijheatmasstransfer.2019.05.045.
[48] Wright, L. M.; McClain, S. T.; Clemenson, M. D. Effect of Density Ratio on Flat Plate Film Cooling With Shaped Holes Using PSP. *J. Turbomach.*, **2011**, *133* (4), 041011 (11 pp.). https://doi.org/10.1115/1.4002988.
[49] Farmer, J. P.; Seager, D. J.; Liburdy, J. A. Effect of Shaping Inclined Slots on Film Cooling Effectiveness and Heat Transfer Coefficient; ASME: 1998173935969, 1997; p ASME. https://doi.org/10.1115/97-GT-339.
[50] Saumweber, C.; Schulz, A. Free-Stream Effects on the Cooling Performance of Cylindrical and Fan-Shaped Cooling Holes. *J. Turbomach.*, **2012**, *134* (6), 061007 (12 pp.). https://doi.org/10.1115/1.4006287.
[51] Li, H.-M.; Ghaly, W.; Hassan, I. Experimental And Computational Investigations of A Comb-Like Film-Cooling Scheme. *Heat Transf. Eng.*, **2021**, *43* (17).
[52] Tan, X.-M.; Zhang, J.-Z.; Cai, Q.-Z. Effects of Pin-Fin Shapes on Mesh-Fed Slot Film Cooling for a Flat-Plate Model. *J. Therm. Sci. Eng. Appl.*, **2019**, *11* (3), 031002 (11 pages). https://doi.org/10.1115/1.4041882.
[53] Soma, L. W.; Ames, F. E.; Acharya, S. The Influence of Turbulence and Reynolds Number on Slot Film Cooling over the Downstream Pressure Surface. In *ASME Turbo Expo 2019: Turbomachinery Technical Conference and Exposition*; Proceedings of the ASME Turbo Expo; American Society of Mechanical Engineers (ASME): Phoenix, AZ, United states, 2019; Vol. 5B-2019, p V05BT19A007-12 pages. https://doi.org/10.1115/GT2019-90508.
[54] Busche, M. L.; Kingery, J. E.; Ames, F. E. Slot Film Cooling in an Accelerating Boundary Layer with High Free-Stream Turbulence. In *ASME Turbo Expo 2014: Turbine Technical Conference and Exposition*; American Society of Mechanical Engineers (ASME): Düsseldorf, Germany, 2014; Vol. 5B, p V05BT13A009 12pages. https://doi.org/10.1115/GT2014-25360.
[55] Kanani, Y.; Acharya, S.; Ames, F. Simulations of Slot Film-Cooling with Freestream Acceleration and Turbulence. *J. Turbomach.*, **2018**, *140* (4), 041005-1–11. https://doi.org/10.1115/1.4038877.
[56] Moffat, R. J. Describing the Uncertainties in Experimental Results. *Exp. Therm. Fluid Sci.*, **1988**, *1* (1), 3–17.
[57] Jia, R.; Sunden, B.; Miron, P.; Leger, B. A Numerical and Experimental Investigation of the Slot Film-Cooling Jet with Various Angles. *J. Turbomach.*, **2005**, *127* (3), 635–645. https://doi.org/10.1115/1.1929821.
[58] Li, H. M.; Ghaly, W.; Hassan, I. The Formation of Counter-Rotating Vortex Pair and the Nature of Liftoff-Reattachment in Film-Cooling Flow. *Fluids*, **2016**, *1* (4), 39 (21 pages). https://doi.org/10.3390/fluids1040039.
[59] Li, H.-M.; Ghaly, W.; Hassan, I. On the Use of High-Aspect-Ratio Film Cooling Scheme. *Heat Transf. Eng.*, **2021**, *43* (6), 1–19. https://doi.org/10.1080/01457632.2021.1887642.

[60] Sautner, M.; Clouser, S.; Han, J.-C. Determination of Surface Heat Transfer and Film Cooling Effectiveness in Unsteady Wake Flow Conditions. In *AGARD Conference Proceedings 527*; AGARD Conference Proceedings; AGARD, 1993; p 6 (12 pages).
[61] Downs, J. P.; Landis, K. K. Turbine Cooling Systems Design - Past, Present and Future. In *Proceedings of ASME Turbo Expo*; Proceedings of the ASME Turbo Expo; American Society of Mechanical Engineers (ASME): Orlando, FL, United States, 2009; Vol. 3, pp 819–828. https://doi.org/10.1115/GT2009-59991.
[62] Bunker, R. S. A Review of Shaped Hole Turbine Film-Cooling Technology. *J. Heat Transf.*, **2005**, *127* (4), 441–453. https://doi.org/10.1115/1.1860562.
[63] Cunha, F. J.; Abdel-Messeh, W.; Chyu, M. K. Thermal Analysis and Durability Design Strategies for Gas Turbine Airfoils. In *Proceedings of the ASME Turbo Expo*; American Society of Mechanical Engineers: Barcelona, Spain, 2006; pp 787–803. https://doi.org/10.1115/GT2006-91013.
[64] Ekkad, S.; Han, J.-C. A Review of Hole Geometry and Coolant Density Effect on Film Cooling. *Front. Heat Mass Transf. FHMT*, **2015**, *6* (1), 1–14. https://doi.org/10.5098/hmt.6.8.
[65] Li, H.-M.; Ghaly, W.; Hassan, I. Numerical Investigations of a Comb-like Film-Cooling Scheme. In *Proceedings of CSME-CFDSC Congress 2019*; CSME-CFDSC Congress 2019: London, Ontario, Canada, 2019; Vol. CSME-CFDSC Congress 2019, pp 1–9.
[66] Wang, Z.; Ireland, P. T.; Jones, T. V. Advanced Method of Processing Liquid Crystal Video Signals from Transient Heat Transfer Experiments. In *International Gas Turbine and Aeroengine Congress and Exposition*; American Society of Mechanical Engineers (Paper); ASME: Cincinnati, OH, USA, 1993; pp 1–7. https://doi.org/Colour image processing system for transient liquid crystal heat transfer experiments.
[67] Wang, Z.; Ireland, P. T.; Jones, T. V.; Davenport, R. Colour Image Processing System for Transient Liquid Crystal Heat Transfer Experiments. In *Proceedings of the International Gas Turbine and Aeroengine Congress and Exposition*; American Society of Mechanical Engineers (Paper); Publ by ASME: Hague, Neth, 1994; pp 1–11. https://doi.org/10.1115/94-GT-290.
[68] Drost, U.; BOIcs, A.; Hoffs, A. Utilization of the Transient Liquid Crystal Technique for Film Cooling Effectiveness and Heat Transfer Investigations on a Flat Plate and a Turbine Airfoil. In *Proceedings of the ASME Turbo Expo 1997*; Proceedings of the ASME Turbo Expo; American Society of Mechanical Engineers (ASME): Orlando, FL, United States, 1997; Vol. 3, pp 1–9. https://doi.org/10.1115/97-GT-026.
[69] Li, H.; Han, F.; Ma, Y.; Wang, H.; Zhou, Z.; Tao, Z. Experimental Investigation on the Effects of Rotation and the Blowing Ratio on the Leading-Edge Film Cooling of a Twist Turbine Blade. *Int. J. Heat Mass Transf.*, **2019**, *129*, 47–58. https://doi.org/10.1016/j.ijheatmasstransfer.2018.09.005.
[70] Farmer, J. P.; Seager, D. J.; Liburdy, J. A. The Effect of Shaping Inclined Slots on Film Cooling Effectiveness and Heat Transfer Coefficient. In *ASME 1997 International Gas Turbine and Aeroengine Congress and Exhibition*; Proceedings of the ASME Turbo Expo; American Society of Mechanical Engineers (ASME): Orlando, FL, United States, 1997; Vol. 3, p V003T09A068 8 pages. https://doi.org/10.1115/97-GT-339.